SCUOLA DI DOTTORATO
UNIVERSITÀ DEGLI STUDI DI MILANO-BICOCCA

Dipartimento di / Department of
FISICA

Dottorato di Ricerca in / PhD program FISICA E ASTRONOMIA Ciclo / Cycle XXXVI

Curriculum in ASTROFISICA

DYNAMICS OF TIDAL DISRUPTIONS AND EXTREME MASS RATIO INSPIRALS IN GALACTIC NUCLEI

Cognome / Surname BROGGI Nome / Name LUCA

Matricola / Registration number 792680

Tutore / Tutor: PROF. MASSIMO DOTTI

Supervisor: PROF. ALBERTO SESANA

Coordinatore / Coordinator: PROF. STEFANO RAGAZZI

ANNO ACCADEMICO / ACADEMIC YEAR 2022/2023

UNIVERSITÀ DEGLI STUDI DI MILANO BICOCCA

Dynamics of tidal disruptions and extreme mass ratio inspirals in galactic nuclei

Luca Broggi

Supervisor prof. Alberto Sesana

Tutor prof. Massimo Dotti

Departimento di Fisica «G. Occhialini»

Scuola di Scienze

A Sofía.

Con l'augurio di un futuro sorprendente.

Contents

List of Figures

List of Tables

1

Introduction

In this chapter, I introduce the framework of my research. After an overview, I focus on the properties of nuclear clusters, tidal disruption events and extreme mass ratio inspirals. Then, I introduce the theory of loss cone, the theory that deals with the stochastic origin of tidal disruptions and extreme mass ratio inspirals in nuclear star clusters and dense stellar system. Finally, I present the considerations that motivate the scientific research I conducted during my doctoral studies.

1.1 | Overview

Black Holes (BHs) are among the fascinating and mysterious subjects of the most recent and advanced research in Astrophysics and Cosmology. They are objects so dense that neither massive nor massless particles can escape their horizon. BHs were proposed as the first solution of Einstein field equations by Karl Schwarzschild, and their origin is one of the most puzzling questions that the scientific community has been investigating for more than a century. Chandrasekhar proposed that stellar black holes (of mass below $\simeq 100\, M_\odot$) are the final stage of the evolution of massive star. Successive mergers among stellar black holes may then result into a heavier intermediate-mass black hole (IMBH, with mass $\simeq 10^5\, M_\odot$) that could grow by means of accretion. Larger black holes – found at the centres of galaxies –are known as massive black holes (MBHs) or supermassive black holes (SMBH), and their origin is not yet fully understood (Kormendy and Ho, 2013; Merritt, 2013).

The first indirect evidence of the existence of stellar BHs dates back to the early 70s with the observations of Cygnus X1, and the first direct evidence of the existence of stellar black hole binaries came in 2015 with GW150914 (LIGO Scientific Collaboration and Virgo Collaboration et al., 2016). Ever since, more and more neutron star - black

Figure 1.1: (Credits: NASA) An artist's concept of a tidal disruption event that happens when a star passes fatally close to a supermassive black hole, which reacts by launching a relativistic jet.

hole and black hole - black hole mergers have been detected via ground based gravitational waves (GWs) observatories: LIGO (Laser Interferometer Gravitational-Wave Observatory) and Virgo.

Current facilities permit to observe the dramatic effects of SMBHs on their host environment, and in particular their accretion on the gas in the proximity. This process emits light, which makes MBHs detectable as quasars or active galactic nuclei. In the case of the MBH in the galactic centre of the Milky Way and in M87, it was also possible to capture the glow of gas just outside the horizon thanks to the observations produced by the EHT collaboration (Collaboration et al., 2019, Event Horizon Telescope).

In addition to constant accretion of gas, there is a class of transient events that happens in the proximity of MBHs and can be observed through its electromagnetic emission: the disruption of stars due to the strength of tidal forces exerted by the MBH itself (see Fig. 1.1 for an artistic representation of a tidal disruption event, TDE). These events are very luminous and emit over a broad range of frequencies with characteristic signatures (Lodato and Rossi, 2011), and may happen often enough that their detection rates can probe the underlying distribution of black holes (Stone and Metzger, 2016). As of today, the number of observed transient events compatible with a Tidal Disruption Event (TDE) is of the order of 100, a number that is anticipated to rapidly grow in the next years (Stone et al., 2020) thanks to high-sensitive time domain surveys like LSST (Bricman and Gomboc, 2020, Large Synaptic Survey Telescope), and the dedicated space probe ULTRASAT (Ultraviolet Transient Astronomy Satellite; Sagiv et al., 2014). Based on theoretical predictions, these probes will yield a sufficient number of detec-

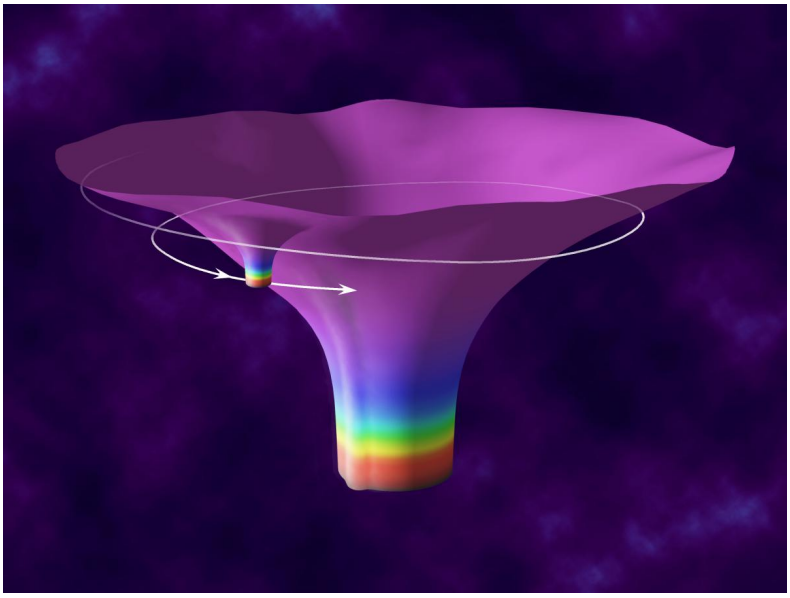

Figure 1.2: (Credits: NASA) Artist impression of the spacetime generated by an extreme mass ratio inspiral.

tions to obtain statistically robust constraints on the underlying population of MBHs and IMBHs that are generally not luminous enough to be detected as persistently accreting sources.

Another class of transient events occurs when a compact object with zero tidal deformability, like a stellar black hole, approaches a MBH so deeply that it enters its event horizon. In this case, one can have a direct plunge (DP), with a weak pulse of gravitational waves emission, or a gradual emission of gravitational waves that shrink the orbit of the stellar BH over many orbital periods, a phenomenon known as Extreme Mass Ratio Inspiral (EMRI, see Fig. 1.2 for an artistic representation). Unfortunately, the frequency of their signal is too low to be detected by ground-based interferometers, but future Gravitational Waves detectors like LISA (Large Interferometer Space Antenna) will likely detect a number of them (Amaro-Seoane, 2020; Babak et al., 2017), hopefully contributing to our knowledge on the population of black holes (Barack and Cutler, 2007).

The origin of the stellar objects that will end up in a TDE, a DP or an EMRI is the subject of active research. At the moment, a promising mechanism for their origin happens in the so-called nuclear star clusters. Those are extremely dense distributions of stellar objects often found in the nucleus of galaxies, surrounding the MBH hosted by the nucleus itself. While the properties of nuclear clusters are still uncertain (Neumayer

et al., 2020), their typical size is around $0.1 - 1\%$ of the observed size of a galaxy and extend over the regions dominated by the gravitational influence of the central black hole. These environments are so crowded that stars will often cross each other in their motion. These random encounters can change the orbital parameters of stellar objects, and some of them may be pushed by these interactions on deeply penetrating orbits resulting in a TDE, a DP, or an EMRI.

The theoretical framework to study the stochastic evolution of a stellar system has been developed in the 70s of the 20th century for TDEs, and was later adapted to account for the formation of DPs and EMRIs at the beginning of the 21st century. The theory is capable of predicting the rate of these events from a model of the stellar distribution, even accounting for nuclear evolution. In this work, we will present the first public implementation of the state-of-the-art loss cone theory. Moreover, we will explore some attempts towards a deeper understanding of the discrepancy between theoretical and observed rates, and we will consistently build an advanced theory for assessing EMRI rates.

1.2 | Plunges and TDEs in Galactic Nuclei

Massive black holes (MBHs) with masses in the range $10^4 - 10^{10} M_\odot$ are found to reside in the centre of many galaxies (Kormendy and Ho, 2013) and they are often surrounded by very dense, compact stellar systems, whose densities can reach $10^7\ M_\odot\ \mathrm{pc}^{-3}$, named nuclear star clusters (Neumayer et al., 2020). It is hard to detect and distinguish the properties of the nucleus, but current observations suggest correlations with the structure of the galaxy and the central massive black hole. More in general, observations show a correlation between the velocity dispersion σ of galaxies and the mass $M_\bullet$ of their central MBHs, generally known as the mass–sigma relation (Gültekin et al., 2009; Kormendy and Ho, 2013)

$$\sigma \simeq 70\ \mathrm{Km/s} \left(\frac{M_\bullet}{1.53\, 10^6\, M_\odot} \right)^{1/4.24} \tag{1.1}$$

which can be used to define the influence radius, r_h, delimiting the region where the influence of the central MBH will mostly contribute to the orbital energy of a star

$$\frac{G M_\bullet}{2\, r_h} = \frac{1}{2}\sigma^2 \qquad \Rightarrow \qquad r_h = \frac{G\, M_\bullet}{\sigma^2} \simeq 1.4\,\mathrm{pc} \left(\frac{M_\bullet}{1.53\, 10^6 M_\odot} \right)^{0.53} . \tag{1.2}$$

We therefore expect the nuclear stellar cluster to have this typical length-scale.

Within such a crowded environment, stars and compact objects are randomly deflected by relaxation processes and can be scattered onto very low angular momentum

orbits, closely approaching the central MBHs, and giving rise to violent and exotic phenomena (Merritt, 2013).

1.2.1 | Tidal disruption events

One of the processes through which a massive black hole (MBH) can reveal itself and increase its mass is via a so-called stellar tidal disruption event (Evans and Kochanek, 1989; Hills, 1988; Phinney, 1989). A TDE occurs when a star gets too close to the MBH so that the MBH tidal shear overcomes the star self-gravity, resulting in the disruption and accretion of the star by the MBH (e.g. Lodato et al., 2009; Rees, 1988). The event produces an extremely bright electromagnetic flare, observable up to cosmological distances. TDEs are very interesting phenomena in many ways: in particular, they can probe the dynamical properties of the galactic nuclei in which they are generated (see e.g. the recent review by Stone et al., 2020). Theoretical works focusing on the dynamical origin of TDEs typically assess their occurrence rate given the properties of the MBH and host environment (e.g. Magorrian and Tremaine, 1999; Merritt and Wang, 2005; Ulmer, 1999). If the central MBH exceeds the limit known as Hills mass ($\sim 10^8 M_\odot$ for main sequence stars), stars will plunge into the horizon without producing detectable flares (Stone et al., 2020).

Several TDEs have been observed in recent years in the optical, UV and X-ray band (Saxton et al., 2021; van Velzen et al., 2021). This growing body of TDE observations (now of the order of ~ 100) has sparked growing interest in assessing TDE rates and has recently allowed to compare predicted TDE rates to the actually observed ones. In particular, recent comparisons between theoretical (Stone and Metzger, 2016; Stone et al., 2020) and observational (Lin et al., 2022; Sazonov et al., 2021; van Velzen et al., 2021; Yao et al., 2023) TDE rate estimates suggest that current detections are on the lower end of the predicted ones (e.g. French et al., 2020), that have been computed according to the classical loss cone theory (see Section 1.3).

1.2.2 | Extreme mass ratio inspirals and Plunges

Compact objects, in particular stellar black holes (sBHs), cannot be torn apart by tidal forces, but if they find themselves on an orbit that reaches a close enough separation to the MBH, they may eventually enter its horizon emitting gravitational waves (GWs) along the way in a plunge.

If a compact object gets deflected on an orbit for which GW emission is significant, but the orbital decay is slow, it may give rise to a detectable, long-lasting GW signal,

eventually plunging onto the MBH after many cycles (see Amaro-Seoane, 2018; Amaro-Seoane et al., 2007, for comprehensive reviews). If the MBH mass is in the range of $\sim 10^4 - 10^7 M_\odot$, the emitted GW signal falls in the mHz frequency window and is anticipated to be one of the primary sources for LISA, (Amaro-Seoane et al., 2017; Babak et al., 2017). Because of the very unequal mass of the two objects involved in the system, those GW sources are called extreme mass ratio inspirals (EMRIs). Besides producing EMRIs, sBHs can also be deflected onto *head on collisions* with the central MBHs, in a Direct Plunge in the event horizon without experiencing any significant inspiral (and GW emission). EMRIs will offer an unprecedented way to probe the immediate vicinity of an MBH, allowing to test General Relativity in the strong field regime through the analysis of the emitted GW signals (Barack and Cutler, 2007; Gair et al., 2013), unveiling the cosmic population of dormant MBHs (Gair et al., 2010), and providing a powerful tool to measure the expansion rate of the Universe (Laghi et al., 2021; MacLeod and Hogan, 2008). These sources can be detected by LISA either as single events (e.g Barack and Cutler, 2004b) or as a cumulative background signal (Barack and Cutler, 2004a; Bonetti and Sesana, 2020).

1.3 | Relaxation and Loss cone theory

Several physical processes can contribute to the cosmic rate of TDE, EMRI and DP, including: tidal separation of binaries (Miller et al., 2005), perturbations due to a MBH binary (Bode and Wegg, 2014; Chen et al., 2011; Mazzolari et al., 2022; Naoz et al., 2022), capture and migration within AGN accretion disks (Levin, 2007; Pan and Yang, 2021) and supernovae explosions (Bortolas and Mapelli, 2019). Still, the main formation mechanism is expected to be associated with dynamical relaxation processes within dense galactic nuclei (e.g. Amaro-Seoane, 2018, and reference therein.). The idea is to combine a statistical treatment of random encounters, with a simple model of TDEs/Plunges where the stellar object is destroyed as soon as it reaches a pericentre inside the loss cone radius (see Fig. 1.3 for a diagrammatic representation of the model). In this context, rates can be obtained via different approaches, perhaps the most popular one being solving the steady-state Fokker-Planck (FP) equation for the distribution function (DF) of the system (Amaro-Seoane and Preto, 2011; Bar-Or and Alexander, 2016; Merritt, 2015; Pfister et al., 2020). In the underlying physical model, by setting the inflow of objects in the galactic nucleus, the steady-state FP equation is solved to obtain a constant DF. The latter is generally constructed in the energy-angular momentum space in a 2D treatment, or in an effective 1D treatment by integrating over angular momentum. An-

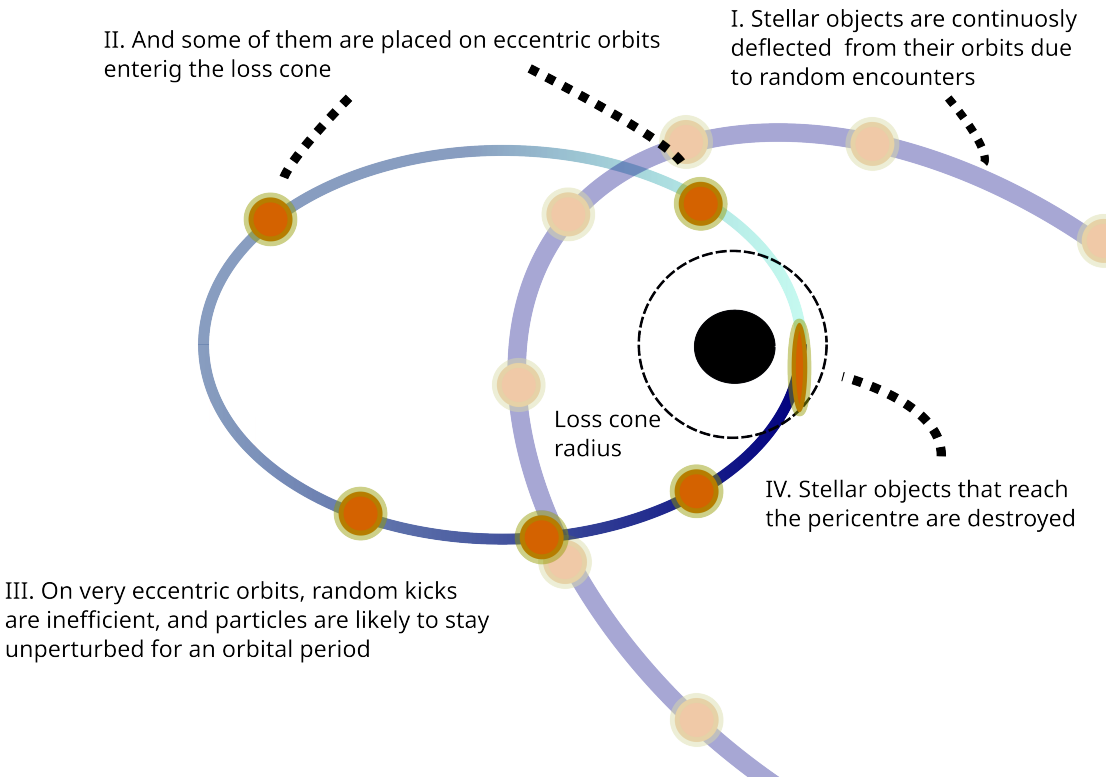

Figure 1.3: Diagrammatic representation of how TDEs and Plunges are modelled in classical loss cone theory. Particles (stars or a compact objects) found in the central regions of galactic nuclei are continuously subject to random encounters that alter their orbits; and some will be deflected on orbits penetrating the loss cone radius. The pericentre of these orbits can be so small that motion is nearly radial, and stochastic kicks are inefficient due to the small cross-section. Therefore, they are likely to complete their orbit up to the pericentre, where they are destroyed.

other possibility widely explored in literature is the solution of the stochastic evolution equation with Monte Carlo methods (Fragione and Sari, 2018; Hopman and Alexander, 2005; Sari and Fragione, 2019; Shapiro and Marchant, 1978; Zhang and Seoane, 2023).

The statistical model of collisional evolution of stellar systems in the gravitational field of a central massive black hole is based on the work by Chandrasekhar (1942), later complemented with the loss cone theory by Lightman and Shapiro (1977), Shapiro and Marchant (1978) and Cohn and Kulsrud (1978). This theory has been developed to address the problem of computing the TDE rate in a stellar cluster surrounding an MBH, relying on the assumption that the disruption of a star happens as soon as the

star reaches a pericentre smaller than

$$r_{\rm TDE} \approx \eta\, r_\star \left(\frac{M_\bullet}{m_\star}\right)^{1/3} \tag{1.3}$$

known as the *tidal disruption radius*. Here $m_\star$ and $r_\star$ respectively represent the stellar mass and radius, while $M_\bullet$ is the MBH mass. The form factor η is of order 1 and depends on the structure of the star considered.

The same approach has been later applied to the process of gravitational captures of a compact object, since the process happens as soon as the pericentre is smaller than the *closest parabolic approach*[1] (Hopman and Alexander, 2005; Merritt, 2013)

$$r_{\rm Plunge} = 4\,\frac{G\,M_\bullet}{c^2} \tag{1.4}$$

where c is the speed of light.

The threshold radius of these phenomena is known as the loss cone radius $r_{\rm LC}$, since from any point in space, the locus of orbits entering this radius appears as a cone. The literature on the subject is vast, and a nice summary can be found in Amaro-Seoane (2018); Stone et al. (2020). As mentioned, FP (and other approximate) models are generally used to describe equilibrium solutions for spherically symmetric systems in the energy-angular momentum space, and sBHs capture rates are derived in the steady-state approximation.

The classical loss cone theory has been used to predict a rate of $\gtrsim 10^{-4}$ yr^{-1} TDEs per galaxy (Stone and Metzger, 2016; Stone et al., 2020). This has been achieved by modelling the stellar distribution function of observed local galaxies and assuming the expected relaxed distribution of angular momentum at each energy, derived by Cohn and Kulsrud (1978). Early estimates from detections of TDEs are of $\sim 10^{-5} - 10^{-4}$ yr^{-1} TDEs per galaxy, on the lower end of the predictions.

1.4 | Motivation for this work

Constraining the distribution of compact objects in galactic nuclei is extremely challenging (Kormendy and Ho, 2013; Neumayer et al., 2020), therefore the current estimates for the EMRI detection rate are based on steady-state solutions of the FP equation. This assumption, however, is problematic when transferred to realistic astrophysical systems. Most notably, sBHs capture rates diverge for small MBHs and are inconsistent with the

[1] The closest parabolic approach is studied in the framework of General Relativity. When far from the central black hole, and the potential is locally Keplerian, the angular momentum of the orbit corresponds to a pericentre $r_{\rm Plunge,\,Kep} = J^2/(2\,G\,M_\bullet) = 8\,G\,M_\bullet/c^2$.

continuous supply of compact objects needed. For example, standard EMRI rates derived with those models are of the order of $10^3\,\mathrm{Gyr}^{-1}$ for a $10^5 M_\odot$ central MBH, and direct plunge rates are estimated to be at least an order of magnitude higher (Bar-Or and Alexander, 2016). This poses two issues to the steady-state picture. First, the need of supplying MBHs in the low mass end with 10^4 sBHs per Gyr. Second, the significant mass growth of the central MBH, which violates the condition of fixed central potential assumed in FP calculations. Moreover, such high rates would exclude the existence of intermediate MBHs (below $10^5\mathrm{M}_\odot$) in galaxy nuclei at the present day because of the large mass accretion. Such rates will require further modelling before they can be combined with theoretical MBH population models to compute LISA detection rates. This is currently done by artificially capping the EMRI rate to avoid MBH overgrowth at the faint end of the mass function, as described in Babak et al. (2017). This is obviously unsatisfactory, and a more consistent approach, able to account for the mass growth of the MBH and the finite supply of sBHs, is particularly desirable. Such a framework will be critical in order to make detailed LISA predictions and to prepare the tools needed to extract those intricate, overlapping signals from the data stream (Babak et al., 2010). As the typical orbital parameters for the production of EMRIs correspond to regions of phase space where the anisotropy of the DF due to the loss cone is relevant (Pan and Yang, 2021), the effective 1D treatment of the system (Vasiliev, 2017) may be inadequate for these phenomena, suggesting that a 2D approach is preferable. This compelling call motivated us to develop the first public code to solve the time-dependent 2D orbit-averaged Fokker-Planck equation.

In parallel to the numerical implementation of the 2D FP on models of nuclear star clusters, we started a careful revision of the classical loss cone theory. A key result of Cohn and Kulsrud (1978) is the prediction of the distribution in angular momentum of the stars, that is crucial to the 2D FP evolution since it determines the rate of particles crossing r_{LC}. The model relies on a simple prescription: either the pericentre is smaller than r_{LC} and a total disruption or plunge occurs, otherwise stellar objects with larger pericentres are assumed to remain unperturbed. However, reality is more complex: a star that is fully destroyed at pericentre closer than r_{TDE}, will not be unperturbed if the pericentre is larger: a portion of the star may be accreted by the MBH, with the stellar remnant surviving the interaction giving rise to a partial disruption (e.g. Mainetti et al., 2017; Ryu et al., 2020a). This event can be repeated if two-body relaxation allows the stellar remnant to fall back again onto the MBH and the first disruption did not substantially perturb the original orbit; only for sufficiently large pericentres, the star would remain unperturbed. This motivated us towards a revision and extension of classical loss cone theory to include the effects of partial tidal disruptions.

The expected relaxed profile in angular momentum is crucial for the applications of loss cone theory. With our code, we are able to test the agreement of this prediction with solutions of the orbit averaged Fokker-Planck equation, showing that the distribution of stellar black holes strongly deviates from the Cohn-Kulsrud profile. We have identified the flaw in the original argument, and extended loss cone theory for reliable estimates of plunge rates.

The manuscript is organized as follows: in Chapter 2 I derive the Fokker-Planck equation for stellar systems and its 2D and 1D approximations, we compute in detail the diffusion coefficients for all these equations, and discuss the application of the Fokker-Planck formalism to multi-mass stellar systems; in Chapter 3 I present the results of classical loss cone theory relative to the computation of the rate of TDEs, DPs and EMRIs, with a detailed solution of the Fokker-Planck equation inside the loss cone; in Chapter 4 I present a 2D Fokker-Planck solver, together with the results of simulations of galactic nuclei and the rate of TDEs, DPs, and EMRIs produced; in Chapter 5 I present an approach for the inclusion of partial TDEs in classical loss cone theory, and some preliminary results on the extension of standard loss cone theory to include the phenomenon; in Chapter 6 I show the limits of classical loss cone theory when compared to 2D Fokker-Planck simulations, and some preliminary work on the discrepancy to consequently improve the boundary conditions of the 2D FP solver at the loss cone. Finally, an overview of the scientific conclusions reached with our work is presented in Chapter 7.

2

Stochastic description of 2-body encounters

At once Dantes resolved to follow the brave example of his energetic companion, and to remember that what has once been done may be done again.
— *Alexandre Dumas, The Count of Monte Cristo*

This chapter begins with a review of the current models of the relaxation of galactic nuclei based on the local Fokker-Planck equation, that describes the stochastic evolution of particles in nuclear star clusters. We will then derive from the local equation some approximate analogues: the orbit averaged Fokker-Planck equation – that describes the evolution of particles in the space of orbital parameters, and the ergodic Fokker-Planck equation – that describes the evolution of a system of particles fully characterized by their energy distribution. After deriving the advection and diffusion coefficients for the equations aforementioned, the Fokker-Planck formalism will be applied self-consistently to a system of stars, where the advection and diffusion coefficients will be computed from the distribution of the same stars.

2.1 | Orbits in galactic nuclei

The prototypical system we consider is composed of these three essential components:

- a central MBH of mass $M_\bullet$,
- a spherical distribution of stars with mass m_s,
- a spherical, subdominant distribution of stellar mass compact objects with mass $m_{\rm BH}$.

To describe the system with a clear notation, we introduce polar coordinates for positions $\{r,\ \theta,\ \phi\}$ such that a particle at a distance $\boldsymbol{x} = (x_1,\ x_2,\ x_3)$ from the central MBH is described by

$$r = \sqrt{x_1^2 + x_2^2} \qquad \tan\phi = \frac{x_2}{x_1} \qquad \cos\theta = \frac{x_3}{\sqrt{x_1^2 + x_2^2}}\,. \tag{2.1}$$

The velocity $v = (v_1,\ v_2,\ v_3)$ can be expanded in a cartesian set with one axis coinciding with the position $\boldsymbol{x}$, namely $\{v_r, v_{t,1}, v_{t,2}\}$ such that

$$v_r = \frac{\boldsymbol{x}\cdot\boldsymbol{v}}{r} \qquad v_{t,1}^2 + v_{t,2}^2 = \frac{|\boldsymbol{x}\times\boldsymbol{v}|^2}{r^2} \tag{2.2}$$

where the relative size of $v_{t,1}$ and $v_{t,2}$ depends on the specific orientation of the free axes in the tangential plane. To better show this dependence, we introduce the set $\{v_r,\ v_t,\ \alpha\}$ such that

$$v_t = \sqrt{v_{t,1}^2 + v_{t,2}^2} \qquad \tan\alpha = \frac{v_{t,1}}{v_{t,2}}\,. \tag{2.3}$$

The Jacobian of the transformation from Cartesian coordinates is

$$d^3x\, d^3v = r^2\, v_t \cos\phi\, dr\, d\theta d\phi\ \ dv_r dv_t d\alpha \tag{2.4}$$

Neglecting relativistic corrections, the integrals of motion for this problem are the energy per unit mass E and the angular momentum per unit mass J, defined by:

$$E = \phi(r) - \frac{v^2}{2} \qquad v^2 = v_r^2 + \frac{J^2}{r^2} \tag{2.5}$$

where $\phi(r)$ is the positive potential[1]. It is common to rescale the squared angular momentum to its circular-orbit value at energy E, introducing the variable

$$\mathcal{R} = \frac{J^2}{r_c^3\,\phi'(r_c(E))} \tag{2.6}$$

where $\phi'(r) = d\phi(r)/dr$, and $r_c(E)$ is the radius of a circular orbit for a test mass with energy E, which can be obtained by solving

$$\phi(r) + r\,\frac{\phi'(r)}{2} - E = 0. \tag{2.7}$$

The quantities E and $\mathcal{R}$ completely characterise an orbit in a given potential. All the properties of the orbit can be derived from these parameters.

[1] With this definition, the energy of a bound orbit is positive.

Among them, notable quantities are the pericentre and apocentre of the orbit, i.e. the values of r that solve the equation

$$E = \phi(r) - \frac{J^2}{2r^2}; \tag{2.8}$$

another relevant quantity is the radial period of the orbit

$$P(E, \mathcal{R}) = 2\int_{r_-}^{r_+} \frac{dr}{v_r} \tag{2.9}$$

where r_- and r_+ are the pericentre and the apocentre of the orbit. For a circular orbit the integral does not exist, but it can be defined by continuity. Expanding around a given energy on an orbit with angular momentum J_c^2 the equation for the apocenter and pericenter becomes

$$E - \delta E = \psi_c + \frac{\psi_c''}{2}(r - r_c)^2 \qquad \Rightarrow \qquad r - r_c = \pm\sqrt{\frac{2\,\delta E}{|\psi_c''|}} \tag{2.10}$$

where $\psi \equiv \phi - J^2/(2r^2)$. The explicit value of ψ_c'' can be written using the fact that $J_c^2 = -r_c^3\phi_c'$

$$\psi_c'' = \phi_c'' - 3\frac{J^2}{r_c^4} = \phi_c'' + 3\frac{\phi_c'}{r_c}; \tag{2.11}$$

the radial period of a circular orbit is therefore

$$P_c(E) = \lim_{\delta E \to 0} \int_{r_-}^{r_+} \left(\delta E - \frac{\psi_c''}{2}(r - r_c)^2\right)^{-1/2} = 2\pi\sqrt{\frac{1}{-\psi_c''}} = 2\pi\sqrt{\frac{-r_c}{3\phi_c' + \phi_c''}}\,. \tag{2.12}$$

2.2 | Fokker-Planck equation

Typical stellar densities in nuclear clusters are high enough that mutual interactions between particles can significantly modify the original orbits (Merritt, 2013). The evolution of the orbital parameters of an object can be described as a Brownian motion in the (E, J) space with fluctuations that depend on the physics of relaxation, but are more pronounced along the J direction for small J, efficiently directing compact objects toward the MBH at the centre of the system (Bar-Or and Alexander, 2014).

The random nature of these objects can be studied statistically through classical stochastic approaches. A fundamental tool to characterize the properties of a set of particles is the distribution function

$$f(\boldsymbol{x}, \boldsymbol{v})\; d^3x\, d^3v = dN(\boldsymbol{x}, \boldsymbol{v}) \tag{2.13}$$

where $dN(\boldsymbol{x}, \boldsymbol{v})$ is the number of objects whose phase space coordinates are within an infinitesimal volume $d^3x\, d^3v$ centered at $(\boldsymbol{x}, \boldsymbol{v})$.

Since we are considering spherical distributions of stellar objects, their distribution function in phase space only depends on $\{v_r,\ v_t,\ \alpha,\ r\}$. Since v_r can be positive and negative, and we can then map each branch into a value of energy, we first split the distribution function in the two branches:

$$f(v_r, v_t, r) = \begin{cases} f^{\text{out}}(v_r, v_t, r) & v_r > 0 \\ f^{\text{in}}(-v_r, v_t, r) & v_r < 0 \end{cases} \tag{2.14}$$

so that both f^{out} and f^{out} are defined for a positive first argument. Considering each branch separately, we can then change variable to $\{E,\ \mathcal{R},\ r\}$. Only at equilibrium, when the system will be steady and $f^{\text{out}} = f^{\text{in}}$, the set of varibles to describe the whole distribution of our particles reduces to $\{E, \mathcal{R}, r\}$ (and does not depend on the sign of v_r).

We will now derive the Fokker-Planck equation that describes the evolution of f due to stochastic interactions. There is a key assumption we will make to derive the equation:

- The stochastic deflections due to 2-body encounters are Gaussian, which means that the expectation value of any combination of δv_i of order greater than two can be neglected.

Defining the transition probability $\psi(v_r, v_t, r; \delta v)$ as the probability density of δv at a given point of phase space, the evolution of the distribution is

$$\begin{aligned} f(v_r, v_t, r, t + \delta t) = {} & f(v_r - \phi' \delta t, v_t, r - v_r \delta t, t) \\ & + \int d\delta \boldsymbol{v} f(v_r - \delta v_r, v_t - \delta v_t, r, t)\, \psi(v_r - \delta v_r, v_t - \delta v_t, r, \boldsymbol{\delta v}) \end{aligned} \tag{2.15}$$

since when the evolution is non-collisional (*i.e.* when 2-body relaxation is negligible) the distribution function evolves according to the Hamiltonian flow, the integral includes all the other physical effects, that collectively go under the name of "collisional terms".

Expanding now the product $(f\,\psi)(v_r - \delta v_r, v_t - \delta v_t, r, \boldsymbol{\delta v})$ around $(v_r, v_t, r, \boldsymbol{\delta v})$ we get

$$\begin{aligned} (f\,\psi)(v_r - \delta v_r, v_t - \delta v_t, r, \boldsymbol{\delta v}) = {} & (f\,\psi)(v_r, v_t, r, \boldsymbol{\delta v}) \\ & - \delta v_r \frac{\partial}{\partial v_r} f\,\psi - \delta v_t \frac{\partial}{\partial v_t} f\,\psi \\ & + \frac{1}{2}\left[\delta v_r^2 \frac{\partial^2}{\partial v_r^2} f\,\psi + 2\,\delta v_r \delta v_t \frac{\partial^2}{\partial v_t\, \partial v_r} f + \delta v_t^2 \frac{\partial^2}{\partial v_t^2} f\,\psi\right] \\ & + \dots \end{aligned} \tag{2.16}$$

we remark that δv_r and δv_t are independent variables, so that we can move them inside the derivatives. Substituting now in Eq. (2.15) we get terms of the form

$$\int d\boldsymbol{\delta v} \frac{\partial}{\partial v_x} \left[\delta v_y f(v_r, v_t, r, t)\psi(v_r, v_t, r; \delta v)\right] = \frac{\partial}{\partial v_x}\left[f(v_r, v_t, r, t)\int d\boldsymbol{\delta v}\psi(v_r, v_t, r; \delta v)\delta v_x\right] \tag{2.17}$$

and we see that the integral is the expectation value of δv_x, that we represent as $\langle \delta v_x \rangle$. Therefore, the evolution equation is

$$\begin{aligned} f(v_r, v_t, r, t+\delta t) = {} & f(v_r - \phi'\delta t, v_t, r - v_r\delta t, t) \\ & - \frac{\partial}{\partial v_r} f\ \langle \delta v_r \rangle - \frac{\partial}{\partial v_t} f\ \langle \delta v_t \rangle \\ & + \frac{1}{2}\left[\frac{\partial^2}{\partial v_r^2} f \left\langle \delta v_r^2 \right\rangle + 2\frac{\partial^2}{\partial v_r\, \partial v_t} f \left\langle \delta v_t\, \delta v_r \right\rangle + \frac{\partial^2}{\partial v_t^2} f \left\langle \delta v_t^2 \right\rangle\right] \\ & + \mathcal{O}(\left\langle \delta v^3 \right\rangle) \end{aligned} \tag{2.18}$$

and given the assumption of a Gaussian profile in $\boldsymbol{\delta v}$, the last term is zero. We can finally write

$$\begin{aligned} \delta t\left[\frac{\partial}{\partial t} f + \phi' \frac{\partial}{\partial v_r} f + v_r \frac{\partial}{\partial r} f\right] = {} & -\frac{\partial}{\partial v_r} f\ \langle \delta v_r \rangle - \frac{\partial}{\partial v_t} f\ \langle \delta v_t \rangle \\ & + \frac{1}{2}\left[\frac{\partial^2}{\partial v_r^2} f \left\langle \delta v_r^2 \right\rangle + 2\frac{\partial^2}{\partial v_r\, \partial v_t} f \left\langle \delta v_t\, \delta v_r \right\rangle + \frac{\partial^2}{\partial v_t^2} f \left\langle \delta v_t^2 \right\rangle\right] \end{aligned} \tag{2.19}$$

dividing by δt and introducing the notation

$$D\left[y\right] = \frac{\langle y \rangle}{\delta t} \tag{2.20}$$

we can write the local **Fokker-Planck equation** for spherical galactic nuclei

$$\begin{aligned} \frac{\partial}{\partial t} f + \phi' \frac{\partial}{\partial v_r} f + v_r \frac{\partial}{\partial r} f = {} & -\frac{\partial}{\partial v_r} f\, D\left[\delta v_r\right] - \frac{\partial}{\partial v_t} f\, D\left[\delta v_t\right] \\ & + \frac{1}{2}\left[\frac{\partial^2}{\partial v_r^2} f D\left[\delta v_r^2\right] + 2\frac{\partial^2}{\partial v_r\, \partial v_t} f D\left[\delta v_t\, \delta v_r\right] + \frac{\partial^2}{\partial v_t^2} f D\left[\delta v_t^2\right]\right] \end{aligned} \tag{2.21}$$

At the left-hand side we recognize the convective derivative of f, whose form naturally depends on the choice of coordinates.

Repeating the steps above with $(E, \mathcal{R})$ as coordinates in the velocity space, we get for f^{in} and f^{out} two equations with the same structure:

$$\begin{aligned} \frac{\partial}{\partial t} f^x + v_r \frac{\partial}{\partial r} f^x = {} & -\frac{\partial}{\partial E} f^x\, D\left[\delta E\right] - \frac{\partial}{\partial \mathcal{R}} f^x\, D\left[\delta \mathcal{R}\right] \\ & + \frac{1}{2}\left[\frac{\partial^2}{\partial E^2} f^x D\left[\delta E^2\right] + 2\frac{\partial^2}{\partial E\, \partial \mathcal{R}} f^x D\left[\delta E\, \delta \mathcal{R}\right] + \frac{\partial^2}{\partial \mathcal{R}^2} f^x D\left[\delta \mathcal{R}^2\right]\right], \end{aligned} \tag{2.22}$$

for $x = \text{in}, \text{out}$. With future applications in mind, we introduce the flux conservation form of the local Fokker-Planck equation

$$\begin{aligned}\frac{\partial}{\partial E}F_E \equiv \frac{\partial}{\partial E}\Bigg[&\left(D\left[\delta E\right] + \frac{1}{2}\frac{\partial}{\partial E}D\left[\delta E^2\right] + \frac{1}{2}\frac{\partial}{\partial \mathcal{R}}D\left[\delta E \delta \mathcal{R}\right]\right) f^x \\ &+ \frac{1}{2}D\left[\delta E^2\right]\frac{\partial}{\partial E}f^x + \frac{1}{2}D\left[\delta E \delta \mathcal{R}\right]\frac{\partial}{\partial \mathcal{R}}f^x\Bigg]\end{aligned} \tag{2.23}$$

that suggests defining

$$D_{\text{E}} \equiv -D\left[\delta E\right] + \frac{1}{2}\frac{\partial}{\partial E}D\left[\delta E^2\right] + \frac{1}{2}\frac{\partial}{\partial \mathcal{R}}D\left[\delta E\, \delta \mathcal{R}\right] \tag{2.24}$$

$$D_{\text{EE}} = \frac{1}{2}D\left[\delta E^2\right] \tag{2.25}$$

$$D_{\text{ER}} = \frac{1}{2}D\left[\delta E\, \delta \mathcal{R}\right] \tag{2.26}$$

similarily, proceeding with F_R one can introduce

$$D_{\text{R}} \equiv -D\left[\delta \mathcal{R}\right] + \frac{1}{2}\frac{\partial}{\partial \mathcal{R}}D\left[\delta \mathcal{R}^2\right] + \frac{1}{2}\frac{\partial}{\partial E}D\left[\delta E\, \delta \mathcal{R}\right] \tag{2.27}$$

$$D_{\text{RR}} = \frac{1}{2}D\left[\delta \mathcal{R}^2\right] \tag{2.28}$$

finally giving (with $\boldsymbol{\nabla} = (\partial_E, \partial_{\mathcal{R}})$)

$$\frac{d}{dt}f^x + \boldsymbol{\nabla}\cdot\boldsymbol{F} = 0 \tag{2.29}$$

where we the flux vector $\boldsymbol{F}$ has components

$$\boldsymbol{F} = \begin{pmatrix} F_E \\ F_R \end{pmatrix} = -\begin{pmatrix} D_{\text{EE}}\,\partial_E f^x + D_{\text{ER}}\,\partial_{\mathcal{R}} f^x + D_{\text{E}}\, f^x \\ D_{\text{RE}}\,\partial_E f^x + D_{\text{RR}}\,\partial_{\mathcal{R}} f^x + D_{\text{R}}\, f^x \end{pmatrix}. \tag{2.30}$$

2.2.1 | The orbit averaged Fokker-Planck equation

In this section we will derive the orbit-averaged Fokker-Planck equation, that describes directly the evolution for the differential distribution n in the $(E, \mathcal{R})$ space. This equation has been used to study the evolution of stellar systems (Cohn and Kulsrud, 1978; Drukier et al., 1999), and the computation of loss cone rates (Bar-Or and Alexander, 2016; Pan and Yang, 2021). The definition of n also shows how it is related to the distribution function f:

$$N_{\text{tot}} = \int dE\, d\mathcal{R}\, n(E, \mathcal{R}) = \int d^3x\, d^3v\, f(\boldsymbol{x}, \boldsymbol{v}) \tag{2.31}$$

Moving to the suitable set of coordinates (2.3) and marginalizing over the angles we get

$$\int d^3x d^3v\, f(E(x,v),\mathcal{R}(x,v),r(x)) = \int dr dv_r dv_t 8\,\pi^2\, v_t\, r^2\, f(E(r,v_r,v_t),\mathcal{R}(r,v_r,v_t),r)\,. \tag{2.32}$$

since f only depends on v_r^2 through the energy, we restrict the domain from $v_r \in (-\infty,+\infty)$ to $|v_r| \in [0,+\infty)$. Thus

$$\int d^3x d^3v\, f(E(x,v),\mathcal{R}(x,v),r(x)) = \int dr d|v_r| dv_t 16\,\pi^2\, v_t\, r^2\, f^{\rm avg}(E(r,v_r,v_t),\mathcal{R}(r,v_r,v_t))\,. \tag{2.33}$$

where we $f^{\rm avg} = (f^{\rm in} + f^{\rm out})/2$. Dropping the superscript avg from now on, we change variable from $|v_r|$ to the energy, and at fixed energy from v_t to $\mathcal{R}$.

$$\begin{aligned}\int d^3x d^3v\, f(E(x,v),\mathcal{R}(x,v),r(x)) &= \int \frac{dE\, dv_t\, dr}{\sqrt{2(\phi-E)-v_t^2}} 16\,\pi^2\, v_t\, r^2\, f(E,\mathcal{R}(r,E,v_t),r) \\ &= \int \frac{dE\, d\mathcal{R}\, dr}{\sqrt{2(\phi-E)-RJ_c^2/r^2}} 8\,\pi^2\, J_c^2\, f(E,\mathcal{R},r)\end{aligned} \tag{2.34}$$

Assuming now that f does not explicitely depend on r, that would correspond to a steady configuration in collisionless dynamics according to Jeans' theorem, we can write

$$\int d^3x d^3v\, f(E(x,v),\mathcal{R}(x,v)) = \int dE\, d\mathcal{R} f(E,\mathcal{R})\, 4\,\pi^2\, J_c^2\, P(E,\mathcal{R})\,. \tag{2.35}$$

And defining $\mathcal{J}(E,\mathcal{R}) \equiv 4\,\pi^2\, J_c^2\, P(E,\mathcal{R})$, we get

$$n(E,\mathcal{R}) = \mathcal{J}(E,\mathcal{R})\, f(E,\mathcal{R})\,. \tag{2.36}$$

We repeat now the same derivation we did for deriving the local Fokker-Planck equation in the reduced space of $(E,\mathcal{R})$. The equation for n is

$$\begin{aligned}\frac{\partial}{\partial t} n(E\,R,t) = &-\frac{\partial}{\partial E} n\,\mathcal{D}\left[\delta E\right] - \frac{\partial}{\partial \mathcal{R}} n\,\mathcal{D}\left[\delta \mathcal{R}\right] \\ &+ \frac{1}{2}\frac{\partial^2}{\partial E^2} n\,\mathcal{D}\left[\delta E^2\right] + \frac{\partial^2}{\partial E\,\partial \mathcal{R}} n\,\mathcal{D}\left[\delta E\,\delta \mathcal{R}\right] + \frac{1}{2}\frac{\partial^2}{\partial \mathcal{R}^2} n\,\mathcal{D}\left[\delta \mathcal{R}^2\right]\end{aligned} \tag{2.37}$$

And inserting $n = \mathcal{J}\, f$ one gets the evolution equation for f. The reader should note the difference in the notation wrt the local Fokker-Planck equation: $D\left[\delta E\right]$ depends on $(E,\mathcal{R},r)$, while $\mathcal{D}\left[\delta E\right]$ does not depend on r. In fact, unlike Eq. (2.21), the dynamics described by this equation does not reduce exactly to the dynamics of a set of particles in any sense nor limit, since 2-body scattering are always local (the diffusion coefficients may strongly depend on r to account for the spatial distribution of stars) and generally do not preserve the steady form $f(E,\mathcal{R})$.

It is possible to reorganize the equation in the so-called flux conservation form for f defining

$$\mathcal{D}_{\mathrm{E}} \equiv -\mathcal{J}\,\mathcal{D}\left[\delta E\right] + \frac{1}{2}\frac{\partial}{\partial E}\mathcal{J}\,\mathcal{D}\left[\delta E^2\right] + \frac{1}{2}\frac{\partial}{\partial \mathcal{R}}\mathcal{J}\,\mathcal{D}\left[\delta E\,\delta\mathcal{R}\right] \tag{2.38}$$

$$\mathcal{D}_{\mathrm{EE}} = \frac{1}{2}\mathcal{J}\,\mathcal{D}\left[\delta E^2\right] \tag{2.39}$$

$$\mathcal{D}_{\mathrm{ER}} = \frac{1}{2}\mathcal{J}\,\mathcal{D}\left[\delta E\,\delta\mathcal{R}\right] \tag{2.40}$$

$$\mathcal{D}_{\mathrm{R}} \equiv -\mathcal{J}\,\mathcal{D}\left[\delta\mathcal{R}\right] + \frac{1}{2}\frac{\partial}{\partial \mathcal{R}}\mathcal{J}\,\mathcal{D}\left[\delta\mathcal{R}^2\right] + \frac{1}{2}\frac{\partial}{\partial E}\mathcal{J}\,\mathcal{D}\left[\delta E\,\delta\mathcal{R}\right] \tag{2.41}$$

$$\mathcal{D}_{\mathrm{RR}} = \frac{1}{2}\mathcal{J}\,\mathcal{D}\left[\delta\mathcal{R}^2\right] \tag{2.42}$$

so that recalling $\boldsymbol{\nabla} = (\partial_E, \partial_{\mathcal{R}})$

$$\frac{\partial}{\partial t}f + \boldsymbol{\nabla}\cdot\boldsymbol{\mathcal{F}} = 0 \tag{2.43}$$

where

$$\boldsymbol{\mathcal{F}} = \begin{pmatrix} -\mathcal{D}_E\, f - \mathcal{D}_{EE}\partial_E f - \mathcal{D}_{ER}\partial_R f \\ -\mathcal{D}_R\, f - \mathcal{D}_{ER}\partial_R f - \mathcal{D}_{RR}\partial_R f \end{pmatrix} \tag{2.44}$$

2.2.2 | The ergodic Fokker-Planck equation

We will now derive a 1-D evolution equation for ergodic or isotropic systems[2], fully described by their distribution function $f(E)$ or, equivalently, their differential distribution in the energy space $\bar{n}(E)$. This is perhaps the most widely used equation in literature, and has proven to be a powerful tool for the computation of loss cone rates with numerical methods (Bondani et al., 2023; Bortolas et al., 2023; Cohn, 1980; Stone et al., 2018), and more in general for modelling stellar systems (Alexander and Hopman, 2009; Bahcall and Wolf, 1977; Bortolas, 2022; Linial and Sari, 2022; Preto and Amaro-Seoane, 2010; Stone et al., 2018; Vasiliev, 2017).

Once again, direct computation shows the relationship among $\bar{n}$ and f

$$N_{tot} = \int dE\,\bar{n}(E) = \int d^3x d^3v\, f(\boldsymbol{x},\boldsymbol{v})\,. \tag{2.45}$$

Repeating the steps for the orbit averaged equation, we get to

$$\int dE\bar{n}(E) = \int dE d\mathcal{R}\mathcal{J}f(E) = f(E)\int d\mathcal{R}\mathcal{J} \tag{2.46}$$

[2]The two notions are equivalent in the context of stellar distributions. In the jargon of Statistical Mechanics, ergodic refers to systems whose distribution function depends exclusively on energy, and ergodic stellar systems have an isotropic velocity dispersion tensor (Binney and Tremaine, 2008).

which suggests defining

$$\begin{aligned}\frac{g(E)}{8\pi^2 J_c^2} &= \frac{1}{2}\int_0^1 d\mathcal{R}\, P(E,\mathcal{R}) \\ &= \int_0^1 d\mathcal{R}\left[\int_{r_-}^{r_c} dr \frac{1}{v_r(E,\mathcal{R},r)} + \int_{r_c}^{r_+} dr \frac{1}{v_r(E,\mathcal{R},r)}\right] \\ &= \int_0^{r_c} dr \int_0^{\mathcal{R}_-} \frac{d\mathcal{R}}{v_r(E,\mathcal{R},r)} + \int_{r_c}^{\phi^{-1}(E)} dr \int_0^{\mathcal{R}_+} \frac{d\mathcal{R}}{v_r(E,\mathcal{R},r)}\end{aligned} \tag{2.47}$$

where $R_\pm(E,r)$ is such that the corresponding orbit has its pericenter/apocenter at r. Since $v_r = \sqrt{2\phi(r) - 2E - \mathcal{R}J_c^2/r^2}$, the inner integral can be performed.

$$\begin{aligned}\int_0^{\mathcal{R}_\pm} \frac{d\mathcal{R}}{\sqrt{2\phi(r) - 2E - \mathcal{R}J_c^2/r^2}} &= -\frac{2r^2}{J_c^2}\left[\sqrt{2\phi(r) - 2E - \mathcal{R}J_c^2/r^2}\right]_0^{\mathcal{R}_\pm} \\ &= \frac{2r^2}{J_c^2}\sqrt{2\left(\phi(r) - E\right)}\end{aligned} \tag{2.48}$$

finally giving

$$\bar{n}(E) = g(E)\, f(E) \qquad g(E) = 16\pi^2 \int_0^{\phi^-(E)} dr\, r^2 \sqrt{2\left(\phi(r) - E\right)}\,. \tag{2.49}$$

In this case we only need two diffusion coefficients

$$\frac{\partial}{\partial t}\bar{n} = -\frac{\partial}{\partial E}\bar{n}\bar{\mathcal{D}}[\delta E] + \frac{1}{2}\frac{\partial^2}{\partial E^2}\bar{n}\,\bar{\mathcal{D}}\left[\delta E^2\right] \tag{2.50}$$

and the coefficients for the flux conservation form in terms of f are

$$\bar{\mathcal{D}}_E = -g\bar{\mathcal{D}}[\delta E] + \frac{1}{2}\frac{\partial}{\partial E} g\,\bar{\mathcal{D}}\left[\delta E^2\right] \tag{2.51}$$

$$\bar{\mathcal{D}}_{EE} = \frac{1}{2} f\bar{\mathcal{D}}\left[\delta E^2\right] \tag{2.52}$$

so that

$$\frac{\partial}{\partial t} g\, f + \frac{\partial}{\partial E}\bar{\mathcal{F}} = 0 \tag{2.53}$$

and

$$\bar{\mathcal{F}} = -\left(\bar{\mathcal{D}}_E\, f + \bar{\mathcal{D}}_{EE}\frac{\partial}{\partial E} f\right) \tag{2.54}$$

2.3 | Diffusion coefficients

We will now compute the diffusion coefficients starting from some basic assumptions:

1. When a test particle m moves, the distribution of the other particles appears to be locally uniform and isotropic.

2. The velocity distribution of scatterers does not depend on angular momentum, but only on their energy.

Under these assumptions one can derive analytical expressions for the diffusion coefficients starting from the study of a single, two-body encounter.

There is a wide use of notation in literature for the quantities we will present. We will here show the full and complete derivation of all the diffusion coefficients (in the standard and in the flux conservation form) of the three Fokker-Planck equations we presented before.

2.3.1 | Diffusion coefficients for the local Fokker-Planck equation

We will now derive the diffusion coefficients for Eqs. (2.21) and (2.22). The notation in this section may look confusing to the reader, since we will consider different reference frames. In order to avoid confusing the diffusion coefficients, we will use the notation v_r to indicate the relative velocity[3] between the scattered object m and the field of scatterers m_s. The diffusion coefficients $D\left[\delta v_r\right]$, $D\left[\delta v_t\right]$ correspond to the expectation value of δv parallel and orthogonal to the relative velocity. On the other hand, we will use the notation $D\left[\delta v_{\parallel}\right]$ and $D\left[\delta v_{\perp}\right]$ to refer to the expectation value of δv parallel and orthogonal to the velocity of m. Textbooks on the subject use the same symbols $v_{\parallel}$ and $v_{\perp}$ in both situations, that may cause some ambiguity.

Single encounter The equation for the relative distance r among two bodies is completely described in the reference frame of the center of mass as

$$\begin{cases} \ddot{r} = \frac{GM}{r^2} - \frac{J^2}{r^3} \\ \dot{\varphi} = \frac{J}{r^2} \end{cases} \tag{2.55}$$

where φ is the polar angle, M is the sum of the two masses and J the total angular momentum of the system, whose conservation implies the presence of an effective potential. See Fig. 2.1 for a plot of a prototypical trajectory and the parameters involved. One can combine the two to find the equation $r = r(\varphi)$ that describes the motion of the particle

$$\frac{1}{r} = C\,\cos(\varphi + \varphi_0) + \frac{GM}{J^2}\,. \tag{2.56}$$

[3] In all the other subsections, the symbol v_r refers to the radial velocity

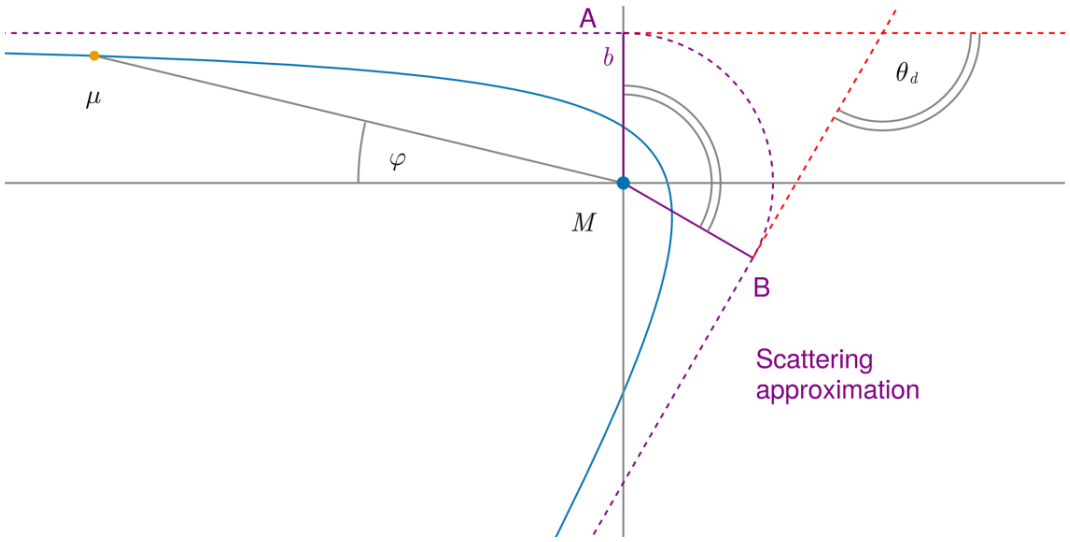

Figure 2.1: Sketch of the two body encounter of two objects with reduced mass μ and total mass M in the center of mass frame. We show the trajectory corresponding to the scattering approximation, where we assume that the particles move on straight lines and interact instantaneously when their relative velocity is orthogonal to the relative distance. In the reduced problem, μ instantaneously passes from A to B.

Applying the time derivative we get

$$\frac{\dot{r}}{r^2} = -C\,\sin(\varphi+\varphi_0)\,\frac{J}{r^2} \tag{2.57}$$

$$\dot{r} = -C\sin(\varphi+\varphi_0)\,J \tag{2.58}$$

once again

$$\ddot{r} = -C\cos(\varphi+\varphi_0)\frac{J^2}{r^2} \tag{2.59}$$

$$\ddot{r} = -\left[\frac{1}{r}-\frac{GM}{J^2}\right]\frac{J^2}{r^2}\,. \tag{2.60}$$

We see that $\varphi = \varphi_0$ corresponds to the pericenter of the system, since $\dot{r} = 0$ there, and in general the transformation $\varphi \to 2\pi - 2\,\varphi_0 - \varphi$ acts as a time reflection.

Setting the initial conditions $\varphi = 0$ and $\dot{r} = v_0$ when $t = -\infty$, we obtain:

$$C\cos(\varphi_0) = -\frac{GM}{J^2} \tag{2.61}$$

$$v_0 = -C\sin(\varphi_0)J \tag{2.62}$$

and solving for φ_0

$$\tan\varphi_0 = \frac{J\,v_0}{G\,M}\,. \tag{2.63}$$

We now define the impact parameter

$$b \equiv \frac{J}{v_0}\,, \tag{2.64}$$

that is the distance between the directions of the intial velocities of the particles. In this description, it is the distance between the inital direction of v_0 and the center.

The total deflection of the particle is therefore determined by the symmetry of the system:

$$\theta_d = 2\varphi_0 - \pi \tag{2.65}$$

giving

$$\tan\frac{\theta_d}{2} = \frac{G\,M}{b\,v_0^2} \equiv \frac{b_0}{b} \tag{2.66}$$

Where we introduced b_0 that corresponds to $\theta_d = \pi/2$. Since the initial speed equals the final speed, we can estimate the variation $\delta\boldsymbol{v}$

$$\delta v = \begin{pmatrix} v_0(\cos\theta_d - 1) \\ -v_0\sin\theta_d \end{pmatrix} = \begin{pmatrix} -\frac{2\,v_0}{1+b^2/b_0^2} \\ -\frac{2v_0\,b/b_0}{1+b^2/b_0^2} \end{pmatrix} \equiv -\begin{pmatrix} \delta v_\parallel \\ \delta v_\perp \end{pmatrix} \tag{2.67}$$

where the first component is the variation parallel to the initial direction v, the second component the orthogonal one.

This process is usually referred to as hyperbolic encounter, since the resulting orbit is not bound (indeed the initial conditions imply negative binding energy $E = -v_0^2/2$).

We further proceed to model this time-extended two body encounter as a **scattering event** fully characterized by b and v_0 and happening as soon as the relative distance is orthogonal to the relative velocity.

In a system where the center of mass has velocity $v_{\rm CDM}$, the parameter v_0 in Eq. (2.67) must be recovered from the velocities v_1 and v_2 of the two binaries considered. In particular we have

$$\boldsymbol{v}_{\rm CDM} = \frac{m_1\,\boldsymbol{v_1} + m_2\,\boldsymbol{v_2}}{m_1 + m_2} \tag{2.68}$$

and in the reference frame of the center of mass, the velocity of the two particles is such that

$$m_1\boldsymbol{v}_1' = -m_2\boldsymbol{v}_2' \qquad \Rightarrow \qquad \boldsymbol{v_1'} = -\frac{m_2}{m_1+m_2}\boldsymbol{v_0} \tag{2.69}$$

where we used the definition $\boldsymbol{v}_0 = \boldsymbol{v}_2 - \boldsymbol{v}_1$. This means the variation of the velocity v_1 is μ/m_1 times the variation of the velocity v_0 in any (inertial) reference frame, since vector differences are invariant.

Encounter with an ergodic distribution of scatterers. Starting from the variation $\delta \boldsymbol{v}$ due to a single encounter, we will now estimate what happens when a particle with mass m is subject to multiple encounters in a time δt, with scatterers placed on an isotropic distirbution (with respect to the moving body). The key assumption is:

- The distribution of scatterers appears to be isotropic and spatially uniform on a timescale of δt and length $|v_t|\delta t$, where v_t is the typical relative velocity between m and the bulk velocity of the scatterers.

The effect of a single encounter is fully characterized by the relative velocity v_0 and the impact parameter; if we assume that the change in velocity due to a single encounter happens on a timescale shorter than δt, we can therefore describe the statistical effect on the distribution of particles.

A uniform and isotropic distribution of particles can only depend on the absolute value of the velocity, or equivalently its squared value v^2. Defining as $f_s(v^2)$ the distribution function of scatterers, v_0 is the relative velocity of the moving body m and the center of mass of the scatterers. We assume that the particle will undergo a scattering event with all the particles inside the volume covered by the transverse plane in δt. Naturally it is unrealistic to assume that the particles will interact up to $b = \infty$, since (i) realistic systems do not have an infinite spatial extent, and (ii) the scattering approximation for the 2-body encounter holds until the interaction time is larger than, at least, the time for a significant change of v. The integration must therefore be limited to $b < b_{\max}$, where the latter must be estimated from the system.

The number of particles with impact parameter between b and $b + db$ and velocity between $\boldsymbol{v'}$ and $\boldsymbol{v'} + d\boldsymbol{v'}$ is

$$dN = 2\,\pi\, b\, db\; f_s(\boldsymbol{v'})\, d^3v'\; v_r \delta t\,. \tag{2.70}$$

where v_r is the relative velocity

$$\boldsymbol{v_r} = \boldsymbol{v'} - \boldsymbol{v_0}\,. \tag{2.71}$$

Since the distribution of scatterers is spatially symmetric, the cumulative effect of

the transverse kicks δv_t orthogonal to v_r is zero. The relevant quantities result in:

$$d\delta v_r = \frac{m_s}{m+m_s}\frac{4\pi\, b\, \boldsymbol{v_r}^2}{1+b^2/b_0^2} f_s(\boldsymbol{v'})\, db\;\, d^3v'\;\, \delta t\,. \tag{2.72}$$

$$d\delta v_t = 0 \tag{2.73}$$

$$d\delta v_r^2 = \left(\frac{m_s}{m+m_s}\right)^2 \frac{8\pi\, b\, |\boldsymbol{v_r}|^3}{(1+b^2/b_0^2)^2} f_s(\boldsymbol{v'})\, db\;\, d^3v'\;\, \delta t \tag{2.74}$$

$$d\delta v_t^2 = \left(\frac{m_s}{m+m_s}\right)^2 \frac{8\pi\, b^3\, |\boldsymbol{v_r}|^3}{b_0^2\,(1+b^2/b_0^2)^2} f_s(\boldsymbol{v'})\, db\;\, d^3v\;\, \delta t\,. \tag{2.75}$$

Note that b_0 depends on the total mass of the two bodies participating in the scattering, that is $m+m_s$, and on the relative velocity v_r. We can now marginalize over b integrating from $b=0$ to $b=b_{\max}$ and we get:

$$d\delta v_r = 2\pi\, b_0^2\, \log\frac{b_{\max}^2}{b_0^2}\, \frac{m_s}{m+m_s}\, \boldsymbol{v_r}^2\, f_s(\boldsymbol{v'}) d^3v'\, \delta t + \mathcal{O}((b^2/b_0^2)^0) \tag{2.76}$$

$$d\delta v_t = 0 \tag{2.77}$$

$$d\delta v_r^2 = \mathcal{O}((b^2/b_0^2)^{-1}) \tag{2.78}$$

$$d\delta v_t^2 = 4\pi\, b_0^2\, \log\frac{b_{\max}^2}{b_0^2}\, \left(\frac{m_s}{m+m_s}\right)^2\, \boldsymbol{v_r}^3\, f_s(\boldsymbol{v'}) d^3v'\, \delta t + \mathcal{O}((b^2/b_0^2)^0) \tag{2.79}$$

$$d\delta v_r \delta v_t = 0\,. \tag{2.80}$$

Keeping only the leading terms, we can now move to the reference frame parallel to v_0, defining the versor $e_\parallel = v_0/|v_0|$, and two versors $e_{\perp,1}$ and $e_{\perp,2}$ in the orthogonal plane. This will allow us to use the same reference frame for all the particles and integrate over the distribution. In general, we have

$$\boldsymbol{\delta v} = \delta v_\parallel\, \boldsymbol{e}_\parallel + \delta v_\perp\, (\cos\varphi\, \boldsymbol{e}_{\perp,1} + \sin\varphi \boldsymbol{e}_{\perp,2}) \tag{2.81}$$

$$= \delta v_r\, \boldsymbol{e}_r + \delta v_t\, (\cos\alpha\, \boldsymbol{e}_{t,1} + \sin\alpha \boldsymbol{e}_{t,2}) \tag{2.82}$$

therefore

$$\delta v_\parallel = \delta v_r\, e_\parallel \cdot \boldsymbol{e}_r + \delta v_t\, \left(\cos\alpha\, e_\parallel \cdot e_{t,1} + \sin\alpha\, e_\parallel \cdot e_{t,2}\right) \tag{2.83}$$

$$\delta v_{\perp,1/2} = \delta v_r e_{\perp,1/2} \cdot \boldsymbol{e}_r + \delta v_t\, (\cos\alpha\, e_{\perp,1/2} \cdot e_{t,1} + \sin\alpha\, e_{\perp,1/2} \cdot e_{t,2}) \tag{2.84}$$

Since we are interested in the effects of a spherical distribution of scattering particles, we average over the orientation of $e_{\perp,1/2}$ or, equivalently, the value of φ. This means that when considering the fluctuations due to the axisymmetric distribution of particles, we

account for the average over the angle φ, namely $\langle e_{\perp,1/2} \cdot e_{t,1/2} \rangle_\varphi = 0$. Inserting then the explicit expressions

$$d\delta v_\parallel = e_r \cdot e_\parallel \, d\delta v_r \tag{2.85}$$

$$d\delta v_{\perp,1/2} = 0 \tag{2.86}$$

$$d\delta v_\parallel^2 = \frac{1}{2} \left(1 - (e_\parallel \cdot e_r)^2\right) \, d\delta v_t^2 \tag{2.87}$$

$$d\delta v_{\perp,1/2}^2 = \frac{1}{2} \left(1 - (e_{\perp,1/2} \cdot e_r)^2\right) \, d\delta v_t^2 \tag{2.88}$$

$$d\delta v_r \, d\delta v_{\perp,1/2} = 0 \,. \tag{2.89}$$

Considering for example $\delta v_\parallel$, and assuming that $\Lambda \equiv b_{\max}/b_0$ does not depend on v_r, we find

$$\left\langle \delta v_\parallel \right\rangle = 4\pi \, \delta t \, \log\Lambda \, G^2 \, m_s(m_s + m) \int d^3v' \frac{1}{\boldsymbol{v_r^2}} \, f_s(\boldsymbol{v'}) e_r \cdot e_\parallel \tag{2.90}$$

The quantity $e_r \cdot e_\parallel = \boldsymbol{v_r} \cdot e_\parallel / |v_r|$ can be deduced from its definition

$$v_r = \sqrt{(v_{0\parallel} - v'_\parallel)^2 + (v_{0\perp,1} - v'_{\perp,1})^2 + (v_{0\perp,2} - v'_{\perp,2})^2} \tag{2.91}$$

$$\frac{\partial}{\partial v_0} v_r = \frac{v_0 - v'_\parallel}{v_r} = -e_r \cdot e_\parallel \tag{2.92}$$

(and we have $v_{0\perp,1} = v_{0\perp,2} = 0$); inserting this result we compute the expected kick:

$$\begin{aligned} \left\langle \delta v_\parallel \right\rangle &= 4\pi \, \delta t \, \log\Lambda \, G^2 \, m_s(m_s + m) \int d^3v' \frac{\partial}{\partial v_0} \frac{1}{v_r} \, f_s(\boldsymbol{v'}) d^3v' \\ &= 4\pi \, \delta t \, \log\Lambda \, G^2 \, m_s(m + m_s) \frac{\partial}{\partial v_0} \int d^3v' \frac{f_s(\boldsymbol{v'})}{|v_0 - v'|} \end{aligned} \tag{2.93}$$

To approach the integrals for $\delta v_\parallel^2$ and $\delta v_{\perp,1/2}^2$ we can show that

$$\frac{\partial^2}{\partial v_{0\parallel}^2} v_r = \frac{1 - (e_r \cdot e_\parallel)^2}{v_r} \qquad \frac{\partial^2}{\partial v_{0\perp,1/2}^2} v_r = \frac{1 - (e_r \cdot e_{\perp,1/2})^2}{v_r} \tag{2.94}$$

giving

$$\begin{aligned} \left\langle \delta v_\parallel^2 \right\rangle &= 4\pi\delta t \, G^2 \, m_s^2 \log\Lambda \int d^3v' f(v') \, \frac{\partial^2}{\partial v_{0\parallel}^2} \, v_r \\ &= 4\pi\delta t \, G^2 \, m_s^2 \log\Lambda \, \frac{\partial^2}{\partial v_0^2} \int d^3v' f(v') \, |v_0 - v'| \end{aligned} \tag{2.95}$$

$$\left\langle \delta v_{\perp,1/2}^2 \right\rangle = 4\pi\delta t \, G^2 \, m_s^2 \log\Lambda \, \frac{\partial^2}{\partial v_{0\perp,1/2}^2} \int d^3v' f(v') \, |v_0 - v'| \tag{2.96}$$

We have therefore written all the diffusion coefficients in terms of the so-called Rosenbluth potentials (Binney and Tremaine, 2008). Since the integration covers the whole space, it is clear that the result will only depend on v_0. It is possible to expand $1/|v_0 - v'|$ in the basis of Legendre Polynomials (see e.g. Arfken and Weber (2012) sec. 15.3) to perform the integral. However, we perform the integration directly in the spherical system with azimuthal angle θ from the direction of $\boldsymbol{v_0}$

$$\begin{aligned} h(v_0) &\equiv \int d^3v' \frac{f_s(v')}{|v_0 - v'|} \\ &= 2\pi \int_0^\infty d|v'||v'|^2 f_s(v') \int_{-1}^1 \frac{d\cos\theta}{\sqrt{v_0^2 + v'^2 - 2v_0\, v'\, \cos\theta}} \\ &= 2\pi \int_0^\infty dv' v'^2\, f_s(v') \, \frac{\sqrt{v'^2 + v_0^2 + 2\, v_0\, v'} - \sqrt{v'^2 + v_0^2 - 2\, v_0\, v'}}{v_0\, v'} \\ &= 2\pi \int_0^\infty dv' v'^2\, f_s(v') \, \frac{|v' + v_0| - |v' - v_0|}{v_0\, v'} \\ &= 4\pi \left[\int_0^{v_0} dv' \frac{v'^2}{v_0} f_s(v') + \int_{v_0}^{+\infty} dv' v'\, f_s(v') \right] . \end{aligned} \tag{2.97}$$

Similarily

$$\begin{aligned} g(v_0) &\equiv \int d^3v' f_s(v')\, |v_0 - v'| \\ &= 2\pi \int_0^\infty d|v'||v'|^2 f_s(v') \int_{-1}^1 d\cos\theta \, \sqrt{v_0^2 + v'^2 - 2v_0\, v'\, \cos\theta} \\ &= 2\pi \int_0^\infty dv' v'^2\, f_s(v') \, \frac{\sqrt{v'^2 + v_0^2 + 2\, v_0\, v'}^3 - \sqrt{v'^2 + v_0^2 - 2\, v_0\, v'}^3}{3\, v_0\, v'} \\ &= \frac{2}{3}\pi \int_0^\infty dv' v'^2\, f_s(v') \, \frac{|v' + v_0|^3 - |v' - v_0|^3}{v_0\, v'} \\ &= \frac{4}{3}\pi \left[\int_0^{v_0} dv' v'^2 \, \frac{3v_0^2 + v'^2}{v_0} \, f_s(v') + \int_{v_0}^{+\infty} dv' v' (3v'^2 + v_0^2) f_s(v') \right] . \end{aligned} \tag{2.98}$$

We can compute now the derivatives needed in the computation of the diffusion coefficients:

$$\begin{aligned} \frac{\partial}{\partial v_{0\parallel}} h(v_0) &= \frac{v_{0\parallel}}{v_0} \frac{\partial}{\partial v_0} h(v_0) \\ &= 4\pi \, \frac{v_{0\parallel}}{v_0} \left[v_0\, f_s(v_0) - \int_0^{v_0} dv' \frac{v'^2}{v_0^2} \, f_s(v') - v_0 f_s(v_0) \right] \\ &= -4\pi \frac{v_{0\parallel}}{v_0} \int_0^{v_0} dv' \frac{v'^2}{v_0^2} \, f_s(v') \, , \end{aligned} \tag{2.99}$$

and

$$\begin{aligned}\frac{\partial^2}{\partial v_{0\parallel}^2} g(v_0) &= \frac{\partial}{\partial v_{0\parallel}} \frac{v_{0\parallel}}{v_0} \frac{\partial}{\partial v_0} g(v_0) \\ &= \frac{1}{v_0}\left(1 - \frac{v_{0\parallel}}{v_0}\right) \frac{\partial}{\partial v_0} g(v_0) + \left(\frac{v_{0\parallel}}{v_0}\right)^2 \frac{\partial^2}{\partial v_0^2} g(v_0) \\ &= \frac{4}{3}\pi \left(1 - \frac{v_{0\parallel}}{v_0}\right) \left[\int_0^{v_0} dv' \frac{v'^2}{v_0}\left(3 - \frac{v'^2}{v_0^2}\right) f_s(v') + 2\int_{v_0}^{\infty} dv'\, v' f_s(v')\right] \\ &\quad + \frac{4}{3}\pi \left(\frac{v_{0\parallel}}{v_0}\right)^2 \left[2\int_0^{v_0} dv' \frac{v'^4}{v_0^3} f_s(v') + 2\int_{v_0}^{\infty} dv' v' f_s(v')\right] .\end{aligned} \tag{2.100}$$

Computing then the expected values of $\left\langle \delta v_{\parallel}^2 \right\rangle$ and $\left\langle \delta v_{\perp}^2 \right\rangle$ and dividing by δt, we get the complete set of non-vanishing diffusion coefficients:

$$D\left[\delta v_{\parallel}\right] = -\Gamma\, m_s (m + m_s) \frac{I_2}{v_0} \tag{2.101}$$

$$D\left[\delta v_{\parallel}^2\right] = \frac{2}{3}\Gamma\, m_s^2 \left[I_{s,4} + J_{s,1}\right] \tag{2.102}$$

$$D\left[\delta v_{\perp}^2\right] = 2\, D\left[\delta v_{\perp,1/2}^2\right] = \frac{2}{3}\Gamma\, m_s^2 \left[3I_{s,2} - I_{s,4} + 2J_{s,1}\right] \tag{2.103}$$

$$I_{s,k}(v_0) = \int_0^{v_0} dv' \frac{v'^k}{v_0^{k-1}}\, f_s(v') \tag{2.104}$$

$$J_{s,k}(v_0) = \int_{v_0}^{\infty} dv' \frac{v'^k}{v_0^{k-1}}\, f_s(v') \tag{2.105}$$

$$\Gamma = 16\pi^2 G^2 \log\Lambda \tag{2.106}$$

that enter directly into Eq. (2.21).

2.3.2 | Local diffusion coefficients for E and $\mathcal{R}$

We are now ready to propagate the fluctuations on v to fluctuations of any quantity we are interested in. Specifically, we are interested in the diffusion coefficients of energy E and angular momentum J (or equivalently $\mathcal{R}$). We will make yet another useful change of coordinates that will allow us to better represent δE, δJ and $\delta\mathcal{R}$. In this subsection, as in the rest of the manuscript and unlike in the previous section, v_r refers to the radial velocity.

First, we can choose the radial direction to define our set of coordinates, introducing an axis parallel to the position vector $\boldsymbol{e_r}$, an axis parallel to the tangential velocity $\boldsymbol{e_t}$ and a random direction $\boldsymbol{e_3}$ orthogonal to the previous ones. The velocity is then

$$\boldsymbol{v} = v_r\, \boldsymbol{e_r} + v_t\, \boldsymbol{e_t} + 0\, \boldsymbol{e_3} \tag{2.107}$$

while the variation $\delta \boldsymbol{v}$ has components

$$\boldsymbol{\delta v} = \left[\delta v_{\parallel} \frac{v_r}{v} - \delta v_{\perp,1} \frac{v_t}{v}\right] \boldsymbol{e_r} + \left[\delta v_{\parallel} \frac{v_t}{v} + \delta v_{\perp,1} \frac{v_r}{v}\right] \boldsymbol{e_t} + \delta v_{\perp,2}\, \boldsymbol{e_3} \tag{2.108}$$

The energy fluctuation is readily computed

$$\begin{aligned} \delta E &= -\frac{(\boldsymbol{v}+\boldsymbol{\delta v})^2}{2} + \frac{v^2}{2} = -\frac{\boldsymbol{\delta v}^2}{2} + \boldsymbol{v}\cdot\boldsymbol{\delta v} \\ &= -v\,\delta v_{\parallel} - \frac{1}{2}\delta v_{\parallel}^2 - \frac{1}{2}\delta v_{\perp}^2 \end{aligned} \tag{2.109}$$

The (vector) fluctuation of angular momentum is

$$\delta \boldsymbol{J} = r\boldsymbol{e_r} \times \boldsymbol{\delta v} = -r\delta v_{\perp,2}\, \boldsymbol{e_t} + r\left[\delta v_{\parallel} \frac{v_t}{v} + \delta v_{\perp,1} \frac{v_r}{v}\right] \boldsymbol{e_3} \tag{2.110}$$

giving the fluctuation of $J = |\boldsymbol{J}|$

$$\begin{aligned} \delta J &= |\boldsymbol{J} + \delta \boldsymbol{J}| - |\boldsymbol{J}| \\ &= r\left(\sqrt{\delta v_{\perp,2}^2 + \left(v_t + \delta v_{\parallel}\frac{v_t}{v} + \delta v_{\perp,1}\frac{v_r}{v}\right)^2} - v_t\right) \\ &= r v_t \left(\sqrt{1 + 2\frac{\delta v_{\parallel}}{v} + 2\delta v_{\perp,1}\frac{v_r}{v\,v_t} + 2\,\delta v_{\parallel}\delta v_{\perp,1}\frac{v_r}{v_t\,v^2} + \frac{\delta v_{\parallel}^2}{v^2} + \frac{\delta v_{\perp,1}^2\, v_r^2}{v_t^2\, v^2} + \frac{\delta v_{\perp,2}^2}{v_t^2}} - 1\right) \\ &= J\left(\frac{\delta v_{\parallel}}{v} + \delta v_{\perp,1}\frac{v_r}{v\,v_t} + \delta v_{\parallel}\delta v_{\perp,1}\frac{v_r}{v_t\,v^2} + \frac{1}{2}\frac{\delta v_{\parallel}^2}{v^2} + \frac{1}{2}\frac{\delta v_{\perp,1}^2\, v_r^2}{v_t^2\, v^2} + \frac{1}{2}\frac{\delta v_{\perp,2}^2}{v_t^2} - \frac{1}{2}\frac{\delta v_{\parallel}^2}{v^2}\right. \\ &\qquad \left. -\frac{1}{2}\delta v_{\perp,1}^2\frac{v_r^2}{v^2 v_t^2}\right) + \mathcal{O}(\delta v^3) \\ &= J\left(\frac{\delta v_{\parallel}}{v} + \delta v_{\perp,1}\frac{v_r}{v_t\,v} + \delta v_{\parallel}\delta v_{\perp,1}\frac{v_r}{v\,v_t} + \frac{1}{2}\frac{\delta v_{\perp,2}^2}{v_t^2}\right) + \mathcal{O}(\delta v^3) \end{aligned} \tag{2.111}$$

We remark here that, as emerges from the derivation of the Fokker-Planck equation, the second order diffusion coefficients $D\left[\delta x^2\right]$ are indeed related to the expectation value $\left\langle (\delta x)^2 \right\rangle$. We can use the above expressions to compute the second order diffusion coefficients

$$\delta E^2 = v^2 \delta v_{\parallel}^2 + \mathcal{O}(\delta v^3) \tag{2.112}$$

$$\delta J^2 = J^2\left(\frac{\delta v_{\parallel}^2}{v^2} + \delta v_{\perp,1}^2\,\frac{v_r^2}{v_t^2\, v^2} + 2\,\delta v_{\parallel}\,\delta v_{\perp,1}\frac{v_r}{v_t\, v^2}\right) + \mathcal{O}(\delta v^3) \tag{2.113}$$

$$\delta E\,\delta J = -J\left(\delta v_{\parallel}^2 + \delta v_{\parallel}\,\delta v_{\perp,1}\,\frac{v_r}{v_t\, v_r}\right) + \mathcal{O}(\delta v^3) \tag{2.114}$$

so that

$$D\left[\delta E\right] = -v\,D\left[\delta v_{\parallel}\right] - \frac{1}{2}D\left[\delta v_{\parallel}^2\right] - \frac{1}{2}D\left[\delta v_{\perp}^2\right] \tag{2.115}$$
$$= \Gamma m_s^2\left[-J_{s,1} + \frac{m}{m_s}\,I_{s,2}\right]$$
$$D\left[\delta J\right] = J\left(\frac{D\left[\delta v_{\parallel}\right]}{v} + \frac{D\left[\delta v_{\perp}^2\right]}{4\,v_t^2}\right) \tag{2.116}$$
$$= \Gamma m_s^2 J\left[\frac{1}{3\,v_t^2}J_{s,1} + \left(\frac{1}{2\,v_t^2} - \frac{m+m_s}{m_s}\,\frac{1}{v^2}\right)I_{s,2} - \frac{1}{6\,v_t^2}I_{s,4}\right]$$
$$D\left[\delta E^2\right] = v^2 D\left[\delta v_{\parallel}^2\right] \tag{2.117}$$
$$= \frac{2}{3}\,\Gamma\,m_s^2\,v^2\left[J_{s,1} + I_{s,4}\right]$$
$$D\left[\delta J^2\right] = \frac{J^2}{v^2}\left(D\left[\delta v_{\parallel}^2\right] + \frac{1}{2}\frac{v_r^2}{v_t^2}\,D\left[\delta v_{\perp}^2\right]\right) \tag{2.118}$$
$$= \frac{2}{3}\,\Gamma\,m_s^2\,\frac{J^2}{v^2}\left[\frac{v^2}{v_t^2}\,J_{s,1} + \frac{3}{2}\left(\frac{v^2}{v_t^2} - 1\right)\,I_{s,2} + \left(\frac{3}{2} - \frac{v^2}{2\,v_t^2}\right)\,I_{s,4}\right]$$
$$D\left[\delta E\,\delta J\right] = -J\,D\left[\delta v_{\parallel}^2\right] \tag{2.119}$$
$$= -\frac{2}{3}\,\Gamma\,m_s^2\,J\,\left[J_{s,1} + I_{s,4}\right]\,. \tag{2.120}$$

When moving to $\mathcal{R} = J^2/J_c^2$, we need to include the variation of J_c^2. Using the equation for the energy of the circular orbit, we can derive both sides

$$\begin{aligned} 1 &= -\frac{1}{2\,r_c^2}\,\frac{\partial J_c^2}{\partial E} + \frac{\partial}{\partial r}\left(\phi(r) - \frac{J_c^2}{2\,r^2}\right)\frac{\partial r_c}{\partial E} \\ -2\,r_c^2 &= \frac{\partial J_c^2}{\partial E} \end{aligned} \tag{2.121}$$

and using the equation for r_c

$$\left[\frac{3}{2}\phi' + r\frac{\phi''}{2}\right]_{r=r_c}\frac{\partial r_c}{\partial E} = 1 \qquad \frac{\partial r_c}{\partial E} = \frac{1}{\frac{3}{2}\phi_c' + r_c\frac{\phi_c''}{2}} = -\frac{P_c^2}{2\,\pi^2\,r_c} \tag{2.122}$$

Giving

$$\delta J_c^2 = -2\,r_c^2\delta E + \frac{P_c^2}{\pi^2}\,\delta E^2 \tag{2.123}$$
$$\delta\frac{1}{J_c^2} = -\frac{1}{(J_c^2)^2}\delta J_c^2 + \frac{1}{(J_c^2)^3}(\delta J_c^2)^2 = \frac{1}{J_c^2}\left(\frac{2}{v_c^2}\delta E + \left(\frac{P_c^2}{\pi^2\,J_c^2} + \frac{4}{v_c^4}\right)\delta E^2\right) \tag{2.124}$$

The variation of $\mathcal{R}$ is therefore:

$$\begin{aligned}\delta\mathcal{R} &= \frac{(J+\delta J)^2}{J_c^2 - 2\,r_c^2\,\delta E + \frac{P_c^2}{\pi^2}\delta E^2} - \frac{J^2}{J_c^2} \\ &= \frac{J^2 + 2J\,\delta J + \delta J^2}{J_c^2}\left(1 + \frac{2}{v_c^2}\delta E + \left(\frac{4}{v_c^4} - \frac{P_c^2}{J_c^2\,\pi^2}\right)\delta E^2\right) - \frac{J^2}{J_c^2} + \mathcal{O}(\delta v^3) \\ &= 2\mathcal{R}\left(\frac{\delta J}{J} + \frac{\delta E}{v_c^2} + 2\,\frac{\delta J \delta E}{J\,v_c^2} + \frac{1}{2}\frac{\delta J^2}{J^2} + \left(\frac{2}{v_c^4} - \frac{P_c^2}{2\,J_c^2\,\pi^2}\right)\,\delta E^2\right) + \mathcal{O}(\delta v^3)\end{aligned} \tag{2.125}$$

$$\delta\mathcal{R}^2 = 4\,\mathcal{R}^2\left(\frac{\delta J^2}{J^2} + \frac{\delta E^2}{v_c^4} + 2\frac{\delta J\,\delta E}{J\,v_c^2}\right) + \mathcal{O}(\delta v^3) \tag{2.126}$$

And we can then compute the diffusion coefficients in terms of the functions $J_{s,1}$, $I_{s,2}$ and $I_{s,4}$.

$$\begin{aligned}D\left[\delta\mathcal{R}\right] = 2\,\Gamma\mathcal{R}m_s^2\Bigg[&\left(\frac{2}{3\,v_t^2} - \frac{7}{3\,v_c^2} + \frac{4\,v^2}{3\,v_c^4} - \frac{v^2\,P_c^2}{3\,J_c^2\,\pi^2}\right)J_{s,1} \\ &+ \left(\frac{1}{v_t^2} - \left(\frac{m}{m_s} + \frac{3}{2}\right)\frac{1}{v^2} + \frac{m}{m_s}\,\frac{1}{v_c^2}\right)I_{s,2} \\ &+ \left(-\frac{1}{3\,v_t^2} - \frac{4}{3\,v_c^2} + \frac{1}{2\,v^2} + \frac{4\,v^2}{3\,v_c^4} - \frac{v^2\,P_c^2}{3\,J_c^2\,\pi^2}\right)I_{s,4}\Bigg]\end{aligned} \tag{2.127}$$

$$\begin{aligned}D\left[\delta\mathcal{R}^2\right] = \frac{8}{3}\,\Gamma\mathcal{R}^2m_s^2\Bigg[&\left(\frac{1}{v_t^2} + \frac{v^2}{v_c^4} - \frac{2}{v_c^2}\right)J_{s,1} \\ &+ \left(\frac{3}{2\,v_t^2} - \frac{3}{2\,v^2}\right)I_{s,2} + \left(\frac{3}{2\,v^2} - \frac{1}{2\,v_t^2} + \frac{v^2}{v_c^4} - \frac{2}{v_c^2}\right)I_{s,4}\Bigg]\end{aligned} \tag{2.128}$$

$$D\left[\delta E\delta\mathcal{R}\right] = \frac{4}{3}\,\Gamma\mathcal{R}m_s^2\left[\left(-1 + \frac{v^2}{v_c^2}\right)J_{s,1} + \left(-1 + \frac{v^2}{v_c^2}\right)I_{s,4}\right] \tag{2.129}$$

Before proceeding to assembly the coefficients for the flux-conservative form, we introduce some useful expressions.

$$I_{s,k}(E,r) = \int_E^{\phi(r)} dE'\,f_s(E')\left(\frac{\phi(r) - E'}{\phi(r) - E}\right)^{(k-1)/2} \qquad \frac{\partial}{\partial E}I_{s_k} = -f_s(E) + \frac{k-1}{2(\phi - E)}I_{s,k} \tag{2.130}$$

$$J_{s,k}(E,r) = \int_{-\infty}^{E} dE'\,f_s(E')\left(\frac{\phi(r) - E'}{\phi(r) - E}\right)^{(k-1)/2} \qquad \frac{\partial}{\partial E}J_{s_k} = f_s(E) + \frac{k-1}{2(\phi - E)}J_{s,k} \tag{2.131}$$

so that using $\partial_{\mathcal{R}} v_t^2 = v_t^2/\mathcal{R}$ we have

$$\frac{1}{2}\partial_E D\left[\delta E^2\right] = \frac{2}{3}\Gamma m_s^2\left(-J_{s,1} + I_{s,4}\right) \tag{2.132}$$

$$\frac{1}{2}\partial_{\mathcal{R}} D\left[\delta E \delta\mathcal{R}\right] = \frac{2}{3}\Gamma\, m_s^2\left[\left(-1+\frac{v^2}{v_c^2}\right) J_{s,1} + \left(-1+\frac{v^2}{v_c^2}\right) I_{s,4}\right] \tag{2.133}$$

$$\frac{1}{2}\partial_{\mathcal{R}} D\left[\delta\mathcal{R}^2\right] = \frac{8}{3}\Gamma\mathcal{R}\, m_s^2\left[\left(\frac{1}{2\,v_t^2} + \frac{v^2}{v_c^4} - \frac{2}{v_c^2}\right) J_{s,1}\right. \tag{2.134}$$

$$\left. + \left(\frac{3}{4\,v_t^2} - \frac{3}{2\,v^2}\right) I_{s,2} + \left(-\frac{1}{4\,v_t^2} + \frac{3}{2\,v^2} + \frac{v^2}{v_c^4} - \frac{2}{v_c^2}\right) I_{s,4}\right] \tag{2.135}$$

$$\frac{1}{2}\partial_E D\left[\delta E\,\delta\mathcal{R}\right] = \frac{2}{3}\,\Gamma\,\mathcal{R}\,m_s^2\left[\left(-\frac{2}{v_c^2} + \frac{2\,v^2}{v_c^4} - \frac{v^2\,P_c^2}{\pi^2\,J_c^2}\right) J_{s,1}\right. \tag{2.136}$$

$$\left. + \left(\frac{1}{v_c^2} + \frac{2\,v^2}{v_c^4} - \frac{v^2\,P_c^2}{\pi^2\,J_c^2} - \frac{3}{v^2}\right) I_{s,4}\right]$$

And we can finally derive the coefficients of the flux conservative form Eq. (2.22):

$$D_E = \Gamma m_s^2\left[\left(-\frac{1}{3} + \frac{2\,v^2}{3\,v_c^2}\right) J_{s,1} - \frac{m_s}{m}\, I_{s,2} + \frac{2\,v^2}{3\,v_c^2}\, I_{s,4}\right] \tag{2.137}$$

$$D_R = 2\,\Gamma\mathcal{R} m_s^2\left[\left(-\frac{1}{v_c^2} + \frac{2\,v^2}{3\,v_c^4}\right) J_{s,1}\right. \tag{2.138}$$

$$+ \left(\left(\frac{m}{m_s} - \frac{1}{2}\right)\frac{1}{v^2} - \frac{m}{m_s}\frac{1}{v_c^2}\right) I_{s,2}$$

$$\left. + \left(-\frac{1}{v_c^2} + \frac{1}{2\,v^2} + \frac{2\,v^2}{3\,v_c^2}\right) I_{s,4}\right]$$

$$D_{EE} = \frac{1}{3}\,\Gamma\, m_s^2\, v^2\left[J_{s,1} + I_{s,4}\right] \tag{2.139}$$

$$D_{RR} = \frac{4}{3}\,\Gamma\mathcal{R}^2 m_s^2\left[\left(\frac{1}{v_t^2} + \frac{v^2}{v_c^4} - \frac{2}{v_c^2}\right) J_{s,1}\right. \tag{2.140}$$

$$\left. + \left(\frac{3}{2\,v_t^2} - \frac{3}{2\,v^2}\right) I_{s,2} + \left(-\frac{1}{2\,v_t^2} + \frac{3}{2\,v^2} + \frac{v^2}{v_c^4} - \frac{2}{v_c^2}\right) I_{s,4}\right]$$

$$D_{ER} = \frac{2}{3}\,\Gamma\, m_s^2\,\mathcal{R}\left(\frac{v^2}{v_c^2} - 1\right)\left[J_{s,1} + I_{s,4}\right] \tag{2.141}$$

$$\Gamma = 16\pi^2\, G^2 \log\Lambda$$

2.3.3 | Orbit averaged diffusion coefficients

As we discussed under Eq.(2.37), the diffusion coefficients of the Fokker-Planck equation for $n(E,\mathcal{R})$ describe the expectation value of δE and $\delta\mathcal{R}$ (and their products) for an orbit described by $(E,\mathcal{R})$ in an infinitesimal timestep δt. It is clear that, according to our previous calculations, such a variation depends in general on the distance r from

the center of the system, since all the diffusion coefficients we derived in the previous section depend on the instantaneous value of v and v_t. We will now consider an averaged description of the system where the distribution function only depends on E and $\mathcal{R}$. Specifically, we compute the diffusion coefficients $\mathcal{D}[\delta x]$ as the orbital average of their local counterparts $D[\delta x]$.

$$\langle \delta x \rangle_{\text{orb}} = \int_{\text{orb}} \frac{\langle \delta x \rangle}{\delta t} dt \simeq P\,\mathcal{D}[\delta x] \qquad \Rightarrow \qquad \mathcal{D}[\delta x] \simeq \frac{1}{P}\int_{orb} D[\delta x]\, dt\,. \tag{2.142}$$

Therefore we will use the formula

$$\mathcal{D}[\delta x] = \frac{1}{P}\left\{ \int_{r_-}^{r_+} \frac{dr}{v_r} D[\delta x]\,(v_r > 0) + \int_{r_+}^{r_-} \frac{dr}{v_r} D[\delta x]\,(v_r < 0) \right\} \tag{2.143}$$

basically applying it to all of the corresponding coefficients. The variation of the orbital integral defined in this way is simply

$$\begin{aligned} \delta P\,\mathcal{D}[\delta x] = {} & \delta r_+ D[\delta x](v_r = 0) - \delta r_- D[\delta x](v_r = 0) \\ & + \delta r_- D[\delta x](v_r = 0) - \delta r_+ D[\delta x](v_r = 0) \\ & + \left\{ \int_{r_-}^{r_+} \frac{dr}{v_r} \delta \frac{D[\delta x]\,(v_r > 0)}{v_r} + \int_{r_+}^{r_-} dr \delta \frac{D[\delta x]\,(v_r < 0)}{v_r} \right\} \end{aligned} \tag{2.144}$$

and since the diffusion coefficients do not depend on the sign of v_r, we simply get

$$\mathcal{D}[\delta x] = \frac{2}{P}\int_{r_-}^{r_+} \frac{dr}{v_r} D[\delta x] \tag{2.145}$$

We will now proceed to compute the last result of this section, that is the set of the

coefficients for the flux conservation form of the orbit averaged equation.

$$\mathcal{D}\left[\delta E\right] = \frac{2\,\Gamma m_s^2}{P}\int_{r_-}^{r_+}\frac{dr}{v_r}\left[-J_{s,1}+\frac{m}{m_s}\,I_{s,2}\right] \tag{2.146}$$

$$\begin{aligned}\mathcal{D}\left[\delta\mathcal{R}\right] = \frac{4\,\Gamma\mathcal{R} m_s^2}{P}\int_{r_-}^{r_+}\frac{dr}{v_r}\Bigg[&\left(\frac{2}{3\,v_t^2}-\frac{7}{3\,v_c^2}+\frac{4\,v^2}{3\,v_c^4}-\frac{v^2\,P_c^2}{3\,J_c^2\,\pi^2}\right)J_{s,1}\\&+\left(\frac{1}{v_t^2}-\left(\frac{m}{m_s}+\frac{3}{2}\right)\frac{1}{v^2}+\frac{m}{m_s}\,\frac{1}{v_c^2}\right)I_{s,2}\\&+\left(-\frac{1}{3\,v_t^2}-\frac{4}{3\,v_c^2}+\frac{1}{2\,v^2}+\frac{4\,v^2}{3\,v_c^4}-\frac{v^2\,P_c^2}{3\,J_c^2\,\pi^2}\right)I_{s,4}\Bigg]\end{aligned} \tag{2.147}$$

$$\mathcal{D}\left[\delta E^2\right] = \frac{4\,\Gamma\,m_s^2}{3\,P}\int_{r_-}^{r_+}\frac{dr}{v_r}v^2\left[J_{s,1}+I_{s,4}\right] \tag{2.148}$$

$$\begin{aligned}\mathcal{D}\left[\delta\mathcal{R}^2\right] = \frac{16\Gamma\mathcal{R}^2 m_s^2}{3\,P}\int_{r_-}^{r_+}\frac{dr}{v_r}\Bigg[&\left(\frac{1}{v_t^2}+\frac{v^2}{v_c^4}-\frac{2}{v_c^2}\right)J_{s,1}\\&+\left(\frac{3}{2\,v_t^2}-\frac{3}{2\,v^2}\right)I_{s,2}+\left(\frac{3}{2\,v^2}-\frac{1}{2\,v_t^2}+\frac{v^2}{v_c^4}-\frac{2}{v_c^2}\right)I_{s,4}\Bigg]\end{aligned} \tag{2.149}$$

$$\mathcal{D}\left[\delta E\delta\mathcal{R}\right] = \frac{8\Gamma\mathcal{R} m_s^2}{3\,P}\int_{r_-}^{r_+}\frac{dr}{v_r}\left[\left(-1+\frac{v^2}{v_c^2}\right)J_{s,1}+\left(-1+\frac{v^2}{v_c^2}\right)I_{s,4}\right] \tag{2.150}$$

$$\Gamma = 16\pi^2\,G^2\,\log\Lambda\,.$$

Since $\mathcal{J} = 4\pi^2\,J_c^2\,P$, we can immediately start computing the derivatives needed. A key result is

$$\frac{\partial}{\partial E}\frac{1}{v_r} = \frac{1}{v_r^3}\left(1-\frac{v_t^2}{v_c^2}\right) \qquad \frac{\partial}{\partial\mathcal{R}}\frac{1}{v_r} = \frac{1}{v_r^3}\frac{v_t^2}{2\,\mathcal{R}} \tag{2.151}$$

so that

$$\begin{aligned}\frac{\partial}{\partial E}\mathcal{J}\mathcal{D}\left[\delta E^2\right] &= 8\pi^2\frac{\partial}{\partial E}J_c^2\int_{r_-}^{r_+}\frac{dr}{v_r}D\left[\delta E^2\right]\\&= -8\pi^2 J_c^2\int_{r_-}^{r_+}\frac{dr}{v_r}\frac{2}{v_c^2}\,D\left[\delta E^2\right]\\&\quad+8\pi^2 J_c^2\int_{r_-}^{r_+}\frac{dr}{v_r}\left(\frac{1}{v_r^2}\left(1-\frac{v_t^2}{v_c^2}\right)D\left[\delta E^2\right]+\partial_E D\left[\delta E^2\right]\right)\\&= 8\pi^2 J_c^2\int_{r_-}^{r_+}\frac{dr}{v_r}\left(\left(\frac{1}{v_r^2}-\frac{v_t^2}{v_r^2 v_c^2}-\frac{2}{v_c^2}\right)D\left[\delta E^2\right]+\partial_E D\left[\delta E^2\right]\right)\\&= \frac{16}{3}\Gamma\pi^2 m_s^2\,J_c^2\int_{r_-}^{r_+}\frac{dr}{v_r}\Bigg[\left(\frac{v^2}{v_r^2}-\frac{v^2 v_t^2}{v_r^2 v_c^2}-\frac{2\,v^2}{v_c^2}-2\right)J_{s,1}\\&\quad+\left(\frac{v^2}{v_r^2}-\frac{v^2 v_t^2}{v_r^2 v_c^2}-\frac{2\,v^2}{v_c^2}+1\right)I_{s,4}\Bigg]\end{aligned} \tag{2.152}$$

$$\begin{aligned}\frac{\partial}{\partial\mathcal{R}}\mathcal{J}\mathcal{D}\left[\delta E\delta\mathcal{R}\right] &= 8\pi^2\frac{\partial}{\partial\mathcal{R}}J_c^2\int_{r_-}^{r_+}\frac{dr}{v_r}D\left[\delta E\delta\mathcal{R}\right]\\ &= 8\pi^2 J_c^2\int_{r_-}^{r_+}\frac{dr}{v_r}\left(\frac{1}{2\mathcal{R}}\frac{v_t^2}{v_r^2}D\left[\delta E\,\delta R\right]+\partial_{\mathcal{R}}D\left[\delta E\,\delta R\right]\right)\\ &= \frac{16}{3}\Gamma\,\pi^2\,m_s^2\,J_c^2\int_{r_-}^{r_+}\frac{dr}{v_r}\left(-\frac{v_t^2}{v_r^2}+\frac{v^2\,v_t^2}{v_r^2v_c^2}-2+2\frac{v^2}{v_c^2}\right)\left(J_{s,1}+I_{s,4}\right)\end{aligned} \tag{2.153}$$

$$\begin{aligned}\frac{\partial}{\partial\mathcal{R}}\mathcal{J}\mathcal{D}\left[\delta\mathcal{R}^2\right] &= 8\pi^2\frac{\partial}{\partial\mathcal{R}}J_c^2\int_{r_-}^{r_+}\frac{dr}{v_r}D\left[\delta\mathcal{R}^2\right]\\ &= 8\pi^2 J_c^2\int_{r_-}^{r_+}\frac{dr}{v_r}\left(\frac{1}{2\mathcal{R}}\frac{v_t^2}{v_r^2}D\left[\delta R^2\right]+\partial_{\mathcal{R}}D\left[\delta R^2\right]\right)\\ &= \frac{32}{3}\Gamma\,\pi^2\,m_s^2\,J^2\int_{r_-}^{r_+}\frac{dr}{v_r}\left[\left(\frac{1}{v_r^2}+\frac{v^2\,v_t^2}{v_r^2\,v_c^4}-\frac{2\,v_t^2}{v_c^2\,v_r^2}+\frac{2}{v_t^2}+4\,\frac{v^2}{v_c^4}-\frac{8}{v_c^2}\right)J_{s,1}\right.\\ &\quad+\left(\frac{3}{v_t^2}-\frac{9}{2\,v^2}\right)I_{s,2}\\ &\quad\left.+\left(-\frac{1}{v_t^2}+\frac{9}{2\,v^2}+\frac{1}{v_r^2}+\frac{v^2\,v_t^2}{v_r^2\,v_c^4}-\frac{2\,v_t^2}{v_r^2\,v_c^2}+\frac{4\,v^2}{v_c^4}-\frac{8}{v_c^2}\right)I_{s,4}\right]\end{aligned} \tag{2.154}$$

$$\begin{aligned}\frac{\partial}{\partial E}\mathcal{J}\mathcal{D}\left[\delta E\delta\mathcal{R}\right] &= 8\pi^2\frac{\partial}{\partial E}J_c^2\int_{r_-}^{r_+}\frac{dr}{v_r}D\left[\delta E\delta\mathcal{R}\right]\\ &= -8\pi^2 J_c^2\int_{r_-}^{r_+}\frac{dr}{v_r}\frac{2}{v_c^2}\,D\left[\delta E\delta\mathcal{R}\right]\\ &\quad+8\pi^2 J_c^2\int_{r_-}^{r_+}\frac{dr}{v_r}\left(\frac{1}{v_r^2}\left(1-\frac{v_t^2}{v_c^2}\right)D\left[\delta E\delta\mathcal{R}\right]+\partial_E D\left[\delta E\delta\mathcal{R}\right]\right)\\ &= 8\pi^2 J_c^2\int_{r_-}^{r_+}\frac{dr}{v_r}\left(\left(\frac{1}{v_r^2}-\frac{v_t^2}{v_r^2v_c^2}-\frac{2}{v_c^2}\right)D\left[\delta E\delta\mathcal{R}\right]+\partial_E D\left[\delta E\delta\mathcal{R}\right]\right)\\ &= \frac{32}{3}\pi^2\,\Gamma\,m_s^2J^2\int_{r_-}^{r_+}\frac{dr}{v_r}\left[\left(\frac{v^2}{v_c^2\,v_r^2}-\frac{v^2\,v_t^2}{v_r^2\,v_c^4}-\frac{1}{v_r^2}+\frac{v_t^2}{v_r^2\,v_c^2}-\frac{v^2\,P_c^2}{\pi^2\,J_c^2}\right)J_{s,1}\right.\\ &\quad\left.+\left(\frac{v^2}{v_c^2\,v_r^2}-\frac{v^2\,v_t^2}{v_r^2\,v_c^4}-\frac{1}{v_r^2}+\frac{v_t^2}{v_r^2\,v_c^2}-\frac{3}{v^2}+\frac{3}{v_c^2}-\frac{v^2\,P_c^2}{\pi^2\,J_c^2}\right)I_{s,4}\right]\end{aligned} \tag{2.155}$$

giving

$$\mathcal{D}_E = -8\,\Gamma\,\pi^2\,J_c^2\,m\,m_s\int_{r_-}^{r_+}\frac{dr}{v_r}\,I_{s,2} \tag{2.156}$$

$$\mathcal{D}_R = -16\,\Gamma\pi^2\,m\,m_s J^2\int_{r_-}^{r_+}\frac{dr}{v_r}\left(\frac{1}{v_c^2}-\frac{1}{v^2}\right)\,I_{s,2} \tag{2.157}$$

$$\mathcal{D}_{EE} = \frac{8}{3}\,\Gamma\,\pi^2\,m_s^2\,J_c^2\int_{r_-}^{r_+}\frac{dr}{v_r}v^2\,(J_{s,1}+I_{s,4}) \tag{2.158}$$

$$\mathcal{D}_{ER} = \frac{16}{3}\,\Gamma\,\pi^2\,m_s^2\,J^2\int_{r_-}^{r_+}\frac{dr}{v_r}\left(\frac{v^2}{v_c^2}-1\right)(J_{s,1}+I_{s,4}) \tag{2.159}$$

$$\begin{aligned}\mathcal{D}_{RR} = \frac{16}{3}\Gamma\,\pi^2\,m_s^2 R\,J^2\int_{r_-}^{r_+}\frac{dr}{v_r}\Bigg[&\left(\frac{2}{v_t^2}+\frac{2\,v^2}{v_c^4}-\frac{4}{v_c^2}\right)J_{s,1}\\ &+\left(\frac{3}{v_t^2}-\frac{3}{v^2}\right)I_{s,2}+\left(\frac{3}{v^2}-\frac{1}{v_t^2}+\frac{2\,v^2}{v_c^4}-\frac{4}{v_c^2}\right)I_{s,4}\Bigg]\end{aligned} \tag{2.160}$$

$$\Gamma = 16\pi^2\,G^2\log\Lambda\,.$$

2.3.4 | Ergodic diffusion coefficients

We will now consider the ergodic case, where the distribution function only depends on E. In order to compute the kicks received by the set of particles with energy E, we average over all the kicks received by each orbit (thus in the period of the orbit) in one period. This means that we will define the diffusion coefficients from the equation

$$\langle\delta x\rangle_{orb,\mathcal{R}} = \int_0^1 d\mathcal{R}P(E,\mathcal{R})\,\langle\delta x\rangle_{orb} \simeq \bar{P}(E)\bar{\mathcal{D}}[\delta x] \qquad \bar{\mathcal{D}}[\delta x] = \int_0^1 d\mathcal{R}\frac{P(E,\mathcal{R})}{\bar{P}(E)}\,\mathcal{D}\,[\delta x] \tag{2.161}$$

where the quantity $\bar{P}$ is

$$\bar{P}(E) \equiv \int_0^1 d\mathcal{R}P(E,\mathcal{R}) = \frac{g(E)}{4\,\pi^2\,J_c^2} \tag{2.162}$$

giving

$$\begin{aligned}\bar{\mathcal{D}}[\delta E] &= \int_0^1 d\mathcal{R}\mathcal{D}\,[\delta E] \\ &= 2\,\frac{\Gamma\,m_s^2}{\bar{P}}\int_0^1 d\mathcal{R}\int_{r_-}^{r_+}\frac{dr}{v_r}\left(-J_{s,1}+\frac{m}{m_s}\,I_{s,2}\right)\end{aligned} \tag{2.163}$$

$$\begin{aligned}\bar{\mathcal{D}}\left[\delta E^2\right] &= \int_0^1 d\mathcal{R}\mathcal{D}\left[\delta E^2\right] \\ &= \frac{4\,\Gamma\,m_s^2}{3\,\bar{P}}\int_0^1 d\mathcal{R}\int_{r_-}^{r_+}\frac{dr}{v_r}v^2\,(J_{s,1}+I_{s,4})\end{aligned} \tag{2.164}$$

$$\tag{2.165}$$

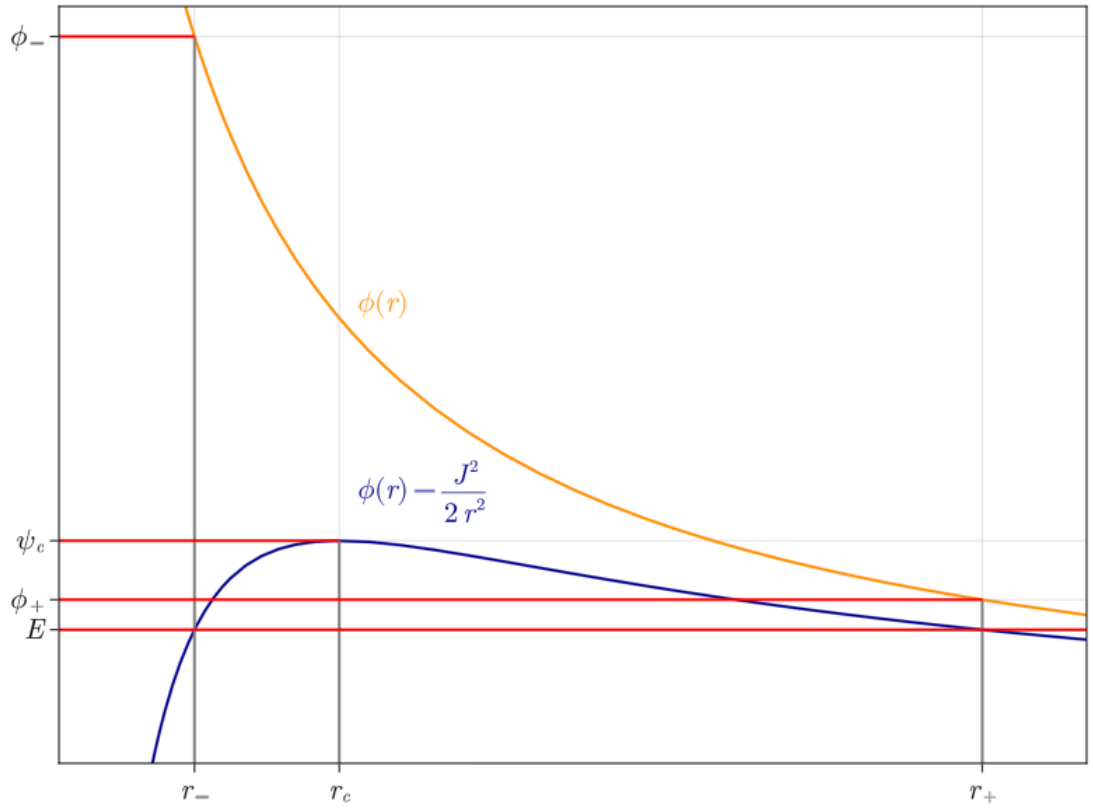

Figure 2.2: Potential $\phi(r)$ and effective potential $\psi(r)$ for an orbit with angular momentum J. We marked on the axes the notable quantities r_- and $\phi_- = \phi(r_-)$, r_+ and $\phi_+ = \phi(r_+)$, r_c and $\psi_c = \phi(r_c) - J^2/(2\,r_c^2)$.

We can now perform the integrals involved in the computations by inserting the explicit form of $I_{s,k}$ and $J_{s,k}$. We will reorder the integration, so it is useful to keep Fig.2.2 in mind to follow the changes.

Since $J_{s,1}$ does not depend on r, the integral simply gives

$$\mathcal{J}_{1,E} = \int_0^1 d\mathcal{R} \int_{r_-}^{r_+} \frac{dr}{v_r} J_{s,1}(E) = \frac{g}{8\,\pi^2 J_c^2}\, J_{s,1}(E)\,. \tag{2.166}$$

When considering $I_{s,2}$, on the other hand, we want to reorder the integration moving the integral over E' outside of the integration in r and $\mathcal{R}$. The same of course applies to $I_{s,4}$, so we will do it operating on the integration operators. Therefore we define

$$\mathcal{I}_{2,E} = \int_0^1 d\mathcal{R} \int_{r_-}^{r_+} dr \int_E^{\phi(r)} dE'\, \frac{1}{v_r} \left(\frac{\phi(r) - E'}{\phi(r) - E}\right)^{\frac{k-1}{2}} \equiv \int_{\mathcal{D}} \frac{1}{v_r} \left(\frac{\phi(r) - E'}{\phi(r) - E}\right)^{(k-1)/2} \tag{2.167}$$

and inverting the order of integration of $\mathcal{R}$ and r

$$\int_{\mathcal{D}} = \int_0^{r_c} dr \int_0^{\mathcal{R}_-} d\mathcal{R} \int_{-\infty}^{\phi(r)} dE' + \int_{r_c}^{\phi^{-1}(E)} dr \int_0^{\mathcal{R}_+} d\mathcal{R} \int_E^{\phi(r)} dE' \tag{2.168}$$

Where $\mathcal{R}_\pm(E, r)$ are such that the pericenter of the corresponding orbit is at r. The integration domain over E' does not depend on $\mathcal{R}$, so we can swap the two integration order

$$\int_{\mathcal{D}} = \int_0^{r_c} dr \int_E^{\phi(r)} dE' \int_0^{\mathcal{R}_-} d\mathcal{R} + \int_{r_c}^{\phi^{-1}(E)} dr \int_E^{\phi(r)} dE' \int_0^{\mathcal{R}_+} d\mathcal{R} \tag{2.169}$$

and, since $\phi_c \equiv \phi(r_c) > E$, we split the first integration in two

$$\begin{aligned} \int_{\mathcal{D}} &= \int_E^{\phi_c} dE' \int_0^{r_c} dr \int_0^{\mathcal{R}_-} d\mathcal{R} + \int_{\phi_c}^{\phi(0)} dE' \int_0^{\phi^{-1}(E')} dr \int_0^{\mathcal{R}_-} d\mathcal{R} \\ &= \int_E^{\phi_c} dE'' \int_{r_c}^{\phi^{-1}(E')} dr \int_0^{\mathcal{R}_+} d\mathcal{R}\,. \end{aligned} \tag{2.170}$$

We are now ready to perform the integral

$$\begin{aligned} \mathcal{I}_2 = &\int_E^{\phi_c} dE' f_s(E') \int_0^{r_c} \frac{2\,r^2}{J_c^2} \sqrt{2\phi - 2\,E'} \\ &+ \int_{\phi_c}^{\phi(0)} dE' f_s(E)' \int_0^{\phi^{-1}(E')} dr \frac{2\,r^2}{J_c^2} \sqrt{2\phi - 2E'} \\ &+ \int_E^{\phi_c} dE' f_s(E') \int_{r_c}^{\phi^{-1}(E')} \frac{2\,r^2}{J_c^2} \sqrt{2\phi - 2\,E'} \\ = &\frac{1}{8\pi^2\,J_c^2} \int_E^{\phi(0)} dE' f_s(E') g(E') \end{aligned} \tag{2.171}$$

When considering the integrals involved in $\bar{\mathcal{D}}\left[\delta E^2\right]$, the one involving $J_{s,1}$ is:

$$\begin{aligned} \mathcal{J}_{1,EE} &= J_{s,1} \int_0^1 d\mathcal{R} \int_{r_-}^{r_+} \frac{dr}{v_r} v^2 \\ &= J_{s,1} \left[\int_0^{r_c} dr (2\phi - 2E) \int_0^{\mathcal{R}_-} \frac{dr}{v_r} + \int_{r_c}^{\phi^{-1}(E)} dr (2\phi - 2E) \int_0^{\mathcal{R}_-} \frac{dr}{v_r} \right] \\ &= J_{s,1} \int_0^{\phi^{-1}(E)} dr \frac{2\,r^2}{J_c^2} \sqrt{2\phi - 2\,E}^3 \\ &= \frac{3}{8\,\pi^2\,J_c^2} J_{s,1} \int_E^{\phi(0)} dE' g(E') \end{aligned} \tag{2.172}$$

where we used the fact that

$$\frac{\partial}{\partial E} \int_0^{\phi^{-1}(E)} dr r^2 \sqrt{2\phi - 2\,E}^3 = -3 \int_0^{\phi^{-1}(E)} dr\, r^2 \sqrt{2\phi - 2E} = \frac{-3}{16\pi^2}\, g(E) \tag{2.173}$$

The integral involving $I_{s,4}$ on the other hand is simplified by the factor v^2 since

$$v^2\, I_{s,4} = \int_E^{\phi(r)} dE'(2\phi - E')\, f_s(E') \tag{2.174}$$

so that the term can be combined with the factor $\sqrt{\phi - E'}$ coming from the inner integration over $\mathcal{R}$:

$$\begin{aligned}\mathcal{I}_{s,4} &= \int_E^{\phi_c} dE' f_s(E') \int_0^{r_c} \frac{2\,r^2}{J_c^2}\sqrt{2\phi - 2\,E'}^3 \\ &\quad + \int_{\phi_c}^{\phi(0)} dE' f_s(E)' \int_0^{\phi^{-1}(E')} dr \frac{2\,r^2}{J_c^2}\sqrt{2\phi - 2E'}^3 \\ &\quad + \int_E^{\phi_c} dE' f_s(E') \int_{r_c}^{\phi^{-1}(E')} \frac{2\,r^2}{J_c^2}\sqrt{2\phi - 2\,E'}^3 \\ &= \frac{3}{8\pi^2\, J_c^2}\int_E^{\phi(0)} dE' f_s(E') \int_{E'}^{\phi(0)} dE'' g(E'')\end{aligned} \tag{2.175}$$

so that we can assembly all the terms

$$\bar{\mathcal{D}}[\delta E] = \Gamma\, m_s^2 \left[-J_{s,1} + \frac{m}{m_s}\frac{1}{g(E)}\int_E^{\phi(0)} f_s(E')g(E')\right] \tag{2.176}$$

$$\bar{\mathcal{D}}\left[\delta E^2\right] = \frac{2\,\Gamma\, m_s^2}{g(E)}\left[J_{s,1}\int_E^{\phi(0)} dE' g(E') + \int_E^{\phi(0)} dE'\, f_s(E')\int_{E'}^{\phi(0)} dE'' g(E'')\right] \tag{2.177}$$

and we can therefore compute the coefficients for the flux conservation form:

$$\begin{aligned}\frac{1}{2}\frac{\partial}{\partial E} g\,\bar{\mathcal{D}}\left[\delta E^2\right] &= \Gamma\, m_s^2\left[f_s(E)\int_E^{\phi(0)} dE' g(E') - J_{s,1} g - f_s(E)\int_E^{\phi(0)} dE' g(E')\right] \\ &= -\Gamma m_s^2 J_{s,1}(E) g(E)\end{aligned}$$

so that

$$\bar{\mathcal{D}}_E = -\Gamma m\, m_s \int_E^{\phi(0)} f_s(E')g(E') \tag{2.178}$$

$$\bar{\mathcal{D}}_{EE} = \Gamma\, m_s^2\left[J_{s,1}(E)\int_E^{\phi(0)} dE' g(E') + \int_E^{\phi(0)} dE'\, f_s(E')\int_{E'}^{\phi(0)} dE'' g(E'')\right] \tag{2.179}$$

2.4 | Averaging of equations to reduce dimensions

The different equations we have considered, the local, the orbit averaged and the ergodic Fokker-Planck equation can be formally obtained one from the other. More specifically, one needs to promote the averaging of the DF to all the equation. For example, considering the local and the orbit averaged equation, the orbit averaging operation is:

$$\langle f(E,\mathcal{R})\rangle = \frac{2}{P}\int_{r_-}^{r_+}\frac{dr}{v_r} f(E,\mathcal{R},r) = \frac{1}{\mathcal{J}}\int\frac{dr}{v_r} 8\pi^2 J_c^2 f(E,\mathcal{R},r) = \frac{n(E,\mathcal{R})}{\mathcal{J}(E,\mathcal{R})} \tag{2.180}$$

with zero endpoints variations. Then, one needs to

1. Replace f with its average $\langle f \rangle$
2. Apply the averaging operator to all the terms

From the local to the orbit averaged equation we have:

$$\begin{aligned}
\left\langle \frac{d}{dt} \langle f \rangle \right\rangle &= \left\langle \frac{\partial}{\partial E} \langle f \rangle \; D\left[\delta E\right] + \frac{1}{2}\frac{\partial^2}{\partial E^2} \langle f \rangle \; D\left[\delta E^2\right] + \ldots \right\rangle \\
\frac{1}{\mathcal{J}}\frac{d}{dt} \langle f \rangle \int \frac{dr}{v_r} 8\pi^2 J_c^2 &= \frac{1}{\mathcal{J}} \int \frac{dr}{v_r} 8\pi^2 J_c^2 \left(\frac{\partial}{\partial E} \langle f \rangle \; D\left[\delta E\right] + \frac{1}{2}\frac{\partial^2}{\partial E^2} \langle f \rangle \; D\left[\delta E^2\right] + \ldots \right) \\
\frac{d}{dt}\mathcal{J} \; \langle f \rangle &= \frac{\partial}{\partial E} \langle f \rangle \; 8\pi^2 J_c^2 \int \frac{dr}{v_r} D\left[\delta E\right] + \frac{1}{2}\frac{\partial^2}{\partial E^2} \langle f \rangle \; 8\pi^2 J_c^2 \int \frac{dr}{v_r} D\left[\delta E^2\right] + \ldots \\
\frac{d}{dt} n &= \frac{\partial}{\partial E} \langle f \rangle \; \mathcal{J}\mathcal{D}\left[\delta E\right] + \frac{1}{2}\frac{\partial^2}{\partial E^2} \langle f \rangle \; \mathcal{J}\mathcal{D}\left[\delta E^2\right] + \ldots \\
\frac{d}{dt} n &= \frac{\partial}{\partial E} n\mathcal{D}\left[\delta E\right] + \frac{1}{2}\frac{\partial^2}{\partial E^2} n\,\mathcal{D}\left[\delta E^2\right] + \ldots
\end{aligned} \tag{2.181}$$

Using now the average

$$\bar{f} \equiv \frac{2}{\bar{P}} \int_0^1 d\mathcal{R} \int_{r_-}^{r_+} \frac{dr}{v_r} f(E, \mathcal{R}, r) = \frac{1}{g} \int_0^1 d\mathcal{R} \int_{r_-}^{r_+} \frac{dr}{v_r} 8\pi^2 \, J_c^2 \, f(E, \mathcal{R}, r) \tag{2.182}$$

on the local Fokker-Planck equation we proceed as before. When the integral arrives at terms with at least $\partial_{\mathcal{R}}$ we can evaluate the corresponding terms at the endpoints.

$$\begin{aligned}
\frac{d}{dt} \bar{f}\, g &= \frac{\partial}{\partial E} \bar{f} 4\pi^2 \, J_c^2 \int_0^1 d\mathcal{R} P \, \mathcal{D}\left[\delta E\right] + \frac{1}{2}\frac{\partial^2}{\partial E^2} \bar{f}\, 4\pi^2 \, J_c^2 \int_0^1 d\mathcal{R} P \, \mathcal{D}\left[\delta E^2\right] \\
&\quad + \frac{1}{2}\frac{\partial}{\partial E} \langle f \rangle 4\pi^2 \, J_c^2 \left[P \, \mathcal{D}\left[\delta E \delta \mathcal{R}\right] \right]_0^1 + \mathcal{F}_R(1) - \mathcal{F}_R(0) \\
\frac{d}{dt} \bar{n} &= \frac{\partial}{\partial E} \bar{n} \bar{\mathcal{D}}[\delta E] + \frac{1}{2}\frac{\partial^2}{\partial E^2} \bar{n} \bar{\mathcal{D}}\left[\delta E^2\right]
\end{aligned} \tag{2.183}$$

where we have used the fact that the diffusion coefficients of involving $\delta\mathcal{R}$ vanish for both $\mathcal{R} = 0$ and $\mathcal{R} = 1$, and so does $\mathcal{F}_R$.

2.5 | Relaxation Timescales

The flux-conservative form of the orbit-averaged Fokker-Planck equation allows one to understand the dynamical evolution of the system. As already shown by Cohn and Kulsrud (1978), relaxation in $\mathcal{R}$ for eccentric orbits is more efficient than relaxation in E.

For small $\mathcal{R}$, the diffusion coefficients involving $\delta\mathcal{R}$ are dominated by the contributions from δJ, in particular by the terms weighted by $1/v_t^2$. Therefore

$$\mathcal{R}\,\mathcal{D}\left[\delta\mathcal{R}\right] \sim \mathcal{D}\left[\delta\mathcal{R}^2\right] \sim \frac{\mathcal{R}}{v_c^2}\int_0^{\phi^{-1}(E)} dr\,\frac{r^2}{r_c^2} D\left[\delta v_\perp^2\right] \tag{2.184}$$

while the energy diffusion coefficients behave like

$$\mathcal{D}\left[\delta E\right] \sim \frac{\mathcal{D}\left[\delta E^2\right]}{E} \sim \int_0^{\phi^{-1}(E)} dr D\left[\delta v_\perp^2\right] \tag{2.185}$$

The contribution of the two integrals is of the same order of magnitude, at least in the Keplerean approximation. In this case $\phi^{-1}(E) = 2r_c(E)$ and $E = v_c^2$. Therefore we have

$$\mathcal{D}\left[\delta\mathcal{R}^2\right] \sim \mathcal{R}\,\frac{\mathcal{D}\left[\delta E\right]}{E} \qquad \Rightarrow \qquad t_\mathcal{R} \simeq \mathcal{R}\,t_E\,. \tag{2.186}$$

Now, since $E \propto 1/r_c$, t_E is representative of the relaxation of the spatial density and, therefore, of the stellar potential. For this reason, the quantity t_E is usally referred to as the relaxation timescale of galactic nuclei.

Given this hierarchy in relaxation timescales for eccentric orbits, the flux of particles whose pericenter r_- is driven below the critical value of the loss cone $r_{\rm LC}$ is set by the relaxation in $\mathcal{R}$, that for a highly eccentric Keplerian orbit corresponds to $\mathcal{R} \simeq 2\,r_-/a$.

2.6 | Multi-mass systems in galactic nuclei

As we anticipated at the beginning of our overview on orbits in galactic nuclei, we will apply the formalism we developed to systems where

- We have $m = 2$ stellar components or stellar species, each described by the corresponding distribution function f_k, with $k = 1, \ldots, m$.
- Each object is subject to stochastic interactions with all the m species.

Considering a time δt that is significantly smaller than the relaxation timescale of the system (that can be estimated directly from the various diffusion coefficients, for example $\mathcal{R}/D\left[\delta\mathcal{R}\right]$ for the local Fokker-Planck equation), one can derive for each component f_k a Fokker-Planck equation:

$$\frac{d}{dt}f^k + \boldsymbol{\nabla}\cdot\boldsymbol{F}^k = 0 \tag{2.187}$$

where the diffusion coefficients must include the contribution from all the m species. The insertion of the various contributions from the different species happens during the

integration over the distribution of the diffusion coefficients for δv_r and δv_t in Eq.(2.72) and following. There, one should merely sum all the diffusion coefficients over the various scatterer distributions, which means

$$D\left[\delta x\right]_k = \sum_{j=1}^{m} D\left[\delta x\right]_{kj} \tag{2.188}$$

where $D\left[\delta x\right]_{ks}$ is the diffusion coefficient computed with $m = m_k$ and $m_s = m_j$, $f_s = f^j$ in the notation of this chapter.

After a time δt, however, the diffusion coefficients might have changed, since the distribution of the particles has evolved. The evolution equation (2.187) acquires a further dependence on f through the diffusion coefficients, and formally ceases to be a Fokker-Planck equation (whose coefficients only depend on $(E, \mathcal{R})$, and not on f).

2.7 | Additional physics

In this work, we model the diffusion coefficients to include 2-body relaxation in the scattering approximation. Naturally, this effective treatment neglects some important physics that plays an important role in the evolution of inner regions of galactic nuclei. In general, inside the influence radius of a galaxy (that typically ranges from 10^{-6} pc up to 1 pc), one can identify three main classes of interactions that can contribute to the evolution of orbital parameters (Bar-Or and Alexander, 2014; Merritt, 2013).

1. **Short-time interactions**. In addition to two body scatterings, other phenomena participate energy and momentum exchange between stars: three-body and multi-body interactions, extremely close (strong) scattering events, and destructive collisions. These events typically require a single close approach of two orbits, which means that the participating objects can move on very different orbits in terms of energy and angular momentum. Therefore, these phenomena dominate the overall relaxation of galactic nuclei since alter significantly the orbital parameters.

2. **Long-time interactions**. This class of interactions affects particles moving on similar orbits, where the scattering approximation does not hold: particles in their orbital motion are never so distant that their mutual force is negligible. This is the case, for example, of stars close to the central massive black hole in galactic nuclei. Here, orbits are almost Keplerian and the mutual interaction can be effectively described treating each orbit as a whole as a disc or - if the orbits are eccentric - as a massive rod. These interactions are typically faster than short-time interactions and are responsible for the relaxation of particles with similar orbital parameters.

3. **General relativistic effects** This class of phenomena is stronger on orbits with pericenters on the scale of the gravitational radius of the central massive black hole. Among them, there are mostly deterministic effects like relativistic precession of the orbital axis, and gravitational waves emission. These deterministic effects change the orbital shape and can affect the efficiency of short-time and long-time interactions.

In the work by Bar-Or and Alexander (2014), the authors examine the interplay of gravitational scatterings, resonant relaxation and gravitational waves emission in the steady state orbit averaged Fokker-Planck equation. They solve directly the differential equation and test their results against Monte Carlo simulations. One of the main conclusions of this work is that resonant relaxation and gravitational wave emission become relevant in the same region of phase space. Here, they mostly cancel and the flux in phase space basically reduces to that of gravitational scatterings only.

3

Classical loss cone theory

Impulsive actions led to trouble, and trouble could have unpleasant consequences.
— *Stieg Larsson, The Girl with the Dragon Tattoo*

This chapter is devoted to the classical theory of loss cone, and in particular to the effects of the loss cone on the stochastic evolution of galactic nuclei. The theory is vast, and I focus on the key results employed and/or challenged by the results of my research, that will be presented in the subsequent chapters.

3.1 | The loss cone

The evolution of the orbital parameters of an object can be described as a Brownian motion in the $(E, \mathcal{R})$ space that is more pronounced along $\mathcal{R}$ for eccentric orbits; therefore, relaxation efficiently directs compact objects toward small pericentres close to the MBH at the centre of the system (Bar-Or and Alexander, 2014).

A compact object like a stellar BH can be considered captured once it crosses the closest parabolic approach (Merritt, 2013)

$$r_{\rm Plunge} = 4\,\frac{GM_\bullet}{c^2}\,. \tag{3.1}$$

Conversely, an extended object (e.g. a regular star) will be disrupted because of the tidal forces induced by the MBH gravitational field at a distance known as *tidal radius* (Stone and Metzger, 2016), given by

$$r_{\rm TDE} \simeq r_\star \left(\frac{M_\bullet}{m_s}\right)^{1/3}, \tag{3.2}$$

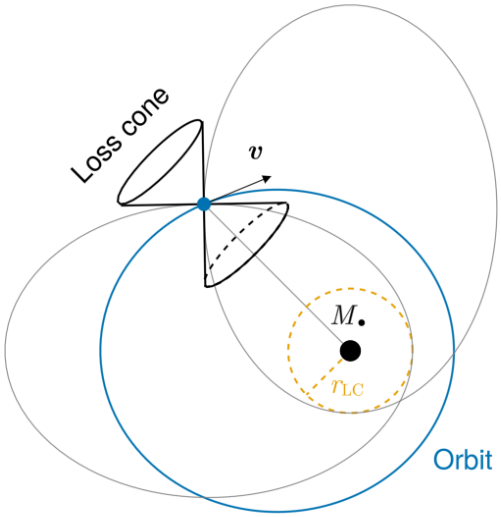

Figure 3.1: Schematic representation of the loss cone for a particle with velocity v around a massive black hole $M_\bullet$. The orbit of the particle is blue; the yellow dashed circle surrounding $M_\bullet$ represents the loss cone radius $r_{\rm LC}$; the light gray lines show the orbits grazing $r_{\rm LC}$ where the particle could be placed by random encounters. The lines tangent to the grazing orbits delimit a cone, known as the loss cone: any orbit with a velocity within this region will approach closer than $r_{\rm LC}$.

where $r_\star$ is the typical radius of the extended object. At this point, the star is disrupted and a fraction of the stellar debris is captured by the MBH, with the rest escaping on unbound orbits.

The radii $r_{\rm Plunge}$ and $r_{\rm TDE}$ are therefore thresholds below which compact and extended objects are respectively captured or destroyed by the central MBH. In practice, regardless of its initial orbit, any object can be driven below its relevant threshold separation $r_{\rm LC}$ by the cumulative effect of two-body relaxation. This occurs when the velocity vector of the object is scattered within a small solid angle of the size of $r_{\rm LC}$ around the central MBH, which defines a cone-like region in the velocity space, named the 'loss cone' because whatever enters this region is 'lost' to the surrounding stellar system; see Amaro-Seoane (2020) for a more complete description. In the (E, R) space, the loss cone is defined by the region below the curve set by the condition on the orbit pericentre

$$r_-(E, R) \leq r_{\rm LC}, \tag{3.3}$$

where $r_{\rm LC} = r_{\rm Plunge}$ for compact objects and $r_{\rm LC} = r_{\rm TDE}$ for extended objects. This

condition gives:

$$\mathcal{R}_{\rm LC}(E) \leq \mathcal{R} \leq 1 \qquad \mathcal{R}_{\rm LC}(E) = 2\, r_{\rm LC}^2\, \frac{E - \phi(r_{lc})}{J_c^2(E)} \tag{3.4}$$

for $E < E_{\rm LC}$, where the latter is the energy of the circular orbit at $r_{\rm LC}$. In Fig. 3.1 we show a graphical representation of the loss cone in the $(\boldsymbol{r}, \boldsymbol{v})$ and the $(E, \mathcal{R})$ space.

In the now classical treatment of the loss cone in the Fokker-Planck approach, one assumes that

- Orbits with percenter larger than the critical value $r_{\rm LC}$ are unaffected by the presence of the loss cone.
- Orbits with pericentre smaller than the critical value $r_{\rm LC}$ will be either disrupted or captured gravitationally at the first pericentre passage.

The different timescale of relaxation in E and $\mathcal{R}$ means that the two relaxation processes will detach for small $\mathcal{R}$; as a consequence we expect $f(E, R)$ to be well represented at low $\mathcal{R}$ by the separated form $f(E, R) \simeq f_E(E)\, f_{\mathcal{R}}(\mathcal{R})$. This fact has been exploited by Cohn and Kulsrud (1978) to derive the expected relaxed profile in $\mathcal{R}$ at small $\mathcal{R}$ corresponding to expected flux of particles that will have pericentre $r_- < r_{\rm LC}$. A boundary condition for the orbit-averaged Fokker-Planck equation can be derived to consistently include the loss cone effects.

Moreover, by assuming the Cohn-Kulsrud relaxed profile one can relate the flux across the loss cone at a given energy and the average value (in $\mathcal{R}$) of the distribution function. This allows one to complement the ergodic Fokker-Planck equation with a sink term effectively including the presence of the loss cone.

3.2 | Cohn Kulsrud distribution in angular momentum

The Cohn boundary layer and the corresponding Cohn-Kulsrud steady profile are obtained under the following assumptions:

1. The flux in energy is steady on the relaxation timescales of $\mathcal{R}$ (thus E is treated as a parameter and $\partial_E \mathcal{F}_E$ neglected).
2. The flux in angular momentum is dominated by $\mathcal{D}_{RR}\, \partial_R f$.
3. $\mathcal{R}_{\rm LC}$ is so small that we can take the $\mathcal{R} \to 0$ limit.

By taking the $\mathcal{R} \to 0$ limit of the $\mathcal{F}_{\mathcal{R}}$ coefficients we have[1]

$$\mathcal{D}_R \sim \mathcal{O}(\mathcal{R}) \tag{3.5}$$

$$\frac{\mathcal{D}_{RR}}{\mathcal{R}} \sim 8\pi^2 \int_0^{\phi^{-1}(E)} \frac{dr}{v} r^2 D\left[\delta v_\perp^2\right] \equiv \mathcal{D}(E) \tag{3.6}$$

$$\frac{\mathcal{D}_{ER}}{E} \sim \mathcal{O}(\mathcal{R}) \tag{3.7}$$

The three assumptions immediately give the analytical form of the equation right above the loss cone

$$\frac{\partial}{\partial t}\mathcal{J}\, f_{\mathcal{R}} = \mathcal{D}(E)\frac{\partial}{\partial \mathcal{R}}\mathcal{R}\,\frac{\partial}{\partial \mathcal{R}} f_{\mathcal{R}} \tag{3.8}$$

and the form of the flux $\mathcal{F}_R$ and the steady solution $f_{\mathcal{R}}$ just above the loss cone.

$$\mathcal{F}_{R,\mathrm{LC}} = \mathcal{R}\,\mathcal{D}\, f'_{\mathcal{R}}(\mathcal{R}_{\mathrm{LC}})\,, \quad f_{\mathcal{R}}(\mathcal{R}) = \frac{\mathcal{F}_{R,\mathrm{LC}}}{\mathcal{D}}\,\log\frac{\mathcal{R}}{\mathcal{R}_0}\,. \tag{3.9}$$

The value of the flux across the loss cone is then set according to the expected rate of particles with $\mathcal{R} < \mathcal{R}_{\mathrm{LC}}$ that complete the orbit until $r_- = r_{\mathrm{LC}}$ without being scattered away. Therefore, we need to solve the local Fokker-Planck equation in the neighbourhood and inside the loss cone with proper boundary conditions. By choosing a domain $\mathcal{R} \in [0, \mathcal{R}_{\max}]$, with $\mathcal{R}_{\max} \gtrsim \mathcal{R}_{\mathrm{LC}}$, we need to apply some boundary conditions summarized in Fig. 3.2.

i $f^{\mathrm{out}}(E, \mathcal{R}, r_-) = 0$ for $\mathcal{R} < \mathcal{R}_{\mathrm{LC}}$, since no particle is generated at the loss cone.

ii $f^{\mathrm{out}}(E, \mathcal{R}, r_+) = f^{\mathrm{in}}(E, \mathcal{R}, r_+)$ for $\mathcal{R}_{\mathrm{LC}} < \mathcal{R} < \mathcal{R}_{\max}$ since particles complete the pericentre without being destroyed.

iii $f^{\mathrm{out}}(E, \mathcal{R}_{\max}, r) = f^{\mathrm{in}}(E, \mathcal{R}_{\max}, r) \equiv f_{\mathrm{LC}}\,\frac{\log \mathcal{R}_{\max}/\mathcal{R}_{\mathrm{LC}}}{\log \mathcal{R}_{\mathrm{LC}}/\mathcal{R}_0}$, matching the orbit-averaged solution

iv $f^{\mathrm{out}}(E, \mathcal{R}, r_+) = f^{\mathrm{in}}(E, \mathcal{R}, r_+)$, since particles not penetrating the loss cone start a new orbit at the pericentre passage.

v $\mathcal{F}^{\mathrm{out}}_{\mathcal{R}}(r, E, 0) = \mathcal{F}^{\mathrm{in}}_{\mathcal{R}}(r, E, 0) = 0$, since crossing the $\mathcal{R} = 0$ boundary physically corresponds to flipping sign in angular momentum, *i.e.* a reflection in $\mathcal{R}$.

[1] In chapter 6 of Merritt (2013) the quantity $\mathcal{D}$ refers to the quantity used here divided by $g(E) = 4\,\pi^2\, J_c^2\, \bar{P}$.

The local coefficients of F_R in the $\mathcal{R} \to 0$ limit are

$$D_R \sim \mathcal{O}(\mathcal{R}) \tag{3.10}$$

$$\frac{D_{RR}}{\mathcal{R}} \sim \frac{r^2}{J_c^2} D\left[\delta v_\perp^2\right] \equiv D(E,r) \tag{3.11}$$

$$\frac{D\left[\delta E\right]}{E} \sim \mathcal{O}(\mathcal{R}) \tag{3.12}$$

The local equation in the steady state approximation takes the shape

$$v_r \frac{\partial}{\partial r} f^{\text{in}} = D \frac{\partial}{\partial \mathcal{R}} \mathcal{R} \frac{\partial}{\partial \mathcal{R}} f^{\text{in}} \qquad v_r \frac{\partial}{\partial r} f^{\text{out}} = D \frac{\partial}{\partial \mathcal{R}} \mathcal{R} \frac{\partial}{\partial \mathcal{R}} f^{\text{out}} \tag{3.13}$$

where $v_r = -|v_r|$ with f^{in} and $v_r = |v_r|$ with f^{out}. The steady state assumption implies that the total flux $\mathcal{F}_{\mathcal{R},\text{LC}}$ entering the region must equate the flux crossing $r = r_-$ in the solution of f^{in}. In order to see it explicitely, we integrate both the equations over the orbit

$$f^{\text{in}}(\mathcal{R}, r_+) - f^{\text{in}}(\mathcal{R}, r_-) = \frac{\partial}{\partial \mathcal{R}} \mathcal{R} \frac{\partial}{\partial \mathcal{R}} \int_{r_-}^{r_+} \frac{dr}{v_r} D\, f^{\text{in}}(\mathcal{R}, r) \tag{3.14}$$

and on the domain of $\mathcal{R}$

$$\int_0^{\mathcal{R}_{\text{LC}}} d\mathcal{R} (f^{\text{in}}(\mathcal{R}, r_+) - f^{\text{in}}(\mathcal{R}, r_-)) = \mathcal{R}_{\text{LC}} \left[\frac{\partial}{\partial \mathcal{R}} \int_{r_-}^{r_+} \frac{dr}{v_r} D\, f^{\text{in}}(\mathcal{R}, r)\right]_{\text{LC}} \tag{3.15}$$

doing the same for f^{out}

$$\int_0^{\mathcal{R}_{\text{LC}}} d\mathcal{R} f^{\text{out}}(\mathcal{R}, r_+) = \mathcal{R}_{\text{LC}} \left[\frac{\partial}{\partial \mathcal{R}} \int_{r_-}^{r_+} \frac{dr}{v_r} D\, f^{\text{out}}(\mathcal{R}, r)\right]_{\text{LC}} \tag{3.16}$$

subtracting the two equations and using the boundary conditions

$$\begin{aligned} \int_0^{\mathcal{R}_{\text{LC}}} d\mathcal{R} f^{\text{in}}(E, \mathcal{R}, r_-) &= \frac{\mathcal{D}}{4\,\pi^2\, J_c^2} \mathcal{R}_{\text{LC}} \frac{\partial}{\partial \mathcal{R}} f_{\mathcal{R}}(\mathcal{R}_{\text{LC}}) \\ &= \frac{\mathcal{F}_{\mathcal{R},\text{LC}}}{4\pi^2\, J_c^2} \end{aligned} \tag{3.17}$$

finally giving

$$\mathcal{F}_{\mathcal{R},\text{LC}} = 4\pi^2 J_c^2 \int_0^{\mathcal{R}_{\text{LC}}} d\mathcal{R}\; f^{\text{in}}(E, \mathcal{R}, r_-)\,. \tag{3.18}$$

3.2.1 | Qualitative trends: full and empty loss cone regime

Armed with these equations, we can already identify two limiting cases. The structure of the equation shows that the expected magnitude of the kick along one orbit is

$$\frac{\left\langle \delta \mathcal{R}^2 \right\rangle}{2} = \frac{\mathcal{D}}{4\,\pi^2\, J_c^2} \equiv q\, \mathcal{R}_{\text{LC}} \tag{3.19}$$

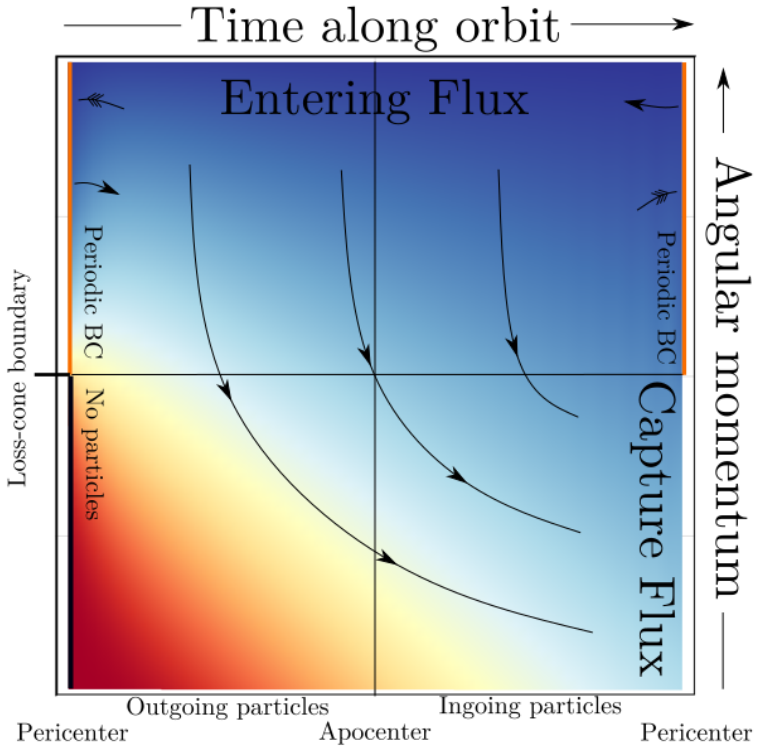

Figure 3.2: Boundary conditions for the solution inside the loss cone at fixed energy. For each value of the angular momentum (vertical axis), we track on the horizontal axis the motion along the orbit from the pericentre, to the apocenter, and back to the pericentre. For angular momentum larger than the loss cone value, particles approaching the pericentre will start another orbit, therefore the distribution function has periodic boundary conditions. For angular momentum smaller than the loss cone value, instead, particles approaching the pericentre will be disrupted / captured. Therefore, on the left of the diagram the function is forced to be zero, and on the right one can compute the capture rate. At the maximum value of angular momentum considered, the function is matched with the soultion of the orbit-averaged Fokker-Planck equation and therefore the function does not depend on the position along the orbit. The lower edge is a reflecting boundary condition, since it corresponds to perfectly radial orbits.

that means that when $q \gg 1$ the particles are likely to escape the loss cone in a time P/q, but when $q \ll 1$ particles can escape the capture, on average, only if their initial angular momentum is $\mathcal{R} \gtrsim \mathcal{R}_{\rm LC}(1-\sqrt{q})$. We define the two regimes:

A. **Full loss cone regime** When $q \gg 1$. In this case the distribution is expected to be flat inside the loss cone, since the fluctuations $\langle \delta\mathcal{R} \rangle$ will let particles enter and exit the interested area many times. Therefore we expect the function to be uniform in $\mathcal{R}$ inside the loss cone; using the boundary condition $f_{\mathcal{R}}(\mathcal{R}, r) = f_{\mathcal{R}}(\mathcal{R}_{\rm LC})$ everywhere, meaning

$$\mathcal{F}_{\mathcal{R},\rm LC} = 4\pi^2 J_c^2 \, \mathcal{R}_{\rm LC} f(E, \mathcal{R}_{\rm LC}) \,, \tag{3.20}$$

and inserting this expression in (3.9) we get

$$\log \frac{\mathcal{R}_{\rm LC}}{\mathcal{R}_0} = q \qquad \frac{\mathcal{R}_0}{\mathcal{R}_{\rm LC}} \simeq 0 \,. \tag{3.21}$$

B. **Empty loss cone or diffusive regime**, where $\mathcal{R}_{\rm LC}$ is much larger than the average fluctuations $\delta\mathcal{R}$. In this case $\partial_R f^{\rm in} \propto f_{\rm LC}/(q\mathcal{R}_{\rm LC}) \gg f_{\rm LC}/\mathcal{R}_{\rm LC}$. Approximating $f^{\rm in}(r_-, E, \mathcal{R})$ as a line with slope $f'_{\rm LC} \equiv \partial_R f(E, \mathcal{R}_{\rm LC})$, the flux conservation equation then becomes

$$\mathcal{F}_{\mathcal{R},\rm LC} = 2\pi^2 J_c^2 \frac{f_{\rm LC}^2}{f'_{\rm LC}} \tag{3.22}$$

since the integral is restricted by the condition $f^{\rm in} > 0$. Inserting this expression in (3.9) we get

$$f'_{\rm LC} = \frac{f_{\rm LC}}{\mathcal{R}_{\rm LC}\sqrt{2\,q}} \quad \mathcal{F}_{\mathcal{R},\rm LC} = D\,\frac{f_{\rm LC}}{\sqrt{2\,q}} \tag{3.23}$$

and, finally

$$\log \frac{\mathcal{R}_{\rm LC}}{\mathcal{R}_0} = \sqrt{2\,q} \qquad \mathcal{R}_0 \simeq \mathcal{R}_{\rm LC} \tag{3.24}$$

The boundary condition, then, is obtained setting either $\mathcal{F}_{\mathcal{R},\rm LC}$ or $f'_{\rm LC}$ depending on $f_{\rm LC}$; the two prescriptions are equivalent if assumptions 2 and 3. hold. The factor of $\sqrt{2}$ in front of $\sqrt{q}$ comes from assuming a straight line inside the loss cone; the correct factor should be $\sqrt{\pi}/2$, as presented in L.E. Strubbe's thesis.

3.2.2 | Analytic estimate

The solution inside the loss cone is better obtained by changing variable to

$$\tau = \frac{4\pi^2 J_c^2}{\mathcal{D}} \times \begin{cases} \int_{r_-}^{r} \frac{dr\,D}{v_r} & u \geq 0 \\ \frac{\mathcal{D}}{4\pi^2 J_c^2} - \int_{r_-}^{r} \frac{dr\,D}{|v_r|} & v_r < 0 \end{cases} \tag{3.25}$$

where we have used the fact that

$$2\int_{r_-}^{r_+}\frac{dr}{|v_r|}D \sim \frac{\mathcal{D}}{4\pi^2 J_c^2} \qquad \mathcal{R}\to 0 \tag{3.26}$$

With this change of variable Eq. (3.13) becomes

$$\frac{\partial}{\partial\tau}f^{\rm out}(\mathcal{R},\tau) = q\,\mathcal{R}_{\rm LC}\,\frac{\partial}{\partial\mathcal{R}}\mathcal{R}\frac{\partial}{\partial\mathcal{R}}\,f^{\rm out}(\mathcal{R},\tau) \qquad 0\le\tau<\frac{1}{2} \tag{3.27}$$

$$\frac{\partial}{\partial\tau}f^{\rm in}(\mathcal{R},\tau) = q\,\mathcal{R}_{\rm LC}\,\frac{\partial}{\partial\mathcal{R}}\mathcal{R}\frac{\partial}{\partial\mathcal{R}}\,f^{\rm in}(\mathcal{R},\tau) \qquad \frac{1}{2}<\tau\le 1 \tag{3.28}$$

$$\tag{3.29}$$

and returning to from $f^{\rm in}$ and $f^{\rm out}$ to f:

$$\frac{\partial}{\partial\tau}f = q\,\mathcal{R}_{\rm LC}\frac{\partial}{\partial\mathcal{R}}\left[\mathcal{R}\frac{\partial}{\partial\mathcal{R}}f\right] \quad \tau\in[0,1],\ \mathcal{R}\in[0;\mathcal{R}_{\rm max}]\,. \tag{3.30}$$

An analytic expansion of the solution can be obtained if we take $\mathcal{R}_{\rm max}=\mathcal{R}_{\rm LC}$. Then, we rescale $\mathcal{R}$ to

$$y=\frac{\mathcal{R}}{q\,\mathcal{R}_{\rm LC}} \tag{3.31}$$

so that the equation becomes

$$\frac{\partial}{\partial\tau}f = \frac{\partial}{\partial y}y\frac{\partial}{\partial y}f \qquad 0\le\tau\le 1 \quad 0\le y\le\frac{1}{q}\,. \tag{3.32}$$

Since the differential equation is first order in τ, we interpret this as an evolution equation with the initial conditions set to $f(\mathcal{R},0)=0$ (that is boundary condition *(i)*), and bound to have $f=f_{\rm LC}$ at $y=1/q$ for $\tau>0$. As in the problem of heat transfer, we express the solution in terms of a basis of separable solutions. First, we realize that the constant function is a solution of the differential equation, so that we can look for a solution of the form

$$f_{\mathcal{R}} = f_{\rm LC}\,[1-g_{\mathcal{R}}(y,\tau)] \tag{3.33}$$

where $g_{\mathcal{R}}$ satisfies the same differential equation. The problem for g has initial conditions $g(y,0)=1$ and $g(1/q,\tau>0)=0$. We dub the basis for $g_{\mathcal{R}}$ with a label λ, so that

$$\sum_\lambda c_\lambda g_\lambda \qquad g_\lambda = T_\lambda(\tau)\,Y_\lambda(y) \tag{3.34}$$

and the differential equation becomes

$$\frac{T'_\lambda}{T_\lambda} = \frac{Y'_\lambda + y\,Y''_\lambda}{Y_\lambda} = \lambda \tag{3.35}$$

so that $T = \exp(\lambda\,\tau)$ and Y is the solution of

$$-\lambda Y_\lambda + Y'_\lambda + y\,Y''_\lambda = 0 \tag{3.36}$$

with the boundary condition $Y(1/q) = 0$ and $Y'_\lambda + y\,Y''_\lambda = 0$ at $y = 0$. The equation can be turned into Bessel equation of the first kind by with $\nu = 0$ by changing variable to $z = \sqrt{-\lambda y}$, so that the general solution is

$$Y_\lambda = C\,J_0\left(2\,\sqrt{-\lambda\,y}\right) \tag{3.37}$$

which satisfies BC *(v)* for any negative λ, and vanishes at $y = 1/q$ when

$$\lambda = -\frac{q\,\alpha_k^2}{4} \tag{3.38}$$

where α_k is one of the infinitely many, countable zeros of $J_0(x)$. The basis for the function $g_{\mathcal{R}}$ is then

$$\left\{C\,e^{-\frac{q\,\alpha^2}{4}\,\tau}\,J_0(\alpha_k\,\sqrt{q\,y})\right\}_{k=1,2,\ldots} \tag{3.39}$$

and it is orthogonal with respect to the weight $w(y) = 1$. We will use the following properties of the Bessel plynomials J_1 and J_0:

$$\frac{d}{dz}z\,J_1(c\,z) = c\,z\,J_0(c\,z) \qquad \frac{d}{dz}J_0(c\,z) = -c\,J_1(c\,z) \qquad J_1(0) = 0\,. \tag{3.40}$$

Thus, we can expand the intiial conditions $g_{\mathcal{R}} = 1$ in this basis as (Arfken and Weber, 2012, Eq. (14.48) with $\nu = 0$, $a^2 = 1/q$, $\rho^2 = y$)

$$c_k = \frac{2\,q}{J_1^2(\alpha_k)}\int_0^{1/\sqrt{q}} d\rho\,\rho\,J_0(\alpha_k\,\sqrt{q}\,\rho) = \frac{2}{\alpha_k\,J_1(\alpha_k)} \tag{3.41}$$

and the general solution becomes

$$f = f_{\rm LC}\left[1 - 2\sum_{k=1}^{\infty}\frac{\exp\{-\tau\,q\,\alpha^2/4\}}{\alpha_k\,J_1(\alpha_k)}\,J_0(\alpha_k\,\sqrt{q\,y})\right]. \tag{3.42}$$

We now impose the boundary condition at $\mathcal{R}_{\rm LC}$ to find the value of $\mathcal{R}_0$. By imposing (3.18) and using (3.9)

$$\begin{aligned}\frac{\mathcal{D}}{4\pi^2\,J_c^2\,\log\mathcal{R}_{\rm LC}/\mathcal{R}_0} &= \mathcal{R}_{\rm LC} - q\mathcal{R}_{\rm LC}\sum_{k=1}^{\infty}\frac{2}{\alpha_k\,J_1(\alpha_k)}\,\exp\left(-\frac{q\,\alpha_k^2}{4}\right)\int_0^{1/q} dy\,J_0\left(\alpha_k\,\sqrt{qy}\right)\\ &= \mathcal{R}_{\rm LC} - q\mathcal{R}_{\rm LC}\sum_{k=1}^{\infty}\frac{4}{\alpha_k\,J_1(\alpha_k)}\,\exp\left(-\frac{q\,\alpha_k^2}{4}\right)\int_0^{1/\sqrt{q}} d\rho\,\rho\,J_0\left(\alpha_k\,\sqrt{q}\,\rho\right)\\ &= \mathcal{R}_{\rm LC}\left[1 - \sum_{k=1}^{\infty}\frac{4}{\alpha_k^2}\,\exp\left(-\frac{q\alpha_k^2}{4}\right)\right]\end{aligned} \tag{3.43}$$

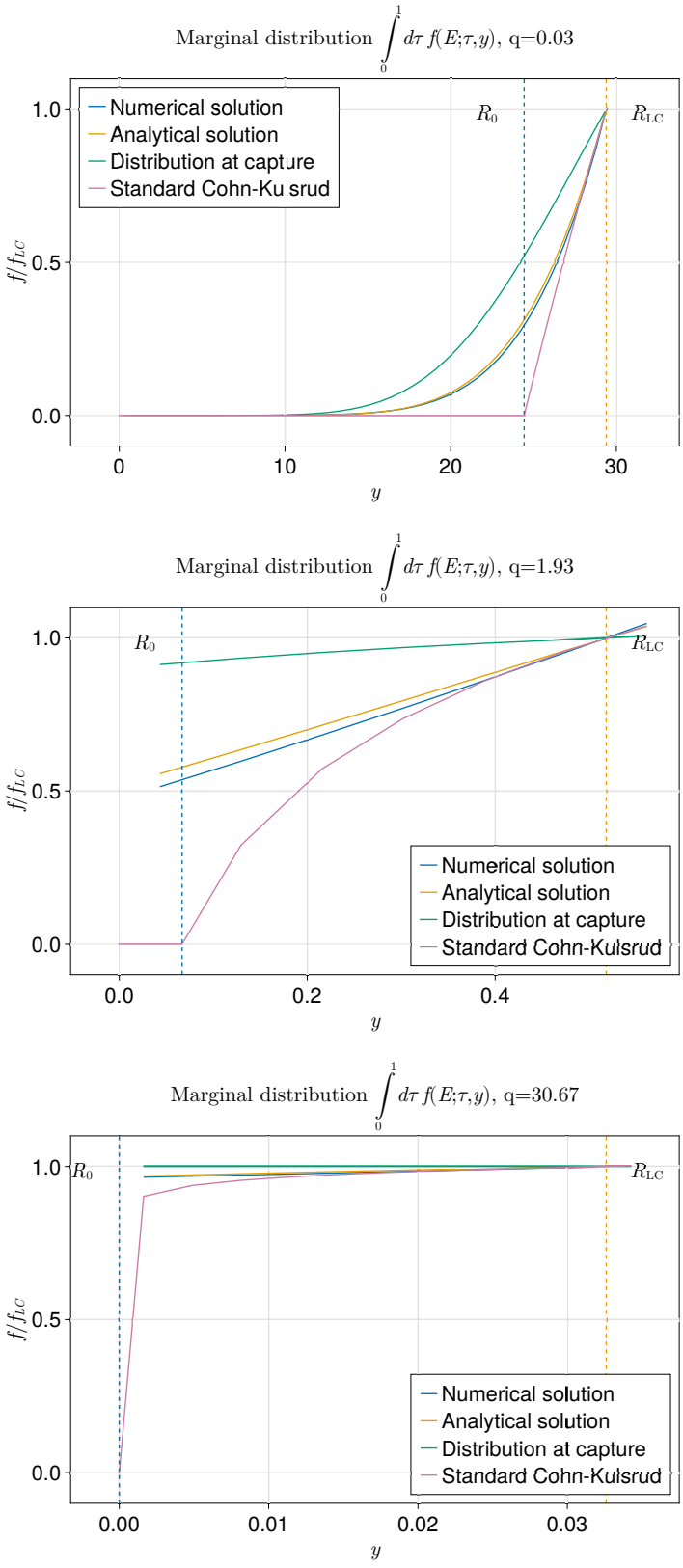

Figure 3.3: Solution of the local Fokker-Planck equation inside the loss cone (*i.e.* for $\mathcal{R} < \mathcal{R}_{\rm LC}$). We show the average distribution inside the loss cone for three cases in the empty (upper panel), intermediate (middle panel) and full loss cone regime (lower panel). The numerical solution (blue line) to the problem with $\mathcal{R}_{\rm max} = 2\mathcal{R}_{\rm LC}$ agrees well with the analytic estimate by Merritt (yellow line). For comparison, we also show the standard Cohn-Kulsrud branch (pink line), that is proportional to $\log \mathcal{R}/\mathcal{R}_0$, and the distribution at $\tau = 1$ from the numerical solution (green line), *i.e.* the distribution at the pericentre (captured by the loss cone).

finally giving

$$\log \frac{\mathcal{R}_0}{\mathcal{R}_{\rm LC}} = -q \left[1 - \sum_{k=1}^{\infty} \frac{4}{\alpha_k^2} \exp\left(-\frac{q\alpha_k^2}{4} \right) \right]^{-1} \equiv \alpha(q) \tag{3.44}$$

By directly computing this function, one can check the fact that $\alpha \sim \sqrt{q}$ for small q and $\alpha \sim q$ for large q, as predicted by our qualitative approaches. Moreover, an estimate that holds over all the typical values of q is $\sqrt[4]{q^2 + q^4}$ (Merritt, 2013; Vasiliev, 2017).

In Fig. 3.3 we plot some solutions, together with a numerical counterpart with the methods explained in Chap. 6. We can see that for $q \simeq 2$ both the average distribution and the distribution at r_c do not vanish at $\mathcal{R} = 0$, which means that we can have tidal disruptions and plunges at highly eccentric orbits even in this regime.

Eq. 3.9 is one of the most powerful results of classical loss cone theory, since it can directly relate the spatial distribution of a spherical system with loss cone rates. By assuming an ergodic model $f(E)$, one can compute the distribution function from the spatial density of a stellar system using Eddington's formula (Binney and Tremaine, 2008; Stone and Metzger, 2016, see Chapter 4 for an example). Then, computing q and $\mathcal{R}_0$, the flux $\mathcal{F}_{\rm LC}(E)$ entering the loss cone is computed from the specific Cohn-Kulsrud profile such that

$$f(E) = \frac{\mathcal{F}_{\rm LC}}{\mathcal{D}} \int_{R_{\rm LC}}^{1} d\mathcal{R} \, \log \mathcal{R}/\mathcal{R}_0 \, . \tag{3.45}$$

The total rate of loss cone events $\dot{N}_{\rm LC}$ is then computed as

$$\dot{N}_{\rm LC} = \int_0^{E_{\rm LC}} dE \, \mathcal{F}_{\rm LC}(E) \tag{3.46}$$

where $E_{\rm LC}$ is the energy of the circular orbit at the loss cone radius. The same approach can be used with solutions of the ergodic Fokker-Planck equation to compute loss cone rates (Vasiliev, 2017).

3.3 | Direct Plunges, EMRIs and 2-body relaxation

In a work by Hopman and Alexander (2005), the formalism developed in Chapter 2 has been applied to a compact object in a Monte Carlo fashion to compute the rate of loss cone phenomena. The authors also included the effects of gravitational wave emission, effectively evolving each orbit period-by-period with fluctuations given by:

$$\delta J = \langle \delta J \rangle + \xi \sqrt{\langle \delta J^2 \rangle} + \delta J_{\rm GW} \tag{3.47}$$

$$\delta E = \delta E_{\rm GW} \, . \tag{3.48}$$

where ξ randomly takes value -1 or 1. $\delta E_{\rm GW} =$ and $\delta J_{\rm GW}$ are computed according to Peters formulas

$$\delta E_{\rm GW} = \frac{8\,\pi}{5\,\sqrt{2}}\,\frac{1+(73/24)\,e^2+(37/96)\,e^4}{(1+e)^{7/2}}\,\frac{m\,c^2}{M_\bullet}\left(\frac{r_S}{r_-}\right)^{7/2} \tag{3.49}$$

$$\delta J_{\rm GW} = -\frac{16\pi}{5}\,\frac{1+(7/8)\,e^2}{(1+e)^2}\,\frac{G\,m}{c}\left(\frac{r_S}{r_-}\right)^{2} \tag{3.50}$$

where m is the mass of the compact object, $e \simeq \sqrt{1-\mathcal{R}}$ is the eccentricity of the orbit and $r_S = 2\,G\,M_\bullet/c^2$ the Schwarzschild radius of the central MBH.

The key result of this work is that you can identify a critical value of the semimajor axis $r_{\rm GW}$ that distinguishes between two qualitatively different types of trajectory in the (E, J).

- **DPs:** the particle starts with semimajor axis $a > a_{\rm GW} \simeq 0.01\,r_h$. Stochastic interactions completely dominate the evolution of orbital parameters, mostly changing the angular momentum of the orbit. Once the particle approaches the loss cone, stochastic kicks may drive it on a deadly orbit.

- **EMRIs:** the particle starts with semimajor axis $a < a_{\rm GW}$. Stochastic interactions are significant to orbital evolution up until the pericentre becomes sufficiently low. For this value of a, stochastic kicks are very small and the deterministic drift in energy angular momentum due to GW emission becomes dominant.

Since the evolution due to GW emission keeps the pericentre approximately constant, trajectories dominated by this process will move parallel to the loss cone boundary – that is the locus of orbits with pericentre $r_{\rm LC}$ – towards a lower and lower semimajor axis. Eventually, the compact object will merge with the central MBH as shown in Fig. 3.4. A crucial consequence of the work presented by Hopman and Alexander (2005) is that direct plunges are generated only in regions dominated by two body relaxation and with semimajor axis $a > a_{\rm GW}$. Assuming a quasi steady system inside the influence radius, particle conservation implies that

- in a system evolving only due to two-body scatterings, the flux of EMRI and direct plunges can be computed by integrating the flux across the loss cone for $a > a_{\rm GW}$ and $a < a_{\rm GW}$ respectively.

This result has been later tested for $M_\bullet \geq 10^6\,M_\odot$ in the comprehensive work by Bar-Or and Alexander (2014), where it is shown that these results hold even with more sophisticated treatments of two body relaxation. However, the validity of this prescription for the computation of DP and EMRI rates has been recently challenged by Qunbar

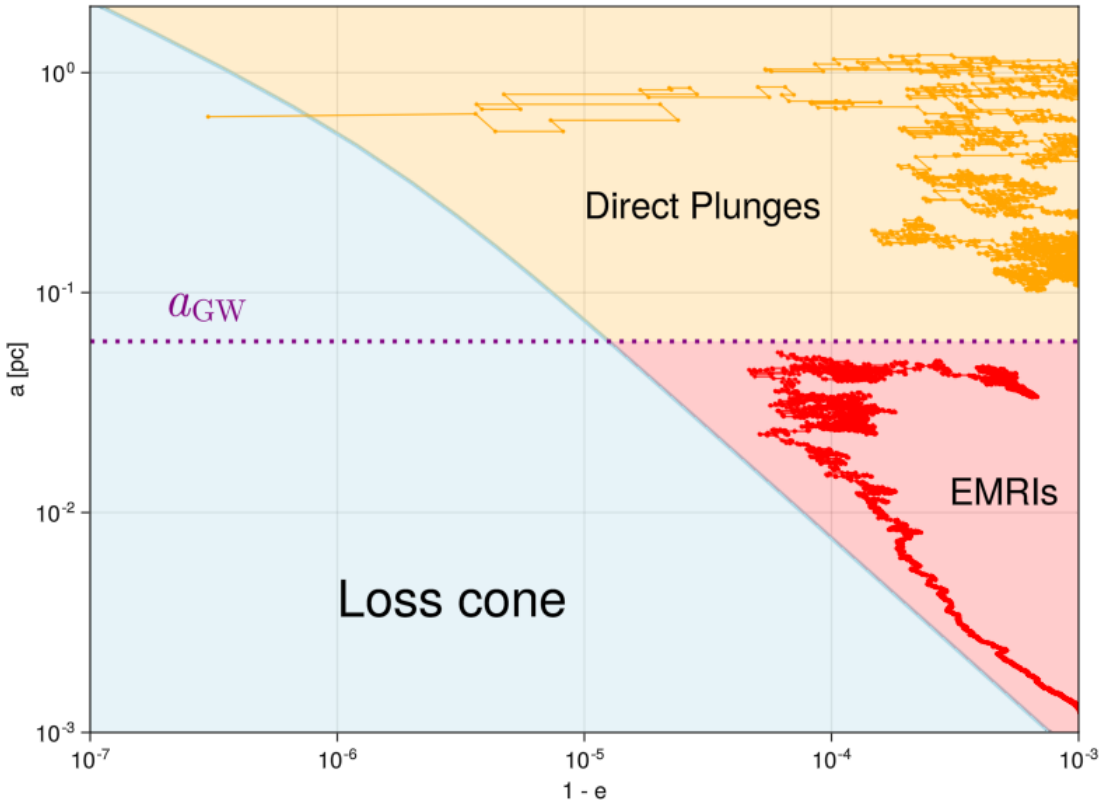

Figure 3.4: (Adapted from Mancieri et al, in prep). Qualitatively different orbits for compact objects: direct plunges for $a > a_{\rm GW}$ and EMRIs for $a < a_{\rm GW}$. The plot assumes a prototypical system with $M_\bullet = 4 \times 10^6\, M_\odot$ and a model of the nuclear star cluster with light stars and heavier black holes as presented in Chapter 4.

and Stone (2023). In this work it is shown that for $M_\bullet \leq 10^6\, M_\bullet$ the distinction between the regions were DPs are produced and the region where EMRIs are produced disappears: both can be produced at any semimajor axis.

In a work led by D. Mancieri (in preparation), we have tested independently the prescription of $a_{\rm GW}$ with a few-body integrator. We included the effect of two body encounters without relying on the orbit averaged assumption, and accounted for relativistic precession and gravitational waves emission by including Post Newtonian corrections to the Hamiltonian of the particle up to order 2.5. Preliminary results agree with the conclusions of Qunbar and Stone (2023).

4

Two-dimensional Fokker-Planck evolution

Being able to read and write did not provide answers to all questions.
It led to other questions, and then to others.
— *Margaret Atwood, The Testaments*

This chapter presents the code I developed for the solution of the orbit averaged Fokker-Planck equation with two stellar species: a light distribution of stars possibly producing tidal disruption events and a heavier distribution of compact objects producing direct plunges and extreme mass ratio inspirals. The results here reported have been published in Broggi et al. (2022).

4.1 | Initial conditions and algorithm

In this section, we will present the initial conditions for the simulated systems and the algorithm used to perform the simulation. The general framework is based on the work of Pan and Yang (2021).

We consider a simple model of a galactic nucleus composed by:

- a central MBH of mass $M_\bullet$,
- a spherical distribution of stars with mass m_s,
- a spherical, subdominant distribution of stellar mass compact objects with mass $m_{\rm BH}$.

4.1.1 | Initial conditions

We fix the total mass of extended objects (stars hereinafter) in the distribution to $M_s = 20\,M_\bullet$, composed by stars of mass $m_s = 1\,M_\odot$ each, and the total mass of compact objects (sBHs hereinafter) to $M_{\rm BH} = 0.2\,M_\bullet$, composed by sBHs of $m_{\rm BH} = 10\,M_\odot$ each. For a uniform notation, in the next sections we will use the symbols $\mathcal{R}^{\rm BH}_{\rm LC}$, $E_{\rm BH}$ and $r_{\rm BH}$ when considering the loss cone relative to gravitational capture of compact objects, and $\mathcal{R}^{s}_{\rm LC}$, E_s and r_s when considering the loss cone relative to TDEs.

Both distributions initially follow the same Dehnen profile with $\gamma = 1.5$ (Tremaine et al., 1994)

$$n_i(r) = \frac{3}{8\pi}\, N_i\, \frac{r_a}{r^{3/2}\,(r+r_a)^{5/2}}\,\theta(r-r_i). \tag{4.1}$$

Here r_a sets the radius at which the distribution changes its behaviour from $r^{-1.5}$ to r^4 and the Heaviside function θ is introduced to truncate the distribution at $r = r_i$, where $r_i = r_{\rm BH}$ for sBHs and $r_i = r_s$ for stars. In order to adequately scale r_a with the properties of the system, we set it to a multiple of the influence radius of the MBH r_h (Merritt, 2013)

$$r_a = 4\,r_h. \tag{4.2}$$

Then, we use the $M_\bullet - \sigma$ relation (Gültekin et al., 2009) to finally set the scale radius of the distribution

$$\sigma = 70\ {\rm Km/s}\cdot\left(\frac{M_\bullet}{1.53\ 10^6 M_\odot}\right)^{1/4.24}. \tag{4.3}$$

The ratio r_a/r_h is somewhat arbitrary, since the velocity dispersion in the central region in our model is not constant and diverges as $\sim r^{-1}$ at the centre. For a comparison, the stellar radial velocity dispersion of the initial conditions can be computed (see Sec. 4.3.1). Neglecting the sBHs contribution, we obtain

$$\sigma_r^2(r_h) \simeq 4.6\,\frac{G\,M_\bullet}{r_a}, \qquad \sigma_r^2(r_a) \simeq 2.4\,\frac{G\,M_\bullet}{r_a} \tag{4.4}$$

and even more sophisticated estimates – *e.g.* averages in the central regions – give similar numerical factors. For an MBH of $M_\bullet = 4\times10^6 M_\odot$ our model has a density of $6\times10^4 M_\odot/pc^3$ at the influence radius $r_h = 2.23$ pc, which is consistent with observational estimates for the Milky Way (e.g. Schodel et al., 2014). The total potential of the MBH plus the extended star and sBH nuclear cluster is

$$\phi(r) = \frac{GM_\bullet}{r} + 2\,G(M_s + M_{\rm BH})\left(1 - \sqrt{\frac{r}{r+r_a}}\right) \tag{4.5}$$

and is not evolved during the simulation. The initial distribution function $f^i(E,R)$ of stars and sBHs is set by computing the isotropic distribution function of equation (4.1) using the Abel transform (Binney and Tremaine, 2008)

$$f^i(E, R, t = 0) = \frac{\sqrt{2}}{4\,\pi^2} \frac{d}{dE} \int_0^E d\phi \, \frac{dn_i(r(\phi))}{d\phi} \, \frac{1}{\sqrt{E - \phi}} \,, \tag{4.6}$$

and restricting only to the phase space region of bound orbits outside the loss cone.

In order to numerically integrate equation (2.37), we represent the distribution function on a uniform grid in the variables (s, R), where s reads

$$s = \log\left(1 + \frac{E}{E_0}\right) . \tag{4.7}$$

Here E_0 is a reference energy scale set to $\sigma^2/5$ in the simulations. Due to the loss cone, the support of f^i is naturally compact and is a subregion of the square domain $s \in [0, s_{lc}]$ and $R \in [0, 1]$. To numerically compute $f^i(s, R, 0)$ we rearrange equation (4.6) in the form

$$f^i(s, R, 0) = \frac{\sqrt{2\,E_0}}{4\pi^2} \int_0^s dw \, \frac{e^w}{\sqrt{e^s - e^w}} \, \frac{d^2\, n^i}{d\phi^2} \tag{4.8}$$

and we use Gauss-Legendre quadrature to compute the function at the grid values of s. We represent the distribution function of each component on a uniform grid $N_s \times N_R$.

4.1.2 | Coefficients computation and boundary conditions

The complete expressions for the flux conservation coefficients and the auxiliary functions needed for their computation are available in Chapter 2. For a unified notation, we define the auxiliary functions $F_0(E) = J_{s,1}(E)$, $F_1(E, r) = I_{s,2}(E, r)$ and $F_2(E, r) = I_{s,4}$. Here we schematically report the set of equations and steps needed for their computation in our numerical approach:

i marginalise f^i over R

$$\bar{f}^i(s) = \int_0^1 dR \, f(s, R) \tag{4.9}$$

and build a linear interpolation of the function;

ii compute a set of auxiliary functions that depend on the variable $w = \log(1 + \phi(r)/E_0)$

$$F_i^k(s, w) = \int_s^w ds' \, h^k(s, w, s') \, \bar{f}^i(s') \tag{4.10}$$

where $h^k(s, w, s')$ is a smooth and compact weighting function. We compute these integrals at a uniform grid $s \times w$; the values of s are the same as those of the grid of f^i and the values of w have the same spacing of s, covering the domain $[0, w(r_{\rm LC})]$. The integration is performed with the Gauss-Legendre quadrature technique;

iii compute the FP coefficients

$$\mathcal{D}_i^j(s,R) = \int_{w_+}^{w_-} dw \sum_{j,k}^{i} \mu_{i,k}^j(s,R,w)\, F_i^k(s,w) \tag{4.11}$$

on the original grid of f^i. The weights $\mu_{i,k}^j$ have a divergent denominator proportional to v_r that behaves like $\sqrt{|w-w_{-/+}|}$ at the endpoints. The divergences have been treated using the Gauss-Chebyshev quadrature technique after explicit extraction.

For both point *(ii)* and point *(iii)* we used 300 nodes for Gauss quadrature. Since the potential is fixed, for a given point of the grid of f the value of the weights μ_{jk}^i at the Chebyshev points of $[w_-, w_+]$ does not change during the evolution; we compute them in advance to make the computation of the coefficients faster.

The boundary conditions for each component are:

- At $s = 0$ all the coefficients vanish and the function does not evolve with time. In our case, this fixes the value $f^i(0,R) = 0$ at all times.
- The line $R = 1$ is the locus of circular orbits. Since at fixed energy a particle cannot exceed $J_c^2(E)$, the flux along $\mathcal{R}$ vanishes by construction for circular orbits and all the $\mathcal{D}_{Rx}^i$ coefficients vanish.
- At the loss cone boundary the dominant coefficient is $\mathcal{D}_{RR}^i$ and one can compute the boundary behaviour of $f^i(s,\mathcal{R})$ (and, in particular, of its derivative) at fixed s (Cohn and Kulsrud, 1978; Merritt, 2013)

$$f^i \approx f(\mathcal{R}_{\rm LC}^i)\left[1 + \frac{\ln \mathcal{R}/\mathcal{R}_{\rm LC}^i}{\ln \mathcal{R}_{\rm LC}^i/\mathcal{R}_0^i}\right] \qquad \text{for } \mathcal{R} \to \mathcal{R}_{\rm LC}^i \tag{4.12}$$

where $\mathcal{R}_0$ is given by the following approximate relation

$$\mathcal{R}_0^i \simeq \mathcal{R}_{\rm LC}^i \ \exp\left(-\sqrt[4]{q_i^4 + q_i^2}\right) \tag{4.13}$$

and

$$q_i = \frac{1}{4\,\pi^2 J_c^2\, \mathcal{R}_{\rm LC}^i(s_i)} \lim_{\mathcal{R}\to\mathcal{R}_{\rm LC}^{i+}} \frac{\mathcal{D}_i^{RR}}{\mathcal{R}}\,. \tag{4.14}$$

The limit at a given value of s is numerically performed by evaluating the quantity q at the first grid point above the loss cone curve.

4.2 | Simulations

In this section we present the results of the simulations that we have run leveraging on the Julia (Bezanson et al., 2017) implementation of the algorithm described in the previous section[1].

4.2.1 | Performed simulations

We considered seven values of $M_\bullet$ evenly spaced in log scale in the range $10^4 M_\odot$ – $10^7 M_\odot$. For each $M_\bullet$ we computed the density ρ_0 corresponding to the value of σ_0 obtained from (4.3) and consider the values $\rho = \{0.01,\ 0.1,\ 1,\ 10\}\ \rho_0$ (which correspond to $\sigma = \{0.464,\ 0.681,\ 1,\ 1.468\}\ \sigma_0$), for a total of 28 simulations.

We performed convergence tests simulating a Milky Way like system with $M_\bullet = 4 \times 10^6\ M_\odot$ using grids of different resolutions (see Fig. 4.1) and we opted for $N_s \times N_R = 200 \times 200$ to balance accuracy and computational time.

The time step is set by limiting the maximum relative variation of the DF on the grid

$$\max_{grid} \frac{\Delta f}{f} = 0.03. \tag{4.15}$$

We run each simulation for a total time

$$t_f = \min\left(10\, t_E,\ 10\ \mathrm{Gyr}\right) \tag{4.16}$$

where t_E is the time when the EMRI rate peaks (see section 4.2.3 for details) and 10 Gyr has been chosen as representative of the Hubble time.

4.2.2 | Final state

In Fig. 4.2 we show the DF at the beginning (t=0 Gyr) and at the end (t=10 Gyr) of the simulation for our model with $M_\bullet = 4 \times 10^6\ M_\odot$. The colour maps highlight the effect of mass segregation, which pushes the BHs towards high values of s while relegating stars to small s, far from the central object. This is more evident when marginalizing the DF over the angular momentum variable R, as shown in Fig. 4.3. At the end of the simulation, the sBHs distribution is more concentrated at circular orbits and higher energies, located at smaller distances from the centre. In Fig. 4.4 we show the radial distribution n_r of the two components in our system at $t = 0$ Gyr and $t = 10$ Gyr, which is defined as

$$n_r^i = \frac{d}{dr} N_i(r) = 4\pi r^2\, n_i(r)\,, \tag{4.17}$$

[1]The interested reader can find a first version of the code at the following repository: `https://gitlab.com/j2970/juliafokkerplanck`

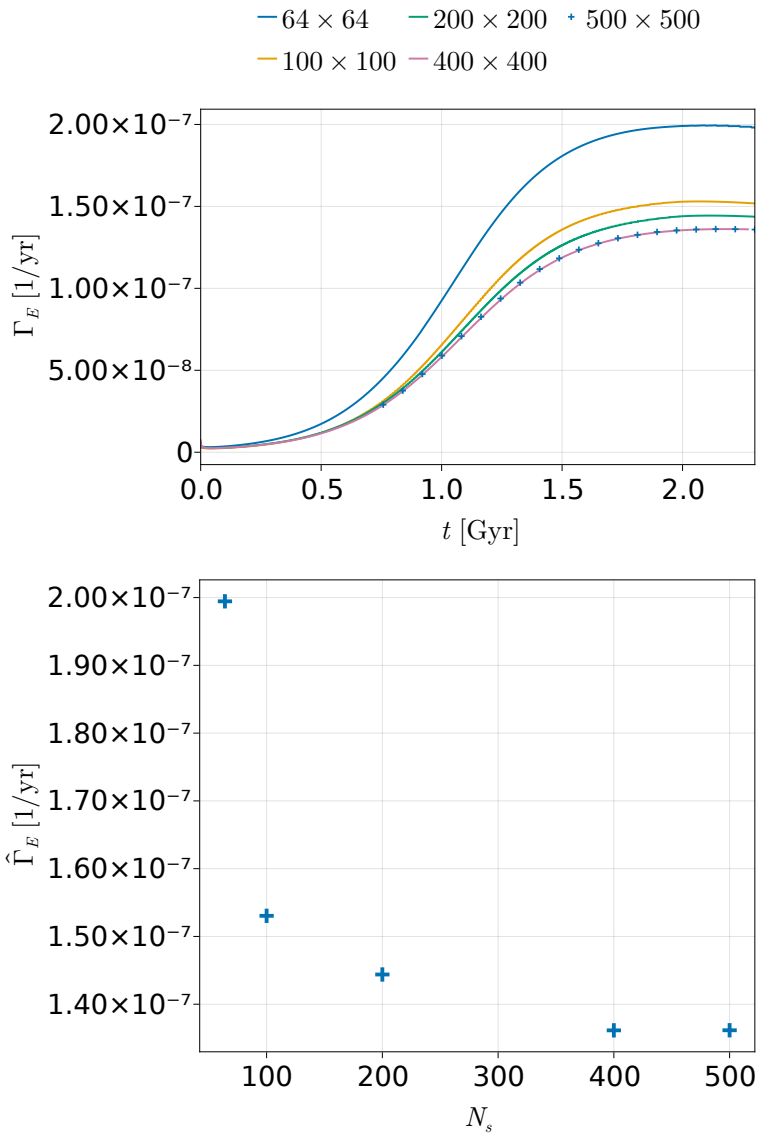

Figure 4.1: Top panel: EMRI formation rate for the same simulation at different resolutions with $N_R = N_s$. The system simulated has $M_\bullet = 4 \cdot 10^6\, M_\odot$ with σ taken from the $M_\bullet - \sigma$ relation. The highest resolution is represented as a point series for better readability. Bottom panel: the maximum of each curve as a function of N_s. In the rest of this work, we set $N_R = N_s = 200$.

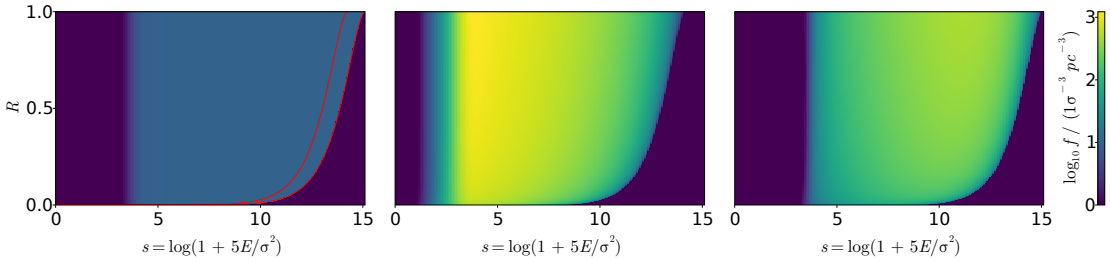

Figure 4.2: Distribution functions for a system with $M_\bullet = 4 \times 10^6\, M_\odot$ and stellar objects distributed as a Dehnen profile with $\gamma = 1.5$ and scale radius $r_a = 4\, r_h$. The left panel shows the initial distribution of sBHs; the initial distribution of stars is larger by a factor of 1000 and vanishes below the stellar loss cone (upper red line). The middle and the right panels show the distribution of stars and sBHs respectively at $t = 10$ Gyr. The maps show the effects of mass segregation (see the main text for details).

where $N_i(r)$ is the total number of the corresponding objects inside the sphere of radius r. Both at the beginning and at the end, we can identify a power-law trend $n_r \sim r^\alpha$ at $r \simeq 10^{-3} r_h$ and a different power-law trend r^β with $\beta = -2$ at $r \gtrsim 10^2 r_h$. The latter corresponds to the $n \sim r^{-4}$ trend of the Dehnen profile, which barely evolves over the considered timescales. The lighter stellar component increases the central slope from $\alpha = 0.5$ to $\alpha = 0.7$, while the heavier sBHs component shows a milder behaviour ($\alpha \simeq 0.3$). These slopes correspond to a 3D particle density that behaves like $n \propto r^{-\gamma}$ with $\gamma = 1.3$ for the light component and $\gamma = 1.7$ for the heavy one. This mass segregation effect is due to the fact that 2-body interactions explicitly depend on the mass of the components. In the FP equation, mass segregation is encoded in the coefficients: while diffusion coefficients are identical for the two components, advection coefficients are proportional to the mass m_i . The inner slopes of stars and sBHs we find at the end of our integrations are slightly shallower than the expectations based on the 1D FP equation Merritt (2013). The presence of the loss cone requires a non-zero (positive) flux towards the central regions, compatible with lower power-law indices. Moreover, the strong anisotropy of the DF in the $E \to E_{\rm LC}$ region may contribute to the flux via the cross-term, which is neglected in the 1D equation.

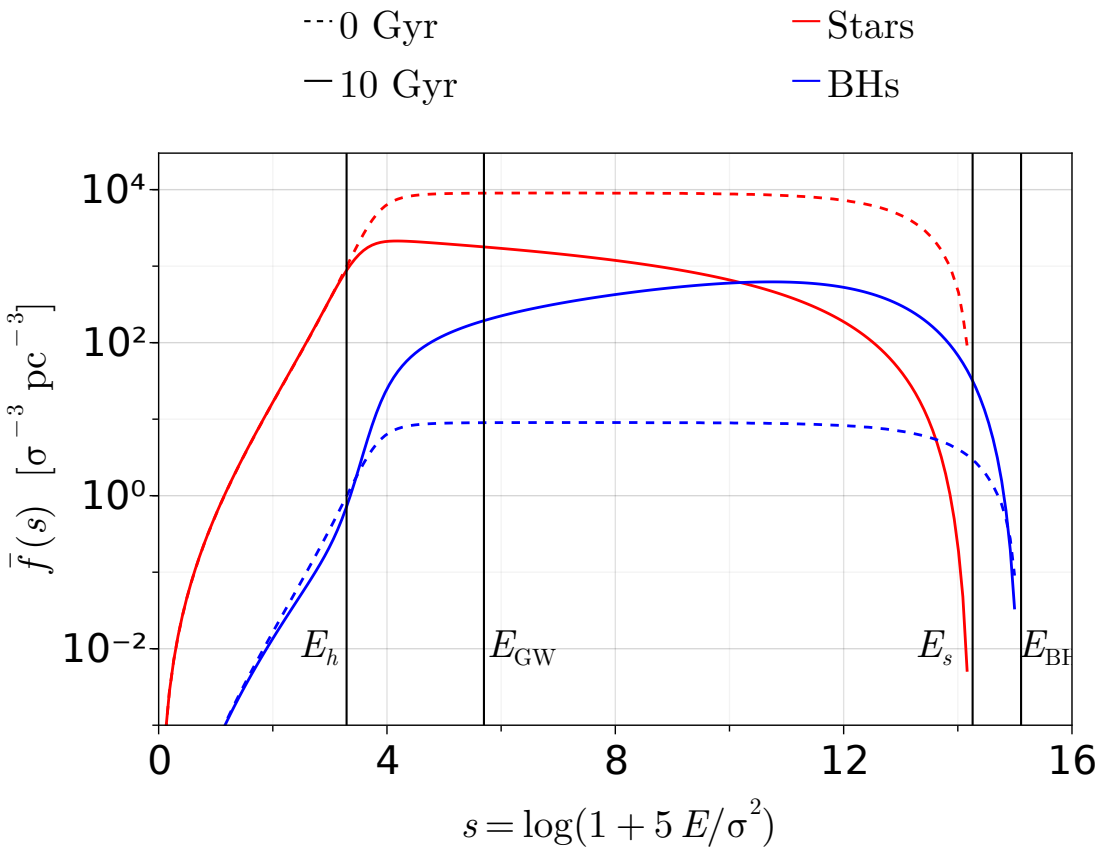

Figure 4.3: Distribution function $\bar{f}(s)$ marginalised over R for the two components at the beginning (0 Gyr) and at the end of the simulation (10 Gyr) for the DFs in Fig. 4.2. The vertical solid black line at E_x corresponds to the circular orbit at r_x; we consider the influence radius r_h, the EMRIs-DPs delimiter $r_{\rm GW}$, and the capture radius for the components r_s and $r_{\rm BH}$

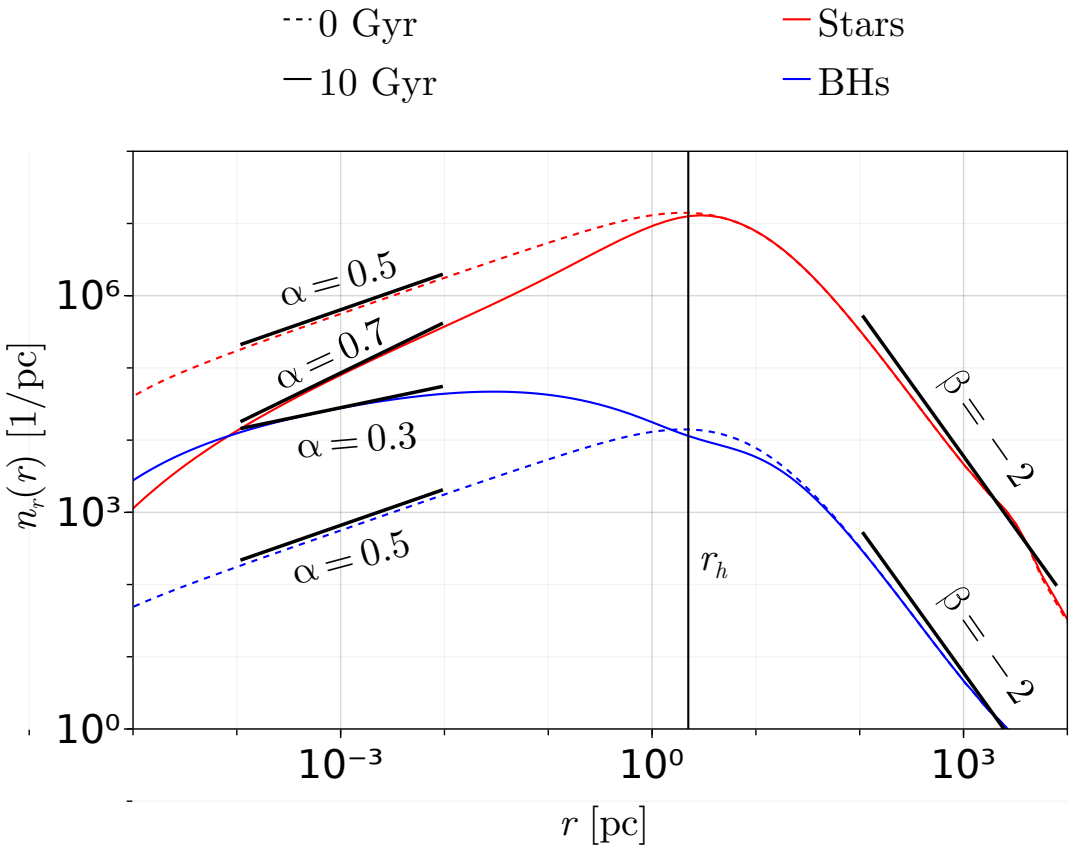

Figure 4.4: Initial and final radial distribution $n_r = dN(r)/dr$ of stars and sBHs at $t = 0$ Gyr and $t = 10$ Gyr for the DFs in Fig. 4.2. The parameters of the simulation are $M_\bullet = 4 \times 10^6\, M_\odot$, $N_R = N_s = 200$. We report a power-law fit at $r \sim 10^{-3}\, r_h$ (index α) and at $r \gtrsim 10^2\, r_h$ (index β).

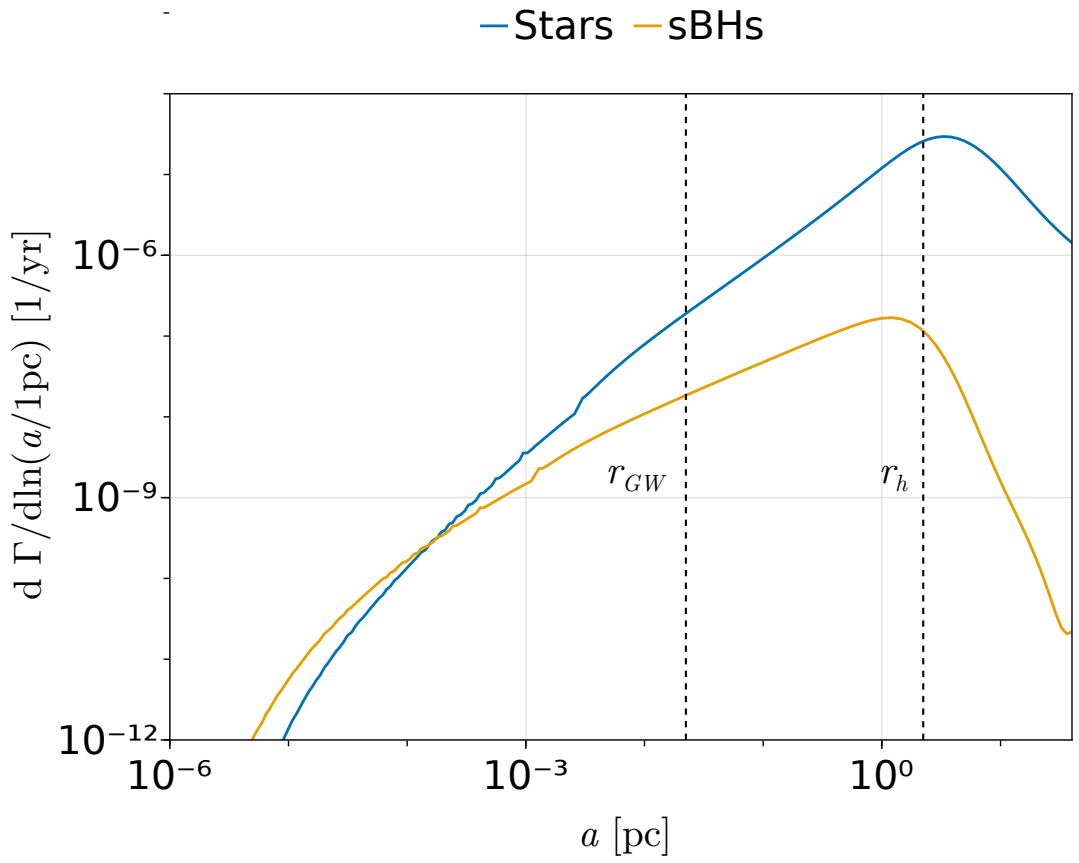

Figure 4.5: Flux of each of the two considered species entering the loss cone as a function of the semimajor axis at 10 Gyr for a system with $M_\bullet = 4 \times 10^6 M_\odot$ on the $M_\bullet - \sigma$ (the correspondent DFs are shown in the central and right panels of Fig. 4.2).

$M_{\rm BH}$ [$M_\odot$]	r_h [pc]	$\rho_s(r_h)$ [$M_\odot$/pc^3]	$\hat{\Gamma}_E$ [1/yr]	t_E [Gyr]	N_E	$\hat{\Gamma}_P$ [1/yr]	t_P [Gyr]	N_P	$\hat{\Gamma}_T$ [1/yr]	t_T [Gyr]	N_T	$t_\bullet$ [Gyr]	t_f [Gyr]	τ
10^4	0.44	2.0×10^4	5.8×10^{-8}	0.089	2.6	5.2×10^{-7}	0.017	37	1.4×10^{-4}	0.0036	6.7×10^3	0.23	0.090	10
10^4	0.2	2.0×10^5	1.9×10^{-7}	0.0029	2.7	1.6×10^{-6}	0.0054	38	4.4×10^{-4}	0.0011	7.3×10^3	0.071	0.029	10
10^4	0.094	2.0×10^6	6.0×10^{-7}	0.00092	2.8	5.1×10^{-6}	0.0017	38	0.0015	5.3×10^{-4}	7.5×10^3	0.022	0.0092	10
10^4	0.44	2.0×10^7	2.0×10^{-6}	0.00030	3.0	1.6×10^{-5}	5.5×10^{-4}	38	0.0047	2.0×10^{-4}	7.9×10^3	0.0068	0.0030	10
3×10^4	0.78	1.1×10^4	4.5×10^{-8}	0.037	8.5	3.8×10^{-7}	0.070	1.1×10^2	1.0×10^{-4}	0.015	2.1×10^4	0.93	0.37	10
3×10^4	0.36	1.1×10^5	1.4×10^{-7}	0.012	8.3	1.2×10^{-6}	0.022	1.1×10^2	3.3×10^{-4}	0.0048	2.2×10^4	0.29	0.12	10
3×10^4	0.17	1.1×10^6	4.7×10^{-7}	0.0038	9.0	3.7×10^{-6}	0.0070	1.1×10^2	0.0011	0.0015	2.3×10^4	0.90	0.038	10
3×10^4	0.78	1.1×10^7	1.5×10^{-6}	0.0012	9.4	1.2×10^{-5}	0.0022	1.1×10^2	0.0035	8.1×10^{-4}	2.4×10^4	0.028	0.012	10
10^5	1.5	5.3×10^3	3.2×10^{-8}	0.18	29	2.7×10^{-7}	0.33	3.8×10^2	7.2×10^{-5}	0.072	7.2×10^4	4.4	1.77	10
10^5	0.69	5.3×10^4	1.0×10^{-7}	0.056	29	8.4×10^{-7}	0.10	3.8×10^2	2.3×10^{-4}	0.023	7.4×10^4	1.4	0.56	10
10^5	0.32	5.3×10^5	3.3×10^{-7}	0.018	30	2.7×10^{-6}	0.033	3.8×10^2	7.8×10^{-4}	0.0072	7.7×10^4	0.42	0.18	10
10^5	0.15	5.3×10^6	1.1×10^{-6}	0.0057	32	8.4×10^{-6}	0.011	3.8×10^2	0.0026	0.0023	9.0×10^4	0.13	0.57	10
3×10^5	2.6	2.8×10^3	2.4×10^{-8}	0.73	88	2.0×10^{-7}	1.4	1.1×10^3	5.2×10^{-5}	0.3	2.1×10^5	18	7.3	10
3×10^5	1.2	2.8×10^4	7.9×10^{-8}	0.23	90	6.2×10^{-7}	0.43	1.1×10^3	1.7×10^{-4}	0.095	2.2×10^5	5.7	2.3	10
3×10^5	0.57	2.8×10^5	2.6×10^{-7}	0.075	97	1.9×10^{-6}	0.14	1.2×10^3	5.6×10^{-4}	0.030	2.3×10^5	1.8	0.75	10
3×10^5	0.26	2.8×10^6	8.7×10^{-7}	0.023	1.0×10^2	6.1×10^{-6}	0.044	1.2×10^3	0.0019	0.0095	2.4×10^5	0.54	0.24	10
10^6	5	1.4×10^3	1.8×10^{-8}	3.5	1.8×10^2	1.4×10^{-7}	6.5	1.1×10^3	3.6×10^{-5}	1.43	3.0×10^5	61	10	2.9
10^6	2.3	1.4×10^4	6.0×10^{-8}	1.1	3.1×10^2	4.4×10^{-7}	2.1	3.5×10^3	1.2×10^{-4}	0.46	6.9×10^5	26	10	9.1
10^6	1.1	1.4×10^5	2.0×10^{-7}	0.35	3.5×10^2	1.4×10^{-6}	0.65	3.8×10^3	3.9×10^{-4}	0.14	7.5×10^5	8.3	3.46	10
10^6	0.5	1.4×10^6	6.8×10^{-7}	0.11	3.7×10^2	4.3×10^{-6}	0.21	3.8×10^3	0.0013	0.45	7.8×10^5	2.6	1.1	10
3×10^6	8.9	7.3×10^2	1.2×10^{-8}	10	41	7.5×10^{-8}	10	4.2×10^2	2.6×10^{-5}	5.8	2.6×10^5	2.2×10^2	10	10	1
3×10^6	4.1	7.2×10^3	4.6×10^{-8}	4.6	3.3×10^2	3.2×10^{-7}	8.5	2.5×10^3	8.5×10^{-5}	1.84	7.5×10^5	74	10	2.2
3×10^6	1.9	7.3×10^4	1.6×10^{-7}	1.5	9.3×10^3	1.0×10^{-6}	2.7	8.5×10^3	2.8×10^{-4}	0.60	1.8×10^6	30	10	6.9
3×10^6	0.89	7.3×10^5	5.6×10^{-7}	0.46	1.3×10^3	3.2×10^{-6}	0.85	1.2×10^4	9.2×10^{-4}	0.19	2.3×10^6	11	4.6	10
10^7	17	3.6×10^2	4.0×10^{-10}	10	2.4	1.9×10^{-8}	10	1.8×10^2	1.8×10^{-5}	9.9	2.0×10^5	1.0×10^3	10	0.090	1
10^7	7.8	3.6×10^3	1.4×10^{-8}	10	41	1.1×10^{-7}	10	7.610^2	5.9×10^{-5}	9.0	6.0×10^5	3.2×10^2	10	0100	1
10^7	3.6	3.6×10^4	1.2×10^{-7}	6.9	8.1×10^2	7.0×10^{-7}	10	4.9×10^3	1.9×10^{-4}	2.7	1.8×10^6	1.0×10^2	10	1.4
10^7	1.7	3.6×10^5	4.4×10^{-7}	2.1	2.8×10^3	2.2×10^{-6}	4.0	2.0×10^4	6.4×10^{-4}	0.87	4.6×10^6	40	10	4.7

Table 4.1: Table summarising the results of all the runs. For each simulation we report the physical parameters (MBH mass $M_\bullet$, influence radius r_h and the density of stars $\rho(r_h)$); for the various rates Γ_x we report the critical point value, the time t_x when the value is reached and the total number of events N_x in the simulation. Finally, we report the typical time of growth $t_\bullet$, the total time of the simulation t_f and the ratio $\tau = t_f/t_E$. The grid resolution is $N_R \times N_s = 200 \times 200$.

γ	r_h [pc]	$\rho_s(r_h)$ [$M_\odot$/pc^3]	$\hat{\Gamma}_E$ [1/yr]	t_E [Gyr]	N_E	$\hat{\Gamma}_P$ [1/yr]	t_P [Gyr]	N_P	$\hat{\Gamma}_T$ [1/yr]	t_T [Gyr]	N_T	$t_\bullet$ [Gyr]	t_f [Gyr]	τ
1.2	2.2	4.6×10^4	5.2×10^{-8}	5.6	1.3×10^3	6.0×10^{-7}	8.7	2.4×10^4	1.2×10^{-4}	3.2	3.9×10^6	1.0×10^2	57	10
1.5	2.2	6.1×10^4	1.5×10^{-7}	2.1	1.5×10^3	9.2×10^{-7}	3.9	1.5×10^4	2.6×10^{-4}	0.93	3.0×10^6	51	21	10
1.8	2.2	7.9×10^4	7.0×10^{-7}	0.44	1.8×10^3	1.7×10^{-6}	1.0	6.6×10^3	9.5×10^{-4}	0.05	1.9×10^6	17	4.4	10

Table 4.2: Data relative to the simulations with $M_\bullet = 4\times10^6\,M_\odot$ and different central slope of the Dehnen profile γ. The grid resolution is $N_R \times N_s = 200 \times 200$.

In Fig. 4.5 we plot the rate across the loss cone at $t = 10$ Gyr with $M_\bullet = 4 \times 10^6 M_\odot$. Most of the particles are captured by the MBH around the influence radius. This is a direct consequence of the higher efficiency of diffusion in $\mathcal{R}$ rather than E. As a consequence, objects are preferentially scattered into the loss cone orbit at very large separations, of the order of r_h, and captured by the central BH onto very eccentric orbits. The effect of mass segregation is also evident here: the stellar rate within loss cone is steeper than the sBHs rate, since the latter are driven towards the MBH.

4.2.3 | Rates

The differential capture rate $d\Gamma/d\ln a$ can be integrated over a to evaluate the formation rate of TDEs, EMRIs and plunges. As described in Chapter 3, the EMRI rate is obtained by integrating the differential rate for $a < a_{\rm GW}$, whereas the plunge rate is obtained from the integral at $a > a_{\rm GW}$, with $a_{\rm GW} = 0.01\, r_h$ (Amaro-Seoane, 2020; Hopman and Alexander, 2005). It should be noted that stars can also be swallowed by the central MBH without being disrupted. Here, however, we do refer to TDEs only, without differentiating between TDEs and swallowed stars. The fraction of the latter is simply given by the ratio of the direct capture radius over the TDE radius, i.e. $r_{\rm BH}/r_\star$. Note that as the MBH mass increases, the fraction of swallowed stars increases, accounting for all stellar captures for MBHs with $M_\bullet \gtrsim 10^8 M_\odot$.

4.2.3.1 | Time evolution

Our formulation allows us to evaluate consistently the evolution over time of the star and BH distribution function and of the rate of TDEs, EMRIs and plunges, since we do not rely on the assumption of an equilibrium solution. TDE, EMRI and plunge rates as a function of time are plotted in Figure 4.6 for all our simulations. For each run, the time axis has been normalised to the peak time of the EMRI rate t_E, whereas the peak of the EMRI and plunge rate as well as the first inflection point of the TDE rate have been normalised to unity. This specific rescaling shows that the time evolution of all rates in all simulation is almost exactly the same. EMRIs and plunges initially grow up to a maximum value reached at slightly different times $t_P/t_E \simeq 1.8$ and then start to decay with a quasi-exponential trend. The TDE rate has no global maximum, but has a critical point around t_E.

One can interpret this picture by considering that advection is responsible for the initial increase in the rates of the sBHs, since it moves BHs on orbits that dominate the contribution to the flux into the loss cone. As the distributions of the two components

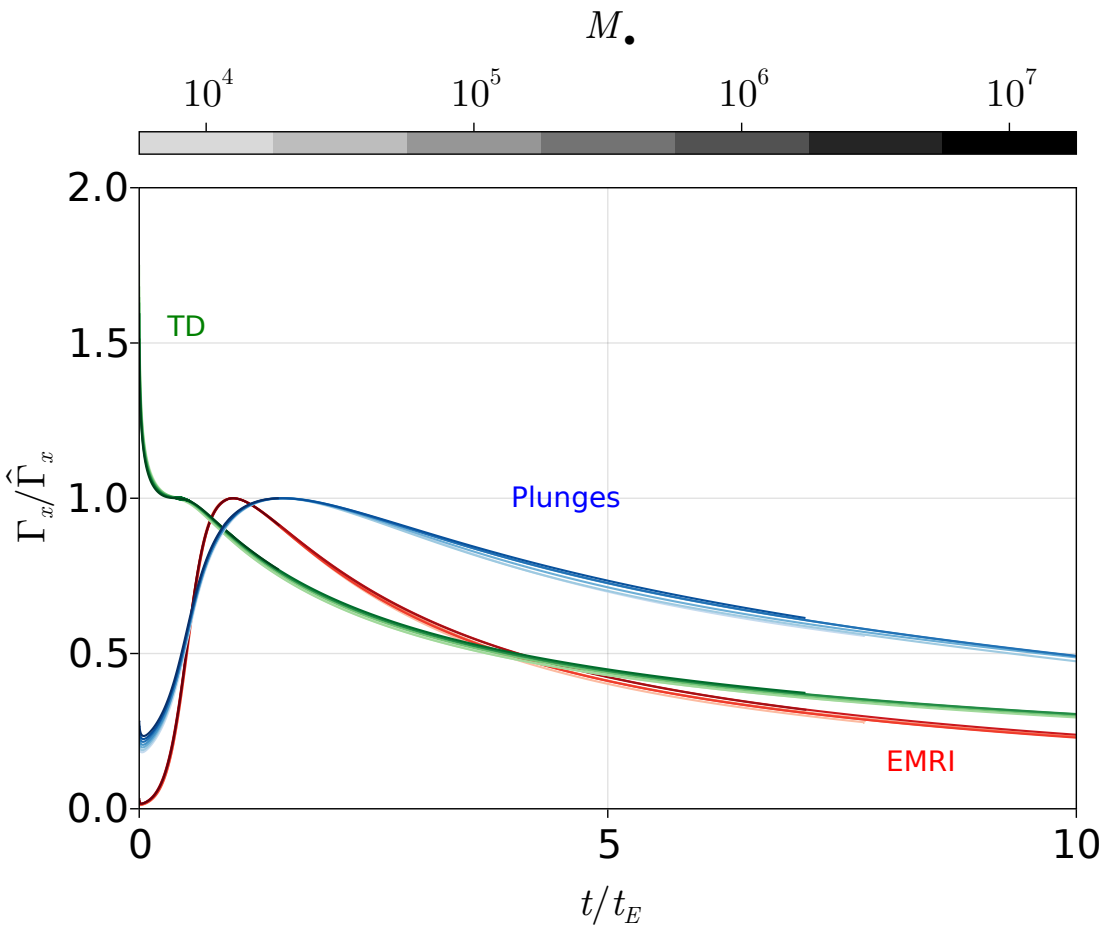

Figure 4.6: Rates for EMRIs (red), plunges (blue) and TD (green) formation in the simulations on the $M_\bullet - \sigma$ branch (refer to Table 4.1); saturation is used to label different masses. The time evolution of the rates in all the simulations show self-similar trends once scaled properly. We express time in units of t_E, the EMRI peak time, EMRI and Plunge rates in units of their maximum value and TDEs rate in units of their plateau value.

are rearranged, advection in the innermost regions becomes less effective until it cannot sustain the capture rate anymore, resulting in the late quasi-exponential decline. Since EMRIs are produced in the innermost region, advection slows down earlier and the EMRI peak is reached before that of plunges. These effects have a smaller impact on the depletion rate of TDEs, which has an inflection point at an early time $t_T < t_E$. This is likely because the initial mass segregation pushes the stars out from the centre increasing the density at the influence radius, where most of the TDEs happen.

4.2.3.2 | Scaling with black hole mass and stellar distribution properties

Table 4.1 summarizes our findings. For each simulation we report the main parameters defining the system, namely MBH mass, r_h and $\rho(r_h)$ and the main features of the TDE, EMRI and plunge rates. For each species x, we report the rate at the critical point (either the maximum or inflection point) $\hat{\Gamma}_x$, the corresponding time and the total number of events occurred during the simulation. In order to estimate the rate of growth of the central MBH, we compute for each simulation the typical time of growth

$$t_\bullet = \frac{M_\bullet}{0.5\, m_s\, N_T + m_{\rm BH}\,(N_E + N_P)}\, t_f, \tag{4.18}$$

where t_f is the total time of the simulation, which we also report in the table in units of t_E. The time $t_\bullet$ can be interpreted as the time the MBH needs to double its mass at the average rate of the simulations. In computing the latter, we made the simplifying assumption that only half the mass of a star being tidally disrupted is captured by the central MBH and thus contributes to its growth. On the other hand, a sBH being captured is considered to contribute with its whole mass.

A visual presentation of $t_\bullet$, the EMRI peak rate $\hat{\Gamma}_E$ and total number N_E for all the simulations is given in Figure 4.7. It is clear that all these quantities have a power-law dependence on the central black hole mass $M_\bullet$ (and on the velocity dispersion), which can be explained with analytical arguments once a $M_\bullet - \sigma$ relation is assumed (Hopman and Alexander, 2005). The average density of the system scales as

$$\rho \simeq \frac{M_i}{r_a^3} \propto M_\bullet^{-2}\, \sigma^6 \propto M_\bullet^{-0.58} \left(\frac{\sigma}{\sigma_0}\right)^6, \tag{4.19}$$

which follows from the fact that the total mass of each component is proportional to $M_\bullet$ and the length scale r_a is proportional to $r_h \propto M_\bullet/\sigma^2 \propto M_\bullet^{0.53}\,(\sigma/\sigma_0)^2$. Note that in the last proportionality of equation (4.19) we made use of equation (4.3) to derive the $M_\bullet$ dependence. Moreover, we allow σ varying with respect to the scaling relation inferred value σ_0, keeping the σ/σ_0 dependence. This is because, for each $M_\bullet$, we explored

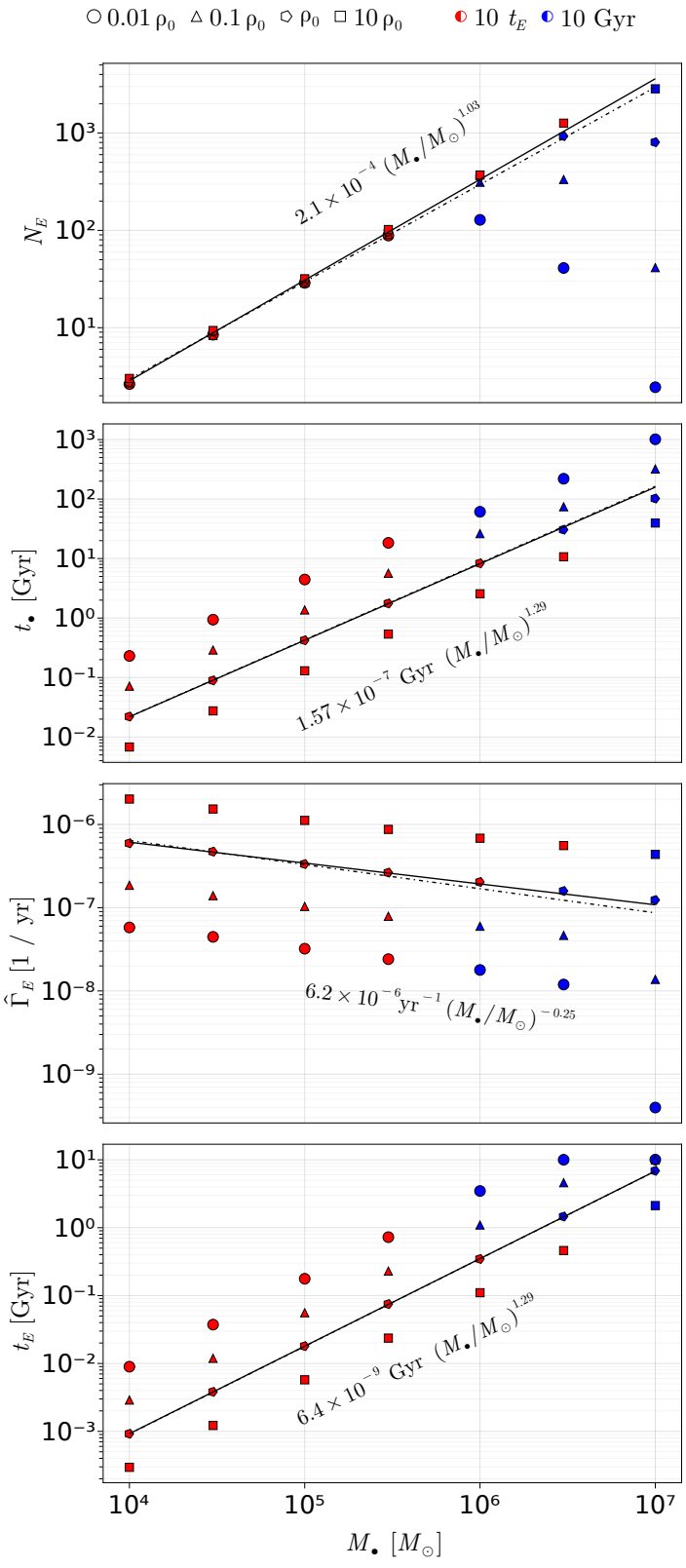

Figure 4.7: From top to bottom: scaling of the total number of EMRIs N_E, evolution timescale $t_\bullet$ of the systems, maximum EMRI rate $\hat{\Gamma}_E$ and time when it is reached as a function of $M_\bullet$ for all runs. For each plot, we fit a two variables power-law in $M_\bullet$ and σ to the $M_\bullet < 10^6 M_\odot$ simulations; we report the case $\sigma = \sigma_0$, and plot the curve in solid black. The dot-dashed line represents the best-fit power law with the theoretically estimated exponents – see Table 4.3 for details. Colours mark the total time of the simulations: in red those ended at 10 times the EMRI peak-time, and in blue those ended at 10 Gyr. For each mass, different shapes mark different values of the density at the influence radius $\rho(r_h)$ in units of ρ_0, that is the density corresponding to σ_0 from the $M_\bullet - \sigma$ relation.

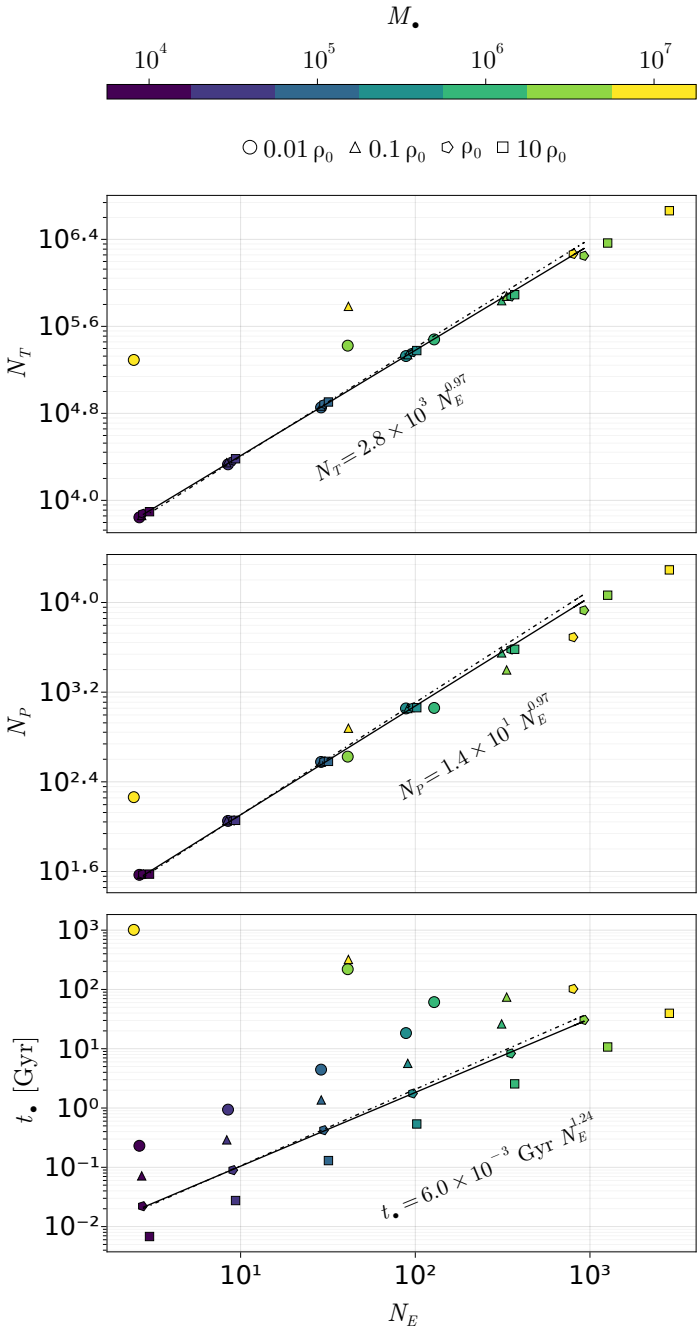

Figure 4.8: From top to bottom: total number of TDEs, total number of plunges and growth timescale $t_\bullet$ as a function of the total number of EMRIs for the different runs. Colours mark the central MBH mass of the simulation, according to the scale displayed by the top bar, and shapes are for different densities at a given mass (see Fig. 4.7). For each panel, we also report the trend-line obtained by fitting a two variables power-law in N_E and σ to the $M_\bullet < 10^6 M_\odot$ simulations in solid black and the fit with the theoretically estimated trends in dot-dashed - see Table 4.4 for details.

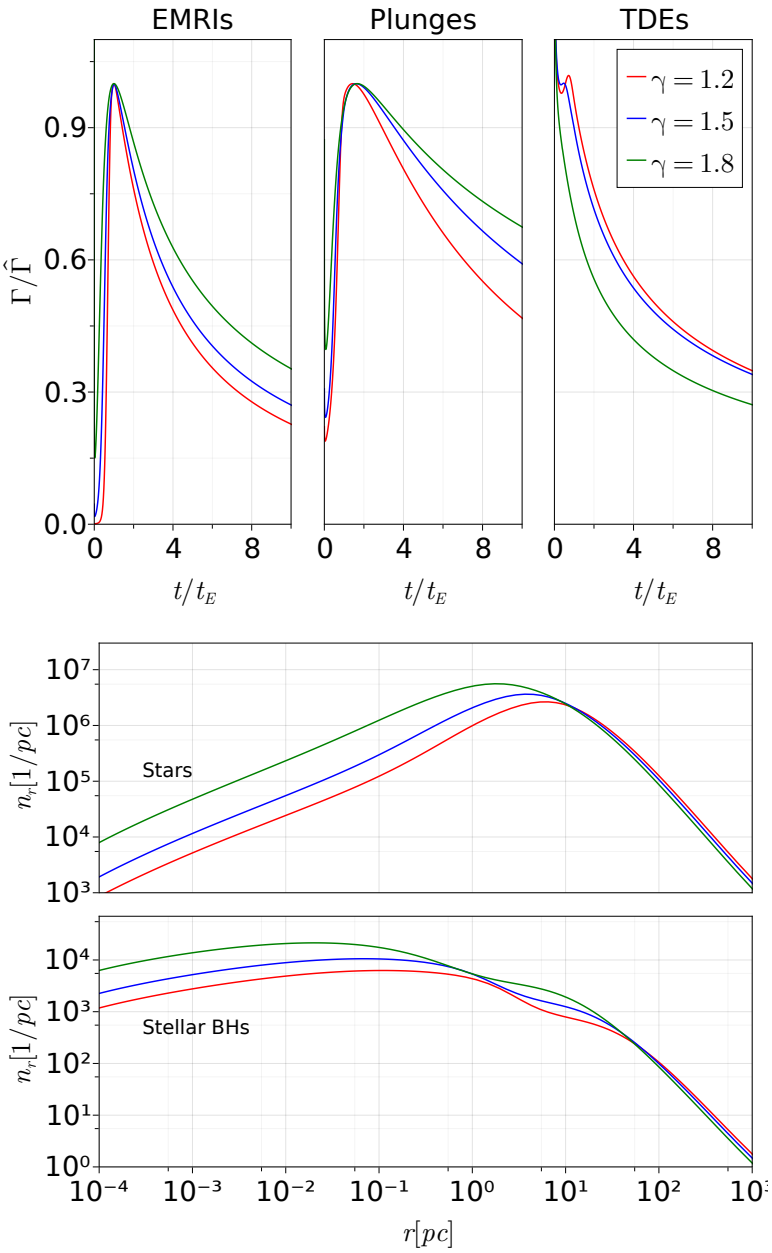

Figure 4.9: Results of simulations for $M_\bullet = 4 \times 10^6 M_\odot$ and stellar objects initially distributed as Dehnen profiles with $\gamma = 1.2,\ 1.5,\ 1.8$ with $r_a = 4\, r_h$. The upper panel shows the rates for EMRIs, plunges and TDEs scaled as in Fig. 4.6; the lower panel shows the radial number distribution $n_r = dN/dr$ at $t = 10\, t_E$. A steeper $\gamma = 1.8$ profile corresponds to no plateau in TDEs, while $\gamma = 1.2$ has a flex. The EMRI and plunge rates show similar trends, with a slower late time decay for steep profiles.

different σ as a way to study how the rates depend on the environment at a fixed black hole mass. Since the scale radius of the stellar distribution depends on σ, by sampling different values of σ we can simulate environments with different typical density, as reported in the third column of Table 4.1.

Once we have the typical density, the relaxation timescale of the system at a given radius is (see Merritt (2013))

$$t_{\rm rlx} \simeq \frac{\sigma^3}{\rho} \propto M_\bullet^2\, \sigma^{-3} \propto M_\bullet^{1.29} \left(\frac{\sigma}{\sigma_0}\right)^{-3}. \tag{4.20}$$

Since the time evolution of the rate is driven by relaxation, this sets also the scaling of the quantity $t_\bullet$ plotted in the middle panel of Figure 4.7. Besides the almost perfect scaling with MBH mass, $t_\bullet$ spans a range of about 1.5dex for the different σ adopted, in line with the scaling in equation (4.20). The typical rate then behaves like

$$\Gamma_x \propto \frac{M_i}{t_{\rm rlx}} \propto M_\bullet^{-1}\, \sigma^3 \propto M_\bullet^{-0.29} \left(\frac{\sigma}{\sigma_0}\right)^{3}. \tag{4.21}$$

This is shown for EMRIs in the lower panel of Figure 4.7.

It can be noted that deviations from the power-law trend appear in our results. This is especially true for N_E (upper panel in Figure 4.7), which is the total number of EMRIs integrated over the simulation duration. Those deviations are due to the fact that the corresponding simulations reached the time limit $t_f = 10$ Gyr, possibly even before the global maximum of Γ_E is reached.

We fit the results of our simulations to the expected power-laws in the region $M < 10^6 M_\odot$ (in order to include only simulations that run for 10 t_E). The general form is

$$y = a_0 \left(\frac{M_\bullet}{M_\odot}\right)^{b_0} \left(\frac{\sigma}{\sigma_0}\right)^{c_0} \tag{4.22}$$

where a_0 is the fitting parameter, whereas b_0 and c_0 are the power-law exponent of $M_\bullet$ and σ predicted by the theoretical scaling for the quantity y under examination. We report the trend line obtained on the $M_\bullet - \sigma$ branches in Fig. 4.7. We also fit the general power law with three free parameters

$$y = a \left(\frac{M_\bullet}{M_\odot}\right)^{b} \left(\frac{\sigma}{\sigma_0}\right)^{c} \tag{4.23}$$

to find the best-fitting exponents and compare them to the expected theoretical scaling. The results of all fits are reported in Tab. 4.3; the fitted slopes are close to the simple scaling we derived.

y	a_0	b_0	c_0	a	b	c
N_E	3.0×10^{-4}	1.00	0.00	2.0×10^{-3}	1.03	0.11
$t_\bullet$	1.5×10^{-7}	1.29	-3.00	1.5×10^{-7}	1.29	-3.07
t_E	6.3×10^{-9}	1.29	-3.00	6.4×10^{-9}	1.29	-2.97
$\hat{\Gamma}_E$	9.3×10^{-6}	-0.29	3.00	6.2×10^{-6}	-0.25	3.09

Table 4.3: Results of the least square fit of the data with a power law $y = a\,(M_\bullet/M_\odot)^b\,(\sigma/\sigma_0)^c$. The subscript 0 refers to the single a_0 parameter fit, while non dubbed quantities are the result of a three parameters fit.

y	a_0	b_0	c_0	a	b	c
N_T	2.5×10^{3}	1.00	0.00	2.7×10^{3}	0.97	7.1×10^{-3}
N_P	1.3×10^{1}	1.00	0.00	1.4×10^{1}	0.97	-8.9×10^{-2}
$t_\bullet$	5.4×10^{-3}	1.29	-3.00	6.0×10^{-3}	1.24	-3.2

Table 4.4: Results of the least square fit of the data with a power law $y = a\,N_E^b\,(\sigma/\sigma_0)^c$. The subscript 0 refers to the single a_0 parameter fit, while non dubbed quantities are the result of a three parameters fit.

Plunges and TDEs naturally show the same scaling with $M_\bullet$ as EMRIs do since, for all species, the total number of captures is proportional to the mass of the central MBH. In Fig. 4.8, we show the trend of N_T, N_P and $t_\bullet$ in terms of N_E. The expected trends scale as

$$N_T \propto N_E \quad N_P \propto N_E \quad t_\bullet \propto N_E^{1.29} \left(\frac{\sigma}{\sigma_0}\right)^{-3} . \tag{4.24}$$

In this case we proceed as before and fit the data with a generic power-law in N_E and (σ/σ_0). The results of the fits are summarised in Tab. 4.4; as in the previous case, the scaling relations are close to the theoretical estimates.

Perhaps the most important feature of these results is that $t_\bullet$, shown in Fig. 4.7, becomes shorter than the Hubble time if $M_\bullet$ is lower than $3 \times 10^5 M_\odot$–$3 \times 10^6 M_\odot$ depending on the value of σ/σ_0 (i.e. depending on the initial density of the stellar distribution). This has two important implications. On the one hand, our assumption of a non evolving potential breaks down for low MBH masses, calling for a more sophisticated treatment including the time evolution of the MBH mass and, consequently, of the overall potential of the system. On the other hand, steady state EMRI rates largely used in the literature to predict LISA detections are inapplicable exactly in the mass range where LISA is most sensitive (i.e. $10^5 M_\odot < M_\bullet < 10^6 M_\odot$ Babak et al., 2017), which calls for a major revision of the problem.

4.2.3.3 | Dependence on the slope of the stellar distribution

In order to understand the dependence of the results on the shape of the stellar distribution, for $M_\bullet = 4 \cdot 10^6 M_\odot$ and σ from Eq. (4.3) we performed two simulations with different initial conditions, initialising a Dehnen potential with $\gamma = 1.2$ and one with $\gamma = 1.8$.

The main results of these runs are reported in Table 4.2 and visualized in Fig. 4.9. In general, by increasing (in modulus) the central slope of the potential, we observe a slowdown of the late quasi-exponential decay of the three rates we consider (upper panel of Figure 4.9). Quantitatively, considering a reference time of $10\,t_E$ as in the previous analysis, the ratio between the total number of plunges and the total number of EMRIs decreases with γ. Since the threshold that distinguishes the two phenomena (i.e. $r_{\rm GW}$) does not depend on γ, a steeper slope implies a relatively higher number of objects inside $r_{\rm GW}$. It is also worth noting that regardless of the initial distribution, the systems approach the same final density profiles: stars tend to $n \propto r^{-1.3}$ and stellar BHs to $n \propto r^{-1.7}$ at the centre, as shown in the lower panel of Figure 4.9.

Overall, steeper density profiles lead to higher peak rates at earlier times, resulting in an overall faster evolution of the system and mass growth of the MBH. As a direct consequence, steady state rates are even less applicable to MBHs growing in steeper density profiles.

4.2.4 | Comparison with literature

The evolved profile of the DF is in substantial agreement with Pan, Lyu, and Yang (2022), at least until the end of their run (at 2 Gyr), despite their nuclear cluster is populated with an additional third stellar component and the fact that they maintain the same loss cone size for different stellar species.

In our runs, the EMRI formation peak rate on the $M_\bullet - \sigma$ is best described by

$$\hat{\Gamma}_E = 140\ \mathrm{Gyr}^{-1} \left(\frac{M_\bullet}{4 \cdot 10^6 M_\odot} \right)^{-0.25} . \tag{4.25}$$

At the reference system $M_\bullet = 4 \cdot 10^6$, this is compatible with other estimates found in the literature (Bar-Or and Alexander, 2016; Pan and Yang, 2021; Pan et al., 2022; Preto and Amaro-Seoane, 2010). The best-fit power-law exponent of $\Gamma_E(M_\bullet)$ is not far from the predicted value of -0.29 (see Fig. 4.7). The best-fit to the number of EMRIs occurring in a Hubble time, so long as $t_E \ll t_H$ (i.e. for small MBH masses, cf Figure 4.7) is well described by

$$N_E = 1.3 \cdot 10^4 \left(\frac{M_\bullet}{4 \cdot 10^6 M_\odot} \right)^{1.03} . \tag{4.26}$$

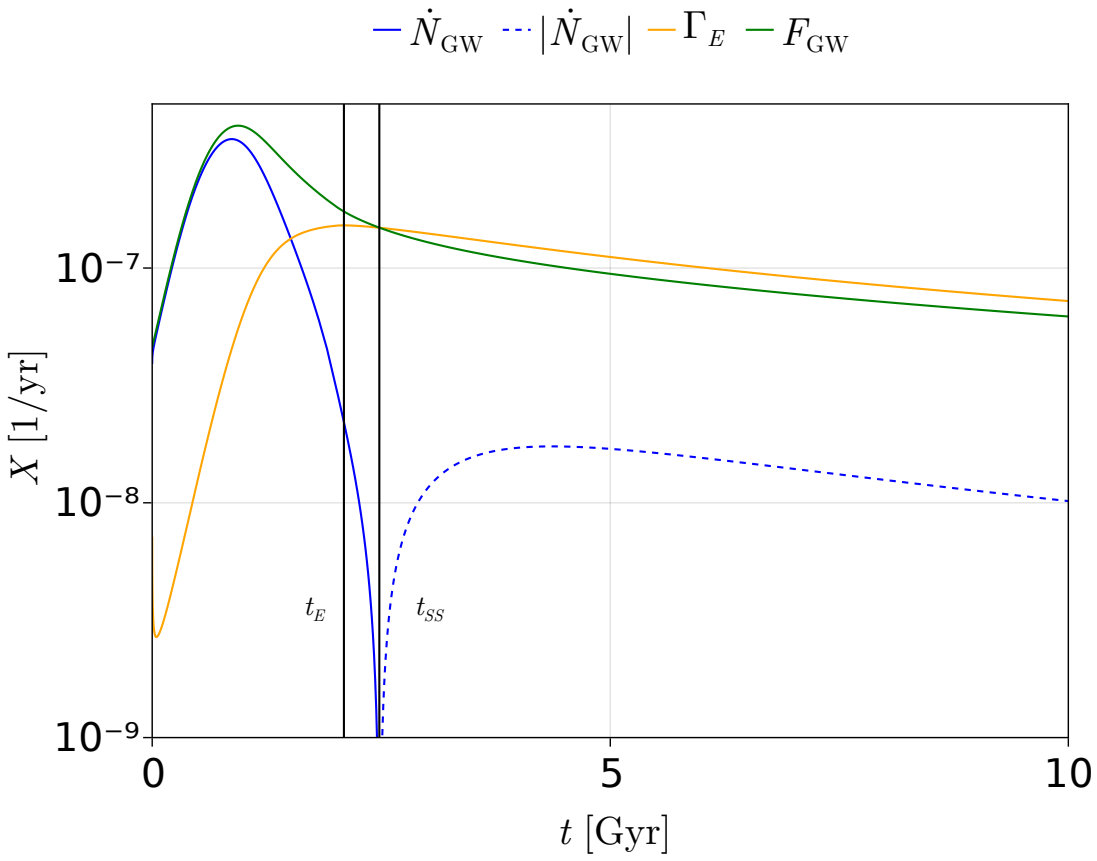

Figure 4.10: Inflow of particle in the $E > E_{\rm GW}$ region $\mathcal{F}_{\rm GW}$, total variation of sBHs in the region $\dot{N}_{\rm GW}$, and EMRI rate Γ_E for the simulation with $M_\bullet = 4 \times 10^6\, M_\odot$, $\sigma = \sigma_0$ and $\gamma = 1.5$. When the steady state approximation better describes the system $\dot{N}_{\rm GW} = \mathcal{F}_{\rm GW} - \Gamma_E = 0$ and $\Gamma_E \simeq \hat{\Gamma}_E$, showing why the peaks $\hat{\Gamma}_x$ show trends similar to steady-state rates.

Pan and Yang (2021) ran all the simulations for $t_f = 5$ Gyr and compared the peak rate with the average rate in the simulation

$$\bar{\Gamma}_E = \frac{N_E}{t_f} = \frac{N_E}{5\,\mathrm{Gyr}} \tag{4.27}$$

showing a trend compatible with ours, despite the fact of cutting the high mass end earlier and the low mass end later than in our simulations. By stopping the evolution at a time that scales with the system, the power-law describing N_E emerges more clearly.

The reason why the steady-state results agree with the maximum in the steady-potential simulations resides both in the properties of the systems we consider and in

the conservation of mass implied by the FP equation. Considering the region $E > E_{GW}$ the FP equation implies that the time derivative of the number of sBHs in this region is

$$\dot{N}_{GW} = F_{GW} - \Gamma_E \tag{4.28}$$

where F_{GW} is the rate of particles that enter the $E > E_{GW}$ region

$$F_{GW} = \int_0^1 d\mathcal{R}\ \mathcal{F}_E(E_{GW}, \mathcal{R})\,. \tag{4.29}$$

During the evolution, the number of sBHs in the region initially increases because of advection and then decreases due to gravitational captures. When it is stationary, the inflow of particles $\mathcal{F}_{GW}$ equals the outflow of particles Γ_E, as in the steady state condition. As shown in Fig. 4.10 at this time Γ_E is around its peak.

As suggested by Pan and Yang (2021), the average rate $\bar{\Gamma}_E$ over a suitable time interval may provide realistic formation rates without the need of an artificial cap. The capped rates derived in Babak et al. (2017) scale as $M_\bullet$ for small $M_\bullet$ and as the steady-state rates at high $M_\bullet$; this trend is qualitatively resembled by that of $\bar{\Gamma}_E$. While at low $M_\bullet$ the trend of $\bar{\Gamma}_E$ is linear, at high $M_\bullet$ it strongly depends on the curve $\Gamma_E(t)$ and is not, in general, a power-law when the Hubble time becomes comparable to t_E. For a better estimate, one could combine $\bar{\Gamma}_E$ with a probabilistic treatment of galactic encounters, since they can replenish the nuclear cluster and could possibly restart the EMRI production phase.

The time evolution of the EMRI rate may play a relevant role for LISA detection rates forecasts, especially at high $M_\bullet$ - where they are strongly dependent on the initial conditions. In order to produce more reliable rates, the best strategy would be to account for realistic initial conditions and a self-consistent evolution in order to directly compute the number of events produced in the evolution of a representative galactic population.

4.3 | Additional material

4.3.1 | Velocity dispersion of the initial conditions

Assuming an isotropic distribution, in a Dehnen system with inner slope $\gamma = 1.5$, the radial velocity dispersion in presence of a central MBH is (Tremaine et al., 1994)

$$\sigma_r^2 = \frac{GM}{r_a}\ \left[s_1\left(\frac{r}{r_a}\right) + \frac{M_\bullet}{M_s}\ s_2\left(\frac{r}{r_a}\right)\right] \tag{4.30}$$

where

$$\begin{aligned} s_1(x) =& x^{0.5}(1+x)^{3.5} - x^{1.5}(1+x)^{2.5}\left[4\log\left(1+\frac{1}{x}\right) - \frac{10}{3}\right] \\ & - 6x^{2.5}(1+x)^{1.5} + 2x^{3.5}(1+x)^{0.5} - \frac{1}{3}x^{4.5}(1+x)^{-0.5} \end{aligned} \tag{4.31}$$

$$\begin{aligned} s_2(x) =& -\frac{256}{15}\,x^{1.5}\,(1+x)^{2.5} + \frac{2}{5}\frac{(1+x)^5}{x} - \frac{8}{3}(1+x)^4 + 12x(1+x)^3 \\ & + 8x^2(1+x)^4 - \frac{2}{3}x^3(1+x)\,. \end{aligned} \tag{4.32}$$

One can use this formula to compute the relation between the scale r_a and the velocity dispersion of the system at different radii. Another possibility is to average this value in a central region, such as in a sphere with radius $r = r_a$

$$\langle\sigma^2\rangle_1 = \frac{\int_0^{2\,r_a} dr\,4\pi\,r^2\,n(r)\,\sigma_r^2(r)}{\int_0^{2\,r_a} dr\,4\pi\,r^2\,n(r)} \simeq \left(0.145 + 5.173\,\frac{M_\bullet}{M_s}\right)\frac{G\,M_s}{r_a} \tag{4.33}$$

or within $r = 0.25\,r_a$ (which is r_h in our model)

$$\langle\sigma^2\rangle_{0.25} = \frac{\int_0^{2\,r_a} dr\,4\pi\,r^2\,n(r)\,\sigma_r^2(r)}{\int_0^{2\,r_a} dr\,4\pi\,r^2\,n(r)} \simeq \left(0.164 + 1.729\,\frac{M_\bullet}{M_s}\right)\frac{G\,M_s}{r_a} \tag{4.34}$$

In the systems adopted in this work we considered (neglecting the sBHs) $M_s = 20\,M_\bullet$, so that

$$\langle\sigma_r^2\rangle_{0.25} \simeq 8.5\,\frac{G\,M_\bullet}{r_a} \qquad \langle\sigma_r^2\rangle_1 \simeq 4.6\,\frac{G\,M_\bullet}{r_a} \tag{4.35}$$

4.3.2 | Derivatives on the grid and time integration

To compute the right-hand side of the orbit averaged Fokker-Planck equation (2.37) we opted for a flux conservative scheme, which proved to be more stable than a simple finite-difference approach. We compute each contribution to the divergence of $\mathcal{F}$ starting from the value of its components on the grid. To compute $\partial_R\mathcal{F}_R$ on a cell centred at $(\bar{s},\bar{R})$, for example, we linearly interpolate the coefficients $\mathcal{D}_i^j$, the distribution function f^i and its partial derivative $\partial_E f^i$ at the upper and lower edges of the cell $(s, R \pm \Delta R/2)$, we compute $\partial_R f^i$ at the edges with the finite difference and assemble the ingredients to give

$$\partial_R\mathcal{F}_i^R(\bar{s},\bar{R}) = \frac{\mathcal{F}_i^R(\bar{s},\bar{R}+\Delta R/2) - \mathcal{F}_i^R(\bar{s},\bar{R}-\Delta R/2)}{\Delta R}\,. \tag{4.36}$$

An analogue scheme applies to $\partial_E \mathcal{F}_i^R$. The boundary conditions are used to set f^i and its derivatives at the corresponding locus. At the loss cone, we rearranged the boundary condition as an equation for the partial derivative of f^i

$$\partial_R f^i(s, \tilde{R} - \Delta R/2) = \frac{f^i(s, \tilde{R})}{\log \tilde{R}/R_0} \frac{1}{\tilde{R}} \tag{4.37}$$

where $\tilde{R}$ is the smallest point on the grid above the loss cone boundary at s.

We integrated the equation in time using an implicit Euler scheme. The flux conservative approach we just described is formally linear in the values of the functions on the grid, that is, for each component we can write

$$\partial_E \mathcal{F}_E^i(s_j, R_l) + \partial_R \mathcal{F}_R^i(s_j, R_l) = \sum_{k,m} M_{j,l}^{i;k,m} f^i(s_k, R_m). \tag{4.38}$$

This means that the expression on the left is a linear combination of the values of f^i. The implicit Euler scheme consists in discretising the left-hand side of equation (2.43) at time t with a forward derivative in time and plugging at the right-hand side expression (4.38) evaluated at $t + \Delta t$. One obtains a linear system for the grid values of $f(s_j, R_l, t + \Delta t)$ that can be recast in a more familiar way by linearising the matrix $f^i(s_j, R_l, t + \Delta t)$ forming the vector $\mathfrak{f}_t^i$

$$\mathfrak{C} \frac{\mathfrak{f}_{t+\Delta t}^i - \mathfrak{f}_t^i}{\Delta t} = \mathfrak{M}_t^i \cdot \mathfrak{f}_{t+\Delta t}^i \tag{4.39}$$

where we also introduced $\mathfrak{C}$, the linearised version of $C(s, R)$, and $\mathfrak{M}$, the matrix version of the tensor M in (4.38). A time integration step consists in solving this equation for $\mathfrak{f}_{t+\Delta t}^i$, returning then to its matrix counterpart. The symbol $\cdot$ indicates matrix-to-vector multiplication.

At each step, we choose the integration time step Δt adaptively, by setting a constraint on the expected variation of f. In the vectorised notation

$$\Delta t = \epsilon \min_{i,\text{grid}} \begin{pmatrix} \mathfrak{f}^t \\ \dot{\mathfrak{f}}_t^i \end{pmatrix} \qquad \dot{\mathfrak{f}}_t^i = \frac{\mathfrak{M}_t^i \cdot \mathfrak{f}_t^i}{\mathfrak{C}} \tag{4.40}$$

where ϵ is a threshold value.

The method we have chosen for the solution of this problem can be certainly improved. As reviewed in Vasiliev (2017), the choice of time discretisation is crucial for the stability and the accuracy of the solution at a fixed integration step dt. In particular, the inclusion of a Poisson step for the update of the stellar potential may require more accurate techniques to ensure orbital energy is modified correctly, and numerical heating is avoided. Even at the current stage of complexity, one can discretise time with

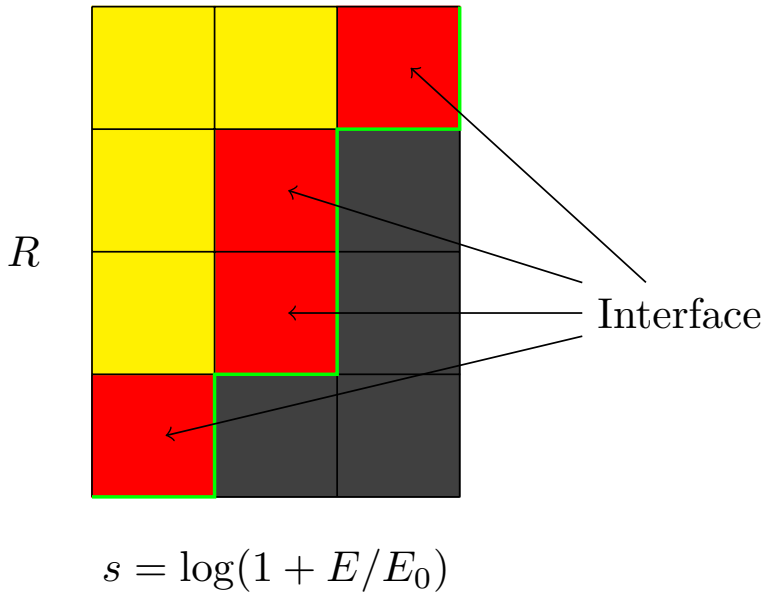

Figure 4.11: Discrete representation of part of the loss cone on the simulation grid. The green line is the effective loss cone in the simulation, and the red cells are used to compute the rate of particles entering the loss cone.

more accurate techniques, such as the method developed by Chang and Cooper (Chang and Cooper, 1970) or *predictor/corrector* schemes. We aim at testing such improvements in order to reduce the computational cost.

4.3.3 | Rate across the loss cone

In order to compute the various rates across the loss cone, we use the definition of the current density. Defining the curves

$$\xi_E : \quad E \to (E, R^{\rm BH}_{\rm LC}(E)) \qquad E_{\rm GW} \leq E \leq E_{\rm BH} \tag{4.41}$$

$$\xi_P : \quad E \to (E, R^{\rm BH}_{\rm LC}(E)) \qquad 0 \leq E \leq E_{GW} \tag{4.42}$$

$$\xi_T : \quad E \to (E, R^{s}_{\rm LC}(E)) \qquad 0 \leq E \leq E_s \tag{4.43}$$

the rates are given by

$$\Gamma_x = \int_{\xi_x} d\boldsymbol{n}_x \cdot \boldsymbol{\mathcal{F}} \tag{4.44}$$

where x stands for the desired event and $\boldsymbol{n}_x$ is the normal to the curve ξ_x. The discretised version of this curvilinear integral can be written as

$$\Gamma_x = -\sum_i \mathcal{F}_{R,i}\, \Delta E_i + \sum_j \mathcal{F}_{E,j}\, \Delta R_j \tag{4.45}$$

where i runs along the cells at the interface of the loss cone for the x event whose neighbour below is empty, j along the cells whose neighbour on the right is empty (see Figure 4.11); ΔE and ΔR indicate the sizes of the corresponding cell.

4.4 | Discussion and Conclusions

In this chapter we presented a two-population, two-dimensional time-dependent Fokker-Planck formalism to study the capture of stars and sBHs by an MBH residing at the centre of a nuclear star cluster. We ran a number of simulations spanning a wide range of MBH masses and properties of the surrounding stellar and sBH distribution, keeping the gravitational potential of the system fixed. We analysed the time dependence of the capture rate of stars and sBHs, their scaling with the properties of the systems and the growth of the central MBH. Our main findings can be summarized as follows:

- Segregation dominates the evolution of the system, causing sBHs to concentrate in the centre, in agreement with theoretical expectations (Bahcall and Wolf, 1977). The time dependent evolution of the distribution implies a time dependent evolution of the TDE, EMRI and plunge rates (as also shown by e.g.Vasiliev 2017). In particular, EMRIs and plunges initially have a steep rise, reach a peak and then decline in a quasi-exponential fashion, whereas TDE rates experiences an initial plateau and a slow late time decay.

- Once normalized to the occurrence time and peak value of the EMRI rate $(t_E, \hat{\Gamma}_E)$, the time evolution of all species (TDEs, EMRIs, plunges) in all simulations overlap almost perfectly. We thus derived simple scalings for t_E and $\hat{\Gamma}_E$ which allows reconstructing the whole time evolution of the rates of each species for any MBH mass and density of the stellar distribution.

- The *peak* of the TDE, EMRI and plunge rates is consistent with steady state estimates from the literature (e.g. Bar-Or and Alexander 2016), however, those peak rates cannot be sustained indefinitely and decay over a timescale that is dependent on the MBH mass and on the properties of the nuclear star cluster (as also shown in Bortolas 2022 for a complete stellar mass function).

- The aforementioned rates are such that the MBH doubles its mass on a timescale shorter than the Hubble time for $M_\bullet \lesssim 10^6 M_\odot$.

These findings have profound implications for evaluating the rates of gravitational capture of stars and stellar mass compact objects (especially sBHs) in galactic nuclei,

which are a key element for building reliable estimates of the number of EMRI events expected for future GW missions (such as LISA) and for interpreting TDEs in electromagnetic transient surveys. Moreover, these captures can contribute significantly to the growth in mass of relatively light ($M_\bullet < 10^6 M_\odot$) MBHs, which is generally neglected in theoretical and numerical models for the evolution of MBHs along the cosmic history.

In the literature, TDE, EMRI and plunge rates are often computed assuming steady state models for Milky-Way like systems and then scaled to lower MBH central MBH masses (e.g. Merritt, 2015). The underlying assumption is that a negligible fraction of the star cluster mass is captured in the loss cone over the relevant system evolution timescale (that in this case is the Hubble time). Although this might be true for heavy MBHs (Milky Way-like or more massive), it is certainly not true for lower mass systems that evolve significantly over much shorter timescales, invalidating the steady state assumption.

Moreover, the inner region of the nuclear star cluster is dominated by the potential of the central MBH itself, and the commonly made assumption of steady state requires that this potential remains unaltered, i.e. that the MBH mass does not grow. Our simulations indicate that, for a central MBH of mass $M_\bullet \lesssim 10^6 M_\odot$ on the $M_\bullet - \sigma$ relation, the mass $M_\bullet$ would change significantly over a Hubble time if all the objects entering the MBH loss cone are accreted, invalidating *a fortiori* the steady potential assumption. The change in mass could relevantly alter the rates, since both the radius of influence and the capture radius depend on it. Moreover, the mass distribution of these systems at the end of the evolution has changed significantly, a fact that should be accounted by changing the critical radius for the EMRI/plunges distinction.

At present time, LISA detection rates are built under the assumption that the rate Γ_E of a galaxy is equal to the steady-state rate computed from the mass of its central MBH (Babak et al., 2017) – and thus require artificial capping for small MBHs. Our findings show that those rates are likely to be biased, since the steady-state rates correspond to the maximum rate of the associated steady-potential system. More specifically, the operation of associating the rates of a steady-potential simulation to a single value of the central MBH mass is non-trivial, since they change over the same timescale. We conclude that in order to reduce the uncertainty of the detection rates, it is necessary to study the whole self-consistent system. In this sense, an aim of our work is to include the rates obtained with our methods for anisotropic, time-dependent systems as in Polkas et al. (2023), where solutions of the 1D Fokker-Planck equation with PHASEFLOW (Vasiliev, 2017) were combined with the powerful semi-analytical model *L-Galaxies* (Izquierdo-Villalba et al., 2019; Springel et al., 2005).

5

Loss cone theory and partial disruptions

Everyone just keeps on disappearing. Some things vanish, like they were cut away.
Others fade slowly into the mist. And all that remains is a desert.
— *Haruki Murakami, South of the Border, West of the Sun*

This chapter is devoted to the presentation of a novel treatment of partial disruptions in the loss cone theory. First we will consider the determination of the rate of full, and partial/repeated disruptions by choosing the loss cone radius $r_{\rm LC} > r_\star(M_\bullet/m_\star)^{1/3}$ that corresponds to a partial mass loss as in Bortolas et al. (2023). Then, some original material will be presented, including a model to systematically quantify the number of repeated partial disruptions and the possible implications on their treatment with classical loss cone theory. The results of this section will be the main body of a publication currently in preparation.

5.1 | Mass loss in partial disruptions

Simulations and theoretical models indicate that stars approaching an MBH will lose part of their mass even when their pericentre is larger than the tidal disruption radius (e.g. Rees, 1988; Ryu et al., 2020a,b). A number of recent works have addressed the expected emission and accretion features associated with the partial disruption of a single star approaching the MBH (Coughlin and Nixon, 2019; Guillochon and Ramirez-Ruiz, 2013; Miles et al., 2020), and a growing body of literature is reporting observational candidates for partial disruptions, which manifest themselves as repeating events (Liu et al., 2023a,b; Malyali et al., 2023; Payne et al., 2021; Somalwar et al., 2023; Wevers et al., 2023) over timescales of $\sim 0.3 - 3$ yr if they happen in regions of phase space where

2-body relaxation is inefficient. However, the theoretical modelling of the event rates associated to partial TDEs is still in its infancy (Bortolas et al., 2023; Chen and Shen, 2021; Krolik et al., 2020; Stone et al., 2020; Zhong et al., 2022).

In fact, classical loss cone theory accounts only for total TDEs (TTDEs), adopting the corresponding value for $r_{\rm TDE}$ as a threshold between unperturbed and destroyed orbits (this approximation has been discussed in Cohn and Kulsrud, 1978, and mantained in derived works). Here we show some arguments that this solution should rather be applied adopting a larger, partial TDE (PTDE) radius.

After a star undergoes a PTDE, its subsequent evolution can proceed in different ways: if the star comes from the empty loss cone region, it can be entirely consumed through a series of repeated PTDEs, or the (possibly repeated) PTDE can significantly deflect the stellar orbit so that the star is scattered on a completely different trajectory before being disrupted. If the star has $q \sim 1$, its orbit may change appreciably after a PTDE, so that the star either gets destroyed on the next passage(s) or gets pushed away from the loss cone (e.g. Cufari et al., 2023). If the star comes from the full loss cone, its orbit following the PTDE would be substantially deflected by relaxation processes so that it will become statistically indistinguishable from other stars in the full loss cone with the same energy. Either way, the theory developed so far for modelling TTDEs (and described in Chapter 3) might be suited for computing TTDE *plus* PTDE rates instead, assuming that the outcome of the process is virtually the same as in the traditional TTDE-only treatment[1]. Below, we also argue that the same traditional treatment yields an overestimated TTDE rate, if it is applied assuming that only TTDEs can occur. For now, we do not account for the complication that each star can undergo a series of subsequent PTDEs when computing the event rates; we focus on this aspect in the next section.

We will now show a simple estimate of the fraction of total disruptions when one assumes that classical loss cone theory applies for TTDEs+PTDEs and a specific value of $r_{\rm TDE}$; with this in mind, we can extrapolate Eq. 3.9 up to $\mathcal{R} \simeq 0$ to know what is the probability of stars to be disrupted at each $\mathcal{R}$ inside this newly defined PTDE loss cone.

In the full loss cone limit, all values of $\mathcal{R}$ in the loss cone are equally probable, so that the ratio of TTDEs to PTDEs can be simply estimated through the ratio between their respective radii. In the empty loss cone limit, instead, all stars tend to be destroyed at $\mathcal{R}_{\rm LC}$, implying that all stars would undergo a PTDE, while TTDEs might be completely

[1]Assuming that the star is lost from the system, or it ends up far away from the the loss cone; even if this process might not be as fast as in the traditional treatment that considers only TTDEs, we can still consider it to be instantaneous as long as the star is lost from the loss cone within a timescale much smaller than the relaxation timescale of the host system

suppressed; this simply comes from the fact that stars approach the loss cone boundary with very small steps in $\mathcal{R}$, and they can only be (partially) destroyed at the first available radius that allows for this to occur, while it is virtually impossible for stars to reach the smaller values of $\mathcal{R}$ at which TTDEs can occur.

This implies that systems in which TDEs mainly come from the empty loss cone would have nearly all stars undergoing PTDEs, and their TTDE rates can be very small in comparison.

More quantitatively, for a fixed value of E, we can use Eq. 3.9 to compute the expected ratio of TTDEs to PTDEs. If $r_{\rm TDE}$ is the largest PTDE radius that guarantees an event to occur (with its associated PTDE $\mathcal{R}_{\rm LC}$), and $r_{\rm TDE}/\kappa$ is the radius below which only TTDEs occur ($\kappa > 1$), the fraction of TTDEs to the global event rate (PTDEs *plus* TTDEs) can be estimated as

$$\delta_{\rm TTDE}(E) = \frac{\int_{\mathcal{R}_0}^{\mathcal{R}_{\rm LC}/\kappa} d\mathcal{R} \ln(\mathcal{R}/\mathcal{R}_0)\, \theta(\mathcal{R}_{\rm LC}/\kappa - \mathcal{R}_0)}{\int_{\mathcal{R}_0}^{\mathcal{R}_{\rm LC}} d\mathcal{R} \ln(\mathcal{R}/\mathcal{R}_0)} \tag{5.1}$$

where θ is the step function, yielding one if its argument is positive and zero otherwise. We stress that all the relevant quantities (α, $\mathcal{R}_0$ etc.) in this framework should be evaluated adopting the PTDE value of $r_{\rm TDE}$. The above equation can be evaluated to be

$$\delta_{\rm TTDE} = \frac{1}{\kappa}\left[1 + \frac{(\kappa-1)\, e^{-\alpha} - \ln\kappa}{\alpha + e^{-\alpha} - 1}\right]\, \theta(\alpha - \ln\kappa) \tag{5.2}$$

that goes to zero with continuity as $\alpha \to \ln\kappa$. As expected, $\delta_{\rm TTDE} \to 1/\kappa$ if $q \gg 1$ ($\alpha \gg 1$), i.e. in the full-loss cone limit, while it becomes 0 through the θ function in the empty loss cone regime. Finally, in the framework described so far, the classically computed rate across the loss cone gives the total rate of PTDEs plus TTDEs; the rate associated to TTDEs only can be computed as

$$\Gamma_{\rm TTDE} = \int \delta_{\rm TTDE}(E)\mathcal{F}(E)dE, \tag{5.3}$$

while the rate of PTDEs is

$$\Gamma_{\rm PTDE} = \int \delta_{\rm PTDE}(E)\mathcal{F}(E)dE, \tag{5.4}$$

where $\delta_{\rm PTDE}(E) = 1 - \delta_{\rm TTDE}(E)$. As outlined in Chap. 3, the loss cone occupation parameter q is the ratio between the average change $\langle\Delta\mathcal{R}\rangle$ and $\mathcal{R}$ itself at the loss cone. Therefore, its inverse

$$N_q(E) \equiv \frac{1}{q} = \frac{\mathcal{R}_{\rm LC}}{P\,\mathcal{D}\,[\delta\mathcal{R}]} \tag{5.5}$$

is an estimate of the expected number of orbits that relaxation needs in order to alter significantly an orbit on the edge of the newly defined loss cone. Therefore, one can account for the possibility of repeated disruptions by using $\delta_{\rm PTDE} = N_q\,(1-\delta_{\rm TTDE})$ in Eq. 5.4 or, for best accuracy, define

$$N_{\rm rep} = \frac{N_q}{\mathcal{R}_{\rm LC}}\,\mathcal{R} \tag{5.6}$$

and compute

$$\delta_{\rm rep}(E) = \frac{\int_{\mathcal{R}_0}^{\mathcal{R}_{\rm LC}/\kappa} d\mathcal{R}\,\log(\mathcal{R}/\mathcal{R}_0)\,N_{\rm rep}\,\theta(\mathcal{R}_{\rm LC}/\kappa-\mathcal{R}_0)}{\int_{\mathcal{R}_0}^{\mathcal{R}_{\rm LC}} d\mathcal{R}\,\ln(\mathcal{R}/\mathcal{R}_0)} \tag{5.7}$$

In Bortolas et al. (2023) we used this prescription to compute how the flux of total and partial disruptions is affected by a different choice of $r_{\rm TDE}$. To relate the choice of r_{TDE} with Δm, we employ a formula obtained by fitting the highly accurate, general-relativistic magneto-hydrodynamical simulations by Ryu et al. (2020a,b):

$$\begin{aligned}\frac{\Delta m}{m_\star} &= \left(\eta_{\rm TTDE}\,\frac{r_{TDE}}{r_p}\right)^{\zeta}\\ \log_{10}\zeta &= 0.3+3.15\times10^{-8}\left(\log_{10}\frac{M_\bullet}{1\,M_\odot}\right)^{8.42}.\end{aligned} \tag{5.8}$$

where η is a form factor of order 1 that depends on the details of the stellar model. The value $\eta_{\rm TTDE}$ corresponding to the model we used is

$$\eta_{\rm TTDE}(m,M_\bullet) = \left(0.80+0.26\sqrt{\frac{M_\bullet}{10^6 M_\odot}}\right)\left(\frac{1.47+\exp\left(\frac{m/M_\odot-0.669}{0.137}\right)}{1+2.34\exp\left(\frac{m/M_\odot-0.669}{0.137}\right)}\right). \tag{5.9}$$

Fig. 5.1 shows how setting the value $r_{\rm TDE}$ corresponding to $\Delta m = 3\%$ affects the rate of total disruptions: they are reduced by roughly an order of magnitude. All systems are affected by the choice of $r_{\rm LC}$, with a larger impact on systems dominated by the empty loss cone regime.

5.2 | Model of partial disruptions

Motivated by the results shown in the previous section, we proceed our study of partial disruptions to constrain the choice of the effective loss cone radius. In fact, in the treatment presented in the previous section, this value was assigned somewhat arbitrarily as the radius stripping at least 3% of the original stellar mass. We build a simple model to

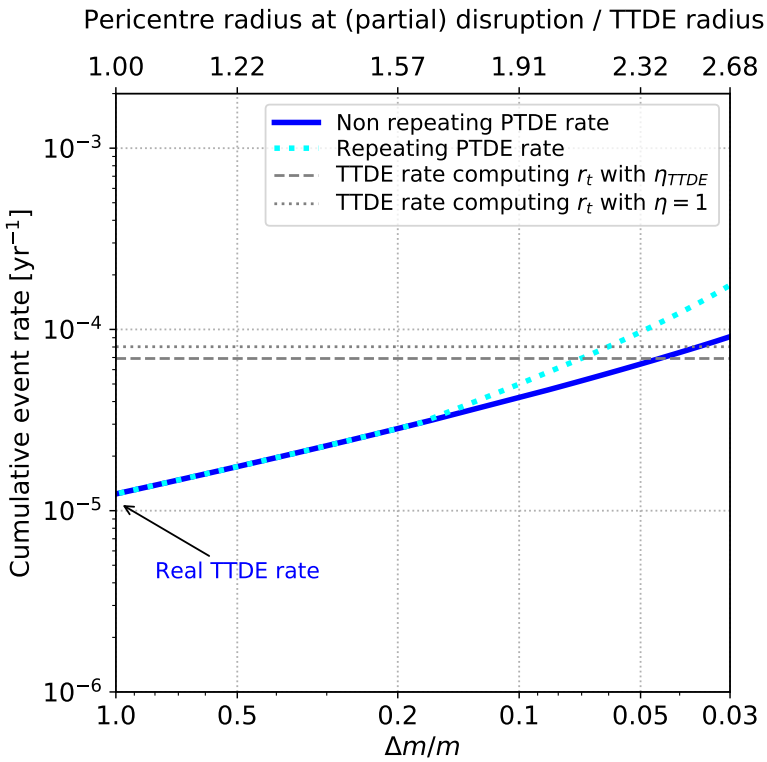

Figure 5.1: *(Courtesy of E. Bortolas)* Cumulative TTDE+PTDE rates as a function of the relative stellar mass stripped in the event, for a model of the Milky Way. The blue solid curve does not allow for repeating PTDEs, while the cyan dotted one assumes a star can undergo multiple PTDEs. The left-most value of the blue curve corresponds to the effective TTDE rate in a system in which PTDEs are allowed to occur. For comparison, the horizontal grey lines mark the TTDE rate one would have estimated neglecting PTDEs, and using either $\eta_{\rm TTDE}$ (dashed) or $\eta = 1$ (dotted). For reference, the top axis shows the value of the PTDE radius with respect to the TTDE radius (computed with $\eta_{\rm TTDE}$) for the different values of $\Delta m/m$. Remarkably, standard estimates of TTDE rates (grey horizontal lines) can easily overestimate the real TTDE rate by almost one order of magnitude, implying that properly accounting for PTDEs is crucial to obtain reliable event rates, especially in systems (as the present one) in which a significant fraction of the total flux comes from the empty loss cone. Details of the model: $M_\bullet = 4\,10^6 M_\odot$ surrounded by stars of $1\,M_\odot$ distributed in a bulge of mass $9.1\,10^9\,M_\odot$, effective radius 1 kpc and Sersic index 1.3 plus a nuclear star cluster with total mass $4\,10^7\,M_\odot$, effective radius 2 pc and Sersic index 2.

identify and characterize the key features of the process, in order to effectively include – if possible – these phenomena in the Fokker-Planck evolution. We want to estimate the typical timescale of mass changes and energy fluctuations, since we have seen in the previous section that they must occur over a timescale much shorter than the relaxation timescale in order to apply the classical loss cone theory. We start by describing how the mass loss experienced by partial disruptions can affect the orbital motion, then considering the cumulative effect of repeated PTDEs.

5.2.1 | Single Partial Disruptions

We consider a star of mass $m_\star$ and radius $r_\star$ undergoing a partial disruption around a massive black hole of mass $M_\bullet$ on an orbit with binding energy E and angular momentum J. Since we expect no significant density of stars inside $r_{\rm TDE}$, the local potential is Keplerian and the pericentre of the orbit for $J^2 \ll G^2\, M_\bullet^2/(2E)$ – as we expect for a tidal disruption – is

$$r_p = \frac{J^2}{2\,GM_\bullet}\,. \tag{5.10}$$

In what follows, we assume the partial disruption only affects the orbital energy of the subject star, and leave its angular momentum unaltered – de facto assuming that the mass lost at the pericentre is lost by ejecting the corresponding mass radially; this is in agreement with what found by Ryu et al. (2020b) through hydrodynamical simulations.

Assuming that the partial disruption corresponds to the deposition of the lost mass Δm from Eq. (5.8), the change in orbital energy due to the mass loss itself is (Metzger et al., 2022, eq. 32)

$$\delta E_{\rm ml} \simeq -\frac{GM_\bullet}{r_{\rm TDE}}\left(\frac{r_\star}{r_{\rm TDE}}\right)^2 \frac{\Delta m}{m-\Delta m}\,. \tag{5.11}$$

Tidal forces may also alter the stellar structure, inducing oscillations of the star by converting part of its orbital kinetic energy. This process, known as tidal excitation, increases the binding energy in competition with the effects of mass loss. The energy of the oscillations can be written as[2] (Press and Teukolsky, 1977)

$$\delta E_{\rm tid} = \left(\frac{G\,M_\bullet^2}{m_\star\, r_\star}\right)\left(\frac{r_\star}{r_p}\right)^6 T(\eta_p) \tag{5.12}$$

where $\eta_p \equiv (r_p/r_{\rm TDE})^{3/2}$ and $T(\eta)$ is an analytic function that depends on the polytropic index assumed. Assuming that the oscillations are weak, one can treat them in the linear

[2]We use here η_p to clearly distinguish this quantity from the form factor in the definition of $r_{\rm TDE}$.

regime, and the term can be expanded as a power law series in $r_p/r_{\rm TDE}$, giving

$$\delta E_{\rm tid} = \left(\frac{G\,M_\bullet^2}{m_\star\,r_\star}\right)\left(\frac{r_\star}{r_p}\right)^6\left[T_2(\eta_p) + \left(\frac{r_\star}{r_p}\right)^2 T_3(\eta_p) + \dots\right] \tag{5.13}$$

where T_2, T_3 are the first terms in the linear expansion of the tidal excitation term (Lee and Ostriker, 1986), whose analytic approximants are available in Portegies Zwart and Meinen (1993, eq. 7 and Tab.1), where the functions

$$\log_{10} T_k(\log_{10}\eta_p) \qquad k = 2,\ 3 \tag{5.14}$$

are fitted by a 5th order polynomial. When the oscillations are strong – and the linear regime for oscillations becomes inadequate – one should solve directly the hydrodynamics of the oscillations. In the case of some polytrope models, an analytic fit of $T(\eta)$ has been presented in Generozov et al. (2018, eq. B1 and B2).

The energy changes presented here allow us to infer whether a star can undergo multiple partial disruptions, and whether it becomes more or less bound at each passage.

5.2.2 | Partial disruptions in a prototypical system

We consider a system composed of a central black hole with mass $M = 4\times10^6 M_\odot$ surrounded by a distribution of stars (total number 8×10^7, individual mass $1M_\odot$) and stellar black holes (total number 8×10^4, individual mass $10M_\odot$) both on a Dehnen profile with scale radius of 8.8 pc and inner slope 1.5, as in Broggi et al. (2022). This system has an influence radius of $r_{\rm inf} \simeq 2.2$ pc and the velocity dispersion at the influence radius corresponds to $\sigma_{\rm inf} = 88$ km/s, coming from the $M-\sigma$ by Gültekin et al. (2009). The function $q = q(E)$ in this system is shown in Fig. 5.2.

In the central panel of Fig. 5.3 we show the cumulative effect of mass loss alone (5.11), with tidal excitation according to the linear expansion (5.13) or according to the non-linear theory (5.12) for a single passage at the pericentre r_p of a star with mass $m_\star = 1M_\odot$, radius $r = 1\,r_\odot$, and polytropic index $\gamma_p = 1.5$. Different values of the initial binding energy can dramatically change the outcome of the single passage: when $q \sim 10^{-2}$, the energy is substantially altered only when the pericentre is very close to $r_{\rm TDE}$. As E decreases, energy modification becomes relevant at larger pericentre, and in the case of $E_0 = 2.6\,\sigma_{\rm inf}^2$ the ejection of the remnant core at $r_p = 1.2\,r_{\rm TDE}$ becomes possible for the (most conservative) case of the non-linear tidal excitation. Moreover, in this case significant changes in E, and in the corresponding value of $q(E)$, are reached up to 2 or 3 $r_{\rm TDE}$.

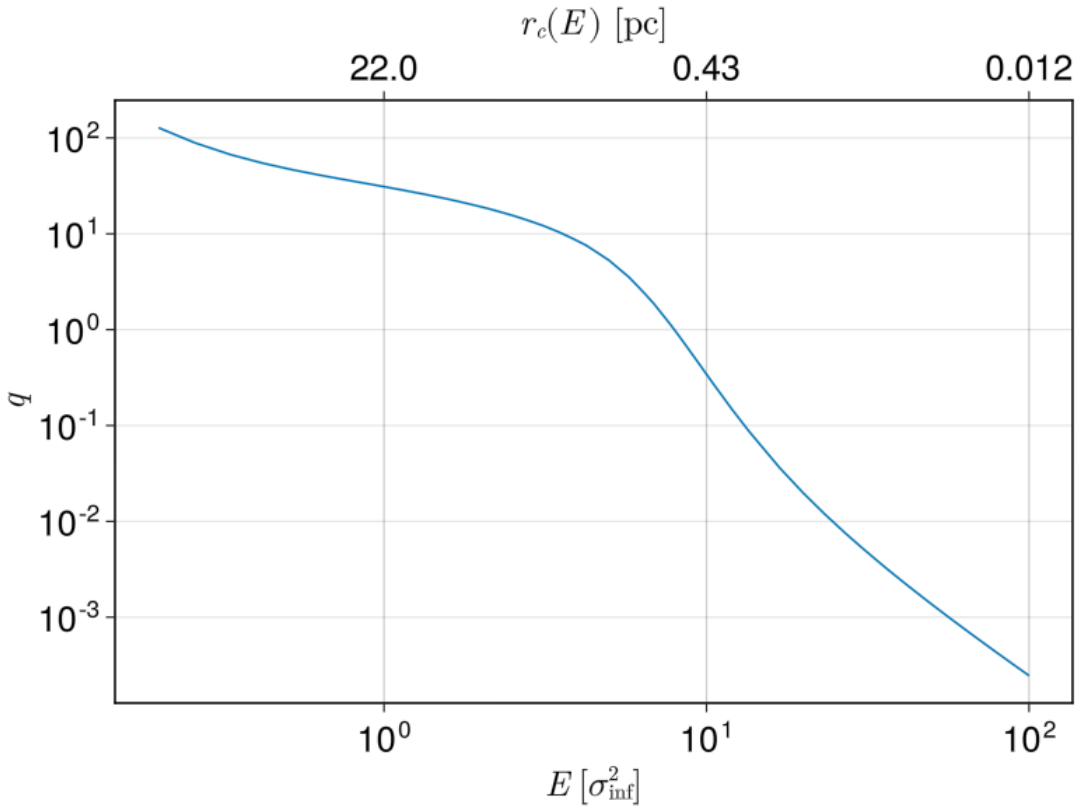

Figure 5.2: The value of the loss cone occupation fraction q as a function of energy (in units of the velocity dispersion at the influence radius) in a system with a central massive black hole of mass $M_\bullet = 4 \times 10^6$. The upper axis shows the value of the radius of the circular orbit at energy E. The details of the stellar distribution are in the text.

Overall, for $r_p \gtrsim 2\, r_{\rm TDE}$ the energy loss due to mass loss dominates over the energy gain due to tidal excitations, disregarding the specific model (linear and non-linear). From this point onward, we take as our fiducial model for tidal excitation the non-linear fit by Generozov et al. (2018); among the alternatives we considered, this is the most conservative choice in terms of energy changes, since can be as strong as $\delta E_{\rm ml}$ at small r_p.

In Fig. 5.4 we show the qualitative effect of single passages at the pericentre as a function of the initial energy E and angular momentum J for our fiducial model; we also report the radius r_c of a circular orbit at energy E for better interpretation. We plot the contours that correspond to $\Delta E/E = -100\%$, $|\Delta E/E| = 10\%$ and $\delta m/m < 1\%$, identifying some notable outcomes.

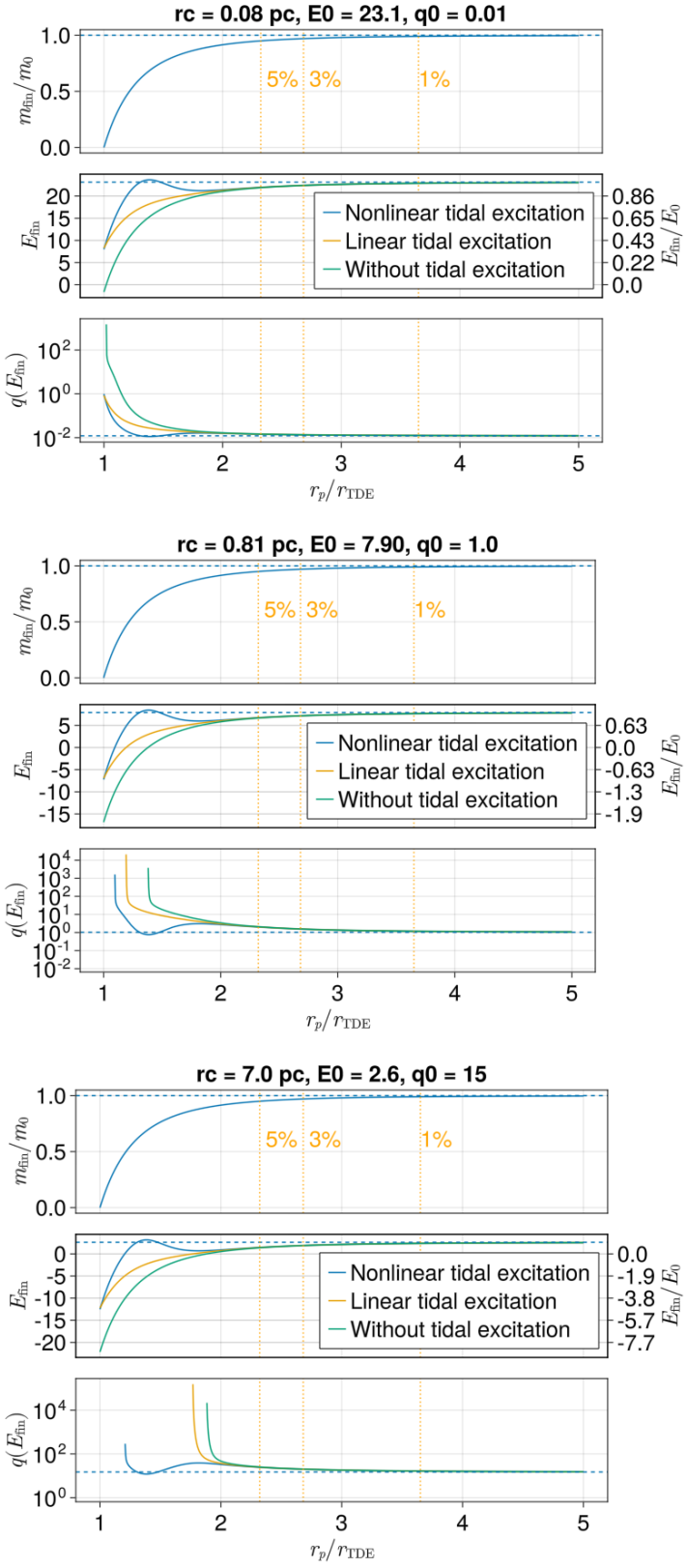

Figure 5.3: Summary of the effects of mass-loss and tidal excitation for a single passage of a partial disruption for a star with different initial energy in the empty (upper figure), intermediate (middle figure) and full (lower figure) loss cone regime. In each figure, the three panels respectively show, as a function of the stellar pericentre divided by the tidal radius, the ratio between the final and the initial mass of the star $m_{\rm fin}/m_0$, the energy after the disruption $E_{\rm fin}$, and the loss cone filling factor for the final energy $q(E_{\rm fin})$ (note that this goes to infinite since for $E_{\rm fin} < 0$ the star gets unbound; the original value of q is marked with a horizontal dashed line). In all plots we show vertical dashed lines at the pericentres corresponding to 1%, 3%, 5% mass stripping.

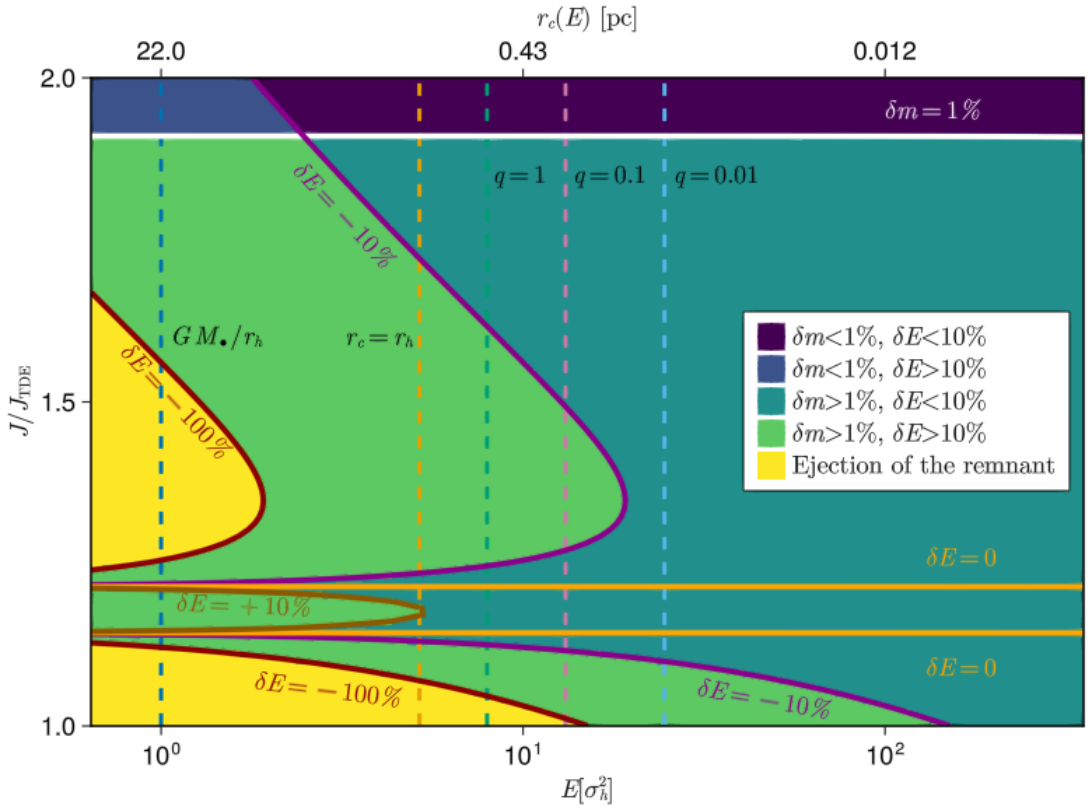

Figure 5.4: Overview of the effect of a single pericentre passage due to tidal excitation and mass-loss in phase space, where we express the angular momentum in units of the critical value $J_{\rm TDE}$ and energy in units of the squared velocity dispersion at the influence radius $\sigma^2_{\rm inf}$. We identify here the regions corresponding to different effects on the orbit: negligible effects ($\delta m < 1\%$, $\delta E < 10\%$), significant change in energy ($|\delta E| > 10\%$ disregarding the mass change) and ejections ($\delta E = -100\%$). We report some values of E that might be of interest through dash lines, and the upper axis shows the corresponding radius of the circular orbit r_c with energy E.

- **Negligible change in the orbit, negligible change in the mass**. This happens when $\Delta E/E < 10\%$ and $\delta m/m < 1\%$. This region includes the vast majority of orbits at $E \gtrsim 100\,\sigma_{\rm inf}^2$ (corresponding to $r_c \lesssim 0.01$ pc) and a significant fraction from $E \gtrsim 25\,\sigma_{\rm inf}^2$ (corresponding to $r_c \lesssim 0.4$ pc). In this region, mass loss is limited, while the initial stellar orbital energy E is very large so that it is hardly affected.

- **Significant change in the orbit.** This happens when $10\% < |\Delta E| < 100\%$ and it is mainly driven by tidal excitation. Typically, it corresponds to $\delta m/m > 1\%$, except for $E \lesssim 3\,\sigma_{\rm inf}^2$ and $r_c \gtrsim 10$ pc. For $r_c > r_{\rm inf}$ a small range of J results in a tighter orbit.

- **Ejection of the remnant.** This happens when $\delta E < -100\%$ and affects orbits with energy $E \lesssim 10\,\sigma_{\rm inf}^2$ and particularly those with $E \lesssim 2\,\sigma_{\rm inf}^2$ and $r_c \gtrsim 10$ pc.

5.3 | Single *vs* Repeated disruptions

We will now try to assess the impact of single and repeated disruptions, first considering the full loss cone regime, where repeated disruptions are unlikely to happen, and then the empty loss cone regime, extending our previous analysis when $N_q > 1$.

5.3.1 | Full loss cone regime

When $q \gtrsim 1$, relaxation acts on timescales shorter than those of partial disruptions. Therefore, the probability of staying on the same orbit and repeat the disruption is small, and virtually negligible since q grows quickly as E decreases (see Fig. 5.2). In this regime, single passages grazing or entering the loss cone radius will alter the orbital parameters once per period P, while the timescale of relaxation in angular momentum is P/q. In this regime, it is possible that partial disruptions mainly result in the ejection of the remnant, and this may be compatible with classical loss cone theory. In fact, since they both imply an instantaneous removal of the subject star from the distribution, ejections can be treated together with total disruptions in the standard approach to loss cone, where particles are removed when they reach a pericentre below a critical value. Therefore, by identifying a suitable, larger threshold radius $r_{\rm LC} > r_{\rm TDE}$ that roughly distinguish the region of Ejections plus Total disruptions, classical loss cone theory may be simply adapted to provide a good description of the system. However, relaxation in this regime is so strong that partial disruptions are very unlikely to repeat in this regime.

5.3.2 | Empty loss cone regime

In the empty loss cone regime, $q \lesssim 1$ and repeated partial disruptions are expected. In fact, the empty loss cone regime is defined as the region of phase space where relaxation needs many orbits to alter significantly the orbital parameters of eccentric orbits.

Since we are interested in understanding whether the classical loss cone theory applies, we need to assess the cumulative effect of repeated partial disruption on the orbits over the local relaxation timescale, that operates in N_q orbits; furthermore, this approach allows us to estimate how many passages a star on a partial disruption orbits manages to complete before being ejected, or surviving the interaction without escaping the system, or being fully disrupted. For $q = \{0.1, 0.01, 0.001\}$ we set up three simulations with the following simple scheme.

1. We set the initial energy E_0 corresponding to the chosen q. We set the initial mass to $m_\star$ and the initial angular momentum $J_0 \in [J_{\rm TDE}, 5\,J_{\rm TDE}]$, where $J_{\rm TDE}$ is the angular momentum of the orbit whose pericentre is $r_{\rm TDE}$.

2. We compute the pericentre r_p and use Eq. (5.8) to determine the mass lost at each pericentre passage.

3. We use Eq. (5.11) and Eq. (5.12) to compute the total energy variation

$$\delta E = \delta E_{\rm ml} + \delta E_{\rm tid} \tag{5.15}$$

4. We compute the new mass $m_\star$, the new tidal disruption radius $r_{\rm TDE}$, and the new energy E.

We repeat steps $2-4$ until **total disruption** ($r_p < r_{\rm TDE}$), **ejection** ($E < 0$), or **survival** (*i.e.* the star completes N_q orbits). For each value of q we choose 30 equally spaced values in $\log J$

$$\log J_i = x_0 + i\,\delta \qquad i = 0 \ldots 29 \tag{5.16}$$

with $x_0 = (\log 5)/60$ and $\delta = (\log 5)/30$.

We treat $r_\star = 1 r_\odot$ as a fixed parameter throughout the evolution, since modelling the readjustment of the star requires to directly solve the complex hydrodynamic evolution of the stellar structure[3]. Finally, we remark that this procedure implies that the specific angular momentum is constant throughout the repeated disruptions.

[3]While we are considering orbital periods of at most 10^4 yr, much less than the Kelvin-Helmholtz timescale(1 Myr, Binney and Tremaine (2008)), dramatic mass loss and strong tidal excitations may indeed be relevant over the orbital period timescale

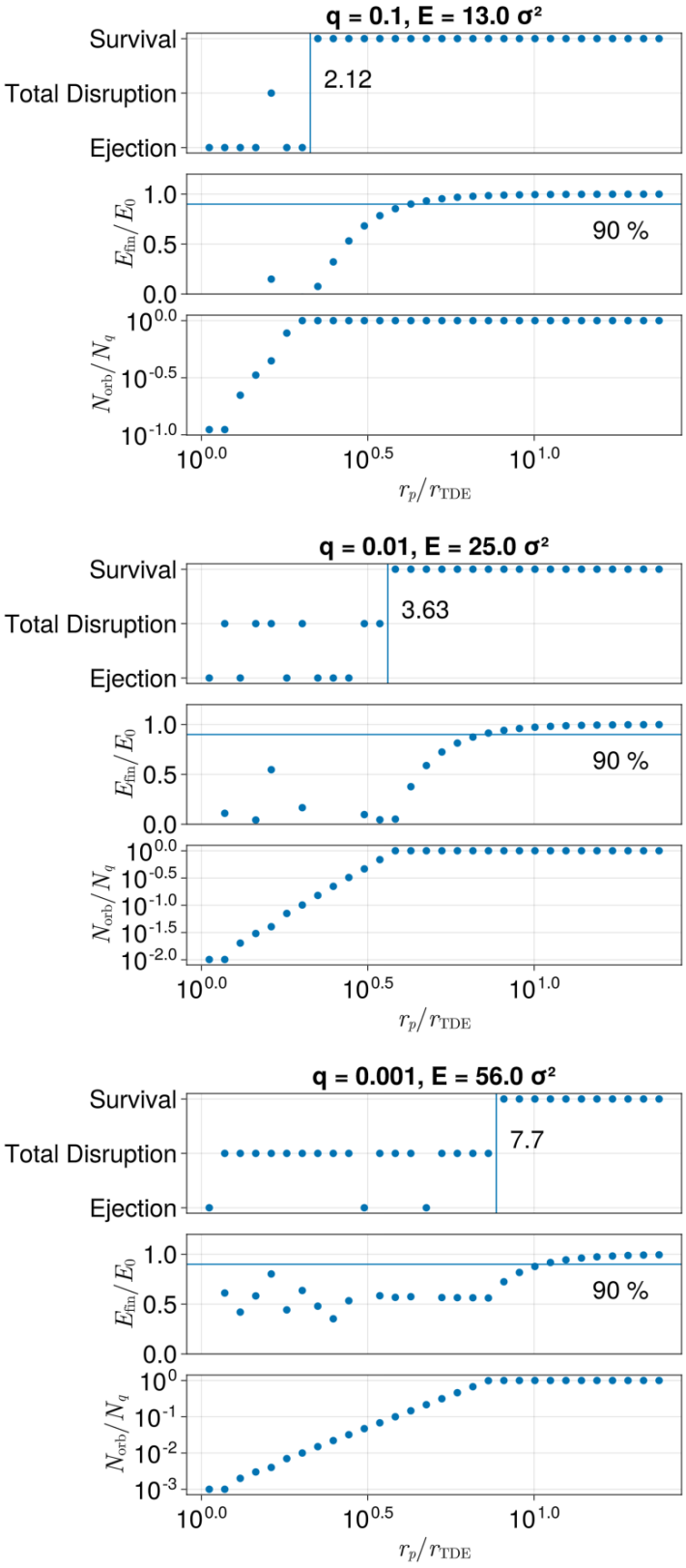

Figure 5.5: Effects of repeated partial disruptions with initial pericentre r_p (in units of $r_{\rm TDE}$) according to our simple step-by-step evolution for $q = 0.1$ (upper figure), $q = 0.01$ (middle figure) and $q = 0.001$ (lower figure); the corresponding energy for our fiducial model is also reported in units of $\sigma^2_{\rm inf}$. In the upper panel of each figure we show the outcome of particles completing less than $N_q = 1/q$ orbits, distinguishing between total disruptions ($r_p < r_{\rm TDE}$) and ejections ($E_{\rm fin} < 0$); we dub as survival the stars that complete N_q orbits. In the middle panel, we report the ratio between the final and initial energy, marking the 90% line for reference. In the lower panel, we show the number of completed orbits in units of N_q. In all cases, surviving particles show significant energy decrease, with $E_{\rm fin} = 90\%\, E_0$ at $r_p \simeq 4\, r_{\rm TDE}$ with $q = 0.1$, $r_p \simeq 6\, r_{\rm TDE}$ with $q = 0.01$ and $r_p \simeq 10\, r_{\rm TDE}$ with $q = 0.001$.

In Fig. 5.5 we show the results of our simulations by reporting the outcome, the final energy and the number of repeating partial disruption orbits for each simulation as a function of its initial pericentre r_p. In all the three cases, there is an effective larger radius where a particle gets disrupted or ejected over the timescale of relaxation: $r_p/r_{\rm TDE} \simeq \{2,\ 4,\ 8\}$ respectively. As argued before, these two classes of events can be commonly treated with classical loss cone theory with a suitable choice of $r_{\rm LC}$, given that they will stop participating diffusion.

However, the results of our simulations show a more complex situation, where the presence of the loss cone decreases the energy of the particles, thanks to the repeated disruptions, up to large values of the initial pericentre, $r_p \simeq 4\,r_{\rm TDE}$, $r_p \simeq 6\,r_{\rm TDE}$ and $r_p \simeq 10\,r_{\rm TDE}$ in the three cases. This unfortunately invalidates the assumption that eccentric orbits mainly evolve in eccentricity at fixed energy; as we have shown, over the timescale of relaxation objects grazing the loss cone alter their orbital energy significantly.

5.4 | Discussion and conclusions

In the first section of this chapter, we discussed the inclusion of the phenomenon of partial disruptions in classical loss cone theory through a suitable choice of the loss cone radius. We have seen how to compute in such a framework the expected fraction of total disruptions, partial disruptions and repeated partial disruptions. The specific value of this threshold radius can be related to the mass fraction lost at the first pericentre passage, and we have shown that

- The rate of total disruptions in systems dominated by loss cone events happening in the empty loss cone regime can be significantly overestimated by classical loss cone theory.

For a system with $M_\bullet = 4 \times 10^6\,M_\odot$, a larger $r_{\rm LC}$ corresponding to a mass loss of 3% predicts an overestimation of the order of 10. An expanded version of what reported in this chapter, assessing how different properties of galactic nuclei affect the relative rate of partial and total disruptions, can be found in Bortolas et al. (2023).

The second part of the chapter was devoted to some preliminary results towards extending the model of tidal disruptions at the base of classical loss cone theory with a model of partial disruptions that accounts for the decrease of the orbital binding energy due to mass loss $\delta E_{\rm ml}$, and its increase due to tidal excitations $\delta E_{\rm tid}$. The possibility of repeated disruptions is then explored in the empty loss cone regime, assessing the

impact on orbits grazing the loss cone radius repeatedly before they are moved to a different orbit by the stochastic interactions of two-body relaxation. The main findings can be summarized as follows:

- For pericentres very close to or much larger than the (total) tidal disruption radius, the effect of mass loss is stronger than that of tidal excitations. Only in the non-linear regime $\delta E_{\rm tid}$ competes relevantly with $\delta E_{\rm ml}$, with its maximum effect around $r_p \simeq 1.3 r_{\rm TDE}$ where it can increase the binding energy.
- In agreement with the previous point, in the full loss cone regime, a large fraction of partial disruptions may result in ejections of the remnant.
- In the empty loss cone regime, the cumulative effect of repeated partial disruptions over the local relaxation timescale can affect the energy of stars with pericentre larger than $r_{\rm TDE}$, where tidal excitations are subdominant and mass loss is responsible for binding energy losses.

While the full loss cone regime can be treated with good approximations by classical loss cone theory with a larger value of $r_{\rm LC}$ (depending on the energy considered), in the empty loss cone regime the treatment of classical loss cone theory is inadequate for the computation of the rates.

In fact, the non-negligible decrease of the orbital binding energy calls for the inclusion of the process into the diffusion coefficients, similarly to what is done for gravitational waves emission in the case of EMRIs. However, there is a deep difference between the two mechanisms: in the case of PTDEs, stars are pushed to regions where q is larger, where the chances of being perturbed and leave the regions immediately close to the loss cone are greater; in the case of EMRIs, the emission of gravitational waves pushes the compact object towards regions of the nucleus with smaller q, where relaxation becomes more and more inefficient.

A general result of this chapter is that the classical theory of loss cone for extended objects needs to be revised to include the phenomenon of partial disruptions. Systems currently expected to produce most of TDEs in the empty loss cone regime will likely see a suppression in the predicted rate.

6

Improved boundary conditions for the orbit averaged equation

Like all walls it was ambiguous, two faced.
What was inside it and what was outside it depended upon which side you were on.
— *Ursula K. Le Guin, The Dispossessed: An Ambiguous Utopia*

In this chapter is shown my preliminary work on the limits of the solution by Cohn and Kulsrud (1978) when determining the expected relaxed distribution in angular momentum at fixed energy. 2D solutions show strong deviations from the expected logarithmic trend in $\mathcal{R}$ as $\mathcal{R} \to \mathcal{R}_{\rm LC}$, and this is due to a non-negligible contribution to the flux entering the loss cone from the cross term. A new version of the local Fokker-Planck equation will be derived, in order to solve the dynamics of particles inside the loss cone and match the solution of the orbit averaged equation at the loss cone interface. The last part of the chapter shows the first attempts towards defining revised boundary conditions for the orbit averaged FP equation and some preliminary results on the impact on the loss cone rates. These results will be the main body of a publication currently in preparation.

6.1 | Quasi stable profile in angular momentum

By using the integrator for the orbit averaged Fokker-Planck equation, one can test and review some of the classical results of loss cone theory. Among these, a special role is played by the prediction of the relaxed profile in angular momentum of particles at a given energy E, that allows to connect the simpler treatment of the ergodic Fokker-Planck equation with the expected rates of loss cone phenomena, including TDE rates

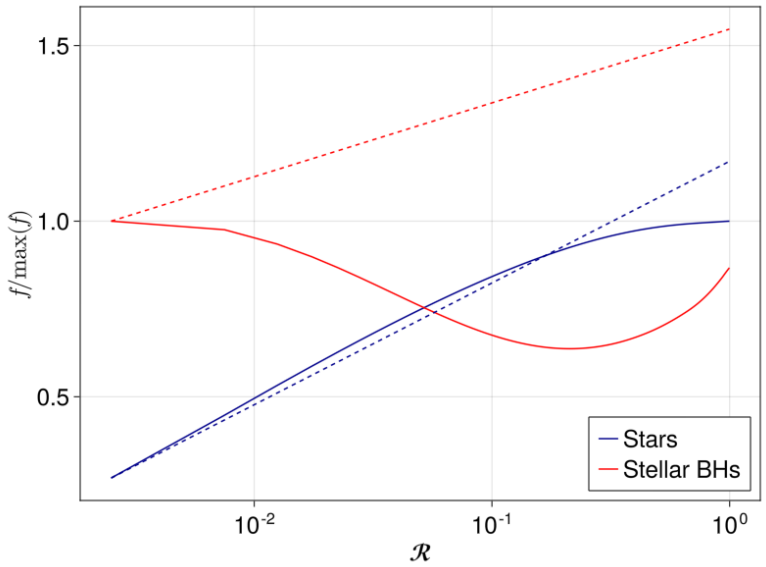

Figure 6.1: The angular momentum distribution for stars (solid blue line) and stellar black holes (solid red line) at the influence radius for a fiducial model with $M_\bullet = 10^6\, M_\odot$. Stars have a trend compatible with the Cohn-Kulsrud asymptotic profile (dashed blue line) for low values of $\mathcal{R}$; stellar black holes show significant deviations from the corresponding expected trend (dashed red line).

and EMRI rates. This motivated us towards testing this basic assumption, by directly checking the relaxation process in angular momentum for some systems.

In Fig. 6.1 we show the distribution at the influence radius (that is the energy such that $r_c(E) = r_h \simeq 1$ pc) at $t = 10$ Gyr. This time is larger than the relaxation timescale in energy (that for this system is of the order of 0.5 Gyr, see Tab. 4.3).

The reason why the stellar black holes do not relax towards the Cohn-Kulsrud distribution resides in the fact that the cross term $\mathcal{D}_{ER}\,\partial_E f$ is not negligible with respect to $\mathcal{D}_{RR}\,\partial_{\mathcal{R}}$.

Unfortunately, one cannot extend the derivation of the standard Cohn-Kulsrud profile inside the loss cone – needed to derive the function $\mathcal{R}_0(E)$ – to include the cross term. The structure of the local Fokker-Planck equation 3.13 is not compatible with a boundary condition that smoothly joins the solution inside the loss cone with the solution of the orbit averaged FP equation, and considering more than one contribution to the flux along $\mathcal{R}$.

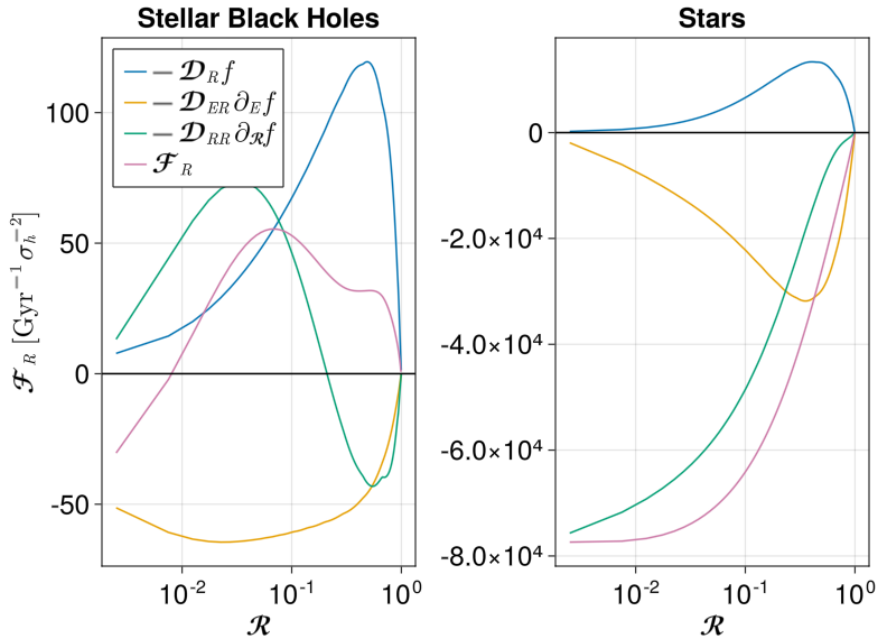

Figure 6.2: Contribution to the total flux in $\mathcal{R}$ at the influence radius for stellar black holes (left) and stars (right). We can see that in the case of compact objects, the contributions of $-\mathcal{D}_{ER}\,\partial_E f$ (orange line) is non-negligible with respect to the contribution of $-\mathcal{D}_{RR}\,\partial_{\mathcal{R}} f$ (green line) at small values of $\mathcal{R}$. The third contribution $-\mathcal{D}_R\, f$ is subdominant in this regime.

6.1.1 | The Jeans compatible Fokker-Planck equation

In the derivation of the Cohn-Kulsrud relaxed profile in angular momentum, we were able to match the steady state solution of the local Fokker-Planck equation with the value $f_{\mathcal{R}}(E)$ coming from the solution of the orbit averaged equation, meaning that it had no explicit dependence on r. This was possible because, in the steady configuration, we were considering only one contribution in the flux

$$v_r \frac{\partial f}{\partial r} = \frac{\partial}{\partial \mathcal{R}} \left[D_{RR}(E,r) \frac{\partial}{\partial \mathcal{R}} f \right] \tag{6.1}$$

and inserting $f = f(E,\mathcal{R})$, one can find a solution that does not explicitly depend on r if and only if D_{RR} is separable; and this is the case as shown in Eq. (3.10). If one tries to go to the next order in $\mathcal{R}$, and has to include other terms in the expansion such as the D_{ER} term, then one would have to solve an equation of the form

$$v_r \frac{\partial f}{\partial r} = \frac{\partial}{\partial \mathcal{R}} \left[D_{RR}(E,r) \frac{\partial}{\partial \mathcal{R}} f(E,\mathcal{R},r) + D_{ER} \frac{\partial}{\partial E} f(E,\mathcal{R},r) \right] \tag{6.2}$$

and given that D_{RR} and D_{ER} have a different dependence on r, the only solution to the equation that is independent on r is the trivial solution $f = 0$, that of course cannot match any solution different from zero in the orbit averaged equation.

From the local Fokker-Planck equation, however, it is possible to build an equation that is compatible with Jeans' theorem (that is, solutions can be independent on r), that not enforce this form and can account for more than one contribution to the flux along $\mathcal{R}$. The procedure is conceptually simple: we retain only the part of each coefficient that does not depend on r. In fact, we can decompose each diffusion coefficient as

$$\tilde{D}_x = \frac{\mathcal{D}_x(E,R)}{\mathcal{J}} + d_x(E,\mathcal{R},r) \tag{6.3}$$

.

Given the definition of $\mathcal{D}_x$, which is proportional to the orbital integral of the diffusion coefficients, it is clear that

$$\int_{r_-}^{r_+} \frac{dr}{v_r}\, d_x(E,\mathcal{R},r) = 0\,. \tag{6.4}$$

Inserting this expansion in the local Fokker-Planck equation (we remind here that $\boldsymbol{\nabla}$ acts on $(E,\mathcal{R})$ only):

$$\frac{d}{dt}f = \boldsymbol{\nabla}\cdot\frac{\boldsymbol{\mathcal{F}}}{\mathcal{J}}(E,\mathcal{R}) + \boldsymbol{\nabla}\cdot\boldsymbol{dF}(E,\mathcal{R},r) \tag{6.5}$$

given the formal linearity of the flux over its coefficients. Since the term at the right-hand side explicitly depends on r, it is clear that the local Fokker-Planck equation has no solutions that do not depend explicitly on r. In order to allow for the distribution to have Jeans' form (i.e. to not depend explicitly on r, as prescribed by Jeans' theorem for collisionless system; Binney and Tremaine, 2008), we will describe the phase space inside the loss cone according to what we may call the *Jeans compatible Fokker-Planck equation*

$$\frac{d}{dt}f^x(E,\mathcal{R},r,t) = \boldsymbol{\nabla}\cdot\frac{\tilde{\boldsymbol{F}}^{\boldsymbol{x}}}{J}(E,R,r) \tag{6.6}$$

where

$$\tilde{\boldsymbol{F}}^{\boldsymbol{x}} = \begin{pmatrix}\tilde{F}^x_E\\ \tilde{F}^x_R\end{pmatrix} = -\begin{pmatrix}\mathcal{D}_{\mathrm{EE}}\,\partial_E f^x + \mathcal{D}_{\mathrm{ER}}\,\partial_{\mathcal{R}} f^x + \mathcal{D}_{\mathrm{E}}\, f^x\\ \mathcal{D}_{\mathrm{RE}}\,\partial_E f^x + \mathcal{D}_{\mathrm{RR}}\,\partial_{\mathcal{R}} f^x + \mathcal{D}_{\mathrm{R}}\, f^x\end{pmatrix}. \tag{6.7}$$

for $x = \{\mathrm{in},\mathrm{out}\}$. The solutions of this equation include functions with an explicit dependence on r, and functions that are constant in r.

6.2 | The cross term in the boundary conditions

We will now consider in detail the consequences of adding the cross term to the derivation of the relaxed profile in angular momentum.

6.2.1 | The cross term

The reason why the picture by Cohn and Kulsrud (1978) breaks down is that the $\mathcal{D}_{RR}$ term in the orbit averaged solution is not dominant for small $\mathcal{R}$. Indeed, for small $\mathcal{R}$ the flux of the orbit averaged equation is significantly contributed by the cross term $\mathcal{D}_{ER}$, due to the local coefficient D_{ER}. In fact, for $\mathcal{R} \to 0$

$$D_{RR} \sim \frac{2}{3} \left[2\, F_0(E) + 3F_1(E,r) - F_2(E,r)\right] \frac{r^2}{J_c^2}\, \mathcal{R} \tag{6.8}$$

$$D_{E\mathcal{R}} \sim \frac{2}{3} \left[\frac{v^2}{v_c^2} - 1\right] \left(F_0(E) + F_2(E,r)\right) \mathcal{R}\,. \tag{6.9}$$

At fixed E and $\mathcal{R}$, we can see that the two coefficients have a different trend in r, thanks to the terms r^2 and $v^2 = 2(\phi(r) - E)$. Since the pericentre r_- goes to zero when $\mathcal{R} \to 0$, the cross term close to the pericentre is asymptotic to

$$D_{ER} \sim \frac{8}{3} \frac{a}{v_c^2} \frac{G\, M_\bullet}{r} \qquad r \to r_-, \quad \mathcal{R} \to 0\,. \tag{6.10}$$

Its orbital integral may estimated by assuming the Keplerian potential due to the supermassive black hole. The expansion of $v_r \sim v$ around r_-

$$\frac{v^2}{2} = \phi(r) - E \simeq \phi'(r_-)\,(r - r_-) \qquad r \to r_-, \quad \mathcal{R} \to 0 \tag{6.11}$$

and inserting it in the computation of $\mathcal{D}_{ER}$ we get

$$\begin{aligned} \mathcal{D}_{ER} &\sim \frac{8\sqrt{2}}{3}\, \pi^2\, G\, M_\bullet\, r_c^2 \int_{r_-}^{r_+} \frac{dr}{r\sqrt{\phi'(r_-)(r - r_-)}} \\ &\sim \frac{16}{3}\, \pi^3 \sqrt{\frac{G\, M_\bullet\, J_c^2}{E}}\, r_c^2\, \sqrt{R} \qquad\qquad \mathcal{R} \to 0. \end{aligned} \tag{6.12}$$

The orbit average of D_{RR} retains the linear trend in $\mathcal{R}$. For small $\mathcal{R}$ we can write $\mathcal{D}_{ER}\partial_E f_E \sim A(E)\sqrt{\mathcal{R}}$ and $\mathcal{D}_{RR} \sim B(E)\,\mathcal{R}$, and the flux $\mathcal{F}_\mathcal{R}$ in the orbit averaged equation can be written as

$$\mathcal{F}_\mathcal{R} \simeq A\sqrt{\mathcal{R}} f + B\mathcal{R}\, \frac{\partial}{\partial R} f\,. \tag{6.13}$$

whose constant-flux solutions are

$$f = \left[c - \frac{\mathcal{F}_\mathcal{R}}{B} \int_\mathcal{R}^1 dx \frac{e^{2\beta\sqrt{x}}}{x}\right] e^{-2\beta\sqrt{\mathcal{R}}} \tag{6.14}$$

where $\beta = A/B$.

6.2.2 | The local equation with cross terms

The Jeans compatible FP equation Eq. 6.6 becomes, in the limit of small $\mathcal{R}$

$$\mathcal{J}\, v_r \frac{\partial}{\partial r} f^i = \frac{\partial}{\partial \mathcal{R}} \left[A \sqrt{\mathcal{R}}\, f + B\, \mathcal{R}\, \frac{\partial}{\partial R} f \right] . \tag{6.15}$$

and it can be rewritten as

$$P\, v_r \frac{\partial}{\partial r} f^i = \frac{\partial}{\partial \mathcal{R}} \left[\frac{A}{4\pi^2 J_c^2} \sqrt{\mathcal{R}}\, f + \frac{B}{4\pi^2 J_c^2} \mathcal{R}\, \frac{\partial}{\partial R} f \right] . \tag{6.16}$$

As we did in the case of the classical Cohn-Kulsrud solution, we define a variable to describe the particle along the orbit (outwards and inwards):

$$\tau(r) = \begin{cases} \frac{1}{P} \int_{r_-}^{r} \frac{dr}{v_r} & \text{out} \\ 1 - \frac{1}{P} \int_{r_-}^{r} \frac{dr}{v_r} & \text{in} \end{cases} \tag{6.17}$$

so that the function

$$f(\tau, R) = \begin{cases} f^{\text{out}}(r, E, \mathcal{R}) & 0 < \tau < \frac{1}{2} \\ f^{\text{in}}(r, E, \mathcal{R}) & \frac{1}{2} < \tau < 1 \end{cases} \tag{6.18}$$

summarizes the two branches. The boundary conditions in the domain of interest ($0 < \tau < 1,\ 0 < \mathcal{R} < \mathcal{R}_{\max}$ with $\mathcal{R}_{\max} \gtrsim \mathcal{R}_{\text{LC}}$) are:

- $f(\tau, \mathcal{R}_{\max}) = f_{\max}$ matching the orbit-averaged solution
- $f(0, \mathcal{R}) = 0$ for $\mathcal{R} < \mathcal{R}_{\text{LC}}$
- $f(0, \mathcal{R}) = f(1, \mathcal{R})$ for $\mathcal{R}_{\text{LC}} < \mathcal{R} < \mathcal{R}_{\max}$
- f smooth at $\tau = 1/2$
- $F_{\mathcal{R}}(\tau, 0) = 0$

and the equation itself is written as

$$\frac{\partial}{\partial \tau} f = \frac{\partial}{\partial \mathcal{R}} \left[\frac{A}{4\pi^2 J_c^2} \sqrt{\mathcal{R}}\, f + \frac{B}{4\pi^2 J_c^2} \mathcal{R}\, \frac{\partial}{\partial R} f \right] . \tag{6.19}$$

In order to study the solution of the equation parametrically, we introduce the parameter

$$p = \frac{A}{4\pi^2 J_c^2 \sqrt{R_{\text{LC}}}} \tag{6.20}$$

and the equation can be rewritten as

$$\frac{\partial}{\partial\tau}f = \mathcal{R}_{\rm LC}\,\frac{\partial}{\partial\mathcal{R}}\left[p\sqrt{\frac{\mathcal{R}}{\mathcal{R}_{\rm LC}}}\,f + q\mathcal{R}\,\frac{\partial}{\partial\mathcal{R}}f\right]. \tag{6.21}$$

Rescaling variable to $y = \mathcal{R}/\mathcal{R}_{\rm LC}$

$$\frac{\partial}{\partial\tau}f = \frac{\partial}{\partial y}\left[p\,\sqrt{y}\,f + q\,y\,\frac{\partial}{\partial y}f\right]. \tag{6.22}$$

Since the function can be freely rescaled, p and q are the sole parameters affecting the solution.

In the $|p| \ll q$ limit, the equation recovers the standard solution of Cohn-Kulsrud. In the $|p| \gg q$ limit, under the following transformation

$$x = \sqrt{y} \quad f = \frac{g}{x} \tag{6.23}$$

the equation can be mapped into the simple advection equation

$$\frac{\partial}{\partial\tau}\,g = \frac{p}{2}\,\frac{\partial}{\partial x}g \tag{6.24}$$

whose general solution is $g = g(\tau + 2\,x/p)$.

Following the classical solution, we set $\mathcal{R}_{\rm max}$ and see if we can find the solution to the equation. The boundary conditions set $g(\tau = 0, x) = 0$ and $g(\tau, x = 1) = f_{\rm LC}$, and the functional form of g through $z = \tau + 2\,x/p$ propagates these value to all the (τ, x) space. When p is negative, one cannot impose both the boundary conditions. In fact, the argument z of the function g assumes the values

$$\tau{=}\ 0 \text{ boundary}: \qquad -\frac{2}{|p|} < z < 0 \tag{6.25}$$

$$\text{x} = 1 \text{ boundary}: \qquad -\frac{2}{|p|} < z < -\frac{2}{|p|} + 1 \tag{6.26}$$

$$\tag{6.27}$$

and the value of the function in the two intervals cannot be set independently. When p is positive, on the other hand, the situation is different

$$\tau{=}\ 0 \text{ boundary}: \qquad 0 < z < \frac{2}{|p|} \tag{6.28}$$

$$\text{x} = 1 \text{ boundary}: \qquad \frac{2}{|p|} < z < \frac{2}{|p|} + 1 \tag{6.29}$$

$$\tag{6.30}$$

and one can apply the boundary conditions we are considering, obtaining

$$f(E,y,r) = \begin{cases} \frac{f_{\mathrm{LC}}}{\sqrt{y}} & \tau + 2\frac{\sqrt{y}}{p} > \frac{2}{p} \\ 0 & \tau + 2\frac{\sqrt{y}}{p} < \frac{2}{p} \end{cases} \tag{6.31}$$

Unfortunately, this solution is discontinuous at $\tau = 1/2$ and, more importantly, the large value of p imply a non-vanishing flux at $y = 0$, that corresponds to $\mathcal{R} = 0$.

The case $|p| \gg q$ with the boundary conditions for our problem needs therefore to be solved through the complete partial differential equation Eq. 6.22. We could not find an analytical solution to the general case, so we solved the differential equation numerically to explore the space of parameters.

6.3 | Numerical solution of the equation inside the loss cone

We solved Eq. (6.6) on a discrete grid in the (τ, y) space with dimension $N_\tau \times N_y$. We discretized the left-hand side and the right-hand side, reducing the problem to the form

$$\mathfrak{A} \cdot \mathfrak{f} = \mathfrak{b} \tag{6.32}$$

where $\mathfrak{f}$ is the coordinate vector with respect to the matrix basis

$$(e_i)_{j,k} = \delta_{j,i \div N_\tau}\, \delta_{k,i\%N_\tau} \quad f = \sum_i \mathfrak{f}_i\, e_i \tag{6.33}$$

where $\delta_{i,j}$ is the Kronecker delta, $\div$ indicates the result of integer division and $\%$ its modulus. The vector $\mathfrak{b}$ is determined by the boundary conditions.

Please note that this method is expected to fail in the limiting case when $|p|$ is too large with respect to q. In this case, the matrix $\mathfrak{A}$ becomes singular since the problem reduces to the advection equation, which is not compatible with the boundary conditions as we have shown in the previous section. However, this does not happen in the range of parameters we present here.

As a test, we compare the solution obtained numerically for the $p = 0$ case against the expected solution. More in detail, we compare the function $\alpha = \log(\mathcal{R}_{\mathrm{LC}}/\mathcal{R}_0)$ as a

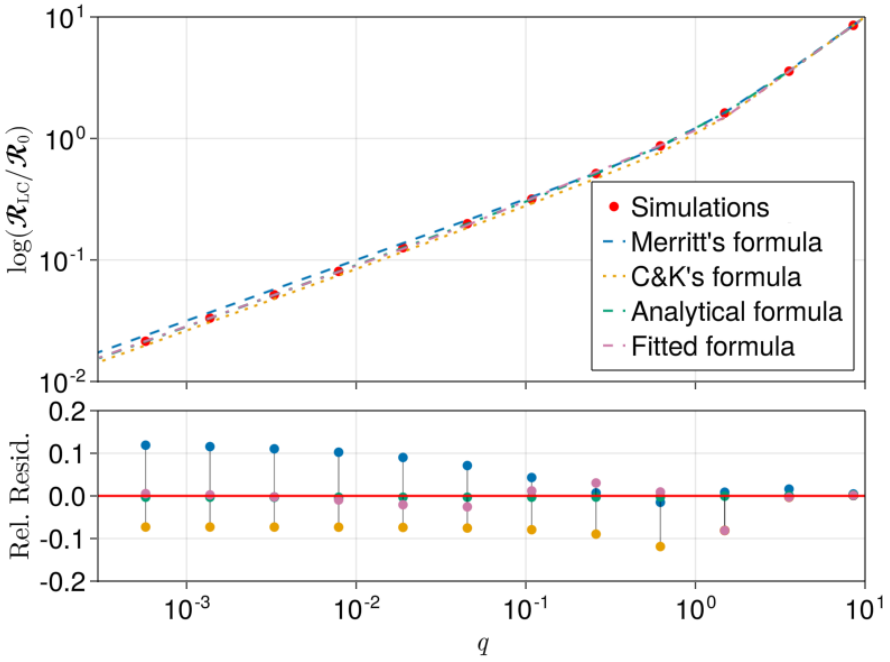

Figure 6.3: Estimate of $\alpha = \log(\mathcal{R}_{\rm LC}/\mathcal{R}_0)$ as a function of q obtained by solving the equation with our numerical method, by using the analytical expectation and the formulas by Merritt and Cohn&Kulsrud. We also include the case $p = 0$ of the general fit (*fitted formula* in the legend) that holds for any value of p and derived in the next Section.

function of q against three estimates

$$\text{Analytical}: \quad \alpha_{MM} = q \left[1 - 4 \sum_{m=1}^{\infty} \frac{e^{-\alpha_m^2 q/4}}{\alpha_m^2}\right]^{-1} \tag{6.34}$$

$$\text{Merritt's formula}: \quad \alpha_{MV} = \sqrt[4]{q^2 + q^4} \tag{6.35}$$

$$\text{C\&K's formula}: \quad \alpha_{CK} = \begin{cases} q & q \geq 1 \\ 0.186\, q + 0.824\, \sqrt{q} & q < 1 \end{cases} \tag{6.36}$$

where α_k is the k-th zero of the Bessel function of first kind with $J_0(x)$.

6.3.1 | Overview of the solutions

In Fig. (6.4) we show the contour plots of the solutions of Eq. (6.6) by setting the function to a constant value (in τ) at $y = 2$ and rescaling the obtained solution so that

$$\bar{f}(y) \equiv \int_0^1 d\tau\, f(\tau, y) = 1 \qquad \text{at} \quad y = 1\,. \tag{6.37}$$

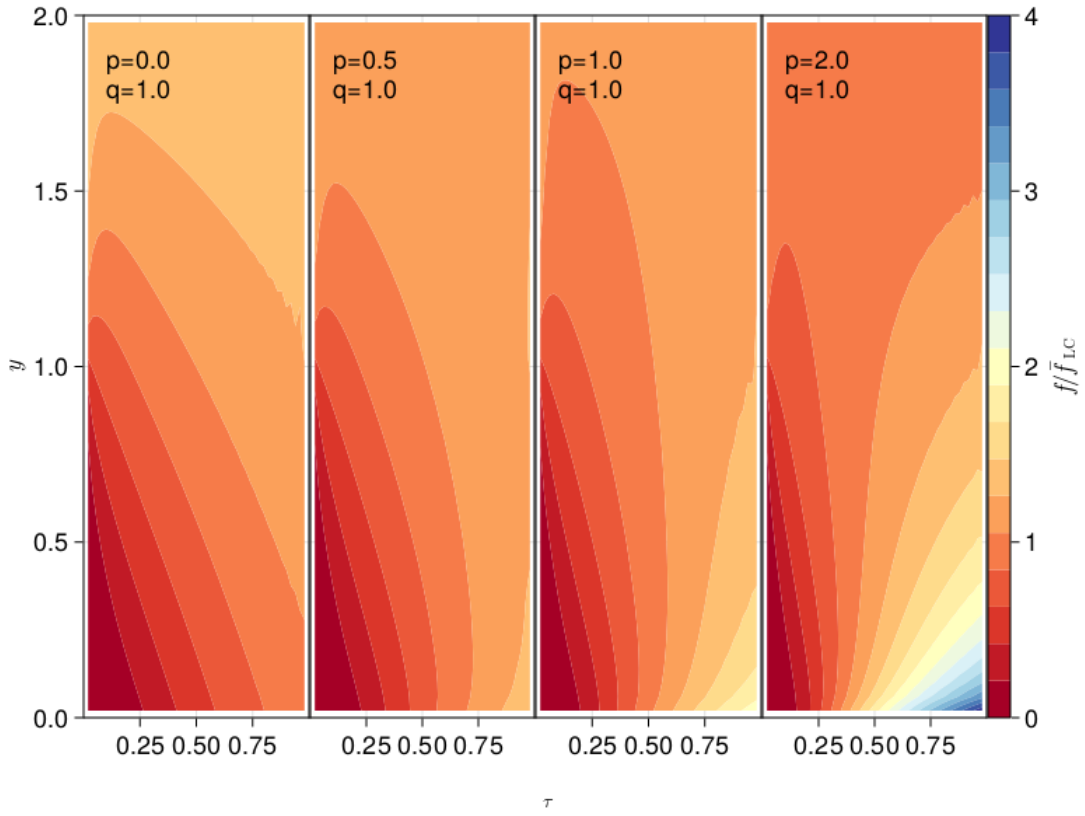

Figure 6.4: Contour plots of the solutions inside the loss cone in the plane $(\tau, y = \mathcal{R}/\mathcal{R}_{\rm LC})$. We set $q = 1$ and $p = \{0,\ 0.5,\ 1,\ 2\}$ and $\mathcal{R}_{\rm max} = 2\,\mathcal{R}_{\rm LC}$. The solutions have been rescaled to their average value in τ at $\mathcal{R} = \mathcal{R}_{\rm LC}$. The advective effect of the cross term accumulates stars inside the region and favours captures at low $\mathcal{R}$, meaning high eccentricities.

The result corresponding to $q = 1$ are reported in Fig.6.4. As p increases, the derivative of the function at $\tau = 1$ increases, effectively transitioning from a bias towards higher angular momentum to the opposite bias towards captures on radial orbits.

In Fig. 6.5 we show the solution inside and outside the loss cone, by solving the equation in the domain $0 < \mathcal{R} < 10\,\mathcal{R}_{\rm LC}$ with periodic boundary conditions for τ outside the loss cone $\mathcal{R} > \mathcal{R}_{\rm LC}$. We show the performance of extrapolating the main solution at $\mathcal{R} \sim 10\,\mathcal{R}_{\rm LC}$ with a function of the Cohn-Kulsrud form $c_1\, log\mathcal{R} + c_2$ or its generalisation Eq. 6.14, as it is typically performed in numerical solutions in order to apply the boundary conditions[1]. For higher values of p, the Cohn-Kulsrud extrapolations system-

[1]We remark that our code presented in Chapter 4 matches the function at the grid point $\mathcal{R}_i$ with the Cohn-Kulsrud by imposing the slope of the partial derivative. This approach is equivalent to the extrapo-

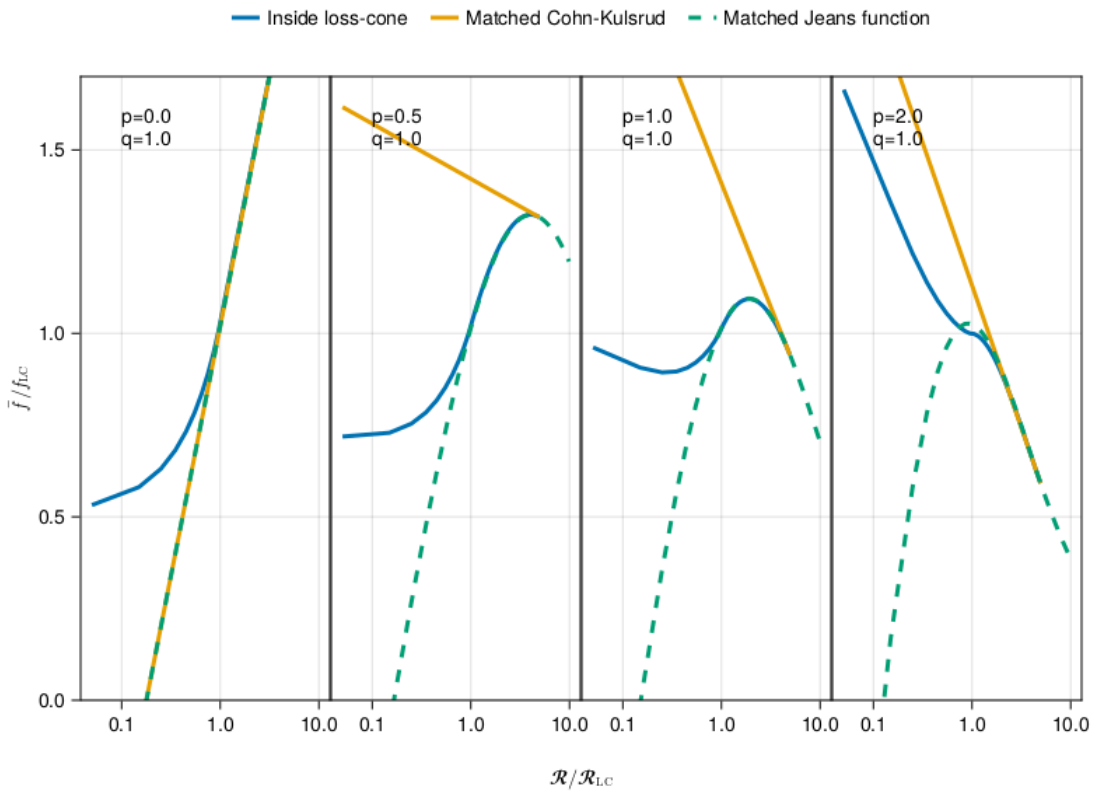

Figure 6.5: Performance of the matched Cohn-Kulsrud profile, that is the logarithmic profile matching the function and its derivative according to Cohn-Kulsrud prescription, and the corresponding solution from Eq. (6.14). Despite its better performance, the predicted value at small $\mathcal{R}$ starts to differ from the real solution with $p \neq 0$ because the effects of the cross term are perceived farther away from the $y = 1$ region.

atically predict larger values of the distribution $f_{\rm LC}$ at the loss cone due to the negative derivative.

6.3.2 | Boundary condition for the orbit-averaged FP equation

In Fig. 6.6 we show the flux of disruptions as a function of p/q. We see that for any value of p/q the asymptotic trends at $q \to 0$ and $q \to \infty$ recover the asymptotic trends of the standard Cohn-Kulsrud solution. We now extract from this set of solutions an analytical prescription for setting the generic boundary conditions in terms of p and q in the orbit averaged Fokker-Planck formalism.

lation discussed here when the main solution follows a Cohn-Kulsrud, but imposes the expected value of $\mathcal{R}_0$ even when the distribution does not approach the loss cone logarithmically.

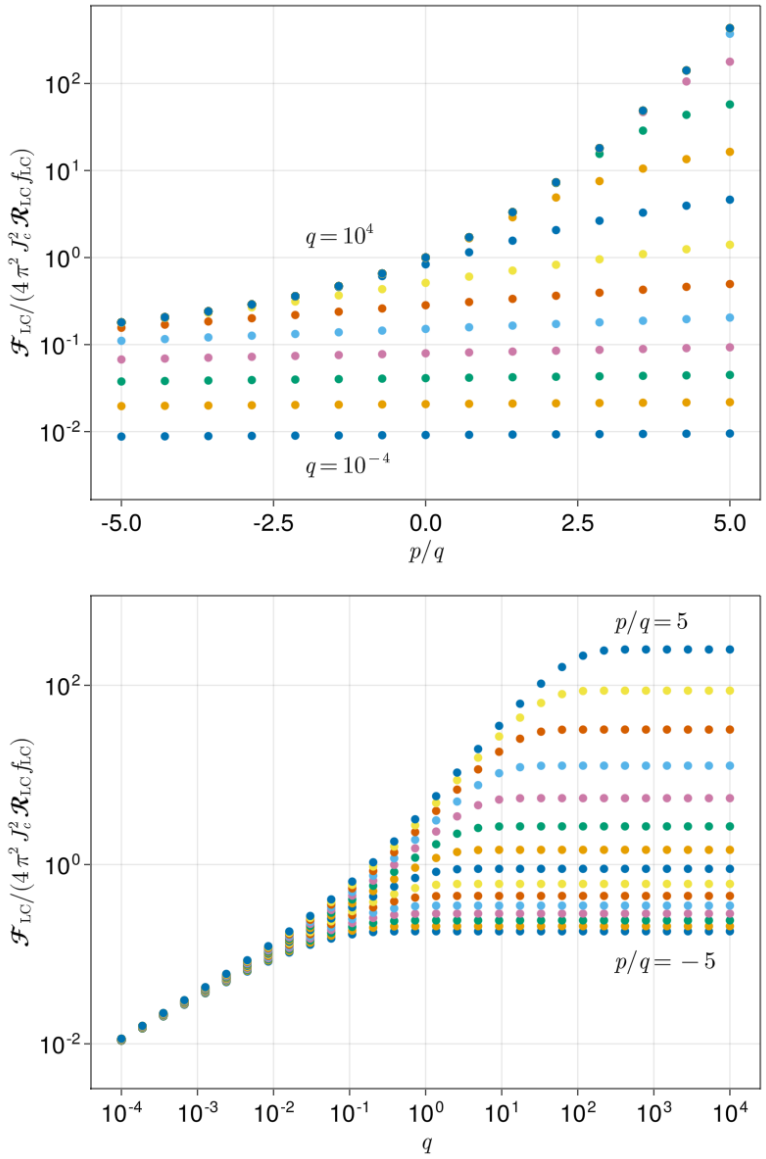

Figure 6.6: The upper panel shows the flux of captured objects as a function of the ratio p/q, with colours representing different values of q. The lower panel shows the flux of captured objects as a function of q, with colours representing different values of p/q. In the lower panel, one can see that the limiting trends at low and large q for any value of p/q are the same, including the classical solution corresponding to $p = 0$.

At a given value of p/q, the flux $\mathcal{F}_R$ of disruptions tends to a constant in q for large q. We can estimate its asymptote by writing the corresponding equation as

$$\frac{\mathcal{F}_R}{4\,\pi^2\,J_c^2\,\mathcal{R}\,q} = \frac{p}{q}\sqrt{y}\,f + y\,f' \tag{6.38}$$

and we see that when q is large the equation resembles the zero flux solution in terms of p and q. In the $\mathcal{F}_\mathcal{R} = 0$ limit:

$$\frac{f(\tau, y)}{f_{\rm LC}} \simeq e^{2\,\frac{p}{q}} e^{-2\,\frac{p}{q}\,\sqrt{y}} \tag{6.39}$$

that does not depend on τ. The flux of disruptions will be

$$\eta(a) \equiv \int_0^1 dy\,\frac{f}{f_{\rm LC}} = -\frac{-2a - e^{-2a} + 1}{2a^2}\,, \quad a = \frac{p}{q} \tag{6.40}$$

which matches the horizontal asymptote reached for different values of p/q in Fig. 6.6. As it is evident from their plots, the function $\mathcal{F}(q)$ at fixed p/q shows a nice piecewise log-log plot, that corresponds to three different power law behaviours at different values of q. By parametrizing the piecewise linear function as

$$G(x) = \begin{cases} q_3 & x > x_2 \\ m_1\,x + q_1 & x < \min\left(\frac{q_1 + m_2\,x_2 - q_3}{m_2 - m_1}, x_2\right) \\ m_2\,x + q_3 - m_2\,x_2 & \text{elsewhere} \end{cases} \tag{6.41}$$

with free parameters $\{q_1, m_1, m_2, x_2, q_3\}$, we provide formulas to obtain the function $\mathcal{F}(q, p)$ at any value of q and p as

$$\mathcal{F}(q, p) = 4\,\pi^2\,J_c^2\,\mathcal{R}_{\rm LC}\,\exp\{G(q, p)\}\,f_{\rm LC} \tag{6.42}$$

where the parameters of $G(q, p)$ are

$$q_3 = \eta(p/q) \tag{6.43}$$

$$m_1 = 0.5 \tag{6.44}$$

$$q_1 = 0.107 + 0.0170\left(\frac{p}{q}\right) + 0.00102\left(\frac{p}{q}\right)^2 \tag{6.45}$$

$$x_2 = 0.336 + 0.711\left(\frac{p}{q}\right) + 0.037\left(\frac{p}{q}\right)^2 + 0.0012\left(\frac{p}{q}\right)^3 \tag{6.46}$$

$$m_2 = 0.630 + 0.370\,\frac{2}{\pi}\,\text{atan}\left[0.575\,\left(\frac{p}{q} - 2.08\right)\right] \tag{6.47}$$

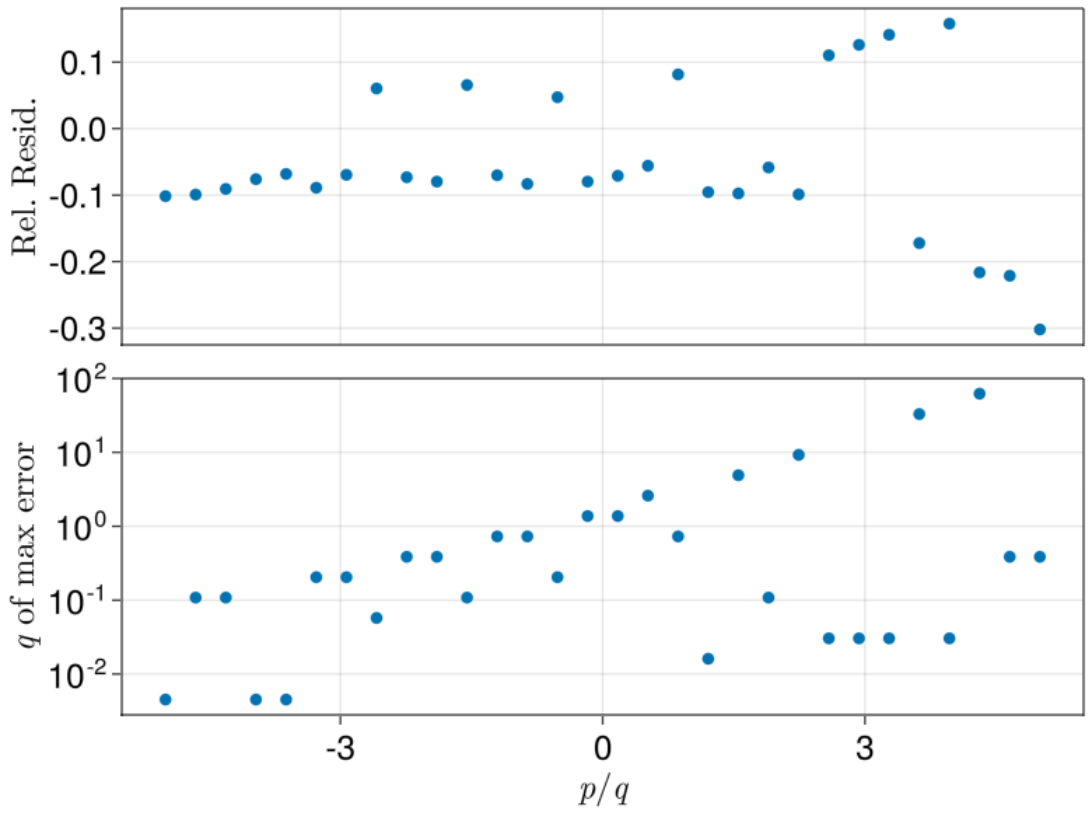

Figure 6.7: Maximum relative error obtained by estimating the flux of captures (see Fig. 6.6) using the piecewise interpolation function detailed in the text.

In the range $p/q \in [-5, 5]$ the maximum relative error of these estimates and the value of q where it is reached are shown in Fig. 6.7. The piecewise representation obtained for $p = 0$ is compared through the function $\alpha = q/\mathcal{F}$ with the other estimates in Fig. 6.3, where we can see that the performance is compatible with the other approximants, with a maximum error of 10% at $q \simeq 1$.

6.4 | Impact on capture rates

We now implement Eq. 6.42 as a boundary condition in the code presented in Chap. 4. Inserting the expression of $\mathcal{F}^{\rm orb}_{\mathcal{R}}$ we can write $\partial_{\mathcal{R}} f$ as a function of $f_{\rm LC}$

$$\partial_{\mathcal{R}} f_{\rm LC} = \left[\frac{\exp\{G(q,p)\}}{q} - \frac{p}{q}\right] \frac{f_{\rm LC}}{\mathcal{R}_{\rm LC}} \,. \tag{6.48}$$

We evaluate the cross term parameter p on the first grid point above the loss cone (as

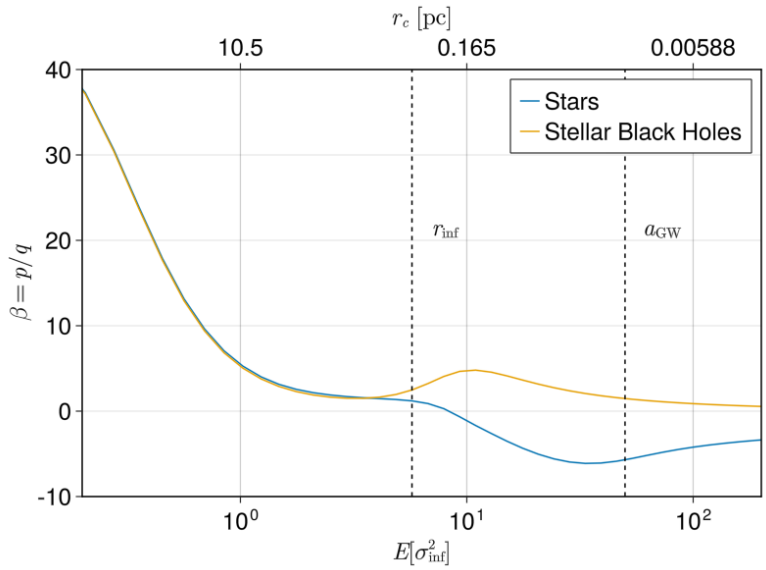

Figure 6.8: Trend of the ratio $\beta = p/q$ for a system in our fiducial model with central mass $M = 10^6\, M_\odot$. At larger radii both the species have a positive, large β, while at smaller radii star have negative β of order one, and stellar black hole positive β of order one.

in the case of q).

We tested the impact on the rates for the case of $M_\bullet = 10^6\, M_\odot$ (with the environment presented in Chap. 4). In Fig. 6.8 we show the value of the variable $\beta = p/q$ as a function of energy in the system. For the light component of stars β moves from values larger than 30 at smaller energies, and reaches values of order 1 from $E = \sigma^2_{\rm inf}$ with a local maximum of $\beta \simeq 5$ around $E = 10\,\sigma^2_{\rm inf}$, corresponding to Keplerian semimajor axis ~ 0.2 pc. In general, for stars β in this system is always positive, since the partial derivative $\partial_E f$ is always increasing close to the loss cone interface. In the case of compact objects, on the other hand, beta has a similar trend up to $E \simeq 3\sigma^2_{\rm inf}$, where it decreases reaching negative values. Around $E = 30\sigma^2_{\rm inf}$ ($r_c \simeq 0.01$ pc), the minimum value of $\beta \simeq -7$ is reached. Then, β remains negative and of order 1.

To see how $\beta \neq 0$ affects the computation of the rates, we compare the flux entering the loss cone after an evolution of $\simeq 0.65$ Gyr (twice the time to peak of the 2D code in Broggi et al. (2022)) and compare the distribution of the flux entering the loss cone with an estimate obtained with the ergodic Fokker-Planck equation. The public code `phaseflow` (Vasiliev, 2017) computes all the quantities needed for this comparison, that is shown in Fig. 6.9. In general, we can see that the peak of the flux is moved towards larger binding energies, meaning that the contributions from inner regions are larger.

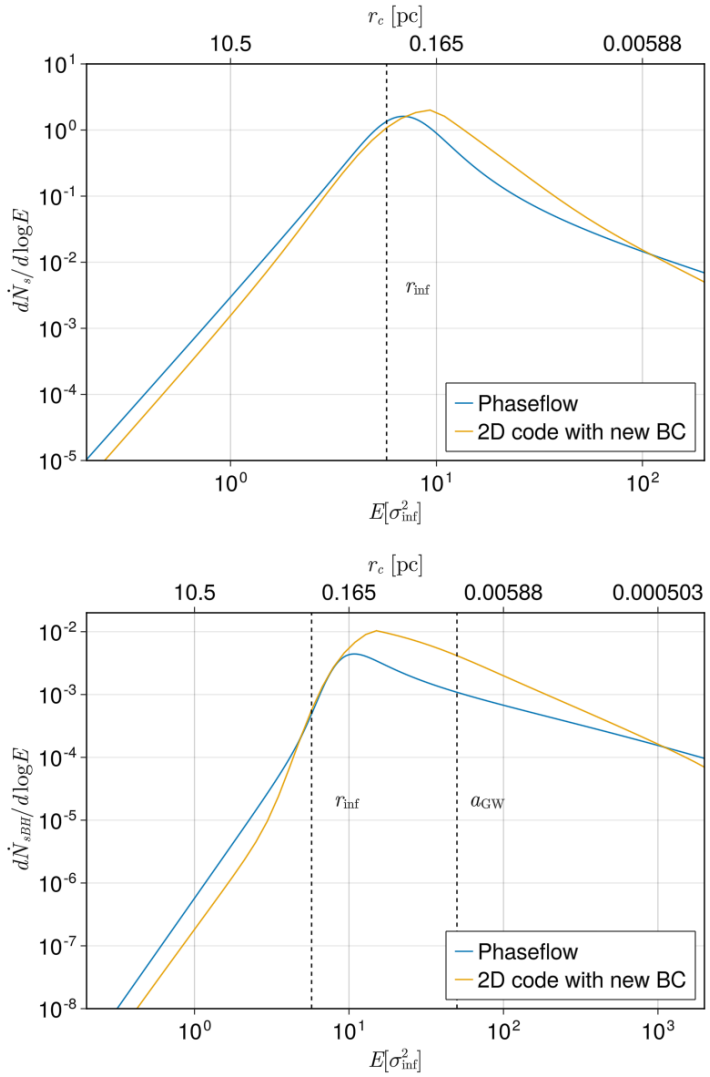

Figure 6.9: Flux entering the loss cone according to the 2D Fokker-Planck solver with our newly proposed boundary conditions, and the code `phaseflow`, that computes the flux according to the Cohn-Kulsrud profile. We plot $d\dot{N}/d\ \log E$, so that comparison at different energies is easier. For both stars and stellar black holes, the maximum of the flux entering the loss cone is moved towards smaller radii.

Therefore, we expect a bigger impact on EMRIs, that are produced for $E > 50\,\sigma^2$ ($r_c < a_{\rm GW} \simeq 0.01$ pc). Among the two species, the larger impact is on stellar Black Holes, that are more concentrated at inner regions due to the effects of mass segregation. As we have seen at the beginning of this chapter, this was expected since the deviations from a logarithmic profile appear to be stronger for the heavier species, possibly due to the negative slope of the distribution function due to mass segregation in energy, and maybe a relevant contribution from mass segregation in angular momentum due to the advective term $\mathcal{D}_R$ of the orbit averaged equation.

In Fig. 6.10 we can compare the evolution of the rates in time when computed with `phaseflow`, our 2D FP integrator with classical CK, and our integrator with the new

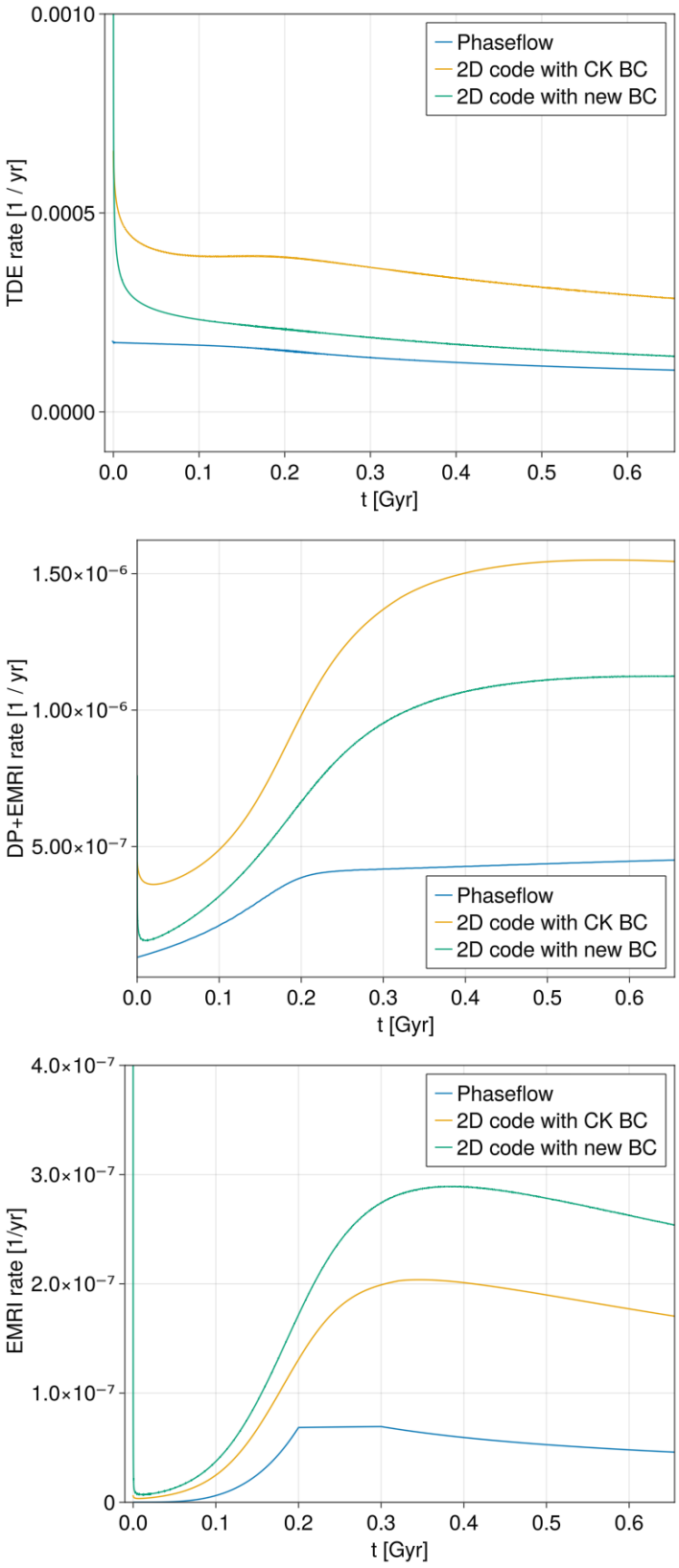

Figure 6.10: A first example of the effect of implementing the revised boundary conditions in our 2D FP solver, showing the comparison with the standard Cohn-Kulsrud boundary conditions in the 2D FP solver and the 1D estimation with the code *phaseflow*. The overall rate of TDEs and Plunges (DP+EMRIs) is slightly reduced by applying the new boundary conditions, still not compatible with 1D estimates when considering the captures of compact objects. However, the contribution of EMRIs to the total capture rate is slightly larger, and at their peak they account for $\sim$ 30% of the total capture rate. In this region, the performance of the 1D approximation seems to be worse and underestimates the rate of EMRIs by a factor of $\simeq 5$.

boundary conditions. In agreement with our previous analysis, the total rate of TDEs and DP+EMRIs computed with the 2D Fokker-Planck solvers are higher with respect to the 1D counterpart, with more pronounced differences for stellar Black Holes and in particular EMRIs. By comparing the results of the two 2D simulations, we see that the new boundary conditions reduce by around $30-40\%$ the total rate of TDEs and Plunges. However, the impact on EMRI rates has the opposite trend: the fraction of captures in this regime can be enhanced by 50% with the new BC.

6.5 | Discussion and conclusions

In this chapter, it was shown that the classical theory of loss cone is unable to predict the quasi-stable, relaxed profile in angular momentum that arises in the solutions of the orbit averaged Fokker-Planck equation with two components. This is due to the relevance of the contributions to the flux usually neglected. At low $\mathcal{R}$, where the theory only includes the $\mathcal{D}_{RR}$ term, the cross term $\mathcal{D}_{ER}$ cannot be neglected; this suggests that the boundary conditions classically derived may be inadequate. Unfortunately, the approach developed by Cohn-Kulsrud cannot be immediately extended to include the cross term. The Jeans compatible Fokker-Planck equation was then introduced to replace the local Fokker-Planck equation in the original derivation, and allow the inclusion of the cross term and the matching to the main solution of the orbit averaged equation. By parametrising the contribution of the cross term with a parameter p, a set of simulations in the relevant parameter was fitted to a semi-analytic formula for the boundary conditions that include p, together with the loss cone occupation fraction q. Thanks to the implementation of the revised boundary conditions in our solver for the orbit averaged Fokker-Planck equation, it was possible to assess the impact of this new prescription in a system with a central massive black hole of mass $10^6\,M_\odot$. The main findings of this chapter can be summarised as follows:

- Solutions of the orbit averaged Fokker-Planck equation show a greater contribution from inner regions with respect to estimates coming from the ergodic Fokker-Planck equation, since the value of p is comparable to that of q over most of the energy range.

- The revision of the boundary conditions in the solver for the orbit averaged equation marginally impacts the rate of loss cone events: the total number of TDEs and Plunges is reduced by $\sim 30\%$, while the number of EMRIs is larger by $\sim 50\%$.

These preliminary results suggest that the role of the empty loss cone, considered to be dominant for (classical) TDE rates, seems to be enhanced; at least for central black holes with masses around $10^6\,M_\odot$. The solution to the orbit averaged equation shows a smaller rate of loss cone events at large radii, and a larger rate at small radii, with the extreme case of EMRIs that could be underestimated by a factor of 5 in the ergodic approach.

As shown, the distribution of angular momentum inside the loss cone may be strongly affected by the values of p, and can significantly enhance the rate of captures on nearly radial orbits when it is positive. The distribution of particles at capture is of increasing interest to compute the expected rates of total and partial disruptions for a direct comparison against observations.

7

Conclusions

In this chapter, I summarize the work presented in the main chapters of this manuscript, with a focus on their results and the future perspectives they cast.

7.1 | Overview

In this thesis, I present the results of my work primarily focused on the dynamical origin of tidal disruption events, direct plunges and extreme mass ratio inspirals. These transient events offer the opportunity to constrain the population of massive black holes, giving information on their abundance and their properties. The majority of TDEs, Direct Plunges and EMRIs are expected to happen in galactic nuclei, since in these crowded environments close encounters may push a stellar object at the typical small separations from the central black holes at which these events can occur.

The relaxation of stellar systems due to two body encounters can be described statistically with a stochastic Fokker-Planck equation that models the evolution of the distribution function due to two-body encounters. With increasing approximation, one can assume specific analytic forms of the distribution function to obtain the orbit averaged Fokker-Planck equation and the ergodic Fokker-Planck equation, that are increasingly simpler to solve.

When the stochastic evolution of nuclear clusters is complemented with a simple model of the transient events known as loss cone theory, one can estimate the rate at which tidal disruptions (for deformable objects like stars) and plunges (for non-deformable objects like stellar black holes) are expected to happen. Moreover, by looking at the specific dynamics in nuclear cluster it is possible to distinguish between DPs and EMRIs for compact objects, even in the absence of gravitational waves emission.

In this framework, my work has moved in three directions:

1. I wrote the first public code for the solution of the orbit averaged Fokker-Planck equation, that implements the classical theory for two species of stellar objects. I used this code to compute the rate for a variety of models of galactic nuclei.

2. I carefully revised the theoretical foundations of the loss cone theory with the aim of including a proper treatment of partial disruptions.

3. I extended the classical theory of angular momentum relaxation in the presence of the loss cone to account for previously neglected effects, in particular in the case of compact objects.

The three directions have often crossed, explicitly or not, and have offered me the opportunity to assess the capabilities and the limitations of the classical theory of loss cone, the main tool for computing the expected cosmological rates of TDEs, DPs and EMRIs.

7.2 | Main results and future perspectives

With my studies on the solutions of the time dependent orbit averaged Fokker-Planck equation, I was able to compute the rate of TDEs, DPs and EMRIs for a variety of galactic nuclei, and to derive some scaling relations that fully characterize them. Mass segregation of the heavier component towards the centre of the stellar distribution is the phenomenon that drives the stochastic evolution of galactic nuclei, and dictates the typical timescale of rate evolution in time. By translating the total number of loss cone events into an estimate of the mass accreted by the central black holes, I showed that massive black holes with mass below $10^6\ M_\odot$ may grow significantly through these transient events over cosmological timescales, and I quantified their growth timescale.

With my studies on partial disruption events, I showed that their inclusion in classical loss cone theory requires an advection term acting on eccentric orbits with pericentres up to ten times larger than the tidal disruption radius. This term is mainly due to the effect of weak mass-loss, that reduces the binding energy of stars for repeated partial disruptions. This phenomenon prevents stars from reaching the loss cone radius in the inner regions of galactic nuclei, typically found in the so-called empty loss cone regime. Consequently, the rates of TDEs classically expected from these regions may be suppressed by the inclusion of PTDEs in the theory.

I showed that classical loss cone theory fails to predict the relaxed profile in angular momentum of the solution of the 2D Fokker-Planck equation with two-stellar components. I proposed a revised version of the boundary conditions for the equation, determined by a more accurate relaxed profile that includes the contribution of the so-called

cross term. Preliminary tests show that the different relaxed profile may significantly impact the rate of EMRIs. The comparison with 1D estimates of the loss cone rates shows a reduced contribution from distant regions of the galactic nucleus (in the full loss cone regime) and an increased contribution from inner regions (in the empty loss cone regime).

My work on PTDEs and the contribution of the cross-term suggests that the classical theory of loss cone may fail in predicting the rate of TDEs coming from the empty loss cone regime. The decreased relative importance of the full loss cone regime (due to the cross term) and a suppression of the rates coming from the empty loss cone regime (due to repeated PTDEs) may indeed explain why observed rate of TDEs are lower than prediction.

The natural prosecution of this work is to derive an analytic expression for the advection due to repeated PTDEs, and include it together with the improved boundary conditions in my code. The comparison with previous simulations will quantify the combined effect of these improvements, hopefully giving more realistic predictions of the formation rate of TDEs, PTDEs, DPs and EMRIs. This numerical implementation of the orbit averaged Fokker-Planck formalism can be then complemented with a variety of physical phenomena to increase the realism of the simulated evolution of stellar systems. Possible improvements include the emission of gravitational waves, and the evolution of the stellar distribution due to the formation of new stars and their ageing. On the long term, we envisage to derive accurate and realistic formation rates of loss cone events in galaxies by exploiting self-consistent models of the evolution of the galactic population of our Universe. The derived cosmological event rate of tidal disruption events and plunges will serve as a guiding tool to interpret at best their detections in order to get the highest scientific reward from forthcoming experiments.

References

Tal Alexander and Clovis Hopman. Strong mass segregation around a massive black hole. *The Astrophysical Journal*, 697(2):1861–1869, June 2009. ISSN 0004-637X, 1538-4357. doi: 10.1088/0004-637X/697/2/1861.

Pau Amaro-Seoane. Relativistic Dynamics and Extreme Mass Ratio Inspirals. *Living Reviews in Relativity*, 21(1):4, December 2018. ISSN 2367-3613, 1433-8351. doi: 10.1007/s41114-018-0013-8.

Pau Amaro-Seoane. The gravitational capture of compact objects by massive black holes. *arXiv:2011.03059 [astro-ph, physics:gr-qc]*, November 2020.

Pau Amaro-Seoane and Miguel Preto. The impact of realistic models of mass segregation on the event rate of extreme-mass ratio inspirals and cusp re-growth. *Classical and Quantum Gravity*, 28(9):094017, May 2011. ISSN 0264-9381, 1361-6382. doi: 10.1088/0264-9381/28/9/094017.

Pau Amaro-Seoane, Jonathan R. Gair, Marc Freitag, M. Coleman Miller, Ilya Mandel, Curt J. Cutler, and Stanislav Babak. TOPICAL REVIEW: Intermediate and extreme mass-ratio inspirals—astrophysics, science applications and detection using LISA. *Classical and Quantum Gravity*, 24:R113–R169, September 2007. ISSN 0264-9381. doi: 10.1088/0264-9381/24/17/R01.

Pau Amaro-Seoane, Heather Audley, Stanislav Babak, John Baker, Enrico Barausse, Peter Bender, Emanuele Berti, Pierre Binetruy, Michael Born, Daniele Bortoluzzi, Jordan Camp, Chiara Caprini, Vitor Cardoso, Monica Colpi, John Conklin, Neil Cornish, Curt Cutler, Karsten Danzmann, Rita Dolesi, Luigi Ferraioli, Valerio Ferroni, Ewan Fitzsimons, Jonathan Gair, Lluis Gesa Bote, Domenico Giardini, Ferran Gibert, Catia Grimani, Hubert Halloin, Gerhard Heinzel, Thomas Hertog, Martin Hewitson, Kelly Holley-Bockelmann, Daniel Hollington, Mauro Hueller, Henri Inchauspe, Philippe Jetzer, Nikos Karnesis, Christian Killow, Antoine Klein, Bill Klipstein, Natalia Korsakova, Shane L Larson, Jeffrey Livas, Ivan Lloro, Nary Man, Davor Mance, Joseph Martino, Ignacio Mateos, Kirk McKenzie, Sean T McWilliams, Cole Miller, Guido Mueller, Germano Nardini, Gijs Nelemans, Miquel Nofrarias, Antoine Petiteau, Paolo Pivato, Eric Plagnol, Ed Porter, Jens Reiche, David Robertson, Norna Robertson, Elena Rossi, Giuliana Russano, Bernard Schutz, Alberto Sesana, David Shoemaker, Jacob Slutsky, Carlos F. Sopuerta, Tim Sumner, Nicola Tamanini, Ira Thorpe, Michael Troebs, Michele Vallisneri, Alberto Vecchio, Daniele Vetrugno, Stefano Vitale, Marta Volonteri, Gudrun Wanner, Harry Ward, Peter Wass, William Weber, John Ziemer, and Peter Zweifel. Laser Interferometer Space Antenna, February 2017.

George Brown Arfken and Hans Jurgen Weber. *Mathematical Methods for Physicists*. Academic press, 7th ed edition, 2012. ISBN 978-0-12-384654-9.

Stanislav Babak, John G. Baker, Matthew J. Benacquista, Neil J. Cornish, Shane L. Larson, Ilya Mandel, Sean T. McWilliams, Antoine Petiteau, Edward K. Porter, Emma L. Robinson, Michele Vallisneri, Alberto Vecchio, the Mock LISA Data Challenge Task Force, Matt Adams, Keith A. Arnaud, Arkadiusz Błaut, Michael Bridges, Michael Cohen, Curt Cutler, Farhan Feroz, Jonathan R. Gair, Philip Graff, Mike Hobson, Joey Shapiro Key, Andrzej Królak, Anthony Lasenby, Reinhard Prix, Yu Shang, Miquel Trias, John Veitch, John T. Whelan, and the Challenge 3 participants. The Mock LISA Data Challenges: From challenge 3 to challenge 4. *Classical and Quantum Gravity*, 27:084009, April 2010. ISSN 0264-9381. doi: 10.1088/0264-9381/27/8/084009.

Stanislav Babak, Jonathan Gair, Alberto Sesana, Enrico Barausse, Carlos F. Sopuerta, Christopher P. L. Berry, Emanuele Berti, Pau Amaro-Seoane, Antoine Petiteau, and Antoine Klein. Science with the space-based interferometer LISA. V. Extreme mass-ratio inspirals. *Physical Review D*, 95(10):103012, May 2017. doi: 10.1103/PhysRevD.95.103012.

J. N. Bahcall and R. A. Wolf. The star distribution around a massive black hole in a globular cluster. II. Unequal star masses. *The Astrophysical Journal*, 216:883–907, September 1977. ISSN 0004-637X. doi: 10.1086/155534.

Ben Bar-Or and Tal Alexander. The statistical mechanics of relativistic orbits around a massive black hole. *Classical and Quantum Gravity*, 31(24):244003, December 2014. ISSN 0264-9381. doi: 10.1088/0264-9381/31/24/244003.

Ben Bar-Or and Tal Alexander. Steady state relativistic stellar dynamics around a massive black hole. *The Astrophysical Journal*, 820(2):129, March 2016. ISSN 1538-4357. doi: 10.3847/0004-637X/820/2/129.

Leor Barack and Curt Cutler. Confusion noise from LISA capture sources. *Physical Review D*, 70:122002, December 2004a. ISSN 1550-79980556-2821. doi: 10.1103/PhysRevD.70.122002.

Leor Barack and Curt Cutler. LISA capture sources: Approximate waveforms, signal-to-noise ratios, and parameter estimation accuracy. *Physical Review D*, 69:082005, April 2004b. ISSN 1550-79980556-2821. doi: 10.1103/PhysRevD.69.082005.

Leor Barack and Curt Cutler. Using LISA extreme-mass-ratio inspiral sources to test off-Kerr deviations in the geometry of massive black holes. *Physical Review D*, 75(4):042003, February 2007. doi: 10.1103/PhysRevD.75.042003.

Jeff Bezanson, Alan Edelman, Stefan Karpinski, and Viral B. Shah. Julia: A Fresh Approach to Numerical Computing. *SIAM Review*, 59(1):65–98, January 2017. ISSN 0036-1445. doi: 10.1137/141000671.

James Binney and Scott Tremaine. *Galactic Dynamics: Second Edition*. January 2008.

J. Nate Bode and Christopher Wegg. Production of EMRIs in supermassive black hole binaries. *Monthly Notices of the Royal Astronomical Society*, 438(1):573–589, February 2014. ISSN 0035-8711. doi: 10.1093/mnras/stt2227.

Stefano Bondani, Matteo Bonetti, Luca Broggi, Francesco Haardt, Alberto Sesana, and Massimo Dotti. Gravitational waves from an eccentric population of primordial black holes orbiting Sgr A$\hat\star$, March 2023.

Matteo Bonetti and Alberto Sesana. Gravitational wave background from extreme mass ratio inspirals. *Physical Review D*, 102(10):103023, November 2020. doi: 10.1103/PhysRevD.102.103023.

Elisa Bortolas. Tidal disruption events in post-starburst galaxies: The importance of a complete stellar mass function. January 2022. doi: 10.1093/mnras/stac262.

Elisa Bortolas and Michela Mapelli. Can supernova kicks trigger EMRIs in the Galactic Centre? *Monthly Notices of the Royal Astronomical Society*, 485:2125–2138, May 2019. ISSN 0035-8711. doi: 10.1093/mnras/stz440.

Elisa Bortolas, Taeho Ryu, Luca Broggi, and Alberto Sesana. Partial stellar tidal disruption events and their rates, March 2023.

Katja Bricman and Andreja Gomboc. The Prospects of Observing Tidal Disruption Events with the Large Synoptic Survey Telescope. *The Astrophysical Journal*, 890(1):73, February 2020. ISSN 0004-637X. doi: 10.3847/1538-4357/ab6989.

Luca Broggi, Elisa Bortolas, Matteo Bonetti, Alberto Sesana, and Massimo Dotti. Extreme mass ratio inspirals and tidal disruption events in nuclear clusters - I. Time-dependent rates. *Monthly Notices of the Royal Astronomical Society*, 514(3):3270–3284, August 2022. ISSN 0035-8711. doi: 10.1093/mnras/stac1453.

Subrahmanyan Chandrasekhar. *Principles of Stellar Dynamics*. January 1942.

J. S Chang and G Cooper. A practical difference scheme for Fokker-Planck equations. *Journal of Computational Physics*, 6(1):1–16, August 1970. ISSN 0021-9991. doi: 10.1016/0021-9991(70)90001-X.

Jin-Hong Chen and Rong-Feng Shen. Light Curves of Partial Tidal Disruption Events. *The Astrophysical Journal*, 914:69, June 2021. ISSN 0004-637X. doi: 10.3847/1538-4357/abf9a7.

Xian Chen, Alberto Sesana, Piero Madau, and F. K. Liu. Tidal Stellar Disruptions by Massive Black Hole Pairs. II. Decaying Binaries. *The Astrophysical Journal*, 729:13, March 2011. ISSN 0004-637X. doi: 10.1088/0004-637X/729/1/13.

H. Cohn. Late core collapse in star clusters and the gravothermal instability. *The Astrophysical Journal*, 242: 765–771, December 1980. ISSN 0004-637X. doi: 10.1086/158511.

H. Cohn and R. M. Kulsrud. The stellar distribution around a black hole: Numerical integration of the Fokker-Planck equation. *The Astrophysical Journal*, 226:1087–1108, December 1978. ISSN 0004-637X. doi: 10.1086/156685.

The Event Horizon Telescope Collaboration, Kazunori Akiyama, Antxon Alberdi, Walter Alef, Keiichi Asada, Rebecca Azulay, Anne-Kathrin Baczko, David Ball, Mislav Baloković, John Barrett, Dan Bintley, Lindy Blackburn, Wilfred Boland, Katherine L. Bouman, Geoffrey C. Bower, Michael Bremer, Christiaan D. Brinkerink, Roger Brissenden, Silke Britzen, Avery E. Broderick, Dominique Broguiere,

Thomas Bronzwaer, Do-Young Byun, John E. Carlstrom, Andrew Chael, Chi-kwan Chan, Shami Chatterjee, Koushik Chatterjee, Ming-Tang Chen, Yongjun Chen, Ilje Cho, Pierre Christian, John E. Conway, James M. Cordes, Geoffrey B. Crew, Yuzhu Cui, Jordy Davelaar, Mariafelicia De Laurentis, Roger Deane, Jessica Dempsey, Gregory Desvignes, Jason Dexter, Sheperd S. Doeleman, Ralph P. Eatough, Heino Falcke, Vincent L. Fish, Ed Fomalont, Raquel Fraga-Encinas, William T. Freeman, Per Friberg, Christian M. Fromm, José L. Gómez, Peter Galison, Charles F. Gammie, Roberto García, Olivier Gentaz, Boris Georgiev, Ciriaco Goddi, Roman Gold, Minfeng Gu, Mark Gurwell, Kazuhiro Hada, Michael H. Hecht, Ronald Hesper, Luis C. Ho, Paul Ho, Mareki Honma, Chih-Wei L. Huang, Lei Huang, David H. Hughes, Shiro Ikeda, Makoto Inoue, Sara Issaoun, David J. James, Buell T. Jannuzi, Michael Janssen, Britton Jeter, Wu Jiang, Michael D. Johnson, Svetlana Jorstad, Taehyun Jung, Mansour Karami, Ramesh Karuppusamy, Tomohisa Kawashima, Garrett K. Keating, Mark Kettenis, Jae-Young Kim, Junhan Kim, Jongsoo Kim, Motoki Kino, Jun Yi Koay, Patrick M. Koch, Shoko Koyama, Michael Kramer, Carsten Kramer, Thomas P. Krichbaum, Cheng-Yu Kuo, Tod R. Lauer, Sang-Sung Lee, Yan-Rong Li, Zhiyuan Li, Michael Lindqvist, Kuo Liu, Elisabetta Liuzzo, Wen-Ping Lo, Andrei P. Lobanov, Laurent Loinard, Colin Lonsdale, Ru-Sen Lu, Nicholas R. MacDonald, Jirong Mao, Sera Markoff, Daniel P. Marrone, Alan P. Marscher, Iván Martí-Vidal, Satoki Matsushita, Lynn D. Matthews, Lia Medeiros, Karl M. Menten, Yosuke Mizuno, Izumi Mizuno, James M. Moran, Kotaro Moriyama, Monika Moscibrodzka, Cornelia Müller, Hiroshi Nagai, Neil M. Nagar, Masanori Nakamura, Ramesh Narayan, Gopal Narayanan, Iniyan Natarajan, Roberto Neri, Chunchong Ni, Aristeidis Noutsos, Hiroki Okino, Héctor Olivares, Gisela N. Ortiz-León, Tomoaki Oyama, Feryal Özel, Daniel C. M. Palumbo, Nimesh Patel, Ue-Li Pen, Dominic W. Pesce, Vincent Piétu, Richard Plambeck, Aleksandar PopStefanija, Oliver Porth, Ben Prather, Jorge A. Preciado-López, Dimitrios Psaltis, Hung-Yi Pu, Venkatessh Ramakrishnan, Ramprasad Rao, Mark G. Rawlings, Alexander W. Raymond, Luciano Rezzolla, Bart Ripperda, Freek Roelofs, Alan Rogers, Eduardo Ros, Mel Rose, Arash Roshanineshat, Helge Rottmann, Alan L. Roy, Chet Ruszczyk, Benjamin R. Ryan, Kazi L. J. Rygl, Salvador Sánchez, David Sánchez-Arguelles, Mahito Sasada, Tuomas Savolainen, F. Peter Schloerb, Karl-Friedrich Schuster, Lijing Shao, Zhiqiang Shen, Des Small, Bong Won Sohn, Jason SooHoo, Fumie Tazaki, Paul Tiede, Remo P. J. Tilanus, Michael Titus, Kenji Toma, Pablo Torne, Tyler Trent, Sascha Trippe, Shuichiro Tsuda, Ilse van Bemmel, Huib Jan van Langevelde, Daniel R. van Rossum, Jan Wagner, John Wardle, Jonathan Weintroub, Norbert Wex, Robert Wharton, Maciek Wielgus, George N. Wong, Qingwen Wu, Ken Young, André Young, Ziri Younsi, Feng Yuan, Ye-Fei Yuan, J. Anton Zensus, Guangyao Zhao, Shan-Shan Zhao, Ziyan Zhu, Juan-Carlos Algaba, Alexander Allardi, Rodrigo Amestica, Jadyn Anczarski, Uwe Bach, Frederick K. Baganoff, Christopher Beaudoin, Bradford A. Benson, Ryan Berthold, Jay M. Blanchard, Ray Blundell, Sandra Bustamente, Roger Cappallo, Edgar Castillo-Domínguez, Chih-Cheng Chang, Shu-Hao Chang, Song-Chu Chang, Chung-Chen Chen, Ryan Chilson, Tim C. Chuter, Rodrigo Córdova Rosado, Iain M. Coulson, Thomas M. Crawford, Joseph Crowley, John David, Mark Derome, Matthew Dexter, Sven Dornbusch, Kevin A. Dudevoir, Sergio A. Dzib, Andreas Eckart, Chris Eckert, Neal R. Erickson, Wendeline B. Everett, Aaron Faber, Joseph R. Farah, Vernon Fath, Thomas W. Folkers, David C. Forbes, Robert Freund, Arturo I. Gómez-Ruiz, David M. Gale, Feng Gao, Gertie Geertsema, David A. Graham, Christopher H. Greer, Ronald Grosslein, Frédéric Gueth, Daryl Haggard, Nils W. Halverson, Chih-Chiang Han, Kuo-Chang Han, Jinchi Hao, Yutaka Hasegawa, Jason W. Henning, Antonio Hernández-Gómez, Rubén Herrero-Illana, Stefan Heyminck, Akihiko Hirota, James Hoge, Yau-De Huang, C. M. Violette Impellizzeri, Homin Jiang, Atish Kamble, Ryan Keisler, Kimihiro Kimura, Yusuke Kono, Derek Kubo, John Kuroda, Richard Lacasse, Robert A. Laing, Erik M. Leitch, Chao-Te Li, Lupin C.-C. Lin, Ching-Tang Liu, Kuan-Yu Liu, Li-Ming Lu, Ralph G. Marson, Pierre L. Martin-Cocher, Kyle D. Massingill, Callie Matulonis, Martin P. McColl, Stephen R. McWhirter,

Hugo Messias, Zheng Meyer-Zhao, Daniel Michalik, Alfredo Montaña, William Montgomerie, Matias Mora-Klein, Dirk Muders, Andrew Nadolski, Santiago Navarro, Joseph Neilsen, Chi H. Nguyen, Hiroaki Nishioka, Timothy Norton, Michael A. Nowak, George Nystrom, Hideo Ogawa, Peter Oshiro, Tomoaki Oyama, Harriet Parsons, Scott N. Paine, Juan Peñalver, Neil M. Phillips, Michael Poirier, Nicolas Pradel, Rurik A. Primiani, Philippe A. Raffin, Alexandra S. Rahlin, George Reiland, Christopher Risacher, Ignacio Ruiz, Alejandro F. Sáez-Madaín, Remi Sassella, Pim Schellart, Paul Shaw, Kevin M. Silva, Hotaka Shiokawa, David R. Smith, William Snow, Kamal Souccar, Don Sousa, T. K. Sridharan, Ranjani Srinivasan, William Stahm, Anthony A. Stark, Kyle Story, Sjoerd T. Timmer, Laura Vertatschitsch, Craig Walther, Ta-Shun Wei, Nathan Whitehorn, Alan R. Whitney, David P. Woody, Jan G. A. Wouterloot, Melvin Wright, Paul Yamaguchi, Chen-Yu Yu, Milagros Zeballos, Shuo Zhang, and Lucy Ziurys. First M87 Event Horizon Telescope Results. I. The Shadow of the Supermassive Black Hole. *The Astrophysical Journal Letters*, 875(1):L1, April 2019. ISSN 2041-8205. doi: 10.3847/2041-8213/ab0ec7.

Eric R. Coughlin and C. J. Nixon. Partial Stellar Disruption by a Supermassive Black Hole: Is the Light Curve Really Proportional to t -9/4? *The Astrophysical Journal*, 883:L17, September 2019. ISSN 0004-637X. doi: 10.3847/2041-8213/ab412d.

M. Cufari, C. J. Nixon, and Eric R. Coughlin. Tidal capture of stars by supermassive black holes: Implications for periodic nuclear transients and quasi-periodic eruptions. *Monthly Notices of the Royal Astronomical Society*, 520:L38–L41, March 2023. ISSN 0035-8711. doi: 10.1093/mnrasl/slad001.

G. A. Drukier, H. N. Cohn, P. M. Lugger, and H. Yong. Anisotropic Fokker-Planck Models for the Evolution of Globular Star Clusters: The Core-Halo Connection. 518(1):233–245, June 1999. ISSN 0004-637X. doi: 10.1086/307243.

Charles R. Evans and Christopher S. Kochanek. The Tidal Disruption of a Star by a Massive Black Hole. *The Astrophysical Journal*, 346:L13, November 1989. ISSN 0004-637X. doi: 10.1086/185567.

Giacomo Fragione and Re'em Sari. Steeper Stellar Cusps in Galactic Centers from Binary Disruption. *The Astrophysical Journal*, 852:51, January 2018. ISSN 0004-637X. doi: 10.3847/1538-4357/aaa0d7.

K. Decker French, Thomas Wevers, Jamie Law-Smith, Or Graur, and Ann I. Zabludoff. The Host Galaxies of Tidal Disruption Events. *Space Science Reviews*, 216:32, March 2020. ISSN 0038-6308. doi: 10.1007/s11214-020-00657-y.

Jonathan R. Gair, Christopher Tang, and Marta Volonteri. LISA extreme-mass-ratio inspiral events as probes of the black hole mass function. *Physical Review D*, 81:104014, May 2010. ISSN 1550-79980556-2821. doi: 10.1103/PhysRevD.81.104014.

Jonathan R. Gair, Michele Vallisneri, Shane L. Larson, and John G. Baker. Testing General Relativity with Low-Frequency, Space-Based Gravitational-Wave Detectors. *Living Reviews in Relativity*, 16(1):7, September 2013. ISSN 1433-8351. doi: 10.12942/lrr-2013-7.

A. Generozov, N. C. Stone, B. D. Metzger, and J. P. Ostriker. An Overabundance of Black Hole X-Ray Binaries in the Galactic Center from Tidal Captures. *Monthly Notices of the Royal Astronomical Society*, 478 (3):4030–4051, August 2018. ISSN 0035-8711, 1365-2966. doi: 10.1093/mnras/sty1262.

James Guillochon and E. Ramirez-Ruiz. PS1-10jh: The Partial Disruption of a Main-Sequence Star of Near-Solar Composition. 13:403.05, April 2013.

Kayhan Gültekin, Douglas O. Richstone, Karl Gebhardt, Tod R. Lauer, Scott Tremaine, M. C. Aller, Ralf Bender, Alan Dressler, S. M. Faber, Alexei V. Filippenko, Richard Green, Luis C. Ho, John Kormendy, John Magorrian, Jason Pinkney, and Christos Siopis. THEM-$\upsigma$ ANDM-LRELATIONS IN GALACTIC BULGES, AND DETERMINATIONS OF THEIR INTRINSIC SCATTER. *The Astrophysical Journal*, 698(1):198–221, May 2009. ISSN 0004-637X. doi: 10.1088/0004-637X/698/1/198.

J. G. Hills. Hyper-velocity and tidal stars from binaries disrupted by a massive Galactic black hole. *Nature*, 331(6158):687–689, February 1988. ISSN 1476-4687. doi: 10.1038/331687a0.

Clovis Hopman and Tal Alexander. The Orbital Statistics of Stellar Inspiral and Relaxation near a Massive Black Hole: Characterizing Gravitational Wave Sources. *The Astrophysical Journal*, 629(1):362, August 2005. ISSN 0004-637X. doi: 10.1086/431475.

David Izquierdo-Villalba, Silvia Bonoli, Daniele Spinoso, Yetli Rosas-Guevara, Bruno M. B. Henriques, and Carlos Hernández-Monteagudo. The build-up of pseudo-bulges in a hierarchical universe. *Monthly Notices of the Royal Astronomical Society*, 488:609–632, September 2019. ISSN 0035-8711. doi: 10.1093/mnras/stz1694.

John Kormendy and Luis C. Ho. Coevolution (Or Not) of Supermassive Black Holes and Host Galaxies. *Annual Review of Astronomy and Astrophysics*, 51(1):511–653, August 2013. ISSN 0066-4146. doi: 10.1146/annurev-astro-082708-101811.

Julian Krolik, Tsvi Piran, and Taeho Ryu. Tidal Disruptions of Main-sequence Stars. V. The Varieties of Disruptions. *The Astrophysical Journal*, 904:68, November 2020. ISSN 0004-637X. doi: 10.3847/1538-4357/abc0f6.

Danny Laghi, Nicola Tamanini, Walter Del Pozzo, Alberto Sesana, Jonathan Gair, Stanislav Babak, and David Izquierdo-Villalba. Gravitational-wave cosmology with extreme mass-ratio inspirals. *Monthly Notices of the Royal Astronomical Society*, 508:4512–4531, December 2021. ISSN 0035-8711. doi: 10.1093/mnras/stab2741.

Hyung Mok Lee and Jeremiah P. Ostriker. Cross sections for tidal capture binary formation and stellar merger. *The Astrophysical Journal*, 310:176, November 1986. ISSN 0004-637X, 1538-4357. doi: 10.1086/164674.

Yuri Levin. Starbursts near supermassive black holes: Young stars in the Galactic Centre, and gravitational waves in LISA band. *Monthly Notices of the Royal Astronomical Society*, 374:515–524, January 2007. ISSN 0035-8711. doi: 10.1111/j.1365-2966.2006.11155.x.

A. P. Lightman and S. L. Shapiro. The distribution and consumption rate of stars around a massive, collapsed object. *The Astrophysical Journal*, 211:244–262, January 1977. ISSN 0004-637X. doi: 10.1086/154925.

LIGO Scientific Collaboration and Virgo Collaboration, B. P. Abbott, R. Abbott, T. D. Abbott, M. R. Abernathy, F. Acernese, K. Ackley, C. Adams, T. Adams, P. Addesso, R. X. Adhikari, V. B. Adya, C. Affeldt, M. Agathos, K. Agatsuma, N. Aggarwal, O. D. Aguiar, L. Aiello, A. Ain, P. Ajith, B. Allen, A. Allocca, P. A. Altin, S. B. Anderson, W. G. Anderson, K. Arai, M. A. Arain, M. C. Araya, C. C. Arceneaux, J. S. Areeda, N. Arnaud, K. G. Arun, S. Ascenzi, G. Ashton, M. Ast, S. M. Aston, P. Astone, P. Aufmuth, C. Aulbert, S. Babak, P. Bacon, M. K. M. Bader, P. T. Baker, F. Baldaccini, G. Ballardin, S. W. Ballmer, J. C. Barayoga, S. E. Barclay, B. C. Barish, D. Barker, F. Barone, B. Barr, L. Barsotti, M. Barsuglia, D. Barta,

J. Bartlett, M. A. Barton, I. Bartos, R. Bassiri, A. Basti, J. C. Batch, C. Baune, V. Bavigadda, M. Bazzan, B. Behnke, M. Bejger, C. Belczynski, A. S. Bell, C. J. Bell, B. K. Berger, J. Bergman, G. Bergmann, C. P. L. Berry, D. Bersanetti, A. Bertolini, J. Betzwieser, S. Bhagwat, R. Bhandare, I. A. Bilenko, G. Billingsley, J. Birch, R. Birney, O. Birnholtz, S. Biscans, A. Bisht, M. Bitossi, C. Biwer, M. A. Bizouard, J. K. Blackburn, C. D. Blair, D. G. Blair, R. M. Blair, S. Bloemen, O. Bock, T. P. Bodiya, M. Boer, G. Bogaert, C. Bogan, A. Bohe, P. Bojtos, C. Bond, F. Bondu, R. Bonnand, B. A. Boom, R. Bork, V. Boschi, S. Bose, Y. Bouffanais, A. Bozzi, C. Bradaschia, P. R. Brady, V. B. Braginsky, M. Branchesi, J. E. Brau, T. Briant, A. Brillet, M. Brinkmann, V. Brisson, P. Brockill, A. F. Brooks, D. A. Brown, D. D. Brown, N. M. Brown, C. C. Buchanan, A. Buikema, T. Bulik, H. J. Bulten, A. Buonanno, D. Buskulic, C. Buy, R. L. Byer, M. Cabero, L. Cadonati, G. Cagnoli, C. Cahillane, J. Calderón Bustillo, T. Callister, E. Calloni, J. B. Camp, K. C. Cannon, J. Cao, C. D. Capano, E. Capocasa, F. Carbognani, S. Caride, J. Casanueva Diaz, C. Casentini, S. Caudill, M. Cavaglià, F. Cavalier, R. Cavalieri, G. Cella, C. B. Cepeda, L. Cerboni Baiardi, G. Cerretani, E. Cesarini, R. Chakraborty, T. Chalermsongsak, S. J. Chamberlin, M. Chan, S. Chao, P. Charlton, E. Chassande-Mottin, H. Y. Chen, Y. Chen, C. Cheng, A. Chincarini, A. Chiummo, H. S. Cho, M. Cho, J. H. Chow, N. Christensen, Q. Chu, S. Chua, S. Chung, G. Ciani, F. Clara, J. A. Clark, F. Cleva, E. Coccia, P.-F. Cohadon, A. Colla, C. G. Collette, L. Cominsky, M. Constancio, A. Conte, L. Conti, D. Cook, T. R. Corbitt, N. Cornish, A. Corsi, S. Cortese, C. A. Costa, M. W. Coughlin, S. B. Coughlin, J.-P. Coulon, S. T. Countryman, P. Couvares, E. E. Cowan, D. M. Coward, M. J. Cowart, D. C. Coyne, R. Coyne, K. Craig, J. D. E. Creighton, T. D. Creighton, J. Cripe, S. G. Crowder, A. M. Cruise, A. Cumming, L. Cunningham, E. Cuoco, T. Dal Canton, S. L. Danilishin, S. D'Antonio, K. Danzmann, N. S. Darman, C. F. Da Silva Costa, V. Dattilo, I. Dave, H. P. Daveloza, M. Davier, G. S. Davies, E. J. Daw, R. Day, S. De, D. DeBra, G. Debreczeni, J. Degallaix, M. De Laurentis, S. Deléglise, W. Del Pozzo, T. Denker, T. Dent, H. Dereli, V. Dergachev, R. T. DeRosa, R. De Rosa, R. DeSalvo, S. Dhurandhar, M. C. Díaz, L. Di Fiore, M. Di Giovanni, A. Di Lieto, S. Di Pace, I. Di Palma, A. Di Virgilio, G. Dojcinoski, V. Dolique, F. Donovan, K. L. Dooley, S. Doravari, R. Douglas, T. P. Downes, M. Drago, R. W. P. Drever, J. C. Driggers, Z. Du, M. Ducrot, S. E. Dwyer, T. B. Edo, M. C. Edwards, A. Effler, H.-B. Eggenstein, P. Ehrens, J. Eichholz, S. S. Eikenberry, W. Engels, R. C. Essick, T. Etzel, M. Evans, T. M. Evans, R. Everett, M. Factourovich, V. Fafone, H. Fair, S. Fairhurst, X. Fan, Q. Fang, S. Farinon, B. Farr, W. M. Farr, M. Favata, M. Fays, H. Fehrmann, M. M. Fejer, D. Feldbaum, I. Ferrante, E. C. Ferreira, F. Ferrini, F. Fidecaro, L. S. Finn, I. Fiori, D. Fiorucci, R. P. Fisher, R. Flaminio, M. Fletcher, H. Fong, J.-D. Fournier, S. Franco, S. Frasca, F. Frasconi, M. Frede, Z. Frei, A. Freise, R. Frey, V. Frey, T. T. Fricke, P. Fritschel, V. V. Frolov, P. Fulda, M. Fyffe, H. A. G. Gabbard, J. R. Gair, L. Gammaitoni, S. G. Gaonkar, F. Garufi, A. Gatto, G. Gaur, N. Gehrels, G. Gemme, B. Gendre, E. Genin, A. Gennai, J. George, L. Gergely, V. Germain, Abhirup Ghosh, Archisman Ghosh, S. Ghosh, J. A. Giaime, K. D. Giardina, A. Giazotto, K. Gill, A. Glaefke, J. R. Gleason, E. Goetz, R. Goetz, L. Gondan, G. González, J. M. Gonzalez Castro, A. Gopakumar, N. A. Gordon, M. L. Gorodetsky, S. E. Gossan, M. Gosselin, R. Gouaty, C. Graef, P. B. Graff, M. Granata, A. Grant, S. Gras, C. Gray, G. Greco, A. C. Green, R. J. S. Greenhalgh, P. Groot, H. Grote, S. Grunewald, G. M. Guidi, X. Guo, A. Gupta, M. K. Gupta, K. E. Gushwa, E. K. Gustafson, R. Gustafson, J. J. Hacker, B. R. Hall, E. D. Hall, G. Hammond, M. Haney, M. M. Hanke, J. Hanks, C. Hanna, M. D. Hannam, J. Hanson, T. Hardwick, J. Harms, G. M. Harry, I. W. Harry, M. J. Hart, M. T. Hartman, C.-J. Haster, K. Haughian, J. Healy, J. Heefner, A. Heidmann, M. C. Heintze, G. Heinzel, H. Heitmann, P. Hello, G. Hemming, M. Hendry, I. S. Heng, J. Hennig, A. W. Heptonstall, M. Heurs, S. Hild, D. Hoak, K. A. Hodge, D. Hofman, S. E. Hollitt, K. Holt, D. E. Holz, P. Hopkins, D. J. Hosken, J. Hough, E. A. Houston, E. J. Howell, Y. M. Hu, S. Huang, E. A. Huerta, D. Huet, B. Hughey, S. Husa, S. H. Huttner, T. Huynh-Dinh, A. Idrisy, N. Indik, D. R. Ingram, R. Inta, H. N. Isa, J.-M. Isac, M. Isi, G. Islas, T. Isogai, B. R. Iyer, K. Izumi, M. B. Jacobson, T. Jacqmin, H. Jang,

K. Jani, P. Jaranowski, S. Jawahar, F. Jiménez-Forteza, W. W. Johnson, N. K. Johnson-McDaniel, D. I. Jones, R. Jones, R. J. G. Jonker, L. Ju, K. Haris, C. V. Kalaghatgi, V. Kalogera, S. Kandhasamy, G. Kang, J. B. Kanner, S. Karki, M. Kasprzack, E. Katsavounidis, W. Katzman, S. Kaufer, T. Kaur, K. Kawabe, F. Kawazoe, F. Kéfélian, M. S. Kehl, D. Keitel, D. B. Kelley, W. Kells, R. Kennedy, D. G. Keppel, J. S. Key, A. Khalaidovski, F. Y. Khalili, I. Khan, S. Khan, Z. Khan, E. A. Khazanov, N. Kijbunchoo, C. Kim, J. Kim, K. Kim, Nam-Gyu Kim, Namjun Kim, Y.-M. Kim, E. J. King, P. J. King, D. L. Kinzel, J. S. Kissel, L. Kleybolte, S. Klimenko, S. M. Koehlenbeck, K. Kokeyama, S. Koley, V. Kondrashov, A. Kontos, S. Koranda, M. Korobko, W. Z. Korth, I. Kowalska, D. B. Kozak, V. Kringel, B. Krishnan, A. Królak, C. Krueger, G. Kuehn, P. Kumar, R. Kumar, L. Kuo, A. Kutynia, P. Kwee, B. D. Lackey, M. Landry, J. Lange, B. Lantz, P. D. Lasky, A. Lazzarini, C. Lazzaro, P. Leaci, S. Leavey, E. O. Lebigot, C. H. Lee, H. K. Lee, H. M. Lee, K. Lee, A. Lenon, M. Leonardi, J. R. Leong, N. Leroy, N. Letendre, Y. Levin, B. M. Levine, T. G. F. Li, A. Libson, T. B. Littenberg, N. A. Lockerbie, J. Logue, A. L. Lombardi, L. T. London, J. E. Lord, M. Lorenzini, V. Loriette, M. Lormand, G. Losurdo, J. D. Lough, C. O. Lousto, G. Lovelace, H. Lück, A. P. Lundgren, J. Luo, R. Lynch, Y. Ma, T. MacDonald, B. Machenschalk, M. MacInnis, D. M. Macleod, F. Magaña-Sandoval, R. M. Magee, M. Mageswaran, E. Majorana, I. Maksimovic, V. Malvezzi, N. Man, I. Mandel, V. Mandic, V. Mangano, G. L. Mansell, M. Manske, M. Mantovani, F. Marchesoni, F. Marion, S. Márka, Z. Márka, A. S. Markosyan, E. Maros, F. Martelli, L. Martellini, I. W. Martin, R. M. Martin, D. V. Martynov, J. N. Marx, K. Mason, A. Masserot, T. J. Massinger, M. Masso-Reid, F. Matichard, L. Matone, N. Mavalvala, N. Mazumder, G. Mazzolo, R. McCarthy, D. E. McClelland, S. McCormick, S. C. McGuire, G. McIntyre, J. McIver, D. J. McManus, S. T. McWilliams, D. Meacher, G. D. Meadors, J. Meidam, A. Melatos, G. Mendell, D. Mendoza-Gandara, R. A. Mercer, E. Merilh, M. Merzougui, S. Meshkov, C. Messenger, C. Messick, P. M. Meyers, F. Mezzani, H. Miao, C. Michel, H. Middleton, E. E. Mikhailov, L. Milano, J. Miller, M. Millhouse, Y. Minenkov, J. Ming, S. Mirshekari, C. Mishra, S. Mitra, V. P. Mitrofanov, G. Mitselmakher, R. Mittleman, A. Moggi, M. Mohan, S. R. P. Mohapatra, M. Montani, B. C. Moore, C. J. Moore, D. Moraru, G. Moreno, S. R. Morriss, K. Mossavi, B. Mours, C. M. Mow-Lowry, C. L. Mueller, G. Mueller, A. W. Muir, Arunava Mukherjee, D. Mukherjee, S. Mukherjee, N. Mukund, A. Mullavey, J. Munch, D. J. Murphy, P. G. Murray, A. Mytidis, I. Nardecchia, L. Naticchioni, R. K. Nayak, V. Necula, K. Nedkova, G. Nelemans, M. Neri, A. Neunzert, G. Newton, T. T. Nguyen, A. B. Nielsen, S. Nissanke, A. Nitz, F. Nocera, D. Nolting, M. E. N. Normandin, L. K. Nuttall, J. Oberling, E. Ochsner, J. O'Dell, E. Oelker, G. H. Ogin, J. J. Oh, S. H. Oh, F. Ohme, M. Oliver, P. Oppermann, Richard J. Oram, B. O'Reilly, R. O'Shaughnessy, C. D. Ott, D. J. Ottaway, R. S. Ottens, H. Overmier, B. J. Owen, A. Pai, S. A. Pai, J. R. Palamos, O. Palashov, C. Palomba, A. Pal-Singh, H. Pan, Y. Pan, C. Pankow, F. Pannarale, B. C. Pant, F. Paoletti, A. Paoli, M. A. Papa, H. R. Paris, W. Parker, D. Pascucci, A. Pasqualetti, R. Passaquieti, D. Passuello, B. Patricelli, Z. Patrick, B. L. Pearlstone, M. Pedraza, R. Pedurand, L. Pekowsky, A. Pele, S. Penn, A. Perreca, H. P. Pfeiffer, M. Phelps, O. Piccinni, M. Pichot, M. Pickenpack, F. Piergiovanni, V. Pierro, G. Pillant, L. Pinard, I. M. Pinto, M. Pitkin, J. H. Poeld, R. Poggiani, P. Popolizio, A. Post, J. Powell, J. Prasad, V. Predoi, S. S. Premachandra, T. Prestegard, L. R. Price, M. Prijatelj, M. Principe, S. Privitera, R. Prix, G. A. Prodi, L. Prokhorov, O. Puncken, M. Punturo, P. Puppo, M. Pürrer, H. Qi, J. Qin, V. Quetschke, E. A. Quintero, R. Quitzow-James, F. J. Raab, D. S. Rabeling, H. Radkins, P. Raffai, S. Raja, M. Rakhmanov, C. R. Ramet, P. Rapagnani, V. Raymond, M. Razzano, V. Re, J. Read, C. M. Reed, T. Regimbau, L. Rei, S. Reid, D. H. Reitze, H. Rew, S. D. Reyes, F. Ricci, K. Riles, N. A. Robertson, R. Robie, F. Robinet, A. Rocchi, L. Rolland, J. G. Rollins, V. J. Roma, J. D. Romano, R. Romano, G. Romanov, J. H. Romie, D. Rosińska, S. Rowan, A. Rüdiger, P. Ruggi, K. Ryan, S. Sachdev, T. Sadecki, L. Sadeghian, L. Salconi, M. Saleem, F. Salemi, A. Samajdar, L. Sammut, L. M. Sampson, E. J. Sanchez, V. Sandberg, B. Sandeen, G. H. Sanders, J. R. Sanders, B. Sassolas, B. S. Sathyaprakash, P. R. Saulson,

O. Sauter, R. L. Savage, A. Sawadsky, P. Schale, R. Schilling, J. Schmidt, P. Schmidt, R. Schnabel, R. M. S. Schofield, A. Schönbeck, E. Schreiber, D. Schuette, B. F. Schutz, J. Scott, S. M. Scott, D. Sellers, A. S. Sengupta, D. Sentenac, V. Sequino, A. Sergeev, G. Serna, Y. Setyawati, A. Sevigny, D. A. Shaddock, T. Shaffer, S. Shah, M. S. Shahriar, M. Shaltev, Z. Shao, B. Shapiro, P. Shawhan, A. Sheperd, D. H. Shoemaker, D. M. Shoemaker, K. Siellez, X. Siemens, D. Sigg, A. D. Silva, D. Simakov, A. Singer, L. P. Singer, A. Singh, R. Singh, A. Singhal, A. M. Sintes, B. J. J. Slagmolen, J. R. Smith, M. R. Smith, N. D. Smith, R. J. E. Smith, E. J. Son, B. Sorazu, F. Sorrentino, T. Souradeep, A. K. Srivastava, A. Staley, M. Steinke, J. Steinlechner, S. Steinlechner, D. Steinmeyer, B. C. Stephens, S. P. Stevenson, R. Stone, K. A. Strain, N. Straniero, G. Stratta, N. A. Strauss, S. Strigin, R. Sturani, A. L. Stuver, T. Z. Summerscales, L. Sun, P. J. Sutton, B. L. Swinkels, M. J. Szczepańczyk, M. Tacca, D. Talukder, D. B. Tanner, M. Tápai, S. P. Tarabrin, A. Taracchini, R. Taylor, T. Theeg, M. P. Thirugnanasambandam, E. G. Thomas, M. Thomas, P. Thomas, K. A. Thorne, K. S. Thorne, E. Thrane, S. Tiwari, V. Tiwari, K. V. Tokmakov, C. Tomlinson, M. Tonelli, C. V. Torres, C. I. Torrie, D. Töyrä, F. Travasso, G. Traylor, D. Trifirò, M. C. Tringali, L. Trozzo, M. Tse, M. Turconi, D. Tuyenbayev, D. Ugolini, C. S. Unnikrishnan, A. L. Urban, S. A. Usman, H. Vahlbruch, G. Vajente, G. Valdes, M. Vallisneri, N. van Bakel, M. van Beuzekom, J. F. J. van den Brand, C. Van Den Broeck, D. C. Vander-Hyde, L. van der Schaaf, J. V. van Heijningen, A. A. van Veggel, M. Vardaro, S. Vass, M. Vasúth, R. Vaulin, A. Vecchio, G. Vedovato, J. Veitch, P. J. Veitch, K. Venkateswara, D. Verkindt, F. Vetrano, A. Viceré, S. Vinciguerra, D. J. Vine, J.-Y. Vinet, S. Vitale, T. Vo, H. Vocca, C. Vorvick, D. Voss, W. D. Vousden, S. P. Vyatchanin, A. R. Wade, L. E. Wade, M. Wade, S. J. Waldman, M. Walker, L. Wallace, S. Walsh, G. Wang, H. Wang, M. Wang, X. Wang, Y. Wang, H. Ward, R. L. Ward, J. Warner, M. Was, B. Weaver, L.-W. Wei, M. Weinert, A. J. Weinstein, R. Weiss, T. Welborn, L. Wen, P. Weßels, T. Westphal, K. Wette, J. T. Whelan, S. E. Whitcomb, D. J. White, B. F. Whiting, K. Wiesner, C. Wilkinson, P. A. Willems, L. Williams, R. D. Williams, A. R. Williamson, J. L. Willis, B. Willke, M. H. Wimmer, L. Winkelmann, W. Winkler, C. C. Wipf, A. G. Wiseman, H. Wittel, G. Woan, J. Worden, J. L. Wright, G. Wu, J. Yablon, I. Yakushin, W. Yam, H. Yamamoto, C. C. Yancey, M. J. Yap, H. Yu, M. Yvert, A. Zadrożny, L. Zangrando, M. Zanolin, J.-P. Zendri, M. Zevin, F. Zhang, L. Zhang, M. Zhang, Y. Zhang, C. Zhao, M. Zhou, Z. Zhou, X. J. Zhu, M. E. Zucker, S. E. Zuraw, and J. Zweizig. Observation of Gravitational Waves from a Binary Black Hole Merger. *Physical Review Letters*, 116(6):061102, February 2016. doi: 10.1103/PhysRevLett.116.061102.

Zheyu Lin, Ning Jiang, Xu Kong, Shifeng Huang, Zesen Lin, Jiazheng Zhu, and Yibo Wang. The Luminosity Function of Tidal Disruption Flares for the ZTF-I Survey. *The Astrophysical Journal*, 939:L33, November 2022. ISSN 0004-637X. doi: 10.3847/2041-8213/ac9c63.

Itai Linial and Re'em Sari. Stellar Distributions around a Supermassive Black Hole: Strong-segregation Regime Revisited. *The Astrophysical Journal*, 940:101, December 2022. ISSN 0004-637X. doi: 10.3847/1538-4357/ac9bfd.

Chang Liu, Brenna Mockler, Enrico Ramirez-Ruiz, Ricardo Yarza, Jamie A. P. Law-Smith, Smadar Naoz, Denyz Melchor, and Sanaea Rose. Tidal Disruption Events from Eccentric Orbits and Lessons Learned from the Noteworthy ASASSN-14ko. *The Astrophysical Journal*, 944:184, February 2023a. ISSN 0004-637X. doi: 10.3847/1538-4357/acafe1.

Z. Liu, A. Malyali, M. Krumpe, D. Homan, A. J. Goodwin, I. Grotova, A. Kawka, A. Rau, A. Merloni, G. E. Anderson, J. C. A. Miller-Jones, A. G. Markowitz, S. Ciroi, F. Di Mille, M. Schramm, S. Tang, D. A. H. Buckley, M. Gromadzki, C. Jin, and J. Buchner. Deciphering the extreme X-ray variability of the nuclear transient eRASSt J045650.3-203750. A likely repeating partial tidal disruption event. *Astronomy and Astrophysics*, 669:A75, January 2023b. ISSN 0004-6361. doi: 10.1051/0004-6361/202244805.

G. Lodato, A. R. King, and J. E. Pringle. Stellar disruption by a supermassive black hole: Is the light curve really proportional to t-5/3? *Monthly Notices of the Royal Astronomical Society*, 392(1):332–340, January 2009. ISSN 0035-8711. doi: 10.1111/j.1365-2966.2008.14049.x.

Giuseppe Lodato and Elena M. Rossi. Multiband light curves of tidal disruption events. *Monthly Notices of the Royal Astronomical Society*, 410(1):359–367, January 2011. ISSN 0035-8711. doi: 10.1111/j.1365-2966.2010.17448.x.

Chelsea L. MacLeod and Craig J. Hogan. Precision of Hubble constant derived using black hole binary absolute distances and statistical redshift information. *Physical Review D*, 77:043512, February 2008. ISSN 1550-79980556-2821. doi: 10.1103/PhysRevD.77.043512.

John Magorrian and Scott Tremaine. Rates of tidal disruption of stars by massive central black holes. *Monthly Notices of the Royal Astronomical Society*, 309(2):447–460, October 1999. ISSN 0035-8711, 1365-2966. doi: 10.1046/j.1365-8711.1999.02853.x.

Deborah Mainetti, Alessandro Lupi, Sergio Campana, Monica Colpi, Eric R. Coughlin, James Guillochon, and Enrico Ramirez-Ruiz. The fine line between total and partial tidal disruption events. *Astronomy and Astrophysics*, 600:A124, April 2017. ISSN 0004-6361. doi: 10.1051/0004-6361/201630092.

A. Malyali, Z. Liu, A. Rau, I. Grotova, A. Merloni, A. J. Goodwin, G. E. Anderson, J. C. A. Miller-Jones, A. Kawka, R. Arcodia, J. Buchner, K. Nandra, D. Homan, and M. Krumpe. The rebrightening of a ROSAT-selected tidal disruption event: Repeated weak partial disruption flares from a quiescent galaxy? *Monthly Notices of the Royal Astronomical Society*, 520:3549–3559, April 2023. ISSN 0035-8711. doi: 10.1093/mnras/stad022.

Giovanni Mazzolari, Matteo Bonetti, Alberto Sesana, Riccardo M. Colombo, Massimo Dotti, Giuseppe Lodato, and David Izquierdo-Villalba. Extreme mass ratio inspirals triggered by massive black hole binaries: From relativistic dynamics to cosmological rates. *Monthly Notices of the Royal Astronomical Society*, 516:1959–1976, October 2022. ISSN 0035-8711. doi: 10.1093/mnras/stac2255.

David Merritt. *Dynamics and Evolution of Galactic Nuclei*. Princeton University Press, July 2013. ISBN 978-0-691-15860-0.

David Merritt. Gravitational Encounters and the Evolution of Galactic Nuclei. IV. Captures Mediated by Gravitational-Wave Energy Loss. *The Astrophysical Journal*, 814(1):57, November 2015. ISSN 1538-4357. doi: 10.1088/0004-637X/814/1/57.

David Merritt and Jianxiang Wang. Loss Cone Refilling Rates in Galactic Nuclei. *The Astrophysical Journal*, 621:L101–L104, March 2005. ISSN 0004-637X. doi: 10.1086/429272.

Brian D. Metzger, Nicholas C. Stone, and Shmuel Gilbaum. Interacting Stellar EMRIs as Sources of Quasi-periodic Eruptions in Galactic Nuclei. *The Astrophysical Journal*, 926(1):101, February 2022. ISSN 0004-637X, 1538-4357. doi: 10.3847/1538-4357/ac3ee1.

Patrick R. Miles, Eric R. Coughlin, and C. J. Nixon. Fallback Rates from Partial Tidal Disruption Events. *The Astrophysical Journal*, 899:36, August 2020. ISSN 0004-637X. doi: 10.3847/1538-4357/ab9c9f.

M. Coleman Miller, Marc Freitag, Douglas P. Hamilton, and Vanessa M. Lauburg. Binary Encounters with Supermassive Black Holes: Zero-Eccentricity LISA Events. *The Astrophysical Journal*, 631:L117–L120, October 2005. ISSN 0004-637X. doi: 10.1086/497335.

Smadar Naoz, Sanaea C. Rose, Erez Michaely, Denyz Melchor, Enrico Ramirez-Ruiz, Brenna Mockler, and Jeremy D. Schnittman. The Combined Effects of Two-body Relaxation Processes and the Eccentric Kozai–Lidov Mechanism on the Extreme-mass-ratio Inspirals Rate. *The Astrophysical Journal Letters*, 927(1):L18, March 2022. ISSN 2041-8205. doi: 10.3847/2041-8213/ac574b.

Nadine Neumayer, Anil Seth, and Torsten Böker. Nuclear star clusters. *The Astronomy and Astrophysics Review*, 28(1):4, July 2020. ISSN 1432-0754. doi: 10.1007/s00159-020-00125-0.

Zhen Pan and Huan Yang. Formation rate of extreme mass ratio inspirals in active galactic nuclei. *Physical Review D*, 103(10):103018, May 2021. doi: 10.1103/PhysRevD.103.103018.

Zhen Pan, Zhenwei Lyu, and Huan Yang. Mass-gap extreme mass ratio inspirals. *Physical Review D*, 105 (8):083005, April 2022. doi: 10.1103/PhysRevD.105.083005.

Anna V. Payne, Benjamin J. Shappee, Jason T. Hinkle, Patrick J. Vallely, Christopher S. Kochanek, Thomas W. S. Holoien, Katie Auchettl, K. Z. Stanek, Todd A. Thompson, Jack M. M. Neustadt, Michael A. Tucker, James D. Armstrong, Joseph Brimacombe, Paulo Cacella, Robert Cornect, Larry Denneau, Michael M. Fausnaugh, Heather Flewelling, Dirk Grupe, A. N. Heinze, Laura A. Lopez, Berto Monard, Jose L. Prieto, Adam C. Schneider, Scott S. Sheppard, John L. Tonry, and Henry Weiland. ASASSN-14ko is a Periodic Nuclear Transient in ESO 253-G003. *The Astrophysical Journal*, 910:125, April 2021. ISSN 0004-637X. doi: 10.3847/1538-4357/abe38d.

Hugo Pfister, Marta Volonteri, Jane Lixin Dai, and Monica Colpi. Enhancement of the tidal disruption event rate in galaxies with a nuclear star cluster: From dwarfs to ellipticals. *Monthly Notices of the Royal Astronomical Society*, 497:2276–2285, September 2020. ISSN 0035-8711. doi: 10.1093/mnras/staa1962.

E. S. Phinney. Manifestations of a Massive Black Hole in the Galactic Center. 136:543, January 1989.

M. Polkas, S. Bonoli, E. Bortolas, D. Izquierdo-Villalba, A. Sesana, L. Broggi, N. Hoyer, and D. Spinoso. Demographics of Tidal Disruption Events with L-Galaxies: I. Volumetric TDE rates and the abundance of Nuclear Star Clusters, December 2023.

S. F. Portegies Zwart and A. T. Meinen. Quick method for calculating energy dissipation in tidal interaction. *Astronomy and Astrophysics*, 280:174–176, December 1993. ISSN 0004-6361.

W. H. Press and S. A. Teukolsky. On formation of close binaries by two-body tidal capture. *The Astrophysical Journal*, 213:183–192, April 1977. ISSN 0004-637X. doi: 10.1086/155143.

Miguel Preto and Pau Amaro-Seoane. On strong mass segregation around a massive black hole: Implications for lower-frequency gravitational-wave astrophysics. *The Astrophysical Journal*, 708(1):L42–L46, January 2010. ISSN 2041-8205, 2041-8213. doi: 10.1088/2041-8205/708/1/L42.

Ismail Qunbar and Nicholas C. Stone. Enhanced Extreme Mass Ratio Inspiral Rates into Intermediate Mass Black Holes, April 2023.

Martin J. Rees. Tidal disruption of stars by black holes of 106–108 solar masses in nearby galaxies. *Nature*, 333(6173):523–528, June 1988. ISSN 1476-4687. doi: 10.1038/333523a0.

Taeho Ryu, Julian Krolik, Tsvi Piran, and Scott C. Noble. Tidal Disruptions of Main-sequence Stars. III. Stellar Mass Dependence of the Character of Partial Disruptions. *The Astrophysical Journal*, 904:100, December 2020a. ISSN 0004-637X. doi: 10.3847/1538-4357/abb3ce.

Taeho Ryu, Julian Krolik, Tsvi Piran, and Scott C. Noble. Tidal Disruptions of Main-sequence Stars. IV. Relativistic Effects and Dependence on Black Hole Mass. *The Astrophysical Journal*, 904:101, December 2020b. ISSN 0004-637X. doi: 10.3847/1538-4357/abb3cc.

I. Sagiv, A. Gal-Yam, E. O. Ofek, E. Waxman, O. Aharonson, S. R. Kulkarni, E. Nakar, D. Maoz, B. Trakhtenbrot, E. S. Phinney, J. Topaz, C. Beichman, J. Murthy, and S. P. Worden. SCIENCE WITH A WIDE-FIELD UV TRANSIENT EXPLORER. *The Astronomical Journal*, 147(4):79, March 2014. ISSN 1538-3881. doi: 10.1088/0004-6256/147/4/79.

Re'em Sari and Giacomo Fragione. Tidal Disruption Events, Main-sequence Extreme-mass Ratio Inspirals, and Binary Star Disruptions in Galactic Nuclei. *The Astrophysical Journal*, 885:24, November 2019. ISSN 0004-637X. doi: 10.3847/1538-4357/ab43df.

R. Saxton, S. Komossa, K. Auchettl, and P. G. Jonker. Correction to: X-Ray Properties of TDEs. *Space Science Reviews*, 217:18, February 2021. ISSN 0038-6308. doi: 10.1007/s11214-020-00759-7.

S. Sazonov, M. Gilfanov, P. Medvedev, Y. Yao, G. Khorunzhev, A. Semena, R. Sunyaev, R. Burenin, A. Lyapin, A. Meshcheryakov, G. Uskov, I. Zaznobin, K. A. Postnov, A. V. Dodin, A. A. Belinski, A. M. Cherepashchuk, M. Eselevich, S. N. Dodonov, A. A. Grokhovskaya, S. S. Kotov, I. F. Bikmaev, R. Ya Zhuchkov, R. I. Gumerov, S. van Velzen, and S. Kulkarni. First tidal disruption events discovered by SRG/eROSITA: X-ray/optical properties and X-ray luminosity function at $z < 0.6$. *Monthly Notices of the Royal Astronomical Society*, 508:3820–3847, December 2021. ISSN 0035-8711. doi: 10.1093/mnras/stab2843.

R. Schodel, A. Feldmeier, D. Kunneriath, S. Stolovy, N. Neumayer, P. Amaro-Seoane, and S. Nishiyama. Surface Brightness Profile of the Milky Way's Nuclear Star Cluster. *Astronomy & Astrophysics*, 566:A47, June 2014. ISSN 0004-6361, 1432-0746. doi: 10.1051/0004-6361/201423481.

S. L. Shapiro and A. B. Marchant. Star clusters containing massive, central black holes - Monte Carlo simulations in two-dimensional phase space. *The Astrophysical Journal*, 225:603, October 1978. ISSN 0004-637X, 1538-4357. doi: 10.1086/156521.

Jean J. Somalwar, Vikram Ravi, Yuhan Yao, Muryel Guolo, Matthew Graham, Erica Hammerstein, Wenbin Lu, Matt Nicholl, Yashvi Sharma, Robert Stein, Sjoert van Velzen, Eric C. Bellm, Michael W. Coughlin, Steven L. Groom, Frank J. Masci, and Reed Riddle. The first systematically identified repeating partial tidal disruption event, October 2023.

Volker Springel, Simon D. M. White, Adrian Jenkins, Carlos S. Frenk, Naoki Yoshida, Liang Gao, Julio Navarro, Robert Thacker, Darren Croton, John Helly, John A. Peacock, Shaun Cole, Peter Thomas, Hugh Couchman, August Evrard, Jörg Colberg, and Frazer Pearce. Simulations of the formation, evolution and clustering of galaxies and quasars. *Nature*, 435(7042):629–636, June 2005. ISSN 1476-4687. doi: 10.1038/nature03597.

Nicholas C. Stone and Brian D. Metzger. Rates of Stellar Tidal Disruption as Probes of the Supermassive Black Hole Mass Function. *Monthly Notices of the Royal Astronomical Society*, 455(1):859–883, January 2016. ISSN 1365-2966, 0035-8711. doi: 10.1093/mnras/stv2281.

Nicholas C Stone, Aleksey Generozov, Eugene Vasiliev, and Brian D Metzger. The delay time distribution of tidal disruption flares. *Monthly Notices of the Royal Astronomical Society*, 480(4):5060–5077, November 2018. ISSN 0035-8711. doi: 10.1093/mnras/sty2045.

Nicholas C. Stone, Eugene Vasiliev, Michael Kesden, Elena M. Rossi, Hagai B. Perets, and Pau Amaro-Seoane. Rates of Stellar Tidal Disruption. *Space Science Reviews*, 216(3):35, April 2020. ISSN 0038-6308, 1572-9672. doi: 10.1007/s11214-020-00651-4.

Scott Tremaine, Douglas O. Richstone, Yong-Ik Byun, Alan Dressler, S. M. Faber, Carl Grillmair, John Kormendy, and Tod R. Lauer. A Family of Models for Spherical Stellar Systems. *The Astronomical Journal*, 107:634, February 1994. ISSN 0004-6256. doi: 10.1086/116883.

Andrew Ulmer. Flares from the Tidal Disruption of Stars by Massive Black Holes. *The Astrophysical Journal*, 514:180–187, March 1999. ISSN 0004-637X. doi: 10.1086/306909.

Sjoert van Velzen, Suvi Gezari, Erica Hammerstein, Nathaniel Roth, Sara Frederick, Charlotte Ward, Tiara Hung, S. Bradley Cenko, Robert Stein, Daniel A. Perley, Kirsty Taggart, Ryan J. Foley, Jesper Sollerman, Nadejda Blagorodnova, Igor Andreoni, Eric C. Bellm, Valery Brinnel, Kishalay De, Richard Dekany, Michael Feeney, Christoffer Fremling, Matteo Giomi, V. Zach Golkhou, Matthew J. Graham, Anna. Y. Q. Ho, Mansi M. Kasliwal, Charles D. Kilpatrick, Shrinivas R. Kulkarni, Thomas Kupfer, Russ R. Laher, Ashish Mahabal, Frank J. Masci, Adam A. Miller, Jakob Nordin, Reed Riddle, Ben Rusholme, Jakob van Santen, Yashvi Sharma, David L. Shupe, and Maayane T. Soumagnac. Seventeen Tidal Disruption Events from the First Half of ZTF Survey Observations: Entering a New Era of Population Studies. *The Astrophysical Journal*, 908:4, February 2021. ISSN 0004-637X. doi: 10.3847/1538-4357/abc258.

Eugene Vasiliev. A new Fokker-Planck approach for relaxation-driven evolution of galactic nuclei. *arXiv:1709.04467 [astro-ph]*, September 2017. doi: 10.3847/1538-4357/aa8cc8.

T. Wevers, E. R. Coughlin, D. R. Pasham, M. Guolo, Y. Sun, S. Wen, P. G. Jonker, A. Zabludoff, A. Malyali, R. Arcodia, Z. Liu, A. Merloni, A. Rau, I. Grotova, P. Short, and Z. Cao. Live to Die Another Day: The Rebrightening of AT 2018fyk as a Repeating Partial Tidal Disruption Event. *The Astrophysical Journal*, 942:L33, January 2023. ISSN 0004-637X. doi: 10.3847/2041-8213/ac9f36.

Yuhan Yao, Vikram Ravi, Suvi Gezari, Sjoert van Velzen, Wenbin Lu, Steve Schulze, Jean J. Somalwar, S. R. Kulkarni, Erica Hammerstein, Matt Nicholl, Matthew J. Graham, Daniel A. Perley, S. Bradley Cenko, Robert Stein, Angelo Ricarte, Urmila Chadayammuri, Eliot Quataert, Eric C. Bellm, Joshua S. Bloom, Richard Dekany, Andrew J. Drake, Steven L. Groom, Ashish A. Mahabal, Thomas A. Prince, Reed Riddle, Ben Rusholme, Yashvi Sharma, Jesper Sollerman, and Lin Yan. Tidal Disruption Event Demographics with the Zwicky Transient Facility: Volumetric Rates, Luminosity Function, and Implications for the Local Black Hole Mass Function. *The Astrophysical Journal*, 955:L6, September 2023. ISSN 0004-637X. doi: 10.3847/2041-8213/acf216.

Fupeng Zhang and Pau Amaro Seoane. Monte-Carlo Stellar Dynamics near Massive Black Holes: Two-dimensional Fokker-Planck solutions of multiple mass components, June 2023.

Shiyan Zhong, Shuo Li, Peter Berczik, and Rainer Spurzem. Revisit the Rate of Tidal Disruption Events: The Role of the Partial Tidal Disruption Event. *The Astrophysical Journal*, 933:96, July 2022. ISSN 0004-637X. doi: 10.3847/1538-4357/ac71ad.

Acknowledgements

I acknowledge the financial support provided under the European Union's H2020 ERC Consolidator Grant «Binary Massive Black Hole Astrophysics» (B Massive, grant agreement: 818691), funding from MIUR under grant «PRIN 2017-MB8AEZ», and funding from the Ph.D. school «Scuola di dottorato dell'Università degli Studi di Milano Bicocca».